US

University of Sussex

Quantum Enhanced Matter-Wave Gravimetry

Michail Kritsotakis

Department of Physics & Astronomy

University of Sussex

Submitted for the degree of Doctor of Philosophy

July 2020

Declaration

I hereby declare that the results presented in this thesis are product of my own research, carried out under the supervision of both of my supervisors. To the best of my knowledge all sources used for my research has been appropriately acknowledged throughout this thesis. In addition, this thesis has not been and will not be submitted in whole or in part to another University for the award of any other degree.

Some of the results presented in this thesis has been already published, are available in preprints or will be soon realised as:

- Kritsotakis, Michail, Stuart S. Szigeti, Jacob A. Dunningham, and Simon A. Haine. "Optimal matter-wave gravimetry." Physical Review A 98, no. 2 (2018): 023629.

- Kritsotakis, Michail, Jacob A. Dunningham, and Simon A. Haine. "Spin squeezing of a Bose-Einstein condensate via a quantum nondemolition measurement for quantum-enhanced atom interferometry." Physical Review A 103.2 (2021): 023318.

- Kritsotakis, Michail, Jacob A. Dunningham, and Simon A. Haine. "Improving One-Axis Twisting Using Cavity Feedback", in preparation (2020).

<div align="right">Michail Kritsotakis</div>

UNIVERSITY OF SUSSEX

Michail Kritsotakis, Doctor of Philosophy

Quantum Enhanced Matter-Wave Gravimetry

Summary

Over the past two decades there has been considerable and growing interest in the development of quantum sensors. These are devices whose function is based on quantum systems and offer the potential for unprecedented sensitivity in a range of measurements. This PhD has developed three different theoretical projects examining the sensitivity improvement of these devices with a focus on atom gravimeters, which are particularly useful for measuring inertial quantities such as rotations and accelerations. We have investigated the theoretical sensitivity limits of atom gravimeters and we examined different entanglement-enhanced schemes, in order to increase their performance.

To start with, we used tools from estimation theory, in order to quantify the performance of current atom gravimeters. We showed that there is additional metrological potential in these devices, and that we can extract all this information by making innovative measurements, other than the conventional population difference measurement. Our analysis introduces a new way of evaluating the performance of atom gravimeters that could influence future sensor designs.

In addition, we examined entanglement-enhanced schemes, in order to improve the performance of quantum sensors, which are limited by the atom shot-noise limit. We considered entanglement generation schemes based on atom-light interactions, in order for them to be compatible with atom interferometer based sensors. More particularly, we ex-

amined a quantum non-demolition measurement scheme and an one-axis-twisting scheme with cavity feedback. In both schemes we incorporated relevant decoherence mechanisms and we analysed how the optimum parameter regime can be found, by balancing between coherence loss and spin-squeezing strength. We also examined several modifications in both models that could offer additional improvements. The results presented here could have a big impact on the future design and understanding of atom-based quantum-enhanced sensors.

To my parents and sister,
who gave me everything...

Acknowledgements

As all journeys, this would also come to an end soon. Completing my PhD course was a wonderful journey and one of the most exciting experiences in my life. As all things in life, there were some good and bad moments through that time. I would like to thank here the people who were by my side, making the good times even better, while they also supported me during the bad times.

First of all, I would like to gratefully thank my two supervisors for the fantastic opportunity they gave me. I would like to thank my first supervisor Jacob Dunningham for his guidance and support throughout all these years. Jacob, thank you for keeping your door always open to me, for being so encouraging and willing to help. Also, thank you for the very innovative ideas and all the help relevant to physics projects. I also would like thank my second supervisor Simon Haine for all the great project ideas, as well as for his boundless help to enlighten me on the physics behind those projects. Thank you for all your patience, when I persistently could not understand my mistakes and for all the time you devoted helping me with my code. It was a great pleasure and experience to discuss physics, as well as other topics with both of you. I feel so lucky that I was able to work with such insightful, funny and cool people as both of you.

One of the greatest experiences of all this time was, when I travelled two times to Canberra in Australia, in order to visit Simon. Again, I want to gratefully thank both Jacob and Simon, for very generously covering all my travel expenses for those trips. I also would like to thank Nick Robins and his experimental group for covering my accommodation expenses at my first visit. I would like to specially thank here Joe Hope and his theoretical group for being such great hosts and creating a very friendly environment for me. I also would like to thank Simon and Lucy for being so helpful and friendly through my visits there and for trying to give me a wonderful time in Canberra.

I have had a great time studying at the University of Sussex. First of all, I enjoyed discussing with all the other members of Jacob's group, Paul, Anthony, James and Jesus. It was also a great pleasure meeting Sam, when he visited Simon at Sussex. I would like to specially thank Jesus and Sam for all their help and advice about physics and general issues relevant to my PhD course. In addition, I would like to thank Jean-Marc for some great moments, when I visited Paris. Last but not least, I would like to thank my office buddy Charlie, who patiently listened to me talking about my physics projects and for giving me some very useful advice at critical moments.

On a more personal note, I would like to thank all my friends back in Greece. You are fundamental constants in my life. As always, you were there for me when needed, to listen to me, support me and make sarcastic jokes about everything. Special thanks to Evan Raptis, who was there to listen every little detail of my PhD progress.

Even not enough, I believe here is the right place to thank and express my gratitude to my family, my parents and my sister. You were always there for me, supporting me financially and more importantly emotionally. You always helped me to make my dreams and my goals come true. One of them is becoming true as those lines are being written, and it would not be feasible without you in my life. Thank you for everything!

Last but not least, I would like to thank my lovely girlfriend Anthi. Thank you for

bringing me food and for your emotional support through those last hectic months, but more importantly thank you for bringing light in my life!

List of Figures

Chapter 1

Introduction

1.1 Atom Optics and Atom Interferometers

One of the main features that distinguish quantum mechanics from classical mechanics is the wave-particle duality. In the early 20th century Louis de Broglie extended the wave-particle duality notion from massless objects, such as photons, to massive particles, where he suggested that a particle with mass m and momentum p can be described as a wave with wavelength

$$\lambda = \frac{h}{p}.$$ (1.1)

This theory was supported by the subsequent electron and atom diffraction experiments [1, 2]. However, the lack of atom-optical elements, which for example would work as beam-splitters or mirrors (similarly with optics), in combination with the small size of the atomic wavelength at room temperature made the experiments in this field extremely difficult [3]. The advent of the optical laser, and the subsequent development of laser cooling and trapping techniques [4–8] led to the realization of atom-optical elements such as lenses [9, 10], mirrors [11, 12] and diffraction gratings [13]. These advances resulted in the development of atom optics, of which one important element is atom interferometry.

Atom interferometers are the atomic counterpart of optical interferometers, which are used in order to detect phase shifts, which correspond to small differences in the length of the two arms, by observing interference fringes of the optical waves. However, these optical devices are unable to measure quantities that do not interact with the electromagnetic (EM) field, such as inertial quantities. On the other hand, atom interferometers, which use the interference of atomic waves, provide us with extremely sensitive measurements of inertial quantities, such as accelerations and rotations. Also, due to the rich internal structure of an atom we can estimate EM fields, as well as we can use them as clocks.

Atom interferometers have a very similar function with their optical counterparts. Namely they operate between two different atomic states, where after some time of propagation, a phase difference accrues between the two arms, due to the interaction of the atoms with some physical process, e.g. a gravitational field. At the end, we can observe the matter-wave interference and find the total phase difference between the two arms, which is related with the parameter of the physical process we finally want to estimate, in this example the gravitational acceleration g.

The first experiments in atom interferometry were realised in 1991 by using laser-cooled alkali atoms [14–17]. Up to this day, cold atoms have been used as inputs to atom interferometers in many different experiments, measuring the local gravity [18–24], accelerations [25–28], gradients of the gravitational field [29,30], as well as rotations [31–33]. In addition, another input of atom interferometers used for inertial sensing are Bose-Einstein Condensates (BECs) [34,35], which were realised in 1995 [36,37]. We are going to discuss in more detail about BECs in Chapter 2. BECs have a narrower momentum distribution, compared to cold atoms, which makes them more robust to noise in laser pulses, realising more precise beam-splitters and mirrors [38]. That would be essential in the case of atom gravimeters, which have the Mach-Zehnder (MZ) configuration and use laser pulses, in order to realise the optical elements, as we are going to analyse in Chapters 2 and 4. However, the realisation of a BEC needs to reach temperatures below a critical value, which is accomplished by using evaporative cooling. This process reduces the temperature, by excluding the warmer atoms, and consequently limits the atom flux available to the interferometer. Hence, BECs provides us with more reliable optical elements, but with reduced atom flux compared to cold atom sources. A summary of experimental results comparing the metrological gain offered by cold atoms and BECs can be found in [39] (Fig. [2]). In this review, it has been shown that even if BECs show promising results, cold atoms offer better performances up to this date.

Atom interferometers have been used in many experiments that are trying to estimate physical constants, with extremely high precision, such as Newton's gravitational constant [40] and the fine structure constant [41]. We can also use high precision gravitational measurements, in order to experimentally test the weak equivalence principle of general relativity. This principle states that the inertial and gravitational mass are identical, leading to the universality of free fall [42]. Atom interferometers have also many geophysical applications. Using incredibly precise atom gradiometers we can optimize the extraction of resources such as gas and oil. These devices also have applications in detecting cavit-

ies before subsistence, surveying disused mineshafts, as well as in finding water reserves. There is considerable interest in measuring small signals associated with climate change and hazard monitoring, such as volcanic activity, aquifers and mass motion due to water movement, e.g. melting glaciers [43].

1.2 Gravimeters

In this thesis, we are going to focus on the case of atom gravimeters, which have the construction of the well-known MZ interferometer. Gravimeters are devices used in order to precisely measure the absolute value (absolute gravimeters), as well as differences (relative gravimeters or gravity gradiometers) of the gravitational acceleration g. Atom gravimeters can be used for both absolute and relative measurements. Before the development of atom gravimeters, the most efficient device for absolute measurements of the gravitational field were the so-called falling corner cube gravimeter (FCCG). This device uses a laser interferometer and an atomic clock, in order to measure the drop length and the time of the test mass, which is a corner cube [43, 44]. Atom gravimeters have showed better performance than FCCGs, mainly because of their increased tolerance to microseismic vibrations, and because of the lack of mechanical wear. The FCCGs are more susceptible to vibrations caused by the fall of the cube, firstly because the cube has a mass considerably larger than the atomic mass and secondly because of the smaller repetition rate compared to an atom gravimeter. Also, the fact that atom gravimeters do not excite vibrations of the floor, as FCCGs tend to, extends their applicability to a range of different sites [45]. Spring based gravimeters are very common devices for making relative measurements of the gravitational field. As their name indicates their function is based on one or more mechanical springs supporting a mass. Small gravitational signals can be detected by measuring small length differences of the spring, due to the interaction of the mass with the gravitational field. It is difficult to measure slowly varying signals over periods of months or years using these devices, because they suffer from long term instrumental drift due to changes in the length of the spring, caused by environmental factors [43, 44]. Atom gravimeters offer comparable performance to the state of the art spring gravimeters, but more importantly they do not suffer from mechanical wear, because their response to the gravitational signal depends on the atomic properties, which are fixed by laws of physics, and not on any mechanical object. Additionally, atom gravimeters are more appropriate devices for airborne and shipborne gravity surveys, due to their immunity to hysteresis effects which strongly affect the performance of spring

gravimeters during turbulence [45]. Another device which is capable of measuring gravity gradients with high stability is the superconducting gravimeter (SG), whose main function is based on the levitation of a superconducting sphere. Small changes in gravity result in large displacements of the sphere. SGs are very stable devices showing only linear instrumental drift [43, 44]. Up to this day, SGs can measure gravity signal differences with better performance than the atom gravimeters. Besides the fact that atom gravimeters can still not provide us with the best precision of relative gravity measurements, they are extremely promising drift-free devices, which are capable of making absolute and relative measurements of gravity. On the other hand, spring gravimeters and SGs require the use of an absolute gravimeter, such as an FCCG, in order to be calibrated [45]. Many geophysical applications require the measurement of gravity signals with even better precision provided by all aforementioned devices.

Atom interferometers, similarly with their optical counterparts, are ultimately limited by the projection noise of atoms, which scales like $1/\sqrt{N}$ as we are going to see in more detail in Chapter 2 and 3. To be more specific, many experiments are limited by technical noise, such as imperfect matching of Raman pulses wavefronts [45], but the atom shot-noise is the ultimate limit of all these devices in the case of N uncorrelated atoms. In that sense, there are two different paths we could follow, in order to increase the sensitivity of those devices, the classical and the quantum path. In the former, we can increase the sensitivity by increasing the available resources, namely by using a larger number of atoms, or in the case of a MZ interferometer by increasing the space-time area, which means larger initial momentum kick or increased total interferometer time, as we will analyse in more detail in Chapters 2 and 4. In the quantum path we can use appropriate quantum states as the input states of the interferometer, in order to surpass the atom shot-noise limit. As we analyse in more detail in Sec. [1.4], in this thesis we focus on quantum schemes that can be applied in conjunction with classical methods of improving the atom interferometer's sensitivity. Namely, we examine quantum models that do not limit any improvement offered by classical strategies, but rather they can be considered as an additional boost to current methods.

1.3 Quantum Enhanced Atom Interferometry

Quantum states with no correlations amongst the particles offer sensitivities constrained by he atom shot-noise limit (SNL), as mentioned at the end of the previous section. In the interferometer case, this is caused by the "quantum randomness", namely

the atom randomly chooses at which output port of the interferometer will be detected. This uncertainty, which is inherent in quantum states with no correlations, adds noise to the final signal, limiting the final sensitivity. In this section we will discuss the use of entangled states, which are states with correlations amongst the particles that can redistribute the quantum noise and consequently offer sensitivities surpassing the SNL. Conceptually entangled states are divided into two broad categories, the spin-squeezed states and the entangled non-Gaussian states (ENGS). Here, we give a brief overview of the concept of entanglement and spin squeezing, but we are going to discuss them in more detail in Chapter 3. The concept of spin-squeezing refers to the reduction of the inherent quantum noise of atomic collective spin components along a particular direction, at the expense of increased noise in the corresponding perpendicular direction, in such a way that the Heisenberg uncertainty principle is being satisfied at the end. Spin-squeezed states are Gaussian states that permit sub-shot-noise sensitivities, by making a simple population difference measurement. On the other hand, ENGS are more complicated states to be produced and they do not offer improvements with respect to a simple population difference measurement, but you need to examine higher order moments to obtain enhanced sensitivity. Despite their complexity they can provide us with an advantage in quantum enhancement, by making more complicated measurements than the simple population difference. ENGS have been generated using BECs [46], as well as cold atoms [47].

The concept of spin squeezing was introduced in the early 1990s in the context of trapped ions [48], and then the well-known one-axis-twisting (OAT) dynamics, for creating spin-squeezed states, was introduced by Kitagawa and Ueda [49]. Atomic spin-squeezing can be divided in two broad classes. In the first one we create spin-squeezed states by exploiting atom-atom interactions, while in the latter we use atom-light interactions. Initially, OAT was realised by considering the interactions amongst a small number of trapped ions [50,51]. Up to this date, to our knowledge, spin squeezing with up to 219 ions has been demonstrated [52]. Using spin squeezing, created by interactions amongst an ensemble of ions, can not result in large quantum enhancements of atom interferometers, because the total number of ions we can use with current technology is limited to small numbers, due to difficulties to isolate and trap large ensembles of ions. In addition, spin-squeezing has been generated using OAT-like interactions between the atoms in BECs [53–56]. Now, we can create spin squeezing via atom-light interactions, using two different schemes. The first one is called quantum non-demolition (QND) measurement scheme and has been demonstrated in vapour cells [57] and cold atomic ensembles [58–60]. Here, we essentially

entangle atom and light properties, through their interaction and we can reduce the atomic spin noise, by making an appropriate measurement of a light observable. In Chapter 5, we examine a QND measurement scheme in an atomic ensemble of BECs, in order to enhance the performance of an atom gravimeter. The second class produces OAT effective dynamics by using a cavity feedback scheme [61–65]. Here, the interaction of a two-level atomic ensemble with the cavity light mode is considered, while incoming coherent light detuned from the cavity resonance is driving the dynamics of the system. The number of photons entering the cavity depends on the population difference between the two atomic levels, creating entanglement amongst the atoms and resulting in effective OAT dynamics. We will examine this scheme in more detail in Chapter 6.

1.4   Quantum Sensors

As we analysed in the previous section, entangled states can provide us with sensitivities surpassing the inherent quantum noise of an atomic ensemble consisting of uncorrelated particles. However, in many cases the entanglement scheme under consideration constrains the total number of particles that we can use. Hence, although we can obtain sub-shot-noise sensitivities using entanglement, the number of atoms allowed is usually much smaller that the one we could use in uncorrelated states. That is to say, that using uncorrelated particle states would still provide us with better sensitivities compared to the entangled states. More generally, quantum sensors that use atom-atom interactions, in order to create entanglement, would be unable to surpass the performance of current state of the art devices using uncorrelated states. This is due to the following three main reasons:

- Atom-atom interactions, which create the entangled state, are also responsible for an effect known as phase diffusion, which results in sensitivity decrease. This effect does not allow for long interrogation times, due to the deleterious effect of phase diffusion to the sensitivity, limiting the performance of the sensors compared to the case of uncorrelated states, which allow longer interrogation times.

- Increasing the number of atoms in a strongly interacting system, would increase the complicated multi-mode dynamics, resulting in poor mode-matching and fringe contrast.

- Optical elements, such as beam-splitters and mirrors, are implemented in MZ interferometer configurations with Raman laser pulses. The required function of each

element is based on the two photon resonant transition of the atoms, between the two available atomic states, as we will see in more detail in Chapters 2 and 4. Atomic interactions would result in momentum change due to recoil from collisions, which would shift the atoms from the two photon transition resonance, resulting in less efficient optical elements and consequent sensitivity decrease.

In this thesis, in Chapters 5 and 6 we are going to consider entanglement-enhanced schemes, where the entanglement is generated via atom-light interactions. The reason for this is to avoid the incompatibility that the entanglement schemes via atom-atom interactions show, with the classical methods of improving the sensitivity, such as increasing the number of atoms, or considering longer interrogation times. On the contrary, the atom-light entanglement scheme can be implemented in parallel with these methods. In that way, these improved schemes, can be considered as an additional enhancement to current working quantum sensors that are based on atom interferometers.

1.5 Thesis Overview

In this thesis we examine innovative ways of increasing the performance of quantum sensors with a focus in atom gravimeters. More particularly, we use tools from the parameter estimation theory, in order to quantify the performance of current state of the art gravimeters, which use uncorrelated particle states. In addition, we examine two different entanglement-enhanced schemes using atom-light interactions, in order to enhance the performance of current devices limited by atom-shot noise.

More particularly, in **Chapter 2** we introduce some basic concepts of quantum field theory, in order to describe a system of many indistinguishable particles. We also examine the atom-light interaction, as well as we briefly present the basic function of a MZ atom interferometer. In **Chapter 3**, we introduce the concept of quantum noise and we discuss in more detail about entanglement and spin-squeezing. We also outline some basic tools from estimation theory.

The main original contribution begins in **Chapter 4**, where we use theoretical tools from estimation theory to quantify the metrological potential of an atom gravimeter. We show that there is more metrological information available in these devices than what is currently considered. We also examine modified measurements, compared to the conventional measurement of the population difference at the exit ports of the interferometer, which extract almost all this extra information. In addition, we show that the metrological

potential of an atom being in a gravitational field increases with the momentum and the position distribution of the final atomic state. This leads us to consider a modified sensor design that creates an atomic state with a larger position distribution and consequently more metrological information than the conventional design of a two mode interferometer.

In **Chapter 5** we examine a QND measurement scheme. Here, we create entanglement through atom-light interactions. More particularly, we explore the interaction of a BEC with a light field freely propagating in space. After the interaction, we measure an appropriate light observable, which contains information about the atomic ensemble. That reduces the atomic spin noise in one direction, resulting in a spin-squeezed state. We also incorporate the deleterious effect of atomic spontaneous emission and examine the dependence of the final sensitivity over all system parameters. This provides us with extremely useful information about how to reach parameter regimes that give the best sensitivity. Furthermore, we show that we can increase the scheme's performance by using squeezed incoming light. Finally, we investigate the case of using a cavity, since it increases the atom-light interaction and leads to further improvements.

In **Chapter 6** we explore the generation of entanglement and squeezed atomic states by using the effective OAT dynamics via a cavity feedback. Here, the atomic ensemble interacts with the single mode of the cavity, while an incoming laser beam, detuned from the cavity resonance, drives the whole dynamics. As before, we consider atomic spontaneous emission and again find relationships between all the relevant system parameters and how they affect the final sensitivity. We combine the OAT and QND schemes by measuring the photons leaking out of the cavity and consequently extracting some extra information about the atomic state, leading to sensitivity improvements. We also consider the use of squeezed incoming light offering again further sensitivity improvements.

Chapter 2

Background I: Atoms, Photons and their Interaction

The purpose of this chapter is to provide the reader with a basic overview of describing atoms, photons and their interaction in a quantum mechanical way. We start by describing an ensemble of many bosonic particles, using the second quantization formalism. We move to the specific case of photons and the quantization of the electromagnetic (EM) field. We also use this formalism, in order to describe a Bose-Einstein Condensate (BEC). We then give a brief outline of the interaction of atoms and light. We start with the interaction of a single atom with a single mode of light, and then we move to the many particle case interacting with a mutli-mode light field. For both cases we consider the use of a quantum and classical light field (semi-classical approximation). In addition, we introduce the Langevin formalism, in order to describe processes such as the atomic spontaneous emission, as well as photons leaking out of a cavity. Finally, we discuss atom interferometry. More particularly, we examine the case of a Mach-Zehnder (MZ) interferometer with Raman laser pulses. The introduction of all those concepts will be crucial for understanding the main chapters of this thesis.

2.1 The Quantum State of Many Particles

In classical mechanics we can describe a system of many particles by using position vectors for each particle. Also, we explore the dynamics of the system by considering trajectories showing the evolution of the position of each particle. Essentially, we consider that all particles are distinguishable and that we know the position of each particle at each time point. However, we cannot use a similar analysis for a system of many particles in

quantum mechanics. In this case the system is described by the total wave-function of all particles, which we consider as identical, in the sense that the interchange of two particles would only result in a global phase of the total wave-function and thus it has no observable consequence. To illustrate this, we use the exchange operator $\hat{P}_{ij}$, to interchange particle i and j where $i,\ j = 1, 2, ..., N$:

$$\hat{P}_{ij}\Psi(\boldsymbol{r}_1, \boldsymbol{r}_2, ..., \boldsymbol{r}_i..., \boldsymbol{r}_j, ..., \boldsymbol{r}_N, t) = e^{i\theta}\Psi(\boldsymbol{r}_1, \boldsymbol{r}_2, ..., \boldsymbol{r}_j..., \boldsymbol{r}_i, ..., \boldsymbol{r}_N, t). \tag{2.1}$$

Applying it twice we should recover the original wave-function

$$\hat{P}_{ij}^2\Psi(\boldsymbol{r}_1, ..., \boldsymbol{r}_i..., \boldsymbol{r}_j, ..., \boldsymbol{r}_N, t) = \Psi(\boldsymbol{r}_1, ..., \boldsymbol{r}_i..., \boldsymbol{r}_j, ..., \boldsymbol{r}_N, t), \tag{2.2}$$

leading us to:

$$\Psi(\boldsymbol{r}_1, \boldsymbol{r}_2, ..., \boldsymbol{r}_i..., \boldsymbol{r}_j, ..., \boldsymbol{r}_N, t) = \pm\Psi(\boldsymbol{r}_1, \boldsymbol{r}_2, ..., \boldsymbol{r}_j..., \boldsymbol{r}_i, ..., \boldsymbol{r}_N, t), \tag{2.3}$$

which tells us that the total wave-function of the system is either symmetric or anti-symmetric under the interchange of any two particles. The spin-statistics theorem states that particles with integer spin follow Bose-Einstein statistics and they are called bosons, while particles with half integer spin satisfy Fermi-Dirac statistics and they are known as fermions. The total wave-function is symmetric under the exchange of any two bosons and anti-symmetric under the exchange of any two fermions [66].

For simplicity, we start by examining the case of just two indistinguishable particles. As we mentioned above, the total wave-function of the system should be symmetric or antisymmetric under the exchange of the two particles. We write the total state of the system using the single particle states $|\phi_i\rangle$ with $i = 1, 2$

$$|\Psi\rangle_{\pm} = \frac{1}{2}\left(|\phi_1\rangle|\phi_2\rangle \pm |\phi_2\rangle|\phi_1\rangle\right), \tag{2.4}$$

where the single particle states satisfy the orthonormality condition $\langle\phi_i|\phi_j\rangle = \delta_{ij}$. The index $+ (-)$ denotes the symmetric (anti-symmetric) sum of the two possible states. Here, the first (second) *ket* refers to the first (second) particle. In case of two fermions we can see that if $|\phi_1\rangle = |\phi_2\rangle$ then $|\Psi\rangle = 0$, which is the so called Pauli exclusion principle [66]. It essentially means that two fermions can never occupy the exact same quantum state. So, for a system of two fermions the only allowed state is the antisymmetric one

$$|\Psi\rangle_{-} = \frac{1}{2}\left(|\phi_1\rangle|\phi_2\rangle - |\phi_2\rangle|\phi_1\rangle\right), \tag{2.5}$$

while the bosons have three different options, the two particles to be in the same state or in a fully symmetrized state:

$$|\phi_1\rangle|\phi_1\rangle, \qquad |\phi_2\rangle|\phi_2\rangle, \qquad \frac{1}{2}\left(|\phi_1\rangle|\phi_2\rangle + |\phi_2\rangle|\phi_1\rangle\right). \tag{2.6}$$

If we were in the case of two distinguishable particles, which satisfy the Maxwell-Boltzmann statistics and they do not have to obey any symmetry regulations [66], we would have the following possible states

$$|\phi_1\rangle|\phi_1\rangle, \qquad |\phi_2\rangle|\phi_2\rangle, \qquad |\phi_1\rangle|\phi_2\rangle, \qquad |\phi_2\rangle|\phi_1\rangle. \tag{2.7}$$

From the above analysis we conclude that fermions are not even allowed to occupy the same state, while bosons are the particles which are the most likely to occupy the same state (two out of three possible states) even compared with the distinguishable particle case, where no symmetry postulates should be satisfied (two out of four possible states).

We will now restrict our analysis to a bosonic system, as throughout this thesis we will only be interested in bosons. We already know that the total wave-function should be symmetric under the exchange of two bosons, which is something that radically reduces the size of the Hilbert space. We define the Fock state, or number state, $|n_1, n_2, ..., n_k\rangle$, as the symmmetrized permutations of the single particle mode states, where we have n_i particles in the i-th mode, in order the symmetrization condition for bosons to be met

$$|n_1, n_2, ..., n_k\rangle \equiv \sqrt{\frac{n_1! n_2! ...}{N!}} \Big(\underbrace{|\phi_1\rangle ... |\phi_1\rangle}_{n_1 \text{times}} \underbrace{|\phi_2\rangle ... \phi_2\rangle}_{n_2 \text{times}} ... \underbrace{|\phi_k\rangle ... |\phi_k\rangle}_{n_k \text{times}} +$$

$$|\phi_2\rangle \underbrace{|\phi_1\rangle ... |\phi_1\rangle}_{n_1 \text{times}} \underbrace{|\phi_2\rangle ... |\phi_2\rangle}_{n_2 - 1 \text{ times}} ... \underbrace{|\phi_k\rangle ... |\phi_k\rangle}_{n_k \text{times}} + \text{all other permutations} \Big), \tag{2.8}$$

where the total number of particles is the sum of the particles in each mode $N = n_1 + n_2 + ... + n_k$. We also present here the position representation of the Fock states $\Psi(\boldsymbol{r}_1, \boldsymbol{r}_2, ..., \boldsymbol{r}_N) = \langle \boldsymbol{r}_1, \boldsymbol{r}_2, ..., \boldsymbol{r}_N | n_1, n_2, ..., n_k \rangle$, in order for the symmetrization of the total wave-function to be more apparent

$$\Psi(\boldsymbol{r}_1, \boldsymbol{r}_2, ..., \boldsymbol{r}_N) = \sqrt{\frac{n_1! n_2! ...}{N!}} \Big(\phi_1(\boldsymbol{r}_1)\phi_1(\boldsymbol{r}_2)...\phi_1(\boldsymbol{r}_{n_1})\phi_2(\boldsymbol{r}_{n_1+1})\phi_2(\boldsymbol{r}_{n_1+2})...\phi_2(\boldsymbol{r}_{n_1+n_2})... +$$

$$\phi_2(\boldsymbol{r}_1)\phi_1(\boldsymbol{r}_2)...\phi_1(\boldsymbol{r}_{n_1})\phi_1(\boldsymbol{r}_{n_1+1})\phi_2(\boldsymbol{r}_{n_1+2})...\phi_2(\boldsymbol{r}_{n_1+n_2})... +$$

$$\text{all other permutations} \Big), \tag{2.9}$$

where $\phi_i(\boldsymbol{r}_j) = \langle \boldsymbol{r}_j | \phi_i \rangle$ is the position repsresentation of the j-th particle in the i-th single particle mode, where i runs over all the possible single mode states and $j = 1, 2, ..., N$ runs over all the particles.

The Fock state formulates a complete and orthonormal basis, thus we can write a

general many particle state as:

$$|\Psi\rangle = \sum_{n_1=0}^{\infty} \sum_{n_2=0}^{\infty} ... \sum_{n_k=0}^{\infty} ...C_{n_1,n_2,...,n_k,...}(t)|n_1, n_2, ..., n_k, ...\rangle, \tag{2.10}$$

and the orthonormality condition is written as

$$\langle n_1, n_2, ...n_k, ...|n_1', n_2', ...n_k', ...\rangle = \delta_{n_1,n_1'}\delta_{n_2,n_2'}...\delta_{n_k,n_k'}... \tag{2.11}$$

2.2   Quantization of the Radiation Field

Up to this point we were discussing bosons (particles with integer spin) in general. In this section we want to specifically treat the case of photons and examine the basic points of the quantization of the electromagnetic (EM) field. This can be found in many books [67–70], but we present it here for completeness. It is convenient to begin with the classical description of the EM field based on the free source Maxwell's equations [68,69]

$$\boldsymbol{\nabla} \times \boldsymbol{H} = \frac{\partial \boldsymbol{D}}{\partial t} \tag{2.12}$$

$$\boldsymbol{\nabla} \times \boldsymbol{E} = -\frac{\partial \boldsymbol{B}}{\partial t} \tag{2.13}$$

$$\boldsymbol{\nabla} \cdot \boldsymbol{B} = 0 \tag{2.14}$$

$$\boldsymbol{\nabla} \cdot \boldsymbol{D} = 0, \tag{2.15}$$

where $\boldsymbol{E}$, $\boldsymbol{H}$ are the electric and magnetic field respectively and they are related to the displacement and inductive vector $\boldsymbol{D}$, $\boldsymbol{B}$ respectively via

$$\boldsymbol{B} = \mu_0 \boldsymbol{H} \tag{2.16}$$

$$\boldsymbol{D} = \epsilon_0 \boldsymbol{E}. \tag{2.17}$$

Here, ϵ_0 and μ_0 are the free permittivity and permeability respectively, which satisfy $\mu_0\epsilon_0 = 1/c^2$, where c is the speed of light. The free source Maxwell's equations are gauge invariant. A convenient gauge would be the Coulomb gauge that would allow as to determine $\boldsymbol{E}$ and $\boldsymbol{B}$ using a vector potential $\boldsymbol{A}(\boldsymbol{r}, t)$

$$\boldsymbol{B} = \boldsymbol{\nabla} \times \boldsymbol{A} \tag{2.18}$$

$$\boldsymbol{E} = -\frac{\partial \boldsymbol{A}}{\partial t}, \tag{2.19}$$

where the following condition must be satisfied

$$\boldsymbol{\nabla} \cdot \boldsymbol{A} = 0. \tag{2.20}$$

If we substitute Eq. (2.18) into Eq. (2.12) we obtain the wave equation for the vector potential

$$\boldsymbol{\nabla}^2 \boldsymbol{A}(\boldsymbol{r}, t) = \frac{1}{c^2} \frac{\partial^2 \boldsymbol{A}(\boldsymbol{r}, t)}{\partial t^2}. \tag{2.21}$$

We make the standard separation of variables

$$\boldsymbol{A}(\boldsymbol{r}, t) = \sum_m \mathscr{A}_m \boldsymbol{u}_m(\boldsymbol{r}) \alpha_m(t), \tag{2.22}$$

where the separation constant is $k_m^2 = \frac{\omega_m^2}{c^2}$. In the following we are going to confirm that k_m is the common wave-number, ω_m is the frequency of the wave and c is the speed of light. Also, the quantity $\mathscr{A}_m = \sqrt{\frac{\hbar}{2\omega_m \epsilon_0}}$ has dimensions of a vector potential. From the time ordinary differential equation we obtain

$$\alpha_m(t) = \alpha_m e^{-i\omega_m t - \phi} \qquad \alpha_m^*(t) = \alpha_m^* e^{i\omega_m t - \phi}, \tag{2.23}$$

where ϕ is an arbitrary phase. For now α_m and α_m^* are just two complex conjugate numbers. Later in this section we will quantize the EM field by converting these numbers into operators. The solution of the spatial differential equation depends on the boundary conditions of the problem under consideration. For example, if we examine the case of a cavity of length L the mode functions would be standing waves ($\propto \sin(k_m z)$). Here we are going to examine the case of a cubic cavity of side L, where the mode functions have the form

$$\boldsymbol{u}_m(\boldsymbol{r}) = \frac{1}{\sqrt{V}} e^{i\boldsymbol{k}_m \cdot \boldsymbol{r}} \boldsymbol{e}_m, \tag{2.24}$$

where $\boldsymbol{e}_m$ is the unit polarization vector. From the Coulomb gauge condition we obtain

$$\boldsymbol{k}_m \cdot \boldsymbol{e}_m = 0, \tag{2.25}$$

which is the transversality condition of the m-th mode of the field, meaning that the vector potential $\boldsymbol{A}$ (and consequently the electric field $\boldsymbol{E}$) has only two possible polarizations, orthogonal to the direction of the field propagation ($\boldsymbol{k}_m$). Hence, the subscript m denotes the Cartesian components of the propagation vector $\boldsymbol{k}_m = (k_x, k_y, k_z)$, as well as the two possible polarizations of the field. The periodic boundary conditions of our system determine the allowed values for $\boldsymbol{k}_m$.

$$k_x = \frac{2\pi m_1}{L}, \qquad k_y = \frac{2\pi m_2}{L}, \qquad k_z = \frac{2\pi m_3}{L}, \qquad m_1, m_2, m_3 = 0, \pm 1, \pm 2, ..., \tag{2.26}$$

and the set of numbers (m_1, m_2, m_3) defines a specific mode of the field. The mode functions also satisfy the orthogonality condition

$$\int_V \boldsymbol{u}_m^*(\boldsymbol{r}) \boldsymbol{u}_{m'}(\boldsymbol{r}) \, d\boldsymbol{r} = \delta_{mm'}. \tag{2.27}$$

The vector potential can now be written as

$$\boldsymbol{A}(\boldsymbol{r},t) = \sum_m \sqrt{\frac{\hbar}{2\omega_m \epsilon_0}} \boldsymbol{e}_m \left[\alpha_m e^{i(\boldsymbol{k}_m \cdot \boldsymbol{r} - \omega_m t - \phi)} + \alpha_m^* e^{-i(\boldsymbol{k}_m \cdot \boldsymbol{r} - \omega_m t + \phi)} \right]. \tag{2.28}$$

The corresponding electric and the magnetic field would be

$$\boldsymbol{E}(\boldsymbol{r},t) = i \sum_m \sqrt{\frac{\hbar \omega_m}{2\epsilon_0 V}} \boldsymbol{e}_m \left[\alpha_m e^{i(\boldsymbol{k}_m \cdot \boldsymbol{r} - \omega_m t - \phi)} - \alpha_m^* e^{-i(\boldsymbol{k}_m \cdot \boldsymbol{r} - \omega_m t + \phi)} \right] \tag{2.29}$$

$$\boldsymbol{H}(\boldsymbol{r},t) = -\frac{i}{c\mu_0} \sum_m \sqrt{\frac{\hbar \omega_m}{2\epsilon_0 V}} \boldsymbol{e}_m \times \hat{\boldsymbol{k}}_m \left[\alpha_m e^{i(\boldsymbol{k}_m \cdot \boldsymbol{r} - \omega_m t - \phi)} - \alpha_m^* e^{-i(\boldsymbol{k}_m \cdot \boldsymbol{r} - \omega_m t + \phi)} \right], \tag{2.30}$$

where $\hat{\boldsymbol{k}}_m$ is the unit vector pointing towards the propagation direction of the wave. The Hamiltonian for the electromagnetic field is given by

$$H = \frac{1}{2} \int \left(\epsilon_0 \boldsymbol{E}^2 + \mu_0 \boldsymbol{H}^2 \right) d\boldsymbol{r}. \tag{2.31}$$

Using Eq. (2.25) and (2.27) we conclude to

$$H = \sum_m \hbar \omega_m (\alpha_m^* \alpha_m + \frac{1}{2}). \tag{2.32}$$

We notice that the single mode Hamiltonian has exactly the same form with the Hamiltonian of a simple harmonic oscillator (SHO) $\hbar\omega(\hat{a}^\dagger \hat{a} + 1/2)$. So, we quantize the EM field by mapping the complex numbers α and α^* to the quantum harmonic oscillator's annihilation and creation operators $\hat{a}$ and $\hat{a}^\dagger$ respectively

$$\hat{H} = \sum_m \hbar \omega_m (\hat{a}_m^\dagger \hat{a}_m + \frac{1}{2}). \tag{2.33}$$

Thus, our system is dynamically equivalent to a sum of independent SHOs. We finally write the electric field operator in its quantized form

$$\boldsymbol{E}(\boldsymbol{r},t) = \sum_m \sqrt{\frac{\hbar \omega_m}{2\epsilon_0 V}} \boldsymbol{e}_m \left[\hat{a}_m e^{i(\boldsymbol{k}_m \cdot \boldsymbol{r} - \omega_m t)} + \hat{a}_m^\dagger e^{-i(\boldsymbol{k}_m \cdot \boldsymbol{r} - \omega_m t)} \right], \tag{2.34}$$

where we have chosen $\phi = \pi/2$, in order to eliminate the i factor in front of the sum. Just to clarify here that this is the electric field operator in the Heisenberg picture, since as can be noticed it has an explicit time dependence through the annihilation and creation operators $\hat{a}_m(t) = \hat{a}_m e^{-i\omega_m t}$. In the Schrödinger picture it is written as

$$\boldsymbol{E}(\boldsymbol{r},0) = \sum_m \sqrt{\frac{\hbar \omega_m}{2\epsilon_0 V}} \boldsymbol{e}_m \left[\hat{a}_m e^{i\boldsymbol{k}_m \cdot \boldsymbol{r}} + \hat{a}_m^\dagger e^{-i\boldsymbol{k}_m \cdot \boldsymbol{r}} \right], \tag{2.35}$$

where now the annihilation and creation operators are independent of time $\hat{a}_m(0) = \hat{a}_m$.

2.3 Continuous Mode Field Operators

As we can see in Eq. (2.34) the electric operator is expressed as a discrete sum of modes. However, in a typical optical experiment we have light beams that travel in free space, namely without any cavity mediated from the light source to the detector. In this case, we can consider that the light travels towards an infinitely long axis parallel to the z axis, but we consider that the cross-sectional area A, perpendicular to that axis, is still finite [70]. Here, we consider that k would be the one-dimensional continuous mode variable that transfers us from the discrete to the continuous case, but we could equivalently use the frequency. We start from the discretized quantized electric field operator, Eq. (2.34), with a fixed polarization towards the x-axis. The mode spacing would be $\Delta k = \frac{2\pi}{L}$, where L is the length of the aforementioned axis of propagation. When L tends to infinity, Δk tends to zero and we move from the discrete to the continuous case. Thus, the discrete sum is expressed as an integral $\sum_k \to \frac{1}{\Delta k}\int dk$, while the discrete Kronecker delta is replaced with the continuous delta function $\delta_{kk'} \to \Delta k \delta(k - k')$. We also move to the continuous creation and annihilation operators from their discrete counterparts by using [70]

$$\hat{a}_k \to (\Delta k)^{1/2}\hat{a}(k), \qquad \hat{a}_k^\dagger \to (\Delta k)^{1/2}\hat{a}^\dagger(k). \tag{2.36}$$

Hence, the discrete commutation relation $[\hat{a}_k, \hat{a}_{k'}^\dagger] = \delta_{kk'}$ would now be transformed into $[\hat{a}(k), \hat{a}(k')^\dagger] = \delta(k - k')$. After making all the appropriate transformations the electric field operator could be expressed as

$$\hat{\boldsymbol{E}}(z,t) = \int_0^\infty dk \left(\frac{\hbar ck}{4\pi\epsilon_0 A}\right)\left[\hat{a}(k,t)e^{ikz} + \hat{a}^\dagger(k,t)e^{-ikz}\right]\hat{x}, \tag{2.37}$$

where we have used that $V = AL$. We can expand the region of integration to the whole axis $(-\infty \to +\infty)$ and then assume that the bandwidth of the field excitation is much smaller than its central frequency, $\omega_0 = \hbar k_0$. Hence, the electric field operator can be written as

$$\hat{\boldsymbol{E}}(z,t) = \left(\frac{\hbar ck_0}{2\epsilon_0 A}\right)^{1/2}\left[\hat{a}(z,t) + \hat{a}^\dagger(z,t)\right]\hat{x}, \tag{2.38}$$

where we have defined the Fourier transformation of the annihilation and creation operators

$$\hat{a}(z,t) \equiv \frac{1}{\sqrt{2\pi}}\int_{-\infty}^\infty dk\,\hat{a}(k,t)e^{ikz}, \qquad \hat{a}^\dagger(z,t) \equiv \frac{1}{\sqrt{2\pi}}\int_{-\infty}^\infty dk\,\hat{a}^\dagger(k,t)e^{-ikz}, \tag{2.39}$$

where the explicit time dependence of the operators indicates that we are still on the Heisenberg picture.

2.4   Second Quantization

After getting some insight from the quantization of the EM field, we continue with the examination of the Fock basis, which constitutes a corner stone of the second quantization formalism. We introduce the multi-mode creation and annihilation operators $\hat{a}_i^\dagger$ and $\hat{a}_i$, which are the corresponding operators from the SHO, but now they refer to the i-th mode of the field and satisfy the following commutation relations

$$[\hat{a}_i, \hat{a}_j^\dagger] = \delta_{ij}, \qquad [\hat{a}_i, \hat{a}_j] = 0. \tag{2.40}$$

The Fock states, or the number states, have a well-defined number of particles in each mode, since they are defined in such a way, in order to be eigenstates of the number operator of the i-th mode, $\hat{n}_i = \hat{a}_i^\dagger \hat{a}_i$

$$\hat{n}_i|n_1, n_2, ..., n_i, ...n_k\rangle = n_i|n_1, n_2, ..., n_i, ...n_k\rangle. \tag{2.41}$$

Using the above two equations we can derive the common ladder operator formalism, in order to raise(lower) the number of bosons in the i-th mode, by applying the creation(annihilation) operator to the total state, in a similar way as we did in the SHO case

$$\hat{a}_i|n_1, n_2, ..., n_i, ...n_k\rangle = \sqrt{n_i}|n_1, n_2, ..., n_i - 1, ...n_k\rangle \tag{2.42}$$

$$\hat{a}_i^\dagger|n_1, n_2, ..., n_i, ...n_k\rangle = \sqrt{n_i + 1}|n_1, n_2, ..., n_i + 1, ...n_k\rangle, \tag{2.43}$$

We define the vacuum state, as the state with no particles in any of the modes $|0, 0, ..., 0\rangle = |0\rangle$. Hence, now we can create any Fock state by using the creation operators acting on the vacuum state:

$$|n_1, n_2, ...\rangle = \frac{(\hat{a}_1^\dagger)^{n_1}}{\sqrt{n_1!}} \frac{(\hat{a}_2^\dagger)^{n_2}}{\sqrt{n_2!}}...|0\rangle. \tag{2.44}$$

We also define the field operator $\hat{\psi}(\boldsymbol{r})$ which annihilates a particle from position $\boldsymbol{r}$

$$\hat{\psi}(\boldsymbol{r}) = \sum_j \phi_j(\boldsymbol{r})\hat{a}_j, \tag{2.45}$$

where $\phi_j(\boldsymbol{r}) = \langle \boldsymbol{r}|\phi_j\rangle$ and $|\phi_j\rangle$ is the single particle mode basis. We can use the field operator, in order to move from a single particle operator $\hat{O}$, to the corresponding many body operator

$$\hat{\mathcal{O}} = \int d\boldsymbol{r}\,\hat{\psi}^\dagger(\boldsymbol{r})\hat{O}\hat{\psi}(\boldsymbol{r}). \tag{2.46}$$

Also, the field operator satisfies the following commutation relations

$$\left[\hat{\psi}(\boldsymbol{r}), \hat{\psi}^\dagger(\boldsymbol{r}')\right] = \delta(\boldsymbol{r} - \boldsymbol{r}') \qquad \left[\hat{\psi}(\boldsymbol{r}), \hat{\psi}(\boldsymbol{r}')\right] = 0. \tag{2.47}$$

Up to this point we have been considering many indistinguishable particles in the same internal state. We can generalise this formalism for many particles in different internal states in the obvious way. For example, if we consider an atomic ensemble with two internal states $|a\rangle$ and $|b\rangle$, Eq. (2.10) generalises to

$$|\Psi\rangle = \sum_{n_{a_1}=0}^{\infty} ... \sum_{n_{a_k}=0}^{\infty} ... \sum_{n_{b_1}=0}^{\infty} ... \sum_{n_{b_k}=0}^{\infty} ...C_{n_{a_1},...,n_{a_k},...,n_{b_1},...,n_{b_k},...}(t)|n_{a_1}, ..., n_{a_k}, ..., n_{b_1}, ..., n_{b_k}, ...\rangle. \tag{2.48}$$

We can also define the corresponding field operators for each internal state of the system

$$\hat{\psi}_a(\boldsymbol{r}) = \sum_j \phi_{a_j}(\boldsymbol{r})\hat{a}_j \qquad \hat{\psi}_b(\boldsymbol{r}) = \sum_j u_{b_j}(\boldsymbol{r})\hat{b}_j, \tag{2.49}$$

where $\hat{a}_j$ ($\hat{b}_j$) describes the annihilation of a particle with internal state $|a\rangle$ ($|b\rangle$) from the j-th mode. The commutation relations for the field operator generalise to

$$\left[\hat{\psi}_j(\boldsymbol{r}), \hat{\psi}_k^\dagger(\boldsymbol{r}')\right] = \delta_{jk}\delta(\boldsymbol{r} - \boldsymbol{r}') \qquad \left[\hat{\psi}_j(\boldsymbol{r}), \hat{\psi}_k(\boldsymbol{r}')\right] = 0, \tag{2.50}$$

where the indices j, k refer to the two different internal states, as well as $\boldsymbol{r}$ and $\boldsymbol{r}'$ denote two different positions.

2.5 Bose-Einstein Condensate

In Sec. [2.1] we introduced bosons as fundamental particles with integer spin. However, we could also consider an atom with integer spin as a boson, in case we are in a regime where its inner structure does not play a significant role in the dynamics of the system. In that sense, we can talk about atomic bosons and we can use the second quantisation formalism, we have already introduced, in order to describe an ensemble consisting of N atomic bosons. After clarifying that point, we continue with the main subject of this section, which is the atomic Bose-Einstein condensates (BECs).

If we have a dilute gas of bosons, under a critical temperature T_C, a large fraction of the total number of bosons will occupy the ground state, or putting it differently they will "condense" into the ground state, forming a BEC. This is essentially due to the statistics that identical bosons obey, which follow the Bose-Einstein distribution, and it allows two and more bosons to occupy the same quantum state, in contrast with fermions, as we

saw in Sec. [2.1]. For a gas of N non-interacting indistinguishable bosons in thermal equilibrium the mean occupancy of each quantum state is given by

$$\langle n_j \rangle = \frac{1}{e^{(E_j - \mu)/k_B T} - 1}, \tag{2.51}$$

where E_j is the single particle energy that corresponds to the j-th mode, T is the temperature, k_B denotes Boltzmann's constant and μ is the chemical potential. The total number of bosons is given by the sum of the particles in each quantum state $N = \sum_j \langle n_j \rangle$. The mean number of bosons that occupy the ground state, below the critical temperature T_C, for a $3D$ trapping harmonic potential $V(x, y, z) = \frac{1}{2}m\omega(x^2 + y^2 + z^2)$ is given by [71]

$$\langle n_0 \rangle = N \left[1 - \left(\frac{T}{T_C} \right)^3 \right], \tag{2.52}$$

where ω is the trapping frequency and m is the mass of the particles. In this case, the critical temperature is given by [71]

$$T_C \approx 0.94 \frac{\hbar(\omega_x \omega_y \omega_z)^{1/3}}{K_B} T^{1/3}. \tag{2.53}$$

By using the second quantization formalism in order to describe a BEC, we reveal the wave nature, as well as other quantum effects existing in a BEC. The non interacting Hamiltonian of a system of bosons is given by

$$\hat{\mathcal{H}}_0 = \int \hat{\psi}^\dagger(\boldsymbol{r}) \left(-\frac{\hbar^2}{2m}\nabla^2 + V(\boldsymbol{r}) \right) \hat{\psi}(\boldsymbol{r}) d^3\boldsymbol{r} = \sum_j E_j \hat{a}_j^\dagger \hat{a}_j, \tag{2.54}$$

where the second equality is derived by expanding the field operator in the eigenbasis of the single particle Hamiltonian $\hat{H}_0 = -\frac{\hbar^2}{2m}\nabla^2 + V(\boldsymbol{r})$, where the first term is the kinetic energy of the particle and the second one is the external potential. Now, if we consider a two body interaction, namely a particle in position $\boldsymbol{r}$ interacts with a particle in position $\boldsymbol{r'}$ with an interaction energy $U(\boldsymbol{r} - \boldsymbol{r'})$, then the interaction Hamiltonian would be given by

$$\hat{\mathcal{H}}_{\text{int}} = \frac{1}{2} \int \int \hat{\psi}^\dagger(\boldsymbol{r})\hat{\psi}^\dagger(\boldsymbol{r'})U(\boldsymbol{r} - \boldsymbol{r'})\hat{\psi}(\boldsymbol{r})\hat{\psi}(\boldsymbol{r'}) d^3\boldsymbol{r} d^3\boldsymbol{r'}. \tag{2.55}$$

For ultra-cold gases of alkali atoms the range of the inter-particle interaction is much smaller than the distance between the atoms. This is the reason why we can make the approximation for the interaction energy $U(\boldsymbol{r} - \boldsymbol{r'}) = U_0\delta(\boldsymbol{r} - \boldsymbol{r'})$, where $U_0 = \frac{4\pi\hbar^2 a}{m}$ and a is the s-wave scattering length [72]. After this approximation, we can now write the Hamiltonian in the simpler form

$$\hat{\mathcal{H}}_{\text{tot}} = \int \hat{\psi}^\dagger(\boldsymbol{r})\hat{H}_0\hat{\psi}(\boldsymbol{r})d^3\boldsymbol{r} + \frac{U_0}{2}\int \hat{\psi}^\dagger(\boldsymbol{r})\hat{\psi}^\dagger(\boldsymbol{r})\hat{\psi}(\boldsymbol{r})\hat{\psi}(\boldsymbol{r})d^3\boldsymbol{r}. \tag{2.56}$$

We can find the Heisenberg equation of motion for the field operator

$$i\hbar\frac{\partial}{\partial t}\hat{\psi}(\boldsymbol{r},t) = \left(\hat{H}_0 + U_0\hat{\psi}^\dagger(\boldsymbol{r},t)\hat{\psi}(\boldsymbol{r},t)\right)\hat{\psi}(\boldsymbol{r},t). \tag{2.57}$$

This equation fully describes the evolution of a dilute bosonic gas, but its non-linearity in the second term in the right hand side makes it analytically unsolvable. In order to proceed, we consider some approximative methods, such as the mean field theory.

2.5.1 Mean Field Theory

In the mean field, or semi-classical approximation, we essentially ignore the quantum fluctuations of the atomic field and consider that the important dynamics is given by a mean field. This is something similar with the semi-classical approximation we make for the quantized electric field. In that case, we essentially consider the electric field as a wave and ignore the concept of photons as quanta of the EM field, namely we ignore the quantum fluctuations of the light. We will analyse the semi-classical approximation of the EM field in the following sections. The well-known Gross-Pitaevski equation (GPE) is an equation that describes the evolution of the bosonic gas, under the semi-classical approximation. In order to derive this equation, we start from the general state given by Eq. (2.10) and consider that all particles are in the same single particle state denoted here by the index ψ

$$|\Psi\rangle = \sum_{n_\psi=0}^{\infty} c_{n_\psi}|0,0,...,n_\psi,...\rangle = \sum_{N=0}^{\infty} c_N\frac{\left(\hat{a}_\psi^\dagger\right)^N}{\sqrt{N!}}|0,0,...,0\rangle, \tag{2.58}$$

where

$$\hat{a}_\psi = \int d\boldsymbol{r}u_\psi^*(\boldsymbol{r})\hat{\psi}(\boldsymbol{r}), \tag{2.59}$$

which is a reasonable assumption to make for a BEC. In the second equality of Eq. (2.58) we used the vacuum state $|0,0,...,0\rangle$ and Eq. (2.44), in order to denote the creation of all particles in mode ψ and that all the other modes remain empty. More particularly, we choose the coefficients c_N appropriately, in order the BEC to be described by a single Glauber coherent state, hence

$$|\Psi\rangle = |\alpha\rangle|0,0,...,0\rangle. \tag{2.60}$$

We will examine Glauber coherent states in more detail in Chapter 3, Sec. [3.2.1]. For now it is sufficient just to mention that these states are eigenstates of the annihilation operator,

namely $\hat{a}|\alpha\rangle = \alpha|\alpha\rangle$, where α is a complex number. By writing the field operator in an appropriate basis $\hat{\psi}(\boldsymbol{r}) = \sum_i u_i(\boldsymbol{r})\hat{a}_i$ we can calculate its expectation value:

$$\langle\hat{\psi}(\boldsymbol{r})\rangle = u_\psi(\boldsymbol{r})\alpha = \psi(\boldsymbol{r}), \tag{2.61}$$

where $\psi(\boldsymbol{r})$ is called order-parameter or mean-field wave-function. Considering that the BEC can be well approximated by a Glauber coherent state, makes it easier to calculate all symmetrically ordered operators

$$\left\langle\hat{\psi}_i^\dagger(\boldsymbol{r})\hat{\psi}_i(\boldsymbol{r})\hat{\psi}_i(\boldsymbol{r})\right\rangle = |\psi(\boldsymbol{r})|^2\psi(\boldsymbol{r}). \tag{2.62}$$

Hence, the BEC is well approximated by the mean-field (macroscopic) wave-function, $\psi(\boldsymbol{r})$, in the sense that it can be used to calculate expectation values of observables, such as the number density $n(\boldsymbol{r}, t) = \langle\hat{\psi}^\dagger(\boldsymbol{r}, t)\hat{\psi}(\boldsymbol{r}, t)\rangle = |\psi(\boldsymbol{r}, t)|^2$, but not their variances. By assuming such a state for the BEC, we essentially have made the spontaneous symmetry breaking assumption, which assigns a particular phase to the condensate. We can overcome this conceptual difficulty, by considering that the BEC is a mixture of coherent states with different phases, and when we make a measurement the BEC is projected on a state with a particular phase [73,74]. By taking the expectation values of Eq, (2.57) we find the GPE

$$i\hbar\frac{\partial}{\partial t}\psi(\boldsymbol{r}, t) = \left(-\frac{\hbar^2}{2m}\nabla^2 + V(\boldsymbol{r}) + U_0|\psi(\boldsymbol{r}, t)|^2\right)\psi(\boldsymbol{r}, t). \tag{2.63}$$

As we have seen, in the mean field approximation we ignore the quantum fluctuations of the bosonic field. That means that we can not describe quantum effects, such as entanglement or spin squeezing using the semi-classical model. However, this description can realize the wave nature of the atoms and consequently can describe effects such as the matter-wave interference. In Chapters 5 and 6, we examine atom light interaction, which creates entangled and spin squeezed states. In such cases we cannot use the mean field approximation in order to describe the atomic ensemble, but instead we use the truncated Wigner method, which is an approximative phase space method, enabling us to include quantum fluctuations and examine their effects in the dynamics of the system.

2.6 Atom Light Interaction

So far, we have separately examined the quantum state of many particles, and the quantized electric radiation field. Now, it is time to examine the interaction of the radiation field $\hat{\boldsymbol{E}}$ with matter. We are going to consider the simple case of a single atom interacting with a single mode light field at first, in order to derive the famous Jaynes-Cummings

Hamiltonian. Then, we will move to the semi-classical case, by simply turning off the quantum fluctuations of the light. This is how we introduce the concept of Rabi oscillations and Rabi frequency. The next step, is to consider many atoms for both quantum and classical case of the light field. Firstly, we examine the quantum case, by considering a light field freely propagating in space interacting with an atomic ensemble, where we derive the corresponding interaction Hamiltonian. We are going to use this Hamiltonian in Chapter 5, where we explore the dynamics of a quantum non-demolition (QND) measurement scheme. In this case, we adopt the quantum approach for the light, since the quantum fluctuations of the light field play a significant role in the full dynamics of the system. Then, we examine the semi-classical approach for the atom-light interaction, by considering a classical monochromatic wave for the light field. We conclude again to a very similar picture to the one of the single atom semi-classical case, where we had oscillations between the two electronic states, described by the Rabi frequency. The semi-classical description of the atom-light interaction will be important in Chapter 4, where we make use of a two-photon transition, which we analyse in the following sections, in order to describe the optical elements, beam-splitters and mirrors, of a MZ interferometer. These elements are commonly realised by considering bright lasers, where the light quantum noise is insignificant and the full dynamics of the system can be well described by the semi-classical approach.

2.6.1 Single Atom - Single Mode Light Field

The interaction of a single electron atom with the radiation field is described by the Hamiltonian [67, 70]

$$\hat{H} = \frac{1}{2m}\left[\hat{\boldsymbol{p}} - e\hat{\boldsymbol{A}}(\boldsymbol{r},t)\right]^2 + eV(\boldsymbol{r}) + \hat{H}_{\text{light}}, \tag{2.64}$$

where m, $\hat{\boldsymbol{p}}$ and $V(\boldsymbol{r})$ is the mass, momentum and Coulomb potential of the electron respectively. Also, $\hat{\boldsymbol{A}}(\boldsymbol{r},t)$ is the vector potential of the field and $\hat{H}_{\text{light}}$ is the unperturbed light field energy. Here, we briefly explain the basic steps we need to make, in order to go from Eq. (2.64) to Eq. (2.65), but for a detailed derivation the reader is referred to [69]. Firstly, we make the unitary transformation $|\psi'(t)\rangle = \exp[ie\boldsymbol{r}\cdot\hat{\boldsymbol{A}}(\boldsymbol{r},t)]|\psi(t)\rangle$, as well as we use of the Coulomb gauge condition $\boldsymbol{\nabla}\cdot\boldsymbol{A} = 0$. We also make the standard dipole approximation $\boldsymbol{A}(\boldsymbol{r}) \approx \boldsymbol{A}(\boldsymbol{r}_0)$, where $\boldsymbol{r}_0$ is the position of the atomic nucleus, where we essentially assume that the field is uniform over the whole atom, since we consider that the radiation wavelength is much larger than the atomic size. Hence, the Hamiltonian in

the dipole approximation is written as [68]

$$\hat{H} = \hat{H}_{\text{atom}} + \hat{H}_{\text{light}} + \hat{H}_{\text{int}}, \qquad (2.65)$$

where $\hat{H}_{\text{int}} = \hat{\boldsymbol{d}} \cdot \hat{\boldsymbol{E}}$ and $\hat{H}_{\text{atom}}$ is the atomic energy without considering any interaction. As we have already seen the energy of the free field in the second quantization formalism is written by

$$\hat{H}_{\text{light}} = \sum_k \hbar\omega_k \hat{a}_k^\dagger \hat{a}_k, \qquad (2.66)$$

where we have neglected the the zero-point energy. The atomic dipole operator is

$$\hat{\boldsymbol{d}} = -e\hat{\boldsymbol{r}}, \qquad (2.67)$$

where $\hat{\boldsymbol{r}}$ is the vector declaring the distance of the electron and the nucleus. For simplicity, we assume that the nucleus of the atom is at the origin $\boldsymbol{r}_0 = 0$. We expand $\hat{\boldsymbol{d}}$ in the complete set of electronic states $\{|i\rangle\}$, $\sum_i |i\rangle\langle i| = \hat{1}$, and we obtain

$$\hat{\boldsymbol{d}} = \sum_{i,j} |i\rangle\langle i|\hat{\boldsymbol{d}}|j\rangle\langle j| = \sum_{i,j} \boldsymbol{d}_{ij}\sigma_{ij}, \qquad (2.68)$$

where $\boldsymbol{d}_{ij} = -e\langle i|\hat{\boldsymbol{r}}|j\rangle$ is the electric dipole transition matrix element and $\sigma_{ij} = |i\rangle\langle j|$ is the matrix describing the transition $|i\rangle \to |j\rangle$. Due to Hermiticity, the dipole transition matrix elements satisfy $d_{ii} = 0$ and $d_{ij} = d_{ji}$. For simplicity, we consider the case of a two level atom with states $|a\rangle$ and $|b\rangle$, i.e. $i = a$ and $j = b$. Hence,

$$\hat{\boldsymbol{d}} = \boldsymbol{d}_{ab}\left(\hat{\sigma}_+ + \hat{\sigma}_-\right), \qquad (2.69)$$

where we used the raising and lowering operators of the atomic states $\hat{\sigma}_+ = |a\rangle\langle b|$ and $\hat{\sigma}_- = \hat{\sigma}_+^\dagger$ respectively. We consider the zero energy level in the middle between the atomic states $|a\rangle$ and $|b\rangle$, thus

$$\hat{H}_{\text{atom}} = \frac{1}{2}\hbar\omega_{ab}\hat{\sigma}_z, \qquad (2.70)$$

where we have used the second equality of Eq. (2.54) and we have defined $\omega_{ab} = \omega_b - \omega_a$. We have also used the z-component of the Pauli matrices $\hat{\sigma}_z = |a\rangle\langle a| - |b\rangle\langle b|$. Now, we recall the result for the quantized propagating EM field Eq. (2.34)

$$\boldsymbol{E}(\boldsymbol{r}, t) = \sum_k \sqrt{\frac{\hbar\omega_k}{2\epsilon_0 V}}\boldsymbol{e}_k\left[\hat{a}_k e^{i(\boldsymbol{k}\cdot\boldsymbol{r}-\omega_k t)} + \hat{a}_k^\dagger e^{-i(\boldsymbol{k}\cdot\boldsymbol{r}-\omega_k t)}\right], \qquad (2.71)$$

where in our case $\boldsymbol{r} \approx \boldsymbol{r}_0 = 0$, as we aforementioned. Also, for simplicity we move to the single mode light field case. Thus, in the Schrödinger picture the electric field operator is given by

$$\hat{\boldsymbol{E}}(\boldsymbol{r_0}, 0) = \sqrt{\frac{\hbar\omega_0}{2\epsilon_0 V}}\left(\hat{a} + \hat{a}^\dagger\right)\boldsymbol{e}. \qquad (2.72)$$

Hence, the interaction Hamiltonian finally is written as

$$\hat{H}_{\text{int}} = \hat{\boldsymbol{d}} \cdot \hat{\boldsymbol{E}} = \hbar g_{ab} \left(\hat{\sigma}_+ + \hat{\sigma}_- \right) \left(\hat{a} + \hat{a}^\dagger \right), \tag{2.73}$$

where $g_{ab} = \frac{1}{\hbar} \sqrt{\frac{\hbar \omega_0}{2\epsilon_0 V}} \boldsymbol{d}_{ab} \cdot \boldsymbol{e}$ indicates the coupling strength between the light mode and the atom. Just to clarify here that e is the electron's charge, while $\boldsymbol{e}$ is the polarization vector of the light field. From Eq. (2.73) we obtain the following four interaction terms:

- $\hat{\sigma}_+ \hat{a}$: absorption of a photon and the excitation of the atom.

- $\hat{\sigma}_- \hat{a}^\dagger$: emission of a photon and the de-excitation of the atom.

- $\hat{\sigma}_+ \hat{a}^\dagger$: emission of a photon and excitation of the atom.

- $\hat{\sigma}_- \hat{a}$: absorption of a photon and de-excitation of the atom.

It is common procedure to ignore the last two terms, because they do not conserve the total energy of the system. We can show that in a more strict way, by moving to the interaction picture of $\hat{H}_{\text{int}}$, with respect to the unperturbed Hamiltonian $\hat{H}' = \hat{H}_{\text{atom}} + \hat{H}_{\text{light}}$, in order to examine the time evolution of these terms

$$\hat{H}_{\text{int}}^{\text{I}} \equiv e^{i\hat{H}'t} \hat{H}_{\text{int}} e^{-i\hat{H}'t} =$$

$$= -\hbar g_{ab} e^{i\hat{H}_{\text{atom}}t} \left(\hat{\sigma}_+ + \hat{\sigma}_- \right) e^{-i\hat{H}_{\text{atom}}t} e^{i\hat{H}_{\text{light}}t} \left(\hat{a} + \hat{a}^\dagger \right) e^{-i\hat{H}_{\text{light}}t}. \tag{2.74}$$

We finally obtain [69]

$$\hat{H}_{\text{int}}^{\text{I}} = \hbar g_{ab} \left[\hat{\sigma}_+ \hat{a} e^{-i(\omega_0 - \omega_{ab})t} + \hat{\sigma}_- \hat{a}^\dagger e^{i(\omega_0 - \omega_{ab})t} + \hat{\sigma}_- \hat{a} e^{-i(\omega_0 + \omega_{ab})t} + \hat{\sigma}_+ \hat{a}^\dagger e^{-i(\omega_0 + \omega_{ab})t} \right]. \tag{2.75}$$

In the case that we are near resonance, $\omega_0 \approx \omega_{ab}$, we can neglect the fast oscillating terms, $e^{\pm i(\omega_0 + \omega_{ab})t} \approx e^{\pm 2i\omega_{ab}t}$, which is the so called rotating wave approximation (RWA). Going back to the Schrödinger picture and adding the atomic and light unperturbed Hamiltonians we obtain the Jaynes-Cummings Hamiltonian

$$\hat{H} = \frac{\hbar \omega_{ab}}{2} \hat{\sigma}_z + \hbar \omega_0 \hat{a}^\dagger \hat{a} + \hbar g_{ab} \left(\hat{a} \hat{\sigma}_+ + \hat{\sigma}_- \hat{a}^\dagger \right). \tag{2.76}$$

2.6.2 Single Atom - Classical Light (Semi-Classical Approach)

We can write the annihilation operator of the light field in a hand-wavy way as a sum of a large complex number and small quantum noise $\hat{a} = \langle \hat{a} \rangle e^{-i\omega_0 t} + \delta \hat{a}$. In the case of a bright laser beam, we can describe the light field using a Glauber coherent state, where the mean value $\langle \hat{a} \rangle$ is large compared to the fluctuations. Hence, in that specific case we can

move to the classical limit for the light field, by simply ignoring the quantum fluctuations of the light, i.e. $\hat{a} = \alpha e^{-i\omega_0 t}$. Also, we can express $\sigma_+ = |b\rangle\langle a|$ and $\sigma_- = |a\rangle\langle b|$ in a more convenient form, in order to write Eq. (2.76) as

$$\hat{H} = \frac{\hbar\omega_{ab}}{2}\hat{\sigma}_z + \hbar\Omega_{ab}\left(|b\rangle\langle a|e^{-i\omega_0 t} + |a\rangle\langle b|e^{i\omega_0 t}\right), \tag{2.77}$$

where we have also assumed that $\alpha = \alpha^*$. Due to the fact that now we consider a classical light field, we have ignored the second term in Eq. (2.76). Eq. (2.77) is the Hamiltonian describing the interaction of a two level atom with a classical EM field. The last two terms describe the oscillations of the electron between the two available states $|a\rangle$ and $|b\rangle$, which are well known as Rabi oscillations. We have also defined the Rabi frequency as follows

$$\Omega_{ab} = g_{ab}\alpha = \frac{1}{\hbar}\left(\sqrt{\frac{\hbar\omega_0}{2\epsilon_0 V}}\alpha\right)d_{ab} = \frac{E_0 d_{ab}}{\hbar}, \tag{2.78}$$

which denotes the frequency of these oscillations. Also, $E_0 = \sqrt{\frac{\hbar\omega_0}{2\epsilon_0 V}}\alpha$ has dimensions of electric field. The last equality in Eq. (2.78) is the definition of the Rabi frequency, which is usually found in the literature, when we examine the semi-classical approximation of a single atom with a classical light field [68].

2.6.3   Many Atoms - Multi-Mode Light Field

Now we move to the many atoms case, where we consider an ensemble of 2-level atoms interacting with a quantized EM field freely propagating in space. For simplicity we consider the 1-D case, where the light field is propagating along the z-direction, while the polarization of the electric field is along the x-axis. Hence, we use Eq. (2.38) in order to describe the electric field, which we also present here for convenience

$$\hat{\boldsymbol{E}}(z,t) = \left(\frac{\hbar\omega_0}{2\epsilon_0 A}\right)^{1/2}\left[\hat{a}(z,t) + \hat{a}^\dagger(z,t)\right]\hat{x}, \tag{2.79}$$

where we used that $\omega_0 = ck_0$. We make use of Eq. (2.46), in order to move from the single particle interaction Hamiltonian operator to the many particle case

$$\hat{\mathcal{H}}_{\text{int}} = \int_{-\infty}^{\infty} dz\hat{\boldsymbol{\psi}}^\dagger \hat{H}_{\text{int}}\hat{\boldsymbol{\psi}}, \tag{2.80}$$

where $\hat{\boldsymbol{\psi}} = (\hat{\psi}_a(z,t), \hat{\psi}_b(z,t))^T$ and $\hat{\psi}_a(z,t), \hat{\psi}_b(z,t)$ are the field operators corresponding to $|a\rangle$ and $|b\rangle$ electronic states respectively. Again, we make the dipole approximation, hence the interaction would be given by the term $\hat{H}_{\text{int}} = \hat{\boldsymbol{d}} \cdot \hat{\boldsymbol{E}}$, where $\hat{\boldsymbol{d}}$ is given by Eq. (2.69). We should mention here that we are interested on the atomic dynamics only along the z-axis, which is the direction of propagation of the light. Thus,

$$\hat{\mathcal{H}}_{\text{int}} = d_{ab}\int_{-\infty}^{\infty} dz\left[\hat{\psi}_b^\dagger(z,t)\hat{\psi}_a(z,t) + \hat{\psi}_a^\dagger(z,t)\hat{\psi}_b(z,t)\right]\hat{E}(z,t), \tag{2.81}$$

where we have assumed that the dipole moment is aligned with the electric field operator $\boldsymbol{d}_{ab} = d_{ab}\hat{x}$. Substituting Eq. (2.79) here and keeping only the energy conserving terms, similarly with the process we followed in the previous section, we obtain

$$\hat{\mathscr{H}}_{\text{int}} = \hbar g_{ab} \int_{-\infty}^{\infty} dz \left[\hat{\psi}_b^\dagger(z,t)\hat{\psi}_a(z,t)\hat{a}(z,t) + \hat{\psi}_a^\dagger(z,t)\hat{\psi}_b(z,t)\hat{a}^\dagger(z,t) \right], \tag{2.82}$$

where we have defined $g_{ab} = \frac{d_{ab}}{\hbar}\left(\frac{\hbar\omega_0}{2\epsilon_0 A}\right)^{1/2}$, denoting the interaction strength. This is the interaction term of the Hamiltonian we are going to use in Chapter 5, in order to describe the interaction of a free propagating light field with an atomic ensemble of two level atoms.

2.7 Many Atoms - Classical Light (Semi-classical Approach)

We can move to the semi-classical case again, where we examine the interaction of a classical field with a two level atomic ensemble, by just considering in Eq. (2.81) a classical monochromatic electric field operator

$$\boldsymbol{E} = \boldsymbol{E}_0 \left(e^{i(\boldsymbol{k}\cdot\boldsymbol{r}-\omega_0 t)} + e^{-i(\boldsymbol{k}\cdot\boldsymbol{r}-\omega_0 t)} \right), \tag{2.83}$$

where $E_0 = \sqrt{\frac{\hbar\omega_0}{2\epsilon_0 V}}\alpha$ has dimensions of electric field. In this case we have chosen a single mode, from a discretized sum of modes, for the classical electric field given by Eq. (2.29). Now, it is easier to use an arbitrary direction for the light field, compared to the continuous case we examined in the previous section. This is the reason why, here we have moved back to the 3-D case. Substituting Eq. (2.83) into Eq. (2.81) and again keeping only the energy conserving terms we find

$$\hat{\mathscr{H}}_{\text{int}} = \hbar\Omega_{ab} \int d^3\boldsymbol{r} \left(\hat{\psi}_a(\boldsymbol{r})\hat{\psi}_b^\dagger(\boldsymbol{r})e^{i(\boldsymbol{k}\cdot\boldsymbol{r}-\omega_0 t)} + \hat{\psi}_a^\dagger(\boldsymbol{r})\hat{\psi}_b(\boldsymbol{r})e^{-i(\boldsymbol{k}\cdot\boldsymbol{r}-\omega_0 t)} \right), \tag{2.84}$$

where we defined again the Rabi frequency associated with the oscillations between states $|a\rangle$ and $|b\rangle$

$$\Omega_{ab} = \frac{E_0 d_{ab}}{\hbar} = \frac{1}{\hbar}\left(\sqrt{\frac{\hbar\omega_0}{2\epsilon_0 V}}\alpha\right)d_{ab}, \tag{2.85}$$

which is exactly the same with the single atom case Eq. (2.78).

2.7.1 Two Photon Transition

Here, we consider a 3-level system with states $|a\rangle$, $|b\rangle$ and $|c\rangle$, as depicted in Fig. [2.1]. For example $|a\rangle$ and $|b\rangle$ might represent different hyperfine states, such as the $F = 1$ and $F = 2$ hyperfine levels of ^{87}Rb. We also consider a monochromatic light field with
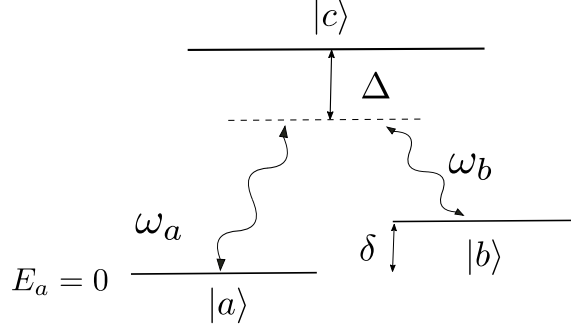
Figure 2.1: Interaction of a 3-level atom with two classical monochromatic beams. We consider that a light beam with frequency ω_a is related to the atomic transition $|a\rangle \to |c\rangle$, while another beam with frequency ω_b corresponds to the $|b\rangle \to |c\rangle$ transition. We also consider that the atomic energy of the ground state $|a\rangle$ is zero.

frequency ω_a and detuning Δ from the atomic transition $|a\rangle \to |c\rangle$, and another monochromatic field with frequency ω_b and the same amount of detuning for the transition $|b\rangle \to |c\rangle$. We also consider that $E_a = 0$, $E_b = \hbar\delta$ and $E_c = \hbar(\omega_a + \Delta)$, Fig. [2.1]. Following the same reasoning as the previous subsection, we find the interaction terms for the two different atomic transitions. So, the total Hamiltonian describing the dynamics of our system is given by

$$\hat{\mathcal{H}}_{tot} = E_b \int d\boldsymbol{r}\, \hat{\psi}_b^\dagger(\boldsymbol{r})\hat{\psi}_b(\boldsymbol{r}) + E_c \int d\boldsymbol{r}\, \hat{\psi}_c^\dagger(\boldsymbol{r})\hat{\psi}_c(\boldsymbol{r}) +$$

$$+ \hbar\Omega_{ac} \int d\boldsymbol{r} \left(\hat{\psi}_a(\boldsymbol{r})\hat{\psi}_c^\dagger(\boldsymbol{r})e^{i(\boldsymbol{k}_a\cdot\boldsymbol{r} - \omega_a t)} + H.c \right) +$$

$$+ \hbar\Omega_{bc} \int d\boldsymbol{r} \left(\hat{\psi}_b(\boldsymbol{r})\hat{\psi}_c^\dagger(\boldsymbol{r})e^{i(\boldsymbol{k}_b\cdot\boldsymbol{r} - \omega_b t)} + H.c \right). \tag{2.86}$$

We find the equations of motion for the atomic operators

$$\partial_t\hat{\psi}_a(t) = -\frac{i}{\hbar}[\hat{\psi}_a(t), \hat{H}_{tot}] = -i\Omega_{ac}\hat{\psi}_c(t)e^{-i(\boldsymbol{k}_a\cdot\boldsymbol{r} - \omega_a t)} \tag{2.87}$$

$$\partial_t\hat{\psi}_b(t) = -\frac{i}{\hbar}[\hat{\psi}_b(t), \hat{H}_{tot}] = -i\delta\hat{\psi}_b(t) - i\Omega_{bc}\hat{\psi}_c(t)e^{-i(\boldsymbol{k}_b\cdot\boldsymbol{r} - \omega_b t)} \tag{2.88}$$

$$\partial_t\hat{\psi}_c(t) = -\frac{i}{\hbar}[\hat{\psi}_c(t), \hat{H}_{tot}] = -i(\omega_a + \Delta)\hat{\psi}_c(t) - i\Omega_{ac}\hat{\psi}_a(t)e^{i(\boldsymbol{k}_a\cdot\boldsymbol{r} - \omega_a t)} - i\Omega_{bc}\hat{\psi}_b(t)e^{i(\boldsymbol{k}_b\cdot\boldsymbol{r} - \omega_b t)}. \tag{2.89}$$

Then, we make the following transformations $\tilde{\psi}_c = \hat{\psi}_c e^{i\omega_a t}$ and $\tilde{\psi}_b = \hat{\psi}_b e^{i\delta t}$, hence

$$\partial_t\tilde{\psi}_c(t) = -i\Delta\tilde{\psi}_c(t) - i\Omega_{ac}\hat{\psi}_a(t)e^{i\boldsymbol{k}_a\cdot\boldsymbol{r}} - i\Omega_{bc}\tilde{\psi}_b(t)e^{i\boldsymbol{k}_b\cdot\boldsymbol{r}}. \tag{2.90}$$

By taking the Fourier transformation of each term in the above equation, we obtain

$$i\omega\tilde{\psi}_c(\omega) = -i\Delta\tilde{\psi}_c(\omega) - i\Omega_{ac}\hat{\psi}_a(\omega)e^{i\boldsymbol{k}_a\cdot\boldsymbol{r}} - i\Omega_{bc}\tilde{\psi}_b(\omega)e^{i\boldsymbol{k}_b\cdot\boldsymbol{r}}, \tag{2.91}$$

where we consider that we are in the low frequency regime, i.e. $\omega << \Delta, \Omega_{ac}, \Omega_{bc}$, and consequently we can eliminate the first term of the above equation. This is the well known adiabatic elimination of the excited state, where we essentially consider that it will not be significantly populated. Hence,

$$\tilde{\psi}_c(t) = -\frac{\Omega_{ac}}{\Delta}\hat{\psi}_a(t)e^{i\boldsymbol{k}_a\cdot\boldsymbol{r}} - \frac{\Omega_{bc}}{\Delta}\tilde{\psi}_b(t)e^{i\boldsymbol{k}_b\cdot\boldsymbol{r}}. \tag{2.92}$$

Substituting Eq. (2.92) into Eq. (2.87) and Eq. (2.88) we obtain

$$\partial_t\hat{\psi}_a(t) = i\frac{\Omega_{ac}^2}{\Delta}\hat{\psi}_a + i\frac{\Omega_{ac}\Omega_{bc}}{\Delta}\tilde{\psi}_b e^{i(\boldsymbol{k}_b-\boldsymbol{k}_a)\boldsymbol{r}} \tag{2.93}$$

$$\partial_t\tilde{\psi}_b(t) = i\frac{\Omega_{bc}^2}{\Delta}\tilde{\psi}_b + i\frac{\Omega_{ac}\Omega_{bc}}{\Delta}\hat{\psi}_a e^{-i(\boldsymbol{k}_b-\boldsymbol{k}_a)\boldsymbol{r}}. \tag{2.94}$$

This result could also be realised using the effective Hamiltonian

$$\hat{H}_{eff} = \hbar\frac{\Omega_{ac}^2}{\Delta}\int\hat{\psi}_a^\dagger(\boldsymbol{r},t)\hat{\psi}_a(\boldsymbol{r},t)d\boldsymbol{r} + \hbar\frac{\Omega_{bc}^2}{\Delta}\int\hat{\psi}_b^\dagger(\boldsymbol{r},t)\hat{\psi}_b(\boldsymbol{r},t)d\boldsymbol{r} +$$
$$\hbar\frac{\Omega_{ac}\Omega_{bc}}{\Delta}\int\left(\hat{\psi}_a^\dagger(\boldsymbol{r},t)\hat{\psi}_b(\boldsymbol{r},t)e^{i(\boldsymbol{k}_b-\boldsymbol{k}_a)\cdot\boldsymbol{r}} + \hat{\psi}_b^\dagger(\boldsymbol{r},t)\hat{\psi}_a(\boldsymbol{r},t)e^{-i(\boldsymbol{k}_b-\boldsymbol{k}_a)\cdot\boldsymbol{r}}\right)d\boldsymbol{r}. \tag{2.95}$$

We can interpret the first two terms of the effective Hamiltonian, which are proportional to $\frac{\Omega_i^2}{\Delta}$ for $i = ac$, bc, as the AC Stark shift of the initial atomic energy levels, due to the interaction with the light. In addition, the last two terms represent transitions between states $|a\rangle$ and $|b\rangle$, with frequency the effective two photon Rabi frequency $\Omega_{ac}\Omega_{bc}/\Delta$, accompanied with corresponding momentum kicks with magnitude equal to the momentum difference of the two light beams $\hbar(\boldsymbol{k}_b - \boldsymbol{k}_a)$. Hence, we have continuous oscillations between the ground state ($|a\rangle$) and another low lying and long lived state ($|b\rangle$) of the 3-level system, as long as the atom-light interaction is on. This kind of interaction is very useful, in order to realise beam-splitters, which create equal superpositions of two states, or mirrors which interchange two states with each other. We can realise beam-splitters or mirrors by appropriately adjusting the time of the atom-light interaction. This will be crucial later, when we are going to explore the dynamics of an atom passing through a Mach-Zehnder interferometer Sec. [2.10].

2.8 Spontaneous Emission - Langevin Formalism

Here we introduce the effect of atomic spontaneous emission taking place during atom-light interaction. Commonly, spontaneous emission is described by considering that the system under consideration (in our case atomic ensemble with light field) interacts with an external bath, leading to the so-called Langevin equation. In Chapter 5 we examine the

interaction of a light field freely propagating in space with a 2-level atomic ensemble. In that case, we consider that the atoms being in the excited state interact with the bath at a specific point in space. This is the reason why, we generalise the conventional Langevin formalism [75], by describing the EM field outside the system, by using a continuous bath operator with respect to frequency and space $\hat{d}(\omega, z)$. Hence, it obeys the following commutation relation

$$\left[\hat{d}(\omega, z), \hat{d}^\dagger(\omega', z')\right] = \delta(\omega - \omega')\delta(z - z'). \tag{2.96}$$

We realize the heat bath using the following Hamiltonian

$$\hat{H}_{\mathrm{B}} = \hbar \int_{-\infty}^{+\infty} dz \int_{-\infty}^{+\infty} d\omega\, \omega\, \hat{d}^\dagger(\omega, z)\hat{d}(\omega, z). \tag{2.97}$$

As aforementioned, only the atoms that are in their excited state interact with the bath, hence the interaction Hamiltonian would be

$$\hat{H}_{\mathrm{int}} = i\hbar \int_{-\infty}^{+\infty} d\omega k(\omega) \int_{-\infty}^{+\infty} dz \left(\hat{d}(\omega, z)^\dagger \hat{\psi}_3(z) - \hat{\psi}_3^\dagger(z)\hat{d}(\omega, z)\right), \tag{2.98}$$

where $\hat{\psi}_3(z)$ is the atomic field operator of the excited state and $k(\omega)$ describes the coupling strength between the atoms and the bath. The total Hamiltonian (system + bath) would be given by

$$\hat{H}_{\mathrm{tot}} = \hat{H}_{\mathrm{sys}} + \hat{H}_{\mathrm{B}} + \hat{H}_{\mathrm{int}}. \tag{2.99}$$

We are going to examine the dynamics of the system in the Heisenberg picture, so both operators, $\hat{\psi}_3(z)$ and $\hat{d}(\omega, z)$, would also depend on time, which was not expressed explicitly above for simplicity. We write the Heisenberg equation of motion for a general system operator $\hat{\psi}_i(z, t)$, where i denotes any atomic state, and $\hat{d}(\omega, z, t)$

$$\partial_t \hat{\psi}_i(z, t) = -\frac{i}{\hbar}\left[\hat{\psi}_i(z, t), \hat{H}_{\mathrm{sys}}\right] - \int_{-\infty}^{+\infty} dz' \left(\left[\hat{\psi}_i(z, t), \hat{\psi}_3(z', t)\right] \int_{-\infty}^{+\infty} d\omega k(\omega)\hat{d}(\omega, z', t)\right) \tag{2.100}$$

$$\partial_t \hat{d}(\omega, z, t) = -i\omega\hat{d}(\omega, z, t) + k(\omega)\hat{\psi}_3(z, t). \tag{2.101}$$

Solving the differential equation for the bath operator, Eq. (2.101) we obtain

$$\hat{d}(\omega, z, t) = e^{-i\omega(t-t_0)}\hat{d}(\omega, z, t_0) + k(\omega) \int_{t_0}^{t} dt' e^{-i\omega(t-t')}\hat{\psi}_3(z, t'). \tag{2.102}$$

Now, we substitute this result into Eq. (2.100) and we make the first Markov approximation, $k(\omega) = \sqrt{\gamma_3/2\pi}$, where γ_3 is the atomic spontaneous emission rate from the excited

state, in order to obtain the general Langevin equation for a continuous system operator in space

$$\partial_t \hat{\psi}_i(z,t) = -\frac{i}{\hbar} \left[\hat{\psi}_i(z,t), \hat{H}_{\text{sys}} \right] - \int_{-\infty}^{+\infty} \left[\hat{\psi}_i(z,t), \hat{\psi}_3^\dagger(z',t) \right] \left(\frac{\gamma_3}{2} \hat{\psi}_3(z',t) + \sqrt{\gamma_3} \hat{d}_{\text{in}}(z',t) \right) dz',$$

$$(2.103)$$

where we have used the following relations

$$\int_{-\infty}^{+\infty} d\omega e^{-i\omega(t-t')} = 2\pi\delta(t-t'), \qquad \int_{t_0}^{t} dt' \delta(t-t') \hat{\psi}_3(z',t') = \frac{1}{2} \hat{\psi}_3(z',t), \qquad (2.104)$$

and we have defined

$$\hat{d}_{\text{in}}(z,t) = \frac{1}{\sqrt{2\pi}} \int_{-\infty}^{+\infty} e^{-i\omega(t-t_0)} \hat{d}(\omega,z,t_0) d\omega. \qquad (2.105)$$

The first term of Eq. (2.103) gives the unitary evolution of the operator, due to the system Hamiltonian, which is what we had before adding spontaneous emission. The second term represents the loss of atoms being in the excited state with rate γ_3, due to the interaction with the bath. The third term is the so-called Langevin noise, where $\hat{d}_{\text{in}}(z,t)$ can be interpreted as noise entering into our system, due to the interaction with the external EM field, given that the bath is in an incoherent state [75].

2.9 Input-Output Formalism for a Cavity

In Chapters 5 and 6, we are also going to consider light interacting with an atomic ensemble using a cavity. In this case, the light bounces back and forth between the mirrors of the cavity, enhancing the interaction with the atomic ensemble. Here, we have an additional physical process taking place, namely a fraction of the photons leaks out of the cavity leading to decoherence and consequently to sensitivity decrease, as we are going to see in more detail in Chapters 5 and 6. We can use the Langevin formalism in order to describe this physical process. In this case, we consider the total system to be a cavity described by an operator $\hat{c}(t)$. We describe the EM field outside the cavity by using an operator $\hat{b}(\omega)$, which is only continuous with respect to frequency and not space, since the cavity is described by a single mode operator. Hence, it satisfies the following commutation relation

$$[\hat{b}(\omega), \hat{b}^\dagger(\omega')] = \delta(\omega - \omega'). \qquad (2.106)$$

Also, now the bath is described by the Hamiltonian

$$\hat{H}_{\text{B}} = \hbar \int_{-\infty}^{\infty} d\omega\, \omega \hat{b}^\dagger(\omega) \hat{b}(\omega). \qquad (2.107)$$

Following the same strategy with the previous section, but using $\hat{c}(t)$ and $\hat{b}(\omega)$ instead of $\hat{\psi}_3(z,t)$ and $\hat{d}(\omega,z)$ respectively, we find the equation of motion for the cavity operator

$$\partial_t \hat{c}(t) = -\frac{i}{\hbar}\left[\hat{c}(t),\hat{H}_{\text{sys}}\right] - \frac{\kappa}{2}\hat{c}(t) + \sqrt{\kappa}\hat{b}_{\text{in}}(t), \tag{2.108}$$

where we have defined

$$\hat{b}_{\text{in}}(t) = \frac{1}{\sqrt{2\pi}}\int_{-\infty}^{+\infty}e^{-i\omega(t-t_0)}\hat{b}(\omega,t_0)d\omega. \tag{2.109}$$

The first term in the right hand side of Eq. (2.108) describes the unitary evolution of the cavity, while the second term shows the loss of photons with rate κ. In the previous section we interpreted the corresponding last term, $\hat{d}_{\text{in}}(z',t)$, as noise entering into our system due to the interaction with the bath, given that the initial state of the bath and the system are factorized and the state of the bath is incoherent. However, in this case we consider that the initial state of the bath is in a coherent or a squeezed state, so the corresponding term, $\hat{b}_{\text{in}}(t)$, can no longer be interpreted as noise, but instead it is considered as a classical field driving the dynamics of the cavity [76].

2.10   Atom Interferometry

Atom interferometers are the matter-wave counterparts of optical interferometers. They make use of the dual wave-particle nature of massive objects shown by Louis de Broglie [77] in the early 20th century. The wave nature of massive particles is allowing to observe interference fringes at the end of the interferometer, similar to the optical case. Hence, atom interferometers provide us with the ability to estimate inertial quantities, such as accelerations and rotations, due to the interaction of massive particles with the gravitational field. This is the reason why, they have a huge impact in many geophysical applications. The basic function of an atom interferometer is similar with the optical one, namely it is based on creating a superposition of two states, which propagate along slightly different paths, acquiring a relative phase difference and finally being recombined and interfered.

In 1991 the first four atom interferometers were realised [14–17]. Importantly, in the last two experiments the atom interferometers were used, in order to measure small rotations and the gravitational acceleration respectively, implementing in that way the first atom interferometer based inertial sensors. More particularly in [14], they created an atom interferometer based on a Young's double slit construction. Namely, a helium atomic beam passes through a single slit creating two spatially separated waves, which

after impinging on a double slit structure, they interfere in a final single slit. However in [15], they used a sodium atomic beam and a three grating geometry, in order to split the initial beam into two separated beams in position and momentum and then recombine them together, in order to observe the atomic interference. On the other hand in [16], they used a calcium atomic beam and an optical Ramsey geometry, in order to implement an atom interferometer. They examined the interaction of the atomic beam with two pairs of separated counter-propagating laser fields, while the atomic beam apparatus was rotated around a perpendicular axis. They were the first to report the Sagnac effect in atoms, by observing the shift of the interference fringes and measuring the corresponding phase shift due to the rotation. Finally in [17], they created an atom interferometer, by using laser cooled sodium atoms in a MZ configuration, where they implemented the two beam-splitters and the mirror by using Raman pulses. They were the first to measure the gravitational acceleration, by using atom interference.

As the reader would have noticed from that description, in the first two experiments, [14, 15], they used Bragg diffraction, while in the last two, [16, 17], they used Raman pulses, in order to implement the optical elements of the atom interferometer. By using Bragg pulses we create a superposition of two different momentum states, while the atoms remain in the same internal state. In that case, at the end of the interferometer, free propagation of the two states is necessary, in order to be spatially separated and consequently distinguished prior to imaging. On the other hand, Raman transitions, create a superposition between two momentum and two internal states. We have already seen in Sec. [2.7.1], how we can use the two photon transition, in order to move to another internal state with different momentum.

Let's consider the case where we have a MZ type interferometer with three Raman pulses, in a gravitational field Fig. [2.2 (a)]. This interferometer can also be found in the literature as Kasevich-Chu (KC) interferometer, named after the corresponding experiment in Stanford [18]. Each pulse consists of two counter-propagating laser beams. Let's examine how the first beam-splitter works, considering that the atoms are initially in the internal state $|1\rangle$. The atoms absorb the light incident from below with wave-vector k_1, increasing their momentum by $\hbar k_1$. Also, due to stimulated emission they emit a photon with wave-vector k_2, which results in an additional momentum kick for the atom, as depicted in Fig. [2.2 (b)]. The total two photon process transfers the atom to the internal state $|2\rangle$ and gives a total momentum boost to the atom Δp

$$\Delta p = \hbar \boldsymbol{k_1} - \hbar \boldsymbol{k_2} = \hbar \boldsymbol{k_0} \approx 2\hbar \boldsymbol{k_1}, \tag{2.110}$$
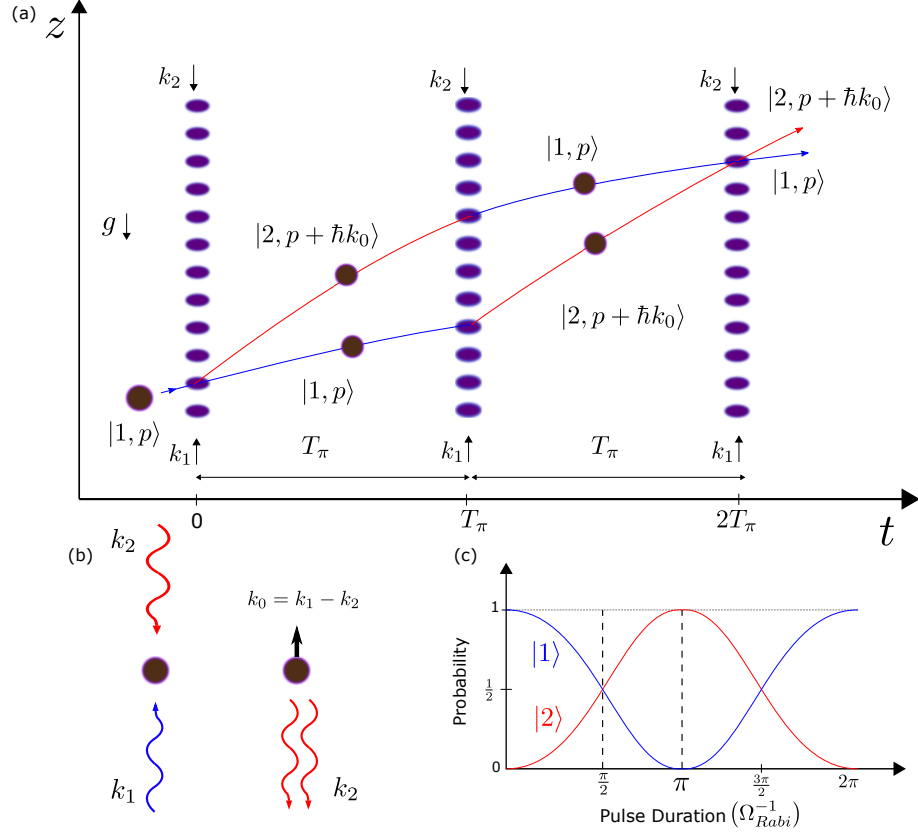
Figure 2.2: (a) Particle passing through the KC interferometer, (b) momentum boost of the atom, due to the interaction with the two counter-propagating beams, (c) Rabi oscillations between states $|1\rangle$ and $|2\rangle$. We can realise different optical elements, by adjusting appropriately the duration of the pulse.

since $\boldsymbol{k_1}$ and $\boldsymbol{k_2}$ point towards opposite directions and we have assumed that $|\boldsymbol{k_1}| \approx |\boldsymbol{k_2}|$. As long as the light is on, the atoms make Rabi oscillations between the two internal states. By adjusting the time of the atom-light interaction we can realise a beam-splitter or a mirror Fig. [2.2 (c)]. The whole interferometric sequence is depicted in Fig. [2.2 (a)]. More, particularly, the first pulse of the KC interferometer acts as a 50/50 beam-splitter, namely it creates an equal superposition of the two internal and momentum states of the atom, i.e $|1, \boldsymbol{p}\rangle \to |2, \boldsymbol{p} + \hbar\boldsymbol{k_0}\rangle$. Then, we have free evolution of the atoms into the gravitational field for time T_π. At $t = T_\pi$ we apply a Raman pulse, which acts as a mirror, namely the two matter-waves interchange internal and momentum states, such that after a second period of free evolution for time T_π, they are spatially overlapping, where we also apply a second 50/50 beam-splitter, in order for the two matter-waves to interfere. At the end of the interferometer we usually measure the population of the atoms in each port, which depends on the phase difference between the two arms, similarly with the optical

case.

The phase shift at the output of an atom interferometer has already been calculated [78, 79]. The common procedure is to separate the total phase shift into three different components and calculate each one by finding the closed integral of the corresponding Lagrangian

$$\Delta\phi_{\text{tot}} = \Delta\phi_{\text{propagation}} + \Delta\phi_{\text{interation}} + \Delta\phi_{\text{separation}}. \tag{2.111}$$

The first term describes the phase difference due to the propagation of the matter-waves along the classical trajectories in the gravitational field and can be separated even further into two parts, namely a phase shift due to the kinetic and potential energies

$$\Delta\phi_{\text{propagation}} = \Delta\phi_{\text{kinetic}} + \Delta\phi_{\text{potential}}, \tag{2.112}$$

where they have same magnitudes and opposite signs [80]

$$\Delta\phi_{\text{kinetic}} = -\Delta\phi_{\text{potential}} = k_0 g T_\pi^2. \tag{2.113}$$

Here, k_0 is the atomic momentum kick, which points towards the opposite direction of the gravitational acceleration, and T_π is the time that we apply the mirror.

The second term in Eq. (2.111) is referred to the phase difference due to the interaction between the atoms and the light pulses. It also constitutes from two different terms, one with the same magnitude and opposite sign with the phase difference obtained from the kinetic energy [80], and one which depends on the phase difference of the laser beams $\Delta\Phi_{\text{laser}}$, which is defined later

$$\Delta\phi_{\text{interaction}} = -k_0 g T_\pi^2 + \Delta\Phi_{\text{laser}}. \tag{2.114}$$

The third term in Eq. (2.111) is a phase difference, which arises only when the two wave-packets do not intersect at the final beam-splitter, so for the symmetrical case that we examine here $\Delta\phi_{\text{separation}} = 0$. Hence, we conclude that the final total phase difference is given by

$$\Delta\phi_{\text{tot}} = k_0 g T_\pi^2 + \Delta\Phi_{\text{laser}}, \tag{2.115}$$

where $\Delta\Phi_{\text{laser}} = \phi_3 - 2\phi_2 + \phi_1$ and ϕ_i with $i = 1,\ 2,\ 3$ is the phase difference between the two counter propagating laser beams, forming the first beam-splitter, the mirror and the second beam-splitter respectively.

The interpretation of the source of the resulting final phase shift has been the reason for the so called redshift controversy [81]. One way to obtain the result given by Eq. (2.115),

is by cancelling the contributions of the kinetic and potential energy, meaning that the total phase shift arises due to the interaction of the atoms with the laser pulses. We can conclude to the exact same result, if we instead cancel the contributions of the kinetic energy and the interaction phase shift, indicating that $\Delta\phi_{\text{tot}}$ comes from the potential energy, i.e. the redshift. Hence, it becomes clear that the interpretation of the total phase shift between the two arms of the interferometer depends on the cancellation of these terms [80].

In [80], except from analysing in a very clear way the source of the redshift controversy, they also performed a calculation of the total phase shift based on an operator algebra approach and they concluded to the exact same result with Eq. (2.115). Essentially, they showed that the phase shift results due to the different time evolution operators that describe the dynamics in the two arms of the interferometer. In both arms we have the same operations but with different orderings, which combined with the non-commutability of the various evolution operators results in the phase shift between the two arms. This non-commutability originates from the very simple commutation relation between the position and momentum operators

$$[\hat{z}, \hat{p}_z] = i\hbar. \tag{2.116}$$

We can clearly see now that the non-commutability of position and momentum operators is at the heart of the origin of the total phase shift between the arms of a KC interferometer. In order to proceed with our calculation we assume that the phase difference of all counter propagating laser pulses, are independent of time, which means that $\Delta\Phi_{\text{laser}} = 0$. Hence, we obtain for the total phase shift

$$\phi_g = k_0 g T_\pi^2, \tag{2.117}$$

where from now on we will call the total phase shift in a KC interferometer as ϕ_g for simplicity. We notice that we can estimate the gravitational field, after finding ϕ_g, with error

$$\Delta g = \frac{\Delta\phi_g}{k_0 T_\pi^2}. \tag{2.118}$$

In Chapter 3, we are going to see that the precision of estimating a phase difference, using an uncorrelated atomic ensemble, is limited by the atom shot-noise limit $\Delta\phi_g = 1/\sqrt{N}$. Hence, we can estimate the gravitational field using a KC interferometer with precision

$$\Delta g = \frac{1}{k_0 T^2} \frac{1}{\sqrt{N}}, \tag{2.119}$$

which is limited by the projection noise of the atoms. We can surpass this noise limit, by using the feature of entanglement, namely by considering atomic ensembles with appropriate correlations amongst the particles. In the case of entangled states, the new limit of precision of a phase difference is the Heisenberg limit $\Delta\phi_g = 1/N$, which for the experimentally realistic value of $N = 10^6$ gives a 1000 factor of improvement, in the final sensitivity of g. We are going to discuss about those concepts in more detail in Chapter 3, as well as they are the focus of our work in Chapters 5 and 6.

In Chapter 4, we follow a very similar approach with the operator algebra developed in [80], in order to examine the evolution of the wave-function of a particle passing through a KC interferometer and calculate the classical and quantum Fisher information, which we are going to define in Chapter 3. During our calculations, we concluded to the same result for $\Delta\phi_{\text{tot}}$, Eq. (2.115), where we also found $\Delta\phi_{\text{separation}}$, since we considered the more general case where the two time intervals of free evolution are not the same. In Chapter 4, we also concluded to the very important outcome, that the result of the whole interferometric sequence is not just a phase deference between the two arms, but it also affects the wave-function of the particle itself. This result would help to gain a better understanding of the whole dynamics, as well as it would help to find improvements in the estimation of the gravitational field. We would analyse that result in more detail in Chapter 4.

Chapter 3

Background II: Basic Concepts of Quantum Metrology and Parameter Estimation Theory

In this chapter we are going to introduce some basic concepts related to the field of quantum metrology and parameter estimation theory, which would be very useful in understanding the main chapters of this thesis. We start by introducing the concept of a single qubit and then we move to the many spins case. We discuss the very useful Dicke states, as well as the coherent spin states (CSSs), which describe the state of an atomic ensemble with fixed number of atoms. We then give a very illustrative description of a Mach-Zehnder (MZ) interferometer, as rotations of angular momentum operators. We also introduce the concept of quantum noise of a measurement signal, and spin-squeezing, as well as we discuss the fundamental limitations of estimating a phase difference between the two arms of an atom interferometer. Furthermore, we talk about two very common states of the electromagnetic field, the Glauber coherent state and the squeezed states. Finally, we introduce some very useful tools from parameter estimation theory, which would help us to quantify the performance of quantum sensors. More particularly, we introduce the quantum Fisher information (QFI), which combined with the quantum Cramer-Rao bound (QCRB) determine the fundamental limit of sensitivity with which a quantum state provides us. In addition, the classical Fisher information (CFI), is a measure of how much information we can extract, from the available metrological information, by making a particular measurement. We are going to derive some very useful relations regarding those quantities, which we are going to use in Chapter 4, in order to evaluate the performance of atom gravimeters.

3.0.1 Single Spin

Firstly, we consider a system consisting of only two modes (single particle states) $|a\rangle$ and $|b\rangle$. For example, these could be two atomic energy levels, two spatially separated arms of a MZ interferometer etc. For convenience, we identify all two mode systems with an effective single spin 1/2 particle, which can be in states $\pm 1/2$, called a qubit. Any pure state of a single qubit can be written as [39]

$$|\psi(\theta,\phi)\rangle = \cos\frac{\theta}{2}|a\rangle + e^{i\phi}\sin\frac{\theta}{2}|b\rangle = \left[\cos\frac{\theta}{2}\hat{a}^\dagger + e^{i\phi}\sin\frac{\theta}{2}\hat{b}^\dagger\right]|0\rangle|0\rangle, \qquad (3.1)$$

where $0 \leq \theta \leq \pi$ and $0 \leq \phi \leq 2\pi$ are the polar and the azimuthal angles respectively and $|0\rangle|0\rangle$ is the vacuum state. The second equality in Eq. (3.1) is the corresponding form in the second quantization formalism, as we use the creation operators, $\hat{a}^\dagger$ and $\hat{b}^\dagger$, in order to create a particle in the corresponding single particle state. We introduce the Pauli vector $\hat{\boldsymbol{\sigma}} = \{\sigma_x, \sigma_y, \sigma_z\}$, where

$$\hat{\sigma}_x = \begin{pmatrix} 0 & 1 \\ 1 & 0 \end{pmatrix}, \qquad \hat{\sigma}_y = \begin{pmatrix} 0 & -i \\ i & 0 \end{pmatrix}, \qquad \hat{\sigma}_z = \begin{pmatrix} 1 & 0 \\ 0 & -1 \end{pmatrix} \qquad (3.2)$$

are the Pauli matrices, and $\boldsymbol{s} = \{\sin\theta\cos\phi, \sin\theta\sin\phi, \cos\theta\}$ is the mean spin direction vector. We note that in this simple case of a single qubit the dimensions of the Hilbert space are $(2\sigma + 1) = 2$. We can realise this two mode state in the so called Bloch sphere. Let's consider for example that the two states indeed represent the spin up, $|\uparrow\rangle$, and spin down, $|\downarrow\rangle$, states, where in this case they lie at the north and the south pole of the Bloch sphere respectively. Any pure quantum state can be associated with a point at the surface of the Bloch sphere.

3.0.2 Many Spins

We generalize the single particle picture with spin 1/2 to N particles with total spin J, by using the collective spin operators

$$\hat{J}_i = \sum_{k=1}^{N} \hat{\sigma}_i^k, \qquad (3.3)$$

where $i = x, y, z$ and we sum over all single spin components of the N particles. Also, the collective spin operators must satisfy the commutation relation $[\hat{J}_i, \hat{J}_j] = i\epsilon_{i,j,k}\hat{J}_k$ and the Heisenberg uncertainty relation

$$\Delta\hat{J}_z^2 \Delta\hat{J}_y^2 \geq \frac{\langle\hat{J}_x\rangle^2}{4}. \qquad (3.4)$$

As we are going to see in the following subsections, the equality holds for the minimum uncertainty states. We can calculate any observable, in a system with total spin J, by using the three spin operator components $\hat{J}_x, \hat{J}_y, \hat{J}_z$ and the identity operator. Now, that we have moved to the many spins case the dimensions of the Hilbert space have rapidly increased to $(2\sigma + 1)^N = 2^N$. However, we consider a system which is symmetric under the exchange of two spins, in the sense that all the operations applied in our ensemble affect each spin in the same way. In this case the total spin of our system is the maximum allowed for an N particle system, $J = N/2$ [39]. Also, after taking into account this symmetry the dimensions of the Hilbert space are dramatically decreased to $(2N\sigma + 1) = (N + 1)$.

3.0.3 Dicke states

We can use the well known Dicke states $|J, m\rangle$, which are eigenstates of $\hat{\boldsymbol{J}}^2$ and $\hat{J}_z$, in order to form a basis and write any general N particle state as

$$|\Psi\rangle = \sum_{m=-J}^{J} c_m |J, m\rangle, \tag{3.5}$$

where $|J, m\rangle$ satisfies

$$\hat{\boldsymbol{J}}^2 |J, m\rangle = J(J + 1)|J, m\rangle, \qquad \hat{J}_z |J, m\rangle = m|J, m\rangle, \tag{3.6}$$

where $J \in \{\frac{N}{2}, \frac{N}{2} - 1, ..., -\frac{N}{2} + 1, -\frac{N}{2}\}$ and $m \in \{-J, -J + 1, ..., J - 1, J\}$. Due to the exchange symmetry of the spins we can treat them as indistinguishable bosons. Hence, we can describe the angular momentum operators using the more elegant Schwinger's formula. We essentially consider that we create (destroy) a particle by using the creation (annihilation) operators in mode $|a\rangle$ and $|b\rangle$, $\hat{a}^\dagger(\hat{a})$ and $\hat{b}^\dagger(\hat{b})$ respectively, following the usual second quantization formalism. So, the general k collective spin component can now be written as

$$\hat{J}_k = \frac{1}{2} \left(\hat{a}^\dagger, \hat{b}^\dagger\right) \sigma_k \begin{pmatrix} \hat{a} \\ \hat{b} \end{pmatrix}, \tag{3.7}$$

with $k = x, y, z$. We can alternatively write the Dicke states in the second quantization formalism as

$$|J, m\rangle = \left|\frac{N}{2} + m\right\rangle_a \left|\frac{N}{2} - m\right\rangle_b = \frac{\left(\hat{a}^\dagger\right)^{\frac{N}{2}+m}}{\sqrt{\left(\frac{N}{2} + m\right)!}} \frac{\left(\hat{b}^\dagger\right)^{\frac{N}{2}-m}}{\sqrt{\left(\frac{N}{2} - m\right)!}} |0\rangle|0\rangle, \tag{3.8}$$

where we have used that $J = \frac{N}{2}$. We should clarify here a subtle point of the notation we are using. The state $|J, m\rangle$, denoted by a single *ket*, describes a state in the angular

momentum basis, while a state denoted by a direct product of two *kets*, $|n_a\rangle|n_b\rangle$, indicates the mode occupation basis. Written in that form we can see that the state $|J, m\rangle$ is essentially a two mode Fock state, meaning that we have $n_a = \frac{N}{2} + m$ particles in mode $|a\rangle$ and $n_b = \frac{N}{2} - m$ in mode $|b\rangle$. We also define the raising and lowering spin operators $\hat{J}_{\pm} = \hat{J}_x \pm i\hat{J}_y$ or $\hat{J}_+ = \hat{a}^\dagger\hat{b}$ and $\hat{J}_- = \hat{b}^\dagger\hat{a}$, which when applied to the Dicke states give

$$\hat{J}_{\pm}|J, m\rangle = \sqrt{\frac{N}{2}\left(\frac{N}{2} + 1\right) - m(m \pm 1)}\,|J, m \pm 1\rangle. \tag{3.9}$$

The state $|J, J\rangle = |N\rangle_a|0\rangle_b$ represents the case, where all the particles are in mode $|a\rangle$, e.g in the interferometer case we send N particles through the one port and none through the other port, or in the spin picture all particles are in the spin up $|\uparrow\rangle$ state. This state is often considered as the initial state of the system in experiments, since it is easy to prepare all atoms in one mode.

3.0.4 Coherent Spin States

Coherent spin states are a generalization of the field coherent states, which we are going to analyse in the following subsections. They are constructed as the normalized product of N single particle states all pointing along the same mean-spin direction $\boldsymbol{s} = \{\sin\theta\cos\phi, \sin\theta\sin\phi, \cos\theta\}$ Eq. (3.1)

$$|\alpha(\theta, \phi)\rangle = \frac{1}{\sqrt{N!}}\left(\cos\frac{\theta}{2}|a\rangle + e^{i\phi}\sin\frac{\theta}{2}|b\rangle\right)^{\otimes N}$$

$$= \frac{1}{\sqrt{N!}}\left(\cos\frac{\theta}{2}\hat{a}^\dagger + e^{i\phi}\sin\frac{\theta}{2}\hat{b}^\dagger\right)^{\otimes N}|0\rangle|0\rangle. \tag{3.10}$$

These states are the eigenstates of $\hat{J}_s$ with maximum eigenvalue $N/2$. The CSSs are defined as a product of states, thus no entanglement is present amongst the particles of the system. We discuss about the concept of entanglement in more detail later. We can also write a CSS in the Dicke basis

$$|\alpha(\theta, \phi)\rangle = \sum_{m=-J}^{J} c_m(\theta)e^{(\frac{N}{2}+m)\phi}|J, m\rangle, \tag{3.11}$$

where the coefficients $c_m(\theta)$ are given by the binomial distribution

$$c_m(\theta) = \left[\frac{N!}{\left(\frac{N}{2} + m\right)!\left(\frac{N}{2} - m\right)!}\right]^{1/2}\cos(\theta/2)^{\frac{N}{2}-m}\sin(\theta/2)^{\frac{N}{2}+m}. \tag{3.12}$$

The main characteristic of CSSs is that there are no correlations amongst the particles, which means no entanglement, since they are the only pure states that can be written as a product of single-particle states. Also, we can move from one CSS to another by making

single particle operations, such as rotations, which could not create entanglement, as we are going to see in the following. CSSs as the Glauber coherent states, are known to be the closest concept we have to classical states. This is true in the sense that they do not generate the quantum feature of entanglement and that they are minimum uncertainty states, namely they satisfy the equality in Eq. (3.4). Thus, if we measure the spin component in any direction orthogonal to the mean spin direction $\boldsymbol{s}$, we get $\langle \hat{J}_s \rangle = 0$ and $(\Delta \hat{J}_n)^2 = N/4$, where $\boldsymbol{n} \cdot \boldsymbol{s} = 0$, since each individual spin is projected in the corresponding up and down states along the s-axis [39,48,82]. Importantly, CSSs are easy to produce, by preparing all particles in the same single particle state and then performing single particle operations, which act as a collective operation, such as rotations, as we are going to see in the next section. This is the reason why, we often consider them as our theoretical starting point.

3.0.5   Mach-Zehnder Interferometer

Here, we examine the dynamics of the well-known MZ interferometer, which consists of three main steps, as we have already seen in Sec. [2.10], where we discussed atom interferometry. Firstly, we have a 50/50 beam-splitter, followed by a phase shift between the arms of the interferometer and finally we have a second beam-splitter, which converts the phase shift into population difference between the two modes (arms) of the interferometer, which results in interference fringes. We are going to use the very illustrative angular momentum formalism, which was firstly introduced by Yurke [82], in order to describe the quantum state passing through the MZ interferometer.

In the simple case of a single qubit we can describe any unitary transformation applied to our state as a rotation of angle θ with respect to an arbitrary n-axis on the Bloch sphere, i.e $\hat{U} = e^{-i\frac{\theta}{2}\hat{\sigma}_n}$. Moving to the N qubit case, we assume that such operations affect all the qubits in the same way, due to the aforementioned exchange symmetry. More particularly, we have the local rotation of each spin through the same angle and axis, giving rise to a collective rotation $\otimes_{l=1}^{N} e^{-i\frac{\theta}{2}\hat{\sigma}_n^{(l)}} = e^{-i\theta \hat{J}_n}$. Hence, we can describe all unitary transformations as rotations of the collective spin on the Bloch sphere. In the following, we present the MZ interferometer evolution step by step, following an excellent relevant description found in [83]. At each step we also depict the state of the system, by using the Husimi Q representation $Q(\theta,\phi) = \langle \alpha(\theta,\phi)|\hat{\rho}|\alpha(\theta,\phi)\rangle$, where $\hat{\rho} = |\psi\rangle\langle\psi|$ is the density matrix of the system.

1. We start with an initial CSS $|\alpha(0,0)\rangle = |N\rangle|0\rangle$ representing N particles in mode $|a\rangle$ and zero particles in mode $|b\rangle$, or putting it differently all spins are in $|\uparrow\rangle$ state.
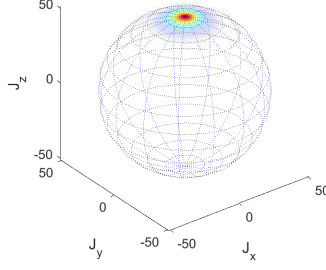
Figure 3.1: Husimi $Q(\theta, \phi)$ representation of collective spin-up state. We consider a system with $N = 100$.

2. As we mentioned before each unitary transformation can be realized by a rotation of the collective spin. The beam-splitter is described by a $\pi/2$ rotation around the x-axis, i.e $e^{-i\hat{J}_x\pi/2}$. This is equivalent to putting each atom in a coherent superposition $\frac{1}{\sqrt{2}}(|a\rangle - i|b\rangle)$. Thus, the initial state would become

$$e^{-i\hat{J}_x\pi/2}|N\rangle|0\rangle = |\alpha(\pi/2, \pi/2)\rangle = \frac{1}{\sqrt{N!}}\left(\frac{\hat{a}^\dagger}{\sqrt{2}} - i\frac{\hat{b}^\dagger}{\sqrt{2}}\right)^{\otimes N}|0\rangle|0\rangle. \qquad (3.13)$$
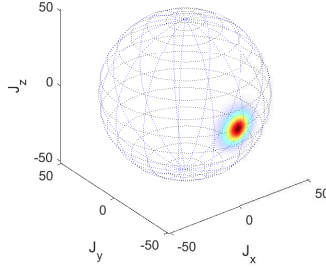

Figure 3.2: Husimi $Q(\theta, \phi)$ representation of the state after the first beam-splitter. We consider a system with $N = 100$.

3. Then, we have a phase difference between the two arms of the interferometer, caused by the interaction of the quantum state with the parameter of interest we want to estimate. For example, in the case of a gravimeter the upper arm is affected in a slightly different way than the lower arm of the interferometer, due to the interaction with the gravitational field, resulting in a phase difference between them. This is described by a rotation of angle ϕ around z-axis, i.e $e^{-i\hat{J}_z\phi}$. The resulting state for

our ensemble would be

$$e^{-i\hat{J}_z\phi}e^{-i\hat{J}_x\pi/2}|N\rangle|0\rangle = |\alpha(\pi/2,\pi/2+\phi)\rangle = \frac{1}{\sqrt{N!}}\left(\frac{\hat{a}^\dagger}{\sqrt{2}} - ie^{-i\phi}\frac{\hat{b}^\dagger}{\sqrt{2}}\right)^{\otimes N}|0\rangle|0\rangle.$$
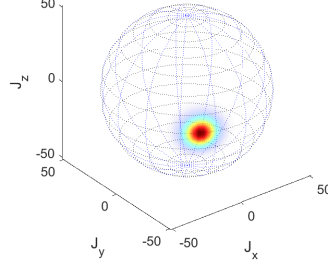
$$(3.14)$$

Figure 3.3: Husimi $Q(\theta,\phi)$ representation of the state after the free evolution. We consider a system with $N = 100$.

4. We finally have the second beam-splitter which creates the interference fringes and translates ϕ into population difference

$$e^{i\hat{J}_x\pi/2}e^{-i\hat{J}_z\phi}e^{-i\hat{J}_x\pi/2}|N\rangle|0\rangle = |\alpha(\phi,0)\rangle = \frac{1}{\sqrt{N!}}\left(\sin(\phi/2)\hat{a}^\dagger + \cos(\phi/2)\hat{b}^\dagger\right)^{\otimes N}|0\rangle|0\rangle,$$
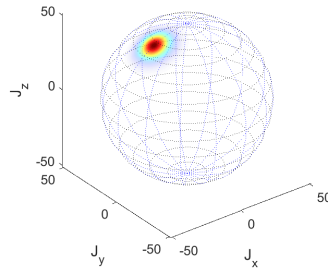
$$(3.15)$$

Figure 3.4: Husimi $Q(\theta,\phi)$ representation of the state after the final beam-splitter. We consider a system with $N = 100$.

where we used Eq. (3.10) in the last equality of all three previous equations. As shown in [82], all the aforementioned interferometric sequence is equivalent to a simple rotation

of angle ϕ around the y-axis, $e^{i\hat{J}_x\pi/2}e^{-i\hat{J}_z\phi}e^{-i\hat{J}_x\pi/2} = e^{i\hat{J}_y\phi}$. One could pictorially confirm that by just rotating the spin-up state of Fig. [3.1] with angle ϕ over the y-axis. In that case the result would be Fig. [3.4]. This can be derived, in a more strict way, by starting with the Taylor expansion of $e^{-i\hat{J}_z\phi}$

$$
\begin{aligned}
\hat{U}_{MZ} &= e^{i\hat{J}_x\pi/2}e^{-i\hat{J}_z\phi}e^{-i\hat{J}_x\pi/2} \\
&= e^{i\hat{J}_x\pi/2}\left(1 - i\hat{J}_z\phi - \frac{1}{2}\hat{J}_z^2\phi^2 + ...\right)e^{-i\hat{J}_x\pi/2} \\
&= 1 - i\phi\left(e^{i\hat{J}_x\pi/2}\hat{J}_z e^{-i\hat{J}_x\pi/2}\right) - \frac{1}{2}\phi^2\left(e^{i\hat{J}_x\pi/2}\hat{J}_z e^{-i\hat{J}_x\pi/2}\right)^2 + ... \\
&= \exp\left(-i\phi e^{i\hat{J}_x\pi/2}\hat{J}_z e^{-i\hat{J}_x\pi/2}\right) = e^{i\hat{J}_y\phi},
\end{aligned}
\tag{3.16}
$$

where in the third equality we used the operator property $\hat{A}\hat{B}^n\hat{A}^\dagger = \left(\hat{A}\hat{B}\hat{A}^\dagger\right)^n$, for any operator $\hat{B}$ and any unitary operator $\hat{A}$ ($\hat{A}\hat{A}^\dagger = 1$). Also, in the last equality we used that $e^{i\hat{J}_x\pi/2}\hat{J}_z e^{-i\hat{J}_x\pi/2} = \hat{J}_y$, as can easily be shown using the known commutation relations of $\hat{J}$ components. Thus, we showed that the MZ interferometer analysed previously in four different steps, can also be equivalently described by a rotation of angle ϕ around the y-axis.

Now that we know how to implement the MZ interferometer, we can easily find how it affects the spin components of the particles. At the output of the interferometer the z-component of the collective angular momentum of the atoms is given by

$$
\hat{J}_z(\phi) = e^{-i\hat{J}_y\phi}\hat{J}_z(0)e^{i\hat{J}_y\phi} = \hat{J}_z(0)\cos\phi - \hat{J}_x(0)\sin\phi,
\tag{3.17}
$$

where $\hat{J}_z(0)$ is the z-component of the collective atomic angular momentum at the input of the interferometer. In the above equation we notice the interference fringes, namely we see that the population difference at the output of the interferometer depends on the phase ϕ between the two arms. In the field of quantum metrology we aim to estimate this phase difference with the highest possible precision. Using an error propagation formula we find

$$
\Delta\phi(\phi) = \frac{\sqrt{\text{Var}(\hat{S}(\phi))}}{|\partial_\phi\langle\hat{S}(\phi)\rangle|},
\tag{3.18}
$$

where $\hat{S}$ is the signal we measure at the output of the interferometer. This is the standard deviation of the phase difference in the asymptotic limit ($\nu \gg 1$, where ν is the number of independent estimates) for a single estimate.
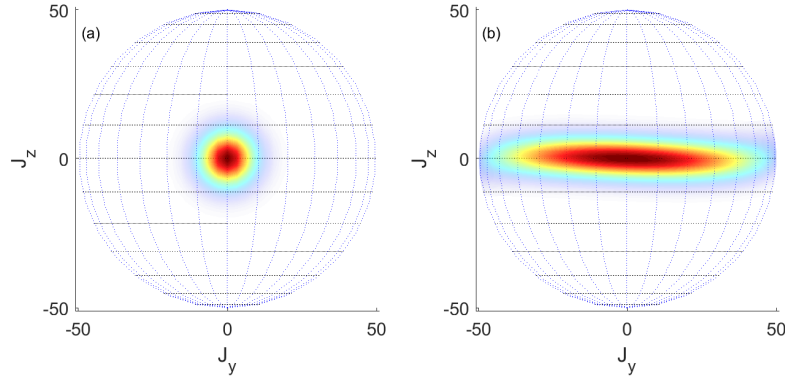
Figure 3.5: Husimi $Q(\theta, \phi)$ representation using $N = 100$ for (a) a maximal $\hat{J}_x$ eigenstate, which is a spin coherent state and (b) a spin-squeezed state along the z-direction.

3.1 Spin Squeezing

We can calculate the phase shift between the two arms of the interferometer, ϕ, with error $\Delta\phi$ given by Eq. (3.18). We consider that we make the common measurement of the population difference at the output of the interferometer, $\hat{S} = \hat{J}_z$, as well as we assume that $\phi = 0$, since we are usually interested about the fluctuations around a small mean value ϕ. Hence, from Eq.(3.17) we obtain $\partial_\phi \langle \hat{J}_z(\phi) \rangle |_{\phi=0} = \langle J_x(0) \rangle$. For a CSS pointing along the x-axis $|\alpha(\pi/2, \pi/2)\rangle$ as the initial state entering the interferometer we have $\text{Var}(\hat{J}_z) = N/4$ and $\langle J_x \rangle = N/2$, which gives

$$\Delta\phi_{\text{SNL}} = \frac{1}{\sqrt{N}}, \tag{3.19}$$

where this is the so called shot-noise limit (SNL). This is the best precision we can have for uncorrelated states, since CSSs are minimum uncertainty states Fig. [3.5(a)]. Uncorrelated, or separable states are states with no inter-particle correlations, where we do not have entanglement, as we are going to analyse in more detail later. The SNL in not limited to the concept of spin measurements, but is instead a fundamental limit for all uncorrelated states where discrete measurements are made.

We define a spin squeezed state as the state that surpasses the SNL, given that we make a measurement of an angular momentum component. Spin squeezed states constitute a class of states, where they have a spin squeezed variance along one direction $\boldsymbol{n}$, at the cost of an appropriately increased variance along an orthogonal direction $\boldsymbol{s}$, i.e. $\boldsymbol{n} \cdot \boldsymbol{s} = 0$, in order the Heisenberg uncertainty principle to be still satisfied Eq. (3.4), Fig. [3.5(b)]. If

we measure the spin component along the $\boldsymbol{n}$ direction, i.e. $\hat{S} = \hat{J}_n$, we can estimate the phase difference between the two arms of the interferometer with precision

$$\Delta\phi(\phi) = \frac{\sqrt{\text{Var}(\hat{J}_n(\phi))}}{|\partial_\phi\langle\hat{J}_n(\phi)\rangle|}. \tag{3.20}$$

The need to have a measure that quantifies the level of spin-squeezing motivates us to write $\Delta\phi$ as

$$\Delta\phi = \frac{\xi}{\sqrt{N}}, \tag{3.21}$$

where we have defined the spin squeezing parameter as

$$\xi = \sqrt{N}\frac{\sqrt{\text{Var}(\hat{J}_n(\phi))}}{|\partial_\phi\langle\hat{J}_n(\phi)\rangle|}. \tag{3.22}$$

Hence, for a CSS we have $\xi = 1$, while $\xi < 1$ is a sufficient and necessary condition for spin-squeezing. A separable state of N particles, namely a state without any correlations amongst the N particles, is described by the product

$$\hat{\rho} = \sum_k P_k\hat{\rho}_k^{(1)} \otimes \hat{\rho}_k^{(2)} \otimes ... \otimes \hat{\rho}_k^{(N)}, \tag{3.23}$$

where $\hat{\rho}_k^{(i)}$ is the density matrix for the i-th particle and P_k is the corresponding probability satisfying $P_k > 0$ and $\sum_k P_k = 1$. It was shown in [53] that these uncorrelated states obey $\xi \geq 1$. This indicates that $\xi < 1$ could be obtained only from non-separable states, i.e entangled states. However, that does not mean that a non-separable state necessarily has $\xi < 1$. There are the so called entangled non-Gaussian states (ENGSs) [46], which are entangled and could offer sub-shot-noise sensitivities, by measuring more complicated quantities other than the spin components. Thus, ENGSs are entangled states, which are not spin-squeezed, i.e. $\xi > 1$. The fact that $\xi < 1$ could be obtained only from entangled states also implies that we cannot surpass the SNL by ordinary operations, such as rotations, but instead we need many body entanglement, namely to create appropriate correlations amongst the particles. Summarizing, $\xi < 1$ is a sufficient and necessary condition for spin-squeezing and it is a sufficient but not necessary condition for entanglement and sub-shot-noise sensitivity with respect to a collective spin measurement, i.e. $\hat{S} = \hat{J}_k$ with $k = x, y, z$.

In [84] a stronger condition was introduced for many body entanglement

$$\chi^2 = \frac{N}{F_Q[\hat{\rho}_0, \hat{G}]} < 1, \tag{3.24}$$

where $F_Q[\hat{\rho}_0, \hat{G}]$ is the quantum Fisher information, which depends on the initial state $\hat{\rho}_0$ and the generator $\hat{G}$ that determines the unitary evolution of the system. We are going to examine in more detail the QFI and other concepts of estimation theory in the next section. This condition recognizes a class of states that can be entangled, $\chi^2 < 1$, but not spin-squeezed $\xi > 1$. We briefly present here the quantum Cramer-Rao bound (QCRB), which we properly derive in the next section

$$(\Delta\Theta_{QCRB})^2_\theta = \frac{1}{F_Q[\hat{\rho}(\theta)]}, \tag{3.25}$$

in order to find the following relation with χ

$$(\Delta\Theta_{QCRB})_\theta = \frac{\chi}{\sqrt{N}} = \frac{\chi}{\Delta\phi_{SNL}}. \tag{3.26}$$

As it becomes apparent from the above result, $\chi < 1$ is a necessary and sufficient condition for sub-shot-noise phase sensitivity. To summarize again, using states which satisfy the condition $\chi < 1$, provides us with metrologically useful entanglement, meaning that we can surpass the SNL. However, as we aforementioned we may have a state with $\chi < 1$ and $\xi > 1$, which means that we have entanglement and we can surpass the SNL, but this may involve a more complicated measurement rather than a simple collective spin measurement. On the other hand, if we have entangled states satisfying $\chi > 1$, then they won't give any improvement to the phase sensitivity compared to the SNL. We should point out here that although χ provides us with a stronger condition for entanglement and sub-shot-noise sensitivity, ξ provides us with a condition based on a particular measurement, which is simple to perform. To point this more clearly, both ξ and χ are essentially two different metrics quantifying the ability to surpass the SNL. The first one is based on the variance of the measurement of a spin component, while the latter is based on the QFI, which makes it a stronger metric, since as we are going to see in the last section of this chapter the QFI determines the ultimate theoretical limit of precision, but it doesn't involve a specific measurement. For that reason, ξ could be more easily used for theoretical predictions in experiments, since it is common to find the z-component of the spin by measuring the population difference between the arms of the interferometer. Also, in case we need to find the spin along another direction, we can firstly apply an appropriate rotation and align it along the z-axis.

3.2   States of the Electromagnetic Field

Here, we are going to examine common states of the electromagnetic field, such as the Glauber coherent states and the squeezed light states. These states do not have a

fixed number of particles, as we saw in the case of CSSs. We are going to use these states in Chapters 5 and 6, where we exploit the atom-light interaction, in order to create entanglement and consequently spin-squeezed states. We also briefly examine the function of an optical MZ interferometer and explore how the use of squeezed light states can offer improvements in the sensitivity. In Chapters 5 and 6, we are going to utilise squeezed light interacting with the atomic ensemble and we will show that this would provide us with additional improvements with respect to the final sensitivity of the atomic state.

3.2.1 Glauber Coherent States

Glauber coherent states belong to a class of states, which satisfy the minimum uncertainty principle, i.e the product of the variances of the amplitude and phase quadrature operators takes the minimum possible value imposed by the Heisenberg uncertainty principle [67–69]

$$\Delta \hat{X} \Delta \hat{Y} = 1, \tag{3.27}$$

where $\hat{X} = \hat{a} + \hat{a}^\dagger$ is the amplitude light quadrature, while $\hat{Y} = i\left(\hat{a} - \hat{a}^\dagger\right)$ is the phase quadrature of the light field. To be more precise, coherent states are a member of a more special class, where the two variances are also equal

$$\Delta \hat{X} = \Delta \hat{Y} = 1. \tag{3.28}$$

This is the reason why, they are well known as the closest quantum mechanical states to
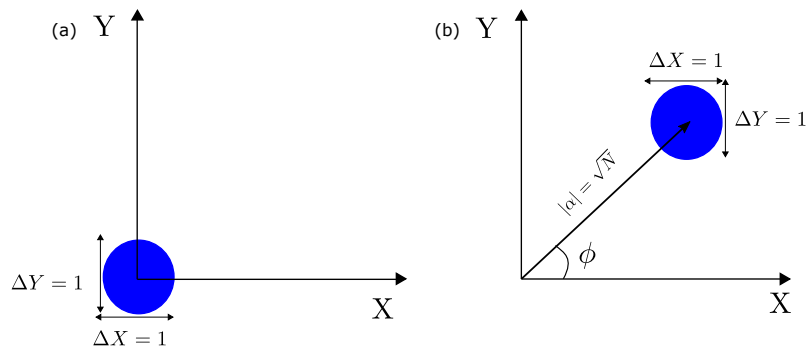

Figure 3.6: Phase diagram for (a) a vacuum state and (b) for a coherent state, which is a displaced vacuum state by the complex number α. In both cases, we see the same uncertainties for both quadratures of the EM field, since they are minimum uncertainty states and they satisfy Eq. (3.28).

a classical description of the field, and hence they are a good approximation to a bright

laser field. The vacuum state of the field, $|0\rangle$, has the same quantum noise properties, namely it satisfies Eq. (3.28). Hence, Glauber coherent states, $|\alpha\rangle$, are usually defined as a displaced vacuum state in the phase space by the complex number $\alpha = X + iY$, where X and Y are the eigenvalues of the amplitude and phase quadrature operators, Fig. [3.6]. Hence, they can be written as

$$|\alpha\rangle = \hat{D}(\alpha)|0\rangle, \tag{3.29}$$

where we have used the displacement operator $\hat{D}(\alpha)$

$$\hat{D}(\alpha) = e^{\alpha a^{\dagger} - \alpha^* \hat{a}}. \tag{3.30}$$

Also, a Glauber coherent state is the eigenstate of the annihilation operator

$$\hat{a}|\alpha\rangle = \alpha|\alpha\rangle, \tag{3.31}$$

as we briefly mentioned in Chapter 2, Sec. [2.5.1]. Using the Baker-Campbell-Hausdorff formula we can write the displacement operator as

$$\hat{D}(\alpha) = e^{-\frac{|\alpha|^2}{2}} e^{\alpha \hat{a}^{\dagger}} e^{-\alpha^* \hat{a}}. \tag{3.32}$$

Making use of Eq. (3.31) and (3.32) we can easily see how the displacement operator affects the amplitude of the coherent state

$$\hat{D}^{\dagger}(\alpha)\hat{a}\hat{D}(\alpha) = \hat{a} + \alpha, \qquad \hat{D}^{\dagger}(\alpha)\hat{a}^{\dagger}\hat{D}(\alpha) = \hat{a}^{\dagger} + \alpha^*. \tag{3.33}$$

Coherent states constitute an over-complete, and an non-orthogonal basis

$$\frac{1}{\pi} \int |\alpha\rangle\langle\alpha| d^2\alpha = 1, \qquad |\langle\alpha|\beta\rangle|^2 = e^{-|\alpha-\beta|^2}, \tag{3.34}$$

where if the distance between the two coherent states is large, they are approximately orthogonal, i.e. if $|\alpha - \beta| >> 1$ then $|\langle\alpha|\beta\rangle|^2 \to 0$. A coherent state has an uncertain number of photons. This could be more clearly seen, if we make an expansion into the Fock basis

$$|\alpha\rangle = e^{-|\alpha|^2/2} \sum_{n=0}^{\infty} \frac{\alpha^n}{\sqrt{n!}} |n\rangle. \tag{3.35}$$

From this we can extract the probability distribution of finding a coherent state with n photons

$$P(n) = e^{-|\alpha|^2} \frac{|\alpha|^{2n}}{n!}. \tag{3.36}$$

Also, we can easily calculate the mean photon number of a coherent state using Eq. (3.31)

$$\langle \hat{N}(\alpha) \rangle = \langle \alpha | \hat{a}^\dagger \hat{a} | \alpha \rangle = |\alpha|^2. \tag{3.37}$$

Substituting Eq. (3.37) into Eq. (3.36) we notice that the coherent states are a Poissonian distribution of number states

$$P(n) = e^{-\bar{n}} \frac{\bar{n}^n}{n!}, \tag{3.38}$$

where $\bar{n} = \langle \hat{N}(\alpha) \rangle$. Using again Eq. (3.31) we can easily calculate the variance of the photon number in a coherent state, which is equal with the expectation value of the photon number operator

$$\text{Var}(\hat{N}(\alpha)) = |\alpha|^2 = \langle \hat{N}(\alpha) \rangle. \tag{3.39}$$
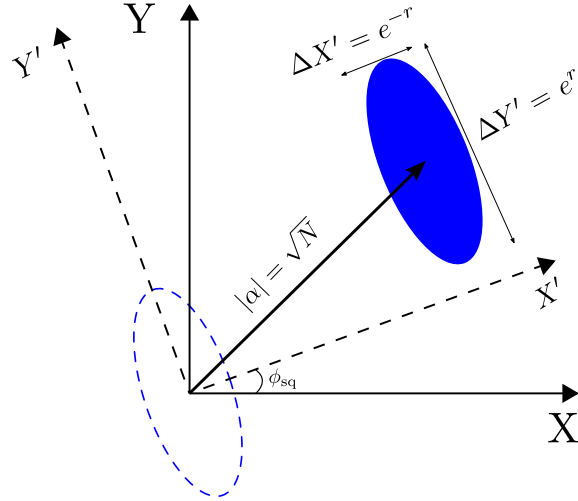
3.2.2 Squeezed States

Figure 3.7: Phase diagram of a squeezed state. We notice that we have squeezed noise in one direction at the cost of increased noise in the other direction, such that the Heisenberg uncertainty principle, Eq. (3.28), would be satisfied at the end.

Squeezed states are also minimum uncertainty states, but now the variance in the one quadrature is decreased at the expense of a corresponding increase in the other quadrature, in order to satisfy Eq. (3.27). In the case of coherent states we saw that we have the same noise in both quadratures, thus they can be depicted in a phase diagram as a circle Fig. [3.6], in contrast to squeezed states, which take the form of an ellipse, Fig. [3.7]. We can create squeezed states, by generating correlations amongst the quadrature fluctuations of the light. In that way, while for Glauber coherent states all quadrature pairs are equal,

the correlations will distinguish a specific set of quadratures, where the fluctuations in one of them would be below the corresponding noise of Glauber coherent states. This type of correlations can be produced only with non-linear processes.

A common method to create squeezed light is by using an optical parametric oscillator (OPO). Here, we briefly present the non-linear process that concludes to the so-called squeezing operator Eq. (3.42), but for a more detailed analysis the reader is referred to [67, 68]. A parametric oscillator consists of two modes, the signal and the idler with frequencies ω_s and ω_i respectively. These two modes are coupled together via a non-linear medium, which is pumped by a bright laser with frequency $\omega_p = \omega_s + \omega_i$ [68, 85]. The Hamiltonian describing the dynamics of this system, in the interaction picture, after the rotating wave approximation is [68]

$$\hat{H}_{\text{sq}}^{\text{I}} = \hbar k \left(\hat{a}_s^\dagger \hat{a}_i^\dagger \hat{b}_p + \hat{a}_s \hat{a}_i \hat{b}_p^\dagger \right), \tag{3.40}$$

where k is the coupling constant, depending on the second order susceptibility of the medium $\chi^{(2)}$. If we consider a degenerate parametric amplifier, meaning same frequencies for the signal and the idler, i.e. $\omega_s = \omega_i = \omega$ and consequently $\omega_p = 2\omega$, we obtain

$$\hat{H}_{\text{sq}}^{I} = \hbar k \left(\beta \hat{a}^2 + \beta^* \hat{a}^{\dagger 2} \right), \tag{3.41}$$

where we have also treated classically the pump laser. The purpose of this short analysis was to shed some light on how we can realise the non-linear dynamics that create squeezed light states through the unitary squeezing operator

$$\hat{S}(\epsilon) = e^{-i\hat{H}_{\text{sq}}^I t/\hbar} = e^{\left(\epsilon^* \hat{a}^2 - \epsilon \hat{a}^{\dagger 2} \right)/2}, \tag{3.42}$$

where $\epsilon = 2ik\beta^* t = re^{2i\phi_{\text{sq}}}$ is an arbitrary complex number and $r = |\epsilon|$ is the so-called squeeze factor, while ϕ_{sq} is the angle over which we have to rotate the initial reference frame of quadratures, in order to obtain squeezing over the new $\hat{X}_{\phi_{\text{sq}}}$ quadrature Fig. [3.7]. Namely the new set of quadratures is defined as

$$\hat{X}_{\phi_{\text{sq}}} = \hat{a}e^{-i\phi_{\text{sq}}} + \hat{a}^\dagger e^{i\phi_{\text{sq}}}, \qquad \hat{Y}_{\phi_{\text{sq}}} = i \left(\hat{a}e^{-i\phi_{\text{sq}}} - \hat{a}^\dagger e^{i\phi_{\text{sq}}} \right). \tag{3.43}$$

A squeezed state $|\alpha, \epsilon\rangle$ can be created by firstly squeezing the vacuum and then displacing it

$$|\alpha, \epsilon\rangle = \hat{D}(\alpha)\hat{S}(\epsilon)|0\rangle. \tag{3.44}$$

Here, we also present some useful properties of the squeezing operator [69]

$$\hat{S}^\dagger(\epsilon)\hat{a}\hat{S}(\epsilon) = \hat{a}\cosh r - \hat{a}^\dagger e^{-2i\phi_{\text{sq}}}\sinh r \tag{3.45}$$

$$\hat{S}^\dagger(\epsilon)\hat{a}^\dagger\hat{S}(\epsilon) = \hat{a}^\dagger\cosh r - \hat{a}e^{-2i\phi_{\text{sq}}}\sinh r \tag{3.46}$$

$$\hat{S}^\dagger(\epsilon)\left(\hat{X}_{\phi_{\text{sq}}} + i\hat{Y}_{\phi_{\text{sq}}}\right)\hat{S}(\epsilon) = \hat{X}_{\phi_{\text{sq}}}e^{-r} + i\hat{Y}_{\phi_{\text{sq}}}e^r, \tag{3.47}$$

Now we can calculate the following expectation values [69]

$$\langle\hat{N}(\alpha,\epsilon)\rangle = |\alpha|^2 + \sinh^2 r \tag{3.48}$$

$$\Delta\hat{X}_{\phi_{\text{sq}}} = e^{-r}, \qquad \Delta\hat{Y}_{\phi_{\text{sq}}} = e^r. \tag{3.49}$$

It is clear that the noise of a squeezed state in the one quadrature (in the rotated plane) has been decreased by a factor of e^{-r}, while the other is increased by a factor of e^r, but they still satisfy the condition of minimum uncertainty states:

$$\Delta\hat{X}_{\phi_{\text{sq}}}\Delta\hat{Y}_{\phi_{\text{sq}}} = 1. \tag{3.50}$$

Let's examine here the very simple cases of $\phi_{\text{sq}} = 0$ and $\phi_{\text{sq}} = \pi/2$. In the first case we have $\hat{X}_{\phi_{\text{sq}}=0} = \hat{X}$ and consequently we squeeze the amplitude quadrature $\Delta\hat{X}_{\phi_{\text{sq}}=0} = \Delta\hat{X} = e^{-r}$. For the second case we obtain $\hat{X}_{\phi_{\text{sq}}=\pi/2} = \hat{Y}$, hence $\Delta\hat{X}_{\phi_{\text{sq}}=\pi/2} = \Delta\hat{Y} = e^{-r}$, namely we squeeze the phase quadrature. That means that we need to make the appropriate rotation, with respect to the initial quadrature reference frame, in order to squeeze the preferred quadrature. We are going to apply those methods in Chapter 6, where we will need to squeeze different quadratures depending on the entanglement scheme under consideration, in order the use of squeezed light to provide us with further improvements.

3.2.3 Optical Interferometry

Up to this point we have highlighted many times the similarities between optical and atom interferometers. We can describe an optical MZ interferometer by using the collective angular momentum operators of the photons in direct analogy with the atomic case. Namely the z-component of the photon angular momentum operator at the output of the optical MZ interferometer would be given by

$$\hat{J}_z(\phi) = e^{-i\hat{J}_y\phi}\hat{J}_z(0)e^{i\hat{J}_y\phi} = \hat{J}_z(0)\cos\phi - \hat{J}_x(0)\sin\phi, \tag{3.51}$$

which is exactly the same with the atomic case Eq. (3.17). We can calculate the phase difference between the two arms of the interferometer, by measuring a signal $\hat{S}$, with precision given by Eq. (3.18). In the optical, as in the atomic case, the common measurement
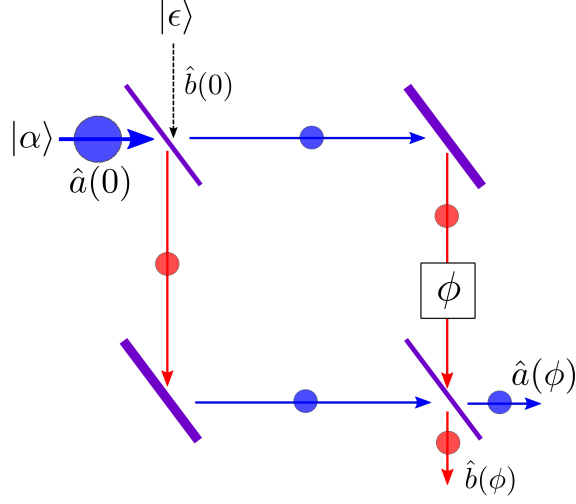
Figure 3.8: Optical MZ interferometer. The use of squeezed vacuum light in the second port provides us with sub-shot-noise sensitivities, Eq. (3.55).

at the end is the population difference between the two arms, i.e. $\hat{S} = \hat{J}_z$, namely the precision of the phase difference would be given by

$$\Delta\phi(\phi) = \frac{\sqrt{\mathrm{Var}(\hat{J}_z(\phi))}}{|\partial_\phi \langle \hat{J}_z(\phi)\rangle|}. \tag{3.52}$$

We consider an input state of the form $|\psi\rangle_{\mathrm{in}} = |\alpha\rangle|0\rangle$, which represents a Glauber coherent state at the one port and no light at all at the other port. After calculating all relevant quantities we obtain the photon-shot noise limit [86]

$$\Delta\phi^{|\alpha\rangle|0\rangle} = \frac{1}{\sqrt{\langle \hat{N}\rangle}}, \tag{3.53}$$

where we have assumed that we operate at the optimal point $\phi = \pi/2$.

In 1981 Carlton Caves suggested that sub-shot-noise sensitivities can be achieved in optical interferometers, by considering instead of no light at all, squeezed vacuum light entering at the second port of the interferometer [87]. Namely, they considered the state $|\psi\rangle_{\mathrm{in}} = |\alpha\rangle|\epsilon\rangle$, i.e. a Glauber coherent state and a squeezed vacuum state entering the first and the second ports respectively. They also assumed squeezing over the amplitude quadrature, i.e. $\phi_{\mathrm{sq}} = 0$. Calculating again the relevant quantities we find [86]

$$\Delta\phi^{|\alpha\rangle|\epsilon\rangle} = \frac{\sqrt{|\alpha|^2 e^{-2r} + \sinh^2 r}}{||\alpha|^2 - \sinh^2 r|}, \tag{3.54}$$

operating at the optimal point, which is again $\phi = \pi/2$. In the regime of many photons, $\langle \hat{N}\rangle >> 1$, the mean population of the squeezed vacuum state will be $\sqrt{\langle \hat{N}\rangle}/2$ and this

would be equal to $\sinh^2 r$ due to Eq. (3.48). So, for a sufficiently large value of r we can make the approximation $\sinh^2 r \approx e^{2r} \approx \sqrt{\langle \hat{N} \rangle}/2$. Thus, from Eq. (3.54) we finally obtain

$$\Delta \phi^{|\alpha\rangle|\epsilon\rangle} \approx \frac{1}{\langle \hat{N} \rangle^{3/4}}, \tag{3.55}$$

indicating that the use of squeezed vacuum states can provide us with better sensitivities than the photon shot-noise limit $\Delta \phi^{|\alpha\rangle|0\rangle}$.

The initial motivation of Caves' work was to enhance the sensitivity of measurements in optical interferometers, in order to be able to measure extremely small length differences between the two arms, which could enable the detection of gravitational waves. In 2016 gravitational waves generated by a pair of black holes were detected for the first time, by the Laser Interferometer Gravitational-Wave Observatory (LIGO) [88]. However, this observation was not achieved by using squeezed light. The first use of squeezed vacuum states in the measurement of gravitational waves was achieved with LIGO detectors in 2019 [89]. This setup consists of two main parts, the squeezed vacuum source and LIGO's Michelson interferometer. The former is equipped with a special geometry for the OPO that creates the squeezing, as described in the beginning of Sec. [3.2.2]. More particularly, two light fields are delivered via optical fibres to the OPO, which consists of a non-linear medium. A second order non-linear interaction between the 532nm pump field and the vacuum fluctuations of the 1064nm field creates a squeezed vacuum state. This state is then circulated back to the interferometric setup. The use of a squeezed state instead of a coherent state light field in LIGO's Michelson interferometer, showed improvement in the sensitivity of the device up to 3dB [89].

3.3   Parameter Estimation Theory

In this section we introduce some basic concepts of parameter estimation theory, which we are going to use in Chapter 4. More particularly, we firstly define the classical Fisher information (CFI) and the Cramer-Rao bound (CRB). Then we move to the quantum case and introduce the quantum Fisher information (QFI) and the quantum Cramer-Rao bound (QCRB), which as we have already seen provide us with a condition about entanglement and sub-shot-noise measurements. Also, we are going to derive some very useful relations for the QFI, some of which we use in Chapter 4. This analysis is based on an excellent review in parameter estimation theory [90].

3.3.1 Basic Concepts

An interferometer could essentially be described as any transformation of the input (probe) state $\hat{\rho}$, which can be parametrized by a real unknown number θ. For example, as we have seen earlier, the MZ interferometer can be realised as a rotation of angle θ around the y-axis. The main aim of parameter estimation theory is to measure some quantity of the output state of the interferometer, $\hat{\rho}(\theta)$, and from the outcome measurements to estimate the value of the parameter θ. The outcomes of our measurement could be discrete or continuous, depending on what kind of measurement we make. For example, the outcomes would be discrete numbers, if we measure the number of particles at the output modes of a MZ interferometer. Here, we are going to consider measurements with discrete outcomes. The most general measurement in quantum theory is described by a positive-operator valued measurement (POVM). A POVM is described by a set of operators $\{\hat{E}_m\}$, which satisfy the following general conditions:

- $\hat{E}_m \geq 0$: all the operators, $\hat{E}_m$, of the set are non-negative (that guarantees non-negative probabilities).

- $\sum_\epsilon \hat{E}_m = \hat{1}$, that guarantees normalization.

For example, the standard projective (von-Neumann) measurement is a particular POVM, where the operators $\hat{E}_m$ are orthogonal projectors, satisfying $\hat{E}_m \hat{E}_{m'} = \hat{E}_m \delta_{m,m'}$. We define the *Likelihood* as the conditional probability to observe the result m for a given value of θ

$$P_m(\theta) = Tr[\hat{E}_m \hat{\rho}(\theta)], \tag{3.56}$$

and the log-likelihood function is defined as

$$L_m(\theta) \equiv \ln[P_m(\theta)]. \tag{3.57}$$

We measure the quantity $\hat{E}_m$, where m is a random variable. So, we get the set of measurement outcomes, $m = \{m_1, m_2, ..., m_n\}$, where m_i are the individual measurement outcomes, for $i = 1, 2.., n$. After that we calculate the estimator Θ_m, which is any mapping from m onto the parameter space. In other words, the estimator is a generic function associating each set of measurement results m, with an estimation Θ of the phase. Hence, the aim of the estimator Θ is to estimate the true value of the unknown parameter θ, as precisely as possible. The estimator Θ_m, depends on m, which is a random variable, and that makes the estimator itself a random variable. We calculate the mean value

(or statistical average) of the estimator using the likelihood, which provides us with the probability to obtain a set of measurement outcomes given a specific value of the unknown parameter θ. Thus, the mean value of the estimator would be θ dependent itself

$$\langle \Theta_m \rangle_\theta = \sum_m P_m(\theta) \Theta_m, \tag{3.58}$$

as is explicitly expressed using the index θ, where the brackets here $\langle ... \rangle$ indicate statistical averaging. Similarly, we calculate the variance of the estimator:

$$(\Delta \Theta_m)_\theta^2 = \sum_m P_m(\theta)(\Theta_m - \langle \Theta_m \rangle_\theta)^2. \tag{3.59}$$

We characterise an estimator as *unbiased*, when its statistical average coincides with the true value of the parameter, i.e

$$\langle \Theta_m \rangle_\theta = \theta, \tag{3.60}$$

or putting it differently, $\frac{\partial \langle \Theta_m \rangle_\theta}{\partial \theta} = 1$, otherwise it is called biased.

Here, we give a brief outline of the main concept of the following subsections. Firstly, we introduce the CRB and we define the CFI. For the interested reader, we also present a detailed proof of the CRB in the subsequent section. Then, we introduce the QFI as the upper limit of the CFI, optimized over all possible measurements, namely we declare a stronger limit to the sensitivity, which essentially is how the QCRB is defined. In the following we derive a relation for the QFI, $F_Q[\hat{\rho}(\theta)] = \text{Tr}\left[\hat{\rho}(\theta)\hat{L}_\theta^2\right]$. This will be very helpful, when we come to calculate the QFI for mixed and pure states, as well as for a specific case of unitary transformations considering both mixed and pure initial states, which is the subject of the remaining subsections. A roadmap of the remainder of this chapter is as follows:

- Introduce the CRB and the definition of the CFI.

- Proof of the CRB.

- Introduce the QCRB and the QFI.

- Derive the relation $F_Q[\hat{\rho}(\theta)] = \text{Tr}\left[\hat{\rho}(\theta)\hat{L}_\theta^2\right]$.

- Calculate the QFI for mixed states.

- Calculate the QFI for pure states.

- Calculate the QFI for unitary transformations of the form $\hat{U} = e^{-i\theta\hat{G}}$ and mixed initial states.

- Calculate the QFI for unitary transformations of the form $\hat{U} = e^{-i\theta\hat{G}}$ and pure initial states.

3.3.2 The Cramer-Rao Bound and the Classical Fisher Information

The Cramer-Rao bound (CRB) sets a lower bound to the variance of any arbitrary estimator

$$(\Delta\Theta)^2_\theta \geq (\Delta\Theta_{CRB})^2_\theta \equiv \frac{\left(\frac{\partial \langle\Theta_m\rangle_\theta}{\partial\theta}\right)^2}{F_C(\theta)} = \frac{1}{F_C(\theta)}, \tag{3.61}$$

where in the last equality we assumed that we have an unbiased estimator. Also, $F_C(\theta)$ is the classical Fisher information (CFI) defined as

$$F_C(\theta) \equiv \left\langle \left(\frac{\partial L_m(\theta)}{\partial\theta}\right)^2 \right\rangle_\theta = \sum_m P_m(\theta) \left(\frac{\partial L_m(\theta)}{\partial\theta}\right)^2. \tag{3.62}$$

Using the definition of the log-likelihood function, Eq. (3.57), we obtain

$$F_C(\theta) = \sum_m \frac{1}{P_m(\theta)} \left(\frac{\partial P_m(\theta)}{\partial\theta}\right), \tag{3.63}$$

where we interchanged the derivation with respect to θ and the summation over m, since we assumed that the range of possible outcomes, values of m, does not depend on θ. An estimator that saturates the CRB, Eq. (3.61), is called *efficient*. The existence of efficient estimators depends on the properties of the probability distribution. In the limit of a large number of measurements, at least one efficient estimator exists, the maximum likelihood estimator. Essentially, the CFI quantifies the change of the probability distribution referring to a particular observable, due to a small change of the parameter of interest. Also, through the CRB it identifies what is the smallest change of the parameter of interest that we can detect, by making that particular measurement.

3.3.3 Proof of the Cramer-Rao Bound

We take the derivative of Eq. (3.57) with respect to θ and rearrange with respect to $\frac{\partial P_m(\theta)}{\partial\theta}$

$$\frac{\partial P_m(\theta)}{\partial\theta} = P_m(\theta)\frac{\partial L_m(\theta)}{\partial\theta}. \tag{3.64}$$

Also, we take the derivative of $\langle\Theta_m\rangle_\theta = \sum_m P_m(\theta)\Theta_m$ with respect θ

$$\frac{\partial \langle\Theta_m\rangle_\theta}{\partial\theta} = \sum_m \Theta_m \left(\frac{\partial P_m(\theta)}{\partial\theta}\right). \tag{3.65}$$

Using equation (3.64) we get

$$\frac{\partial \langle \Theta_m \rangle_\theta}{\partial \theta} = \sum_m \Theta_m P_m(\theta) \frac{\partial L_m(\theta)}{\partial \theta} = \left\langle \Theta_m \frac{\partial L_m(\theta)}{\partial \theta} \right\rangle_\theta. \tag{3.66}$$

Now, by differentiating the normalization condition of the probabilities $\sum_m P_m(\theta) = 1$ we have

$$\sum_m \frac{\partial P_m(\theta)}{\partial \theta} = 0. \tag{3.67}$$

Using equations (3.64) and (3.67) we obtain

$$\sum_m \frac{\partial P_m(\theta)}{\partial \theta} = \sum_m P_m(\theta) \frac{\partial L_m(\theta)}{\partial \theta} = \left\langle \frac{\partial L_m(\theta)}{\partial \theta} \right\rangle_\theta = 0. \tag{3.68}$$

So, now we can write

$$\left\langle \Theta_m \frac{\partial L_m(\theta)}{\partial \theta} \right\rangle_\theta^2 = \left\langle (\Theta_m - \langle \Theta_m \rangle_\theta) \frac{\partial L_m(\theta)}{\partial \theta} \right\rangle_\theta^2, \tag{3.69}$$

since the second term is zero according to Eq. (3.68). Thus, from Eq. (3.66) we have

$$\left(\frac{\partial \langle \Theta_m \rangle_\theta}{\partial \theta} \right)^2 = \left\langle (\Theta_m - \langle \Theta_m \rangle_\theta) \frac{\partial L_m(\theta)}{\partial \theta} \right\rangle_\theta^2. \tag{3.70}$$

We will now make use of the Cauchy-Schwartz inequality

$$\langle A^2 \rangle_\theta \langle B_\theta^2 \rangle \ge \langle AB \rangle_\theta^2, \tag{3.71}$$

where A and B are arbitrary real functions of m and the equality is obtained if $B = \lambda A$, with λ independent of m. We assume that $A = \Theta_m - \langle \Theta_m \rangle_\theta$ and $B = \frac{\partial L_m(\theta)}{\partial \theta}$, thus

$$\left\langle (\Theta_m - \langle \Theta_m \rangle_\theta)^2 \right\rangle \left\langle \left(\frac{\partial L_m(\theta)}{\partial \theta} \right)^2 \right\rangle \ge \left\langle (\Theta_m - \langle \Theta_m \rangle_\theta) \frac{\partial L_m(\theta)}{\partial \theta} \right\rangle_\theta^2. \tag{3.72}$$

Using equation (3.70) we have

$$\left\langle (\Theta_m - \langle \Theta_m \rangle_\theta)^2 \right\rangle \left\langle \left(\frac{\partial L_m(\theta)}{\partial \theta} \right)^2 \right\rangle \ge \left(\frac{\partial \langle \Theta_m \rangle_\theta}{\partial \theta} \right)^2. \tag{3.73}$$

Also, $\left\langle (\Theta_m - \langle \Theta_m \rangle_\theta)^2 \right\rangle$ is the variance of Θ_m, i.e $(\Delta\Theta)_\theta^2 = \left\langle (\Theta_m - \langle \Theta_m \rangle_\theta)^2 \right\rangle$. Hence, we obtain the CRB

$$(\Delta\Theta)_\theta^2 \left\langle \left(\frac{\partial L_m(\theta)}{\partial \theta} \right)^2 \right\rangle \ge \left(\frac{\partial \langle \Theta_m \rangle_\theta}{\partial \theta} \right)^2 \Rightarrow \tag{3.74}$$

$$(\Delta\Theta)_\theta^2 \ge \frac{\left(\frac{\partial \langle \Theta_m \rangle_\theta}{\partial \theta} \right)^2}{F_C(\theta)}, \tag{3.75}$$

where we have used the definition of the CFI, Eq. (3.62). The Cauchy-Schwartz inequality is saturated when: $B = \lambda A$. Hence, the CRB is saturated when

$$\left\langle \frac{\partial L_m(\theta)}{\partial \theta} \right\rangle = \lambda_\theta (\Theta_m - \langle \Theta_m \rangle_\theta). \tag{3.76}$$

3.3.4 The Quantum Cramer-Rao Bound and the QFI

Up to this point we have been expressing F_C as a function of the parameter θ, but it really depends on the probability distribution $P_m(\theta)$, as can be seen from Eq. (3.63). We know that $P_m(\theta) = \text{Tr}\left[\hat{E}_m\hat{\rho}(\theta)\right]$, indicating the the CFI depends on the output state of the interferometer $\hat{\rho}(\theta)$ and the POVM $\{\hat{E}_m\}$. We define the QFI, F_Q, as an upper bound to the CFI, maximizing it over all possible POVMs

$$F_Q[\hat{\rho}(\theta)] \equiv \max_{\{\hat{E}_m\}} F_C\left[\hat{\rho}(\theta), \{\hat{E}_m\}\right]. \tag{3.77}$$

That means that $F_Q \geq F_C$ for all POVMs, where the equality holds for the one particular measurement (POVM) that maximizes F_C. We define

$$(\Delta\Theta_{QCRB})^2_\theta \equiv \frac{\left(\frac{\partial\langle\Theta_m\rangle_\theta}{\partial\theta}\right)^2}{F_Q[\hat{\rho}(\theta)]} = \frac{1}{F_Q[\hat{\rho}(\theta)]}, \tag{3.78}$$

where in the last step we considered again an unbiased estimator. From Eq. (3.61) and the fact that $F_Q \geq F_C$ we obtain the quantum Cramer-Rao bound (QCRB)

$$(\Delta\Theta)^2_\theta \geq (\Delta\Theta_{CRB})^2_\theta \geq (\Delta\Theta_{QCRB})^2_\theta. \tag{3.79}$$

The QFI essentially quantifies the change of the system's quantum state, due to a change of the parameter of interest. Through the QCRB, it identifies what is the smallest change of the parameter of interest that we could detect by using that particular quantum state. Unlike the CFI, it does not refer to a particular measurement, but optimises over all possible measurements. The QCRB is the ultimate bound that gives the best sensitivity with which we can theoretically calculate the precision of a phase at the output of an interferometer.

3.3.5 Proof of: $F_Q[\hat{\rho}(\theta)] = \text{Tr}\left[\hat{\rho}(\theta)\hat{L}^2_\theta\right]$

Now, we are going to prove the very useful relation $F_Q[\hat{\rho}(\theta)] = \text{Tr}\left[\hat{\rho}(\theta)\hat{L}^2_\theta\right]$, where $\hat{L}_\theta$ is a Hermitian operator called symmetric logarithmic derivative (SLD), which is defined as the solution of the equation

$$\frac{\partial\hat{\rho}(\theta)}{\partial\theta} = \frac{\hat{\rho}\hat{L}_\theta + \hat{L}_\theta\hat{\rho}(\theta)}{2}. \tag{3.80}$$

We start from differentiating Eq. (3.56) with respect to θ, $\partial_\theta P_m(\theta) = \text{Tr}\left[\hat{E}_m\partial_\theta\hat{\rho}(\theta)\right]$. Then we substitute Eq.(3.56) and the above result in Eq.(3.63)

$$F_Q[\hat{\rho}(\theta), \hat{E}_m] = \sum_m \frac{\text{Tr}\left[\hat{E}_m\partial_\theta\rho(\hat{\theta})\right]^2}{\text{Tr}\left[\hat{E}_m\hat{\rho}(\theta)\right]}. \tag{3.81}$$

Now, by using Eq. (3.80) we can write $\mathrm{Tr}\left[\hat{E}_m\partial_\theta\hat{\rho}(\theta)\right]$ as

$$\mathrm{Tr}\left[\hat{E}_m\partial_\theta\hat{\rho}(\theta)\right] = \frac{1}{2}\left\{\mathrm{Tr}\left[\hat{E}_m\hat{\rho}(\theta)\hat{L}_\theta\right] + \mathrm{Tr}\left[\hat{E}_m\hat{L}_\theta\hat{\rho}(\theta)\right]\right\} = \frac{1}{2}\left\{\mathrm{Tr}\left[\hat{\rho}(\theta)\hat{L}_\theta\hat{E}_m\right] + \mathrm{Tr}\left[\hat{L}_\theta\hat{\rho}(\theta)\hat{E}_m\right]\right\},$$
(3.82)

where in the second equality we used the circular property of the *trace*. Using a complete basis $\{|n\rangle\}$ we can write the *trace* as

$$\mathrm{Tr}\left[\hat{L}_\theta\hat{\rho}(\theta)\hat{E}_m\right] = \sum_n \langle n|\hat{L}_\theta\hat{\rho}(\theta)\hat{E}_m|n\rangle = \sum_n \left[\langle n|\left(\hat{L}_\theta\hat{\rho}(\theta)\hat{E}_m\right)^\dagger|n\rangle\right]^* = \mathrm{Tr}\left[\hat{E}_m\hat{\rho}(\theta)\hat{L}_\theta\right]^*.$$
(3.83)

Combining the above two results we obtain

$$\mathrm{Tr}\left[\hat{E}_m\partial_\theta\hat{\rho}(\theta)\right] = \mathrm{Re}\left\{\mathrm{Tr}\left[\hat{\rho}(\theta)\hat{L}_\theta\hat{E}_m\right]\right\}.$$
(3.84)

From $|z|^2 = \mathrm{Re}\{z\}^2 + \mathrm{Im}\{z\}^2$, we can write the following inequality for complex numbers

$$\mathrm{Re}\{z\}^2 \leq |z|^2,$$
(3.85)

where the equality holds, if and only if $\mathrm{Im}\{z\} = 0$. So, in our case we obtain

$$\mathrm{Re}\left\{\mathrm{Tr}\left[\hat{\rho}(\theta)\hat{L}_\theta\hat{E}_m\right]\right\}^2 \leq \left|\mathrm{Tr}\left[\hat{\rho}(\theta)\hat{L}_\theta\hat{E}_m\right]\right|^2,$$
(3.86)

and the equality holds when $\mathrm{Im}\left\{\mathrm{Tr}\left[\hat{\rho}(\theta)\hat{L}_\theta\hat{E}_m\right]\right\} = 0$. Now, we use again the Cauchy-Schwarz inequality

$$\left|\mathrm{Tr}\left[\hat{A}^\dagger\hat{B}\right]\right|^2 \leq \mathrm{Tr}\left[\hat{A}^\dagger\hat{A}\right]\mathrm{Tr}\left[\hat{B}^\dagger\hat{B}\right],$$
(3.87)

with $\hat{A} = \sqrt{\hat{\rho}(\theta)}\sqrt{\hat{E}_m}$ and $\hat{B} = \sqrt{\hat{\rho}(\theta)}\hat{L}_\theta\sqrt{\hat{E}_m}$, thus we get

$$\left|\mathrm{Tr}\left[\hat{E}_m\hat{\rho}(\theta)\hat{L}_\theta\right]\right|^2 \leq \mathrm{Tr}\left[\hat{E}_m\hat{\rho}(\theta)\right]\mathrm{Tr}\left[\hat{E}_m\hat{L}_\theta\hat{\rho}(\theta)\hat{L}_\theta\right].$$
(3.88)

From Eq.(3.88) and (3.86) we obtain

$$\mathrm{Re}\left\{\mathrm{Tr}\left[\hat{\rho}(\theta)\hat{L}_\theta\hat{E}_m\right]\right\}^2 \leq \mathrm{Tr}\left[\hat{E}_m\hat{\rho}(\theta)\right]\mathrm{Tr}\left[\hat{E}_m\hat{L}_\theta\hat{\rho}(\theta)\hat{L}_\theta\right].$$
(3.89)

Using Eq.(3.84) and taking the sum with respect to all measurement outcomes we obtain

$$\sum_m \frac{\mathrm{Tr}\left[\hat{E}_m\partial_\theta\hat{\rho}(\theta)\right]^2}{\mathrm{Tr}\left[\hat{E}_m\hat{\rho}(\theta)\right]} \leq \sum_m \mathrm{Tr}\left[\hat{E}_m\hat{L}_\theta\hat{\rho}(\theta)\hat{L}_\theta\right].$$
(3.90)

We can express the classical Fisher information as

$$F_C\left[\hat{\rho}(\theta),\{\hat{E}_m\}\right] = \sum_m \frac{\mathrm{Tr}\left[\hat{E}_m\partial_\theta\hat{\rho}(\theta)\right]^2}{\mathrm{Tr}\left[\hat{E}_m\hat{\rho}(\theta)\right]},$$
(3.91)

where this can be derived by substituting $P_m(\theta) = \mathrm{Tr}\left[\hat{E}_m\hat{\rho}(\theta)\right]$ and $\partial_\theta P_m(\theta) = \mathrm{Tr}\left[\hat{E}_m\partial_\theta\hat{\rho}(\theta)\right]$ in Eq.(3.63). Using Eq.(3.91) and the fact that $\sum_m \hat{E}_m = \hat{1}$ we obtain

$$F_C\left[\hat{\rho}(\theta), \{\hat{E}_m\}\right] \leq \mathrm{Tr}\left[\hat{\rho}(\theta)\hat{L}_\theta^2\right]. \tag{3.92}$$

The left hand side of the above inequality depends on the POVMs $\left\{\hat{E}_m\right\}$, while the right hand side does not, which indicates that this is a maximization of the CFI over all measurements. There is only one measurement (POVM) where the equality holds and the CFI reaches its maximum, which is the QFI as we saw earlier. Thus,

$$F_Q\left[\hat{\rho}(\theta)\right] = \mathrm{Tr}\left[\hat{\rho}(\theta)\hat{L}_\theta^2\right] = \max_{\{\hat{E}_m\}} F_C\left[\hat{\rho}(\theta), \hat{E}_m\right]. \tag{3.93}$$

3.3.6 Quantum Fisher Information for Mixed States

Let us consider a complete basis, $\{|k\rangle\}$, such that

$$\hat{\rho}(\theta) = \sum_k p_k|k\rangle\langle k|, \tag{3.94}$$

where $p_k \geq 0$ and $\sum_k p_k = 1$. Now, we can write the QFI as

$$F_Q\left[\hat{\rho}(\theta)\right] = \mathrm{Tr}\left[\hat{\rho}(\theta)\hat{L}_\theta^2\right] = \mathrm{Tr}\left[\hat{L}_\theta\hat{\rho}(\theta)\hat{L}_\theta\right] = \sum_{k'}\langle k'|\hat{L}_\theta\hat{\rho}(\theta)\hat{L}_\theta|k'\rangle = \sum_{k,k'} p_k\langle k'|\hat{L}_\theta|k\rangle\langle k|\hat{L}_\theta|k'\rangle$$

$$= \sum_{k,k'} p_k\left(\langle k|\hat{L}_\theta|k'\rangle\right)^*\langle k|\hat{L}_\theta|k'\rangle = \sum_{k,k'} p_k\left|\langle k|\hat{L}_\theta|k'\rangle\right|^2 = \sum_{k,k'} \frac{p_k + p_{k'}}{2}\left|\langle k|\hat{L}_\theta|k'\rangle\right|^2, \tag{3.95}$$

where in the intermediate steps we used $\sum_k |k\rangle\langle k| = 1$, while in the last step we made use of the simple relation $\frac{1}{2}\sum_{k,k'} p_k\left|\langle k|\hat{L}_\theta|k'\rangle\right|^2 = \frac{1}{2}\sum_{k,k'} p_{k'}\left|\langle k|\hat{L}_\theta|k'\rangle\right|^2$. From the SLD, Eq. (3.80), and the expansion of the density matrix, Eq. (3.94), we find

$$\frac{\partial\hat{\rho}(\theta)}{\partial\theta} = \frac{\hat{\rho}\hat{L}_\theta + \hat{L}_\theta\hat{\rho}(\theta)}{2} = \frac{1}{2}\left(\sum_m p_m|m\rangle\langle m|\hat{L}_\theta + \hat{L}_\theta\sum_l p_l|l\rangle\langle l|\right). \tag{3.96}$$

Now we want to calculate the elements $\langle k|\hat{L}_\theta|k'\rangle$

$$\langle k|\frac{\partial\hat{\rho}(\theta)}{\partial\theta}|k'\rangle = \frac{1}{2}\left[p_k\langle k|\hat{L}_\theta|k'\rangle + p_{k'}\langle k|\hat{L}_\theta|k\rangle\right]. \tag{3.97}$$

Thus,

$$\langle k|\hat{L}_\theta|k'\rangle = \frac{2}{p_k + p_{k'}}\langle k|\frac{\partial\hat{\rho}(\theta)}{\partial\theta}|k'\rangle. \tag{3.98}$$

Substituting that result in Eq. (3.95), we obtain for the QFI

$$F_Q\left[\hat{\rho}(\theta)\right] = \sum_{k,k'} \frac{2}{p_k + p_{k'}}\left|\langle k|\frac{\partial\hat{\rho}(\theta)}{\partial\theta}|k'\rangle\right|^2. \tag{3.99}$$

By inspecting Eq. (3.94) and due to the fact that the output state depends on θ, we realise that the probabilities $p_k = p_k(\theta)$ and the state vectors $|k\rangle = |k(\theta)\rangle$ also depend on θ themselves. After clarifying that, we take the derivative of Eq. (3.94) with respect to θ

$$\partial_\theta \hat{\rho}(\theta) = \sum_k (\partial_\theta p_k) |k\rangle\langle k| + \sum_k p_k |\partial_\theta k\rangle\langle k| + \sum_k p_k |k\rangle\langle \partial_\theta k|, \tag{3.100}$$

where $|\partial_\theta k\rangle \equiv \partial_\theta |k\rangle$. Now we calculate the matrix elements

$$\langle k|\partial_\theta \hat{\rho}(\theta)|k'\rangle = \langle k|(\partial_\theta p_{k'})|k'\rangle + p_{k'}\langle k|\partial_\theta k'\rangle + p_k\langle \partial_\theta k|k'\rangle. \tag{3.101}$$

Taking the derivative with respect to θ, of the ortho-normality condition $\langle k|k'\rangle = \delta_{k,k'}$ we find

$$\langle \partial_\theta k|k'\rangle = -\langle k|\partial_\theta k'\rangle. \tag{3.102}$$

Hence, for Eq. (3.101) we obtain

$$\langle k|\partial_\theta \hat{\rho}(\theta)|k'\rangle = \partial_\theta p_{k'}\delta_{kk'} + (p_k - p_{k'})\langle \partial_\theta k|k'\rangle. \tag{3.103}$$

So, now we find

$$\left|\langle k|\partial_\theta \hat{\rho}(\theta)|k'\rangle\right|^2 = (\partial_\theta p_{k'})^2 \delta_{kk'}^2 + (\partial_\theta p_{k'})(p_k - p_{k'})\langle k'|\partial_\theta k\rangle\delta_{kk'} +$$
$$+ (\partial_\theta p_{k'})(p_k - p_{k'})\langle \partial_\theta k|k'\rangle\delta_{kk'} + (p_k - p_{k'})^2 \left|\langle \partial_\theta k|k'\rangle\right|^2. \tag{3.104}$$

If we substitute the above result in Eq. (3.99) the second and the third terms would be zero, since only the $k = k'$ term would survive in the sum, and then simply we get $p_k - p_{k'} = 0$. So, we finally obtain

$$F_Q[\hat{\rho}(\theta)] = \sum_k \frac{(\partial_\theta p_{k'})^2}{p_k} + 2\sum_{k,k'} \frac{(p_k - p_{k'})^2}{p_k + p_{k'}}|\langle \partial_\theta k|k'\rangle|^2. \tag{3.105}$$

We expand the SLD operator using the complete basis $\{|k\rangle\}$

$$\hat{L}_\theta = \sum_{k,k'=0}^{\infty} \langle k|\hat{L}_\theta|k'\rangle |k\rangle\langle k'|. \tag{3.106}$$

Using Eq. (3.98) and (3.103) we find

$$\langle k|\hat{L}_\theta|k'\rangle = \frac{2}{p_k + p_{k'}}(\partial_\theta p_{k'})\delta_{kk'} + 2\frac{p_k - p_{k'}}{p_k + p_{k'}}\langle \partial_\theta k|k'\rangle. \tag{3.107}$$

We substitute this into Eq. (3.106)

$$\hat{L}_\theta = \sum_{k=0}^{\infty} \frac{(\partial_\theta p_k)}{p_k}|k\rangle\langle k| + 2\sum_{k,k'=0}^{\infty} \frac{p_k - p_{k'}}{p_k + p_{k'}}\langle \partial_\theta k|k'\rangle |k\rangle\langle k'|. \tag{3.108}$$

Eq. (3.105) and (3.108) are general results that we can use, in order to calculate the QFI and the SLD respectively.

3.3.7 Quantum Fisher Information for Pure States

Now we consider the special case of having a pure state, namely the density matrix is written as

$$\hat{\rho}(\theta) = \sum_{k=0}^{\infty} p_k |k\rangle\langle k| = |\psi(\theta)\rangle\langle\psi(\theta)|. \tag{3.109}$$

Putting it differently that means that $p_k = 1$ only for $k = \psi$ and $p_k = 0$ for all the other values of k ($k \neq \psi$). Splitting the sum in that way in Eq. (3.108) would be really useful, in order to proceed with our calculations. The first term in Eq. (3.108) is zero, since we take the derivative of a constant number and the second term can be written as

$$\hat{L}_\theta = 2\sum_{k=0}^{\infty}\sum_{k'=0}^{\infty} \frac{p_k - p_{k'}}{p_k + p_{k'}} \langle\partial_\theta k|k'\rangle |k\rangle\langle k'| = 2\left[|\psi\rangle\langle\partial_\theta\psi| \left(\sum_{\substack{k=0 \\ k\neq\psi}}^{\infty} |k\rangle\langle k| \right) + \left(\sum_{\substack{k=0 \\ k\neq\psi}}^{\infty} |k\rangle\langle k| \right) |\partial_\theta\psi\rangle\langle\psi| \right]. \tag{3.110}$$

Also, our basis is complete $\sum_{k=0}^{\infty} |k\rangle\langle k| = \hat{1}$, hence

$$\sum_{\substack{k=0 \\ k\neq\psi}}^{\infty} |k\rangle\langle k| = \hat{1} - |\psi\rangle\langle\psi|. \tag{3.111}$$

From the normalization condition $\langle\psi(\theta)|\psi(\theta)\rangle = 1$ we take the derivative with respect to θ and we find

$$\langle\partial_\theta\psi(\theta)|\psi(\theta)\rangle = -\langle\psi(\theta)|\partial_\theta\psi(\theta)\rangle. \tag{3.112}$$

We substitute those two results in Eq. (3.110) and we obtain

$$\hat{L}_\theta = 2\left[|\psi(\theta)\rangle\langle\partial_\theta\psi(\theta)| + |\partial_\theta\psi(\theta)\rangle\langle\psi(\theta)| \right]. \tag{3.113}$$

We can find a more elegant way to express $\hat{L}_\theta$, if we take the derivative of $\hat{\rho}(\theta) = |\psi(\theta)\rangle\langle\psi(\theta)|$ with respect to θ

$$\partial_\theta\hat{\rho}(\theta) = |\partial_\theta\psi(\theta)\rangle\langle\psi(\theta)| + |\psi(\theta)\rangle\langle\partial_\theta\psi(\theta)|. \tag{3.114}$$

Hence,

$$\hat{L}_\theta = 2\partial_\theta\hat{\rho}(\theta). \tag{3.115}$$

If we substitute $\hat{\rho} = |\psi\rangle\langle\psi|$ and Eq. (3.113) into Eq. (3.93) we conclude to an extremely powerful and simple expression for calculating the QFI for pure states

$$F_Q\left[|\psi(\theta)\rangle\right] = 4\left[\langle\partial_\theta\psi(\theta)|\partial_\theta\psi(\theta)\rangle - |\langle\partial_\theta\psi(\theta)|\psi(\theta)\rangle|^2 \right], \tag{3.116}$$

where we have also made use of Eq. (3.112) and the property of the trace that is invariant under cyclic permutations, during the intermediate steps of the calculation. We are going to use that result in Chapter 4, in order to calculate the QFI of a single particle travelling in a gravitational field.

3.3.8 QFI for Unitary Transformations and Mixed Initial States

Here, we consider the special case of unitary transformations, where the parameter of interest is already factorized and appears in the explicit form $\hat{U} = e^{-i\theta\hat{G}}$. Hence, the density matrix $\hat{\rho}(\theta)$ will be given by

$$\hat{\rho}(\theta) = e^{-i\theta\hat{G}}\hat{\rho}_0 e^{i\theta\hat{G}}, \tag{3.117}$$

where $\hat{\rho}_0$ is the initial (probe) state, which for now we keep in the general form $\hat{\rho}_0 = \sum_k p_k|k\rangle\langle k|$, and $\hat{G}$ is a hermitian operator, which is the generator of the unitary transformation. The unitary transformation is described by the evolution operator $\hat{U}_\theta = e^{-i\theta\hat{G}}$ and the following relations hold

$$\hat{U}_\theta^\dagger = e^{i\theta\hat{G}}, \qquad \hat{U}_\theta\hat{U}_\theta^\dagger = \hat{1} \tag{3.118}$$

$$\partial_\theta\hat{U}_\theta = -i\hat{G}\hat{U}_\theta, \qquad \partial_\theta\hat{U}_\theta^\dagger = i\hat{G}\hat{U}_\theta^\dagger. \tag{3.119}$$

The transformed SLD operator will also be given by

$$\hat{L}_\theta = e^{-i\theta\hat{G}}\hat{L}_0 e^{i\theta\hat{G}}, \tag{3.120}$$

where $\hat{L}_0$ is again the initial SLD operator. Taking the derivative of Eq. (3.117) and using Eq. (3.119) as well, we obtain

$$\partial_\theta\hat{\rho}(\theta) = i\left[\hat{\rho}(\theta), \hat{G}\right]. \tag{3.121}$$

Now we can write the equation of SLD, Eq.(3.80), in a more elegant way using the anti-commutator notation

$$\partial_\theta\hat{\rho}(\theta) = \frac{\hat{\rho}(\theta)\hat{L}_\theta + \hat{L}_\theta\hat{\rho}(\theta)}{2} = \frac{1}{2}\left\{\hat{\rho}(\theta), \hat{L}_(\theta)\right\}. \tag{3.122}$$

Thus, from the above two equations we can write

$$\left\{\hat{\rho}(\theta), \hat{L}_\theta\right\} = 2i\left[\hat{\rho}(\theta), \hat{G}\right]. \tag{3.123}$$

This result combined with Eq. (3.117) and (3.120) provides us with the corresponding relation for the initial density matrix and SLD operators

$$\left\{\hat{\rho}_0, \hat{L}_0\right\} = 2i\left[\hat{\rho}_0, \hat{G}\right]. \tag{3.124}$$

We substitute Eq. (3.117) and (3.120) into Eq. (3.93), in order to find

$$F_Q\left[\hat{\rho}(\theta)\right] = \text{Tr}\left[\hat{L}_0 \hat{\rho}_0 \hat{L}_0\right]. \tag{3.125}$$

We use again the complete basis $\{|k\rangle\}$, in order to express the *trace* as well as to expand the density matrix

$$F_Q[\hat{\rho}_0, \hat{G}] = \sum_{k,m=0}^{\infty} \frac{p_m + p_k}{2} \left|\langle m|\hat{L}_0|k\rangle\right|^2, \tag{3.126}$$

where we used again the same relation we had used in the final step of Eq. (3.95). We should point out here that we changed our notation from $F_Q\left[\hat{\rho}(\theta)\right]$ to $F_Q[\hat{\rho}_0, \hat{G}]$ just to clearly present that the QFI would depend on the initial state $\hat{\rho}_0$ and the generator $\hat{G}$ of the unitary transformation. We can find the matrix elements of $\hat{L}_0$ using Eq. (3.124) and the density matrix expansion $\hat{\rho}_0 = \sum_k p_k |k\rangle\langle k|$

$$\langle m|\hat{L}_0|l\rangle = \frac{2i}{p_m + p_l}\langle m|\left[\hat{\rho}_0, \hat{G}\right]|l\rangle. \tag{3.127}$$

Expanding the density matrix again we find

$$\langle m|\hat{L}_0|l\rangle = \frac{2i(p_m - p_l)}{p_m + p_l}\langle m|\hat{G}|l\rangle. \tag{3.128}$$

We substitute this in Eq. (3.126) and we finally obtain

$$F_Q[\hat{\rho}_0, \hat{G}] = 2 \sum_{k,m=0}^{\infty} \frac{(p_m - p_k)^2}{p_m + p_k} \left|\langle m|\hat{G}|k\rangle\right|^2. \tag{3.129}$$

This result provides us with a formula, in order to calculate the QFI of a general input state, but only for unitary transformations.

3.3.9 QFI for Unitary Transformations and Pure Initial States

Now we consider the special case, where we have the same unitary transformation as before and a pure initial state, i.e

$$\hat{\rho}_0 = |\psi_0\rangle\langle\psi_0|. \tag{3.130}$$

So, now the unitary transformed state would be given by

$$|\psi(\theta)\rangle = e^{-i\theta\hat{G}}|\psi_0\rangle, \qquad \langle\psi(\theta)| = e^{i\theta\hat{G}}\langle\psi_0|. \tag{3.131}$$

We calculate the derivative of the state with respect to θ

$$|\partial_\theta\psi(\theta)\rangle = -i\hat{G}e^{-i\theta\hat{G}}|\psi_0\rangle, \qquad \langle\partial_\theta\psi(\theta)| = i\hat{G}e^{i\theta\hat{G}}\langle\psi_0|. \tag{3.132}$$

Here, we have assumed that we have a pure initial state and a unitary transformation, that guarantees that our final state would also be pure, thus we can use Eq. (3.116) in order to calculate the QFI

$$F_Q\left[|\psi_0\rangle, \hat{G}\right] = 4\left(\langle\psi_0|\hat{G}^2|\psi_0\rangle - \left|\langle\psi_0|\hat{G}|\psi_0\rangle\right|^2\right) = 4\left(\Delta\hat{G}\right)_0^2, \qquad (3.133)$$

where the variance in the last step is calculated using the initial state $|\psi_0\rangle$.

In the next chapter, we will examine the motion of a particle into a gravitational field, hence the dynamics would be described by the Hamiltonian $\hat{H} = \frac{\hat{p}^2}{2m} + mg\hat{z}$, and the parameter of interest would be g. Thus, the unitary evolution operator $\hat{U}_g = e^{-\frac{iT}{\hbar}H(g)}$, where T is the total time of propagation into the gravitational field, would not be of the form we examined here. This is the reason why, we will use the Baker-Campbell-Hausdorff formula appropriately, in order to isolate the parameter of interest and conclude to an operator of the form $U \propto e^{-ig\hat{G}}$, as we considered here. Then, we can simply calculate the QFI by using Eq. (3.116) with respect to the final pure state, or by Eq. (3.133) with respect to the initial pure state and the generator, after factorizing the parameter of interest.

Chapter 4

Optimal Matterwave Gravimetry

In this chapter we are going to examine the fundamental limits of precision of an atom gravimeter. We calculate the quantum Fisher information (QFI), of a particle passing through a Kasevich-Chu (KC) interferometer and we find that there is more metrological potential available than it is currently considered by semi-classical methods. We also calculate the classical Fisher information (CFI), and we show that innovative measurements, such as the position or the momentum distribution of the atoms at the output of the interferometer could extract more information compared to the conventional measurement of the population difference. Our analysis gives us the ability to consider a modified design for an atom gravimeter, other than the conventional KC configuration and shows that the sensitivity can be more than doubled.

4.1 Introduction

Atom interferometry is a leading inertial-sensing technology, having demonstrated state-of-the-art gravimetry [19, 20, 22, 35, 45, 91, 92] and gradiometry [29, 93–98] measurements. Nevertheless, orders of magnitude improvement in sensitivity is required for applications in navigation [99] and mineral exploration [100], as well as improved tests of the equivalence principle [42, 101, 102] and quantum gravity [103, 104]. Atom gravimeters use the configuration of a KC interferometer [17, 105], which we analysed in Chapter 2, Sec. [2.10], in order to estimate the gravitational acceleration. We have already shown that the phase shift between the two arms of a KC interferometer is given by

$$\phi_g = gk_0T_\pi^2, \tag{4.1}$$

where g is the gravitational acceleration, $\hbar k_0$ is the component of the momentum separation of the two arms aligned with g, and T_π is the time at which the mirror is applied.

In Chapter 2, we showed that assuming N uncorrelated particles, a population-difference measurement at the interferometer output yields sensitivity

$$\Delta g = \frac{1}{\sqrt{N} k_0 T_\pi^2}. \tag{4.2}$$

Equation (4.2) implies only four routes to improved sensitivity: (1) increase interrogation time, (2) increase the momentum separation of the arms (e.g. via large momentum transfer beam splitters [106–110]), (3) increase the atom flux, and/or (4) surpass the shot-noise limit with quantum correlations [55,64,111–113]. Although all routes are worth pursuing, each has unique limitations. For instance, size, weight, and power constraints limit both T_π and the maximum momentum transferrable via laser pulses. Additionally, evaporative-cooling losses and momentum width requirements constrain atom fluxes [34,38,114–116]. Finally, quantum-correlated states must be compatible with the requirements of high-precision metrology [22, 117–128] (e.g. high atom flux, low phase diffusion), and will only be advantageous if classical noise sources, are sufficiently controlled to yield shot-noise-limited operation *prior* to quantum enhancement. For example, two major factors limiting the performance of current atom interferometers are the Coriolis force and the misalignment of the Raman laser pulses with the atomic waves [129,130].

This assessment assumes that Eq. (4.2) is the *optimal* sensitivity. Here, we prove this conventional wisdom false by showing that matterwave interferometers *can* attain better sensitivities than Eq. (4.2). Ultimately, the gravitational field affects the quantum state beyond the creation of a simple phase shift. We show this additional metrological potential via the QFI, which determines the *best* possible sensitivity. We further determine the set of measurements required to attain this optimal sensitivity via the CFI. Our analysis reveals additional routes to improved sensitivity, such as variations in the measurement procedure and input source, and these should be considered when designing future matterwave gravimeters.

4.2 QFI for a Particle in a Gravitational Field

As we discussed earlier, semi-classical arguments suggest that the only effect of the whole KC interferometric sequence would be a phase difference between the two arms. Hence, the atomic state before the final beam-splitter would be given by [131]

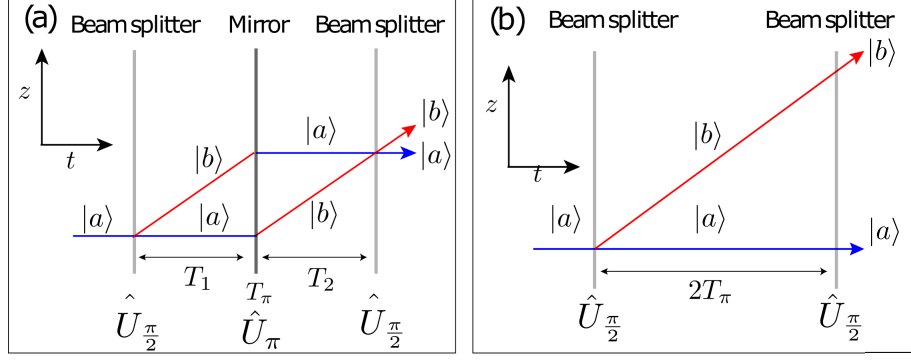$$|\Psi\rangle = \tfrac{1}{\sqrt{2}}(|a\rangle + e^{igk_0 T_\pi^2}|b\rangle). \tag{4.3}$$

Figure 4.1: Spacetime diagrams for (a) KC interferometry and (b) Ramsey interferometry (no mirror pulse), which are both sensitive to gravitational fields and accelerations.

We can calculate the QFI of a pure state using Eq. (3.116). We firstly need to calculate

$$|\partial_g \Psi\rangle = \frac{ik_0 T_\pi^2}{\sqrt{2}} e^{igk_0 T_\pi^2}|b\rangle, \qquad \langle\partial_g \Psi| = -\frac{ik_0 T_\pi^2}{\sqrt{2}} e^{-igk_0 T_\pi^2}\langle b|, \tag{4.4}$$

which gives

$$\langle\partial_g \Psi|\partial_g \Psi\rangle = \frac{1}{2}k_0 T_\pi^2 \tag{4.5}$$

Using Eq. (4.3) we also find

$$|\langle\Psi|\partial_g \Psi\rangle|^2 = \frac{1}{4}k_0^2 T_\pi^2. \tag{4.6}$$

So, we can finally calculate the corresponding semi-classical QFI

$$F_Q^{\text{sc}} = k_0^2 T_\pi^4. \tag{4.7}$$

As discussed in Chapter 3, the QCRB gives the lowest possible bound on the sensitivity. For N uncorrelated particles this is $\Delta g^2 \geq 1/(NF_Q)$, which for $F_Q = F_Q^{\text{sc}}$ is consistent with Eq. (4.2). However, this derivation treats the particle's motion semi-classically, neglecting the non-commutability of position and momentum. We account for this here. For the moment we consider only the centre of mass degrees of freedom. In the presence of a uniform gravitational field g acting along the z-axis, a particle of mass m in state $|\psi_0\rangle$ evolves to $|\psi(T)\rangle = \hat{U}_g|\psi_0\rangle$ after time T, where $\hat{U}_g = \exp\left[-\frac{iT}{\hbar}(\frac{\hat{\mathbf{p}}^2}{2m} + mg\hat{z})\right]$. As shown in Appendix [A.1], we can rewrite

$$\hat{U}_g = e^{-i\frac{T}{\hbar}\frac{\hat{\mathbf{p}}^2}{2m}} e^{-ig\hat{G}_0(T)} e^{i\frac{mg^2T^3}{12\hbar}}, \tag{4.8}$$

where

$$\hat{G}_0(T) = \frac{T}{\hbar}\left(\frac{T}{2}\hat{p}_z + m\hat{z}\right). \tag{4.9}$$

The QFI is

$$F_Q(T) = 4\mathrm{Var}(\hat{G}_0(T)) \tag{4.10a}$$

$$= \tfrac{T^4}{\hbar^2}\mathrm{Var}(\hat{p}_z) + \tfrac{4m^2T^2}{\hbar^2}\mathrm{Var}(\hat{z}) + \tfrac{4mT^3}{\hbar^2}\mathrm{Cov}(\hat{p}_z,\hat{z}), \tag{4.10b}$$

where the variances and covariance are evaluated with respect to $|\psi_0\rangle$. To compare Eq. (4.10a) and F_Q^{sc}, consider a state $|\psi_0\rangle$ with two well-defined peaks in momentum space separated by $\hbar k_0$, giving $\mathrm{Var}(\hat{p}_z) \approx (\hbar k_0)^2$. For sufficiently large k_0 and T such that $(\hbar k_0 T/2)^2 \gg m^2\mathrm{Var}(\hat{z})$, $mT\mathrm{Cov}(\hat{p}_z,\hat{z})$, the first term of Eq. (4.10b) dominates, and $F_Q(2T_\pi) \approx k_0^2 T_\pi^4 = F_Q^{\mathrm{sc}}$. However, the additional terms in Eq. (4.10b) potentially allow sensitivities better than Eq. (4.2).

4.3 QFI for KC Interferometry

Equation (4.10a) is *not* the QFI for a KC interferometer, as we must account for the internal state degrees of freedom, as well as the action of the mirror pulse. The evolution is given by

$$\hat{U}_{\mathrm{KC}} = \hat{U}_{\frac{\pi}{2}}^{\phi_3}\hat{U}_g(T_2)\hat{U}_\pi^{\phi_2}\hat{U}_g(T_1)\hat{U}_{\frac{\pi}{2}}^{\phi_1}, \tag{4.11}$$

where

$$\hat{U}_\theta^\phi = \hat{1}\cos\left(\tfrac{\theta}{2}\right) - i(|b\rangle\langle a|e^{i(k_0\hat{z}-\phi)} + \mathrm{h.c.})\sin\left(\tfrac{\theta}{2}\right) \tag{4.12}$$

governs the beam-splitter and mirror dynamics. As shown in Appendix [A.4], Eq. (4.12) is an excellent approximation to the beam splitting and mirror dynamics, when the pulse duration is much shorter than the timescale for atomic motional dynamics. Here, $T_{1(2)}$ are evolution times before(after) the π pulse and ϕ is the pulse phase, controlled via the relative phase of the two Raman lasers. The first $\pi/2$ pulse maps the initial state $|\Psi_0\rangle = |a\rangle|\psi_0\rangle$ to $|\Psi_0'\rangle = \hat{U}_{\frac{\pi}{2}}^{\phi_1}|\Psi_0\rangle = \tfrac{1}{\sqrt{2}}\left(|a\rangle - ie^{i(k_0\hat{z}-\phi_1)}|b\rangle\right)|\psi_0\rangle$, where $|\psi_0\rangle$ contains the initial state's motional degrees of freedom. As detailed in Appendix [A.2],

$$|\Psi(T)\rangle = \hat{U}_{\mathrm{KC}}|\Psi_0\rangle = \hat{U}_0 e^{-ig(\hat{G}_0(T)+\hat{G}_e)}|\Psi_0'\rangle, \tag{4.13}$$

where

$$\hat{G}_e = \hat{J}_z k_0 T_2^2, \tag{4.14a}$$

$$\hat{J}_z = \frac{1}{2}\left(|a\rangle\langle a| - |b\rangle\langle b|\right), \tag{4.14b}$$

$$\hat{U}_0 = \hat{U}_{\frac{\pi}{2}}^{\phi_3} e^{-i\frac{T_2}{\hbar}\frac{\hat{\mathbf{P}}^2}{2m}}\hat{U}_\pi^{\phi_2} e^{-i\frac{T_1}{\hbar}\frac{\hat{\mathbf{P}}^2}{2m}}, \tag{4.14c}$$

and $T = T_1 + T_2$, giving QFI

$$F_Q^{\text{KC}}(T) = 4\text{Var}(\hat{G}_0(T)) + \tfrac{1}{4}k_0^2 \left(T^2 - 2T_2^2\right)^2, \tag{4.15}$$

where $\text{Var}(\hat{G}_0(T))$ is taken with respect to $|\psi_0\rangle$. For $T_1 = T_2 = T_\pi$,

$$F_Q^{\text{KC}}(T) = 4\text{Var}(\hat{G}_0(T)) + k_0^2 T_\pi^4. \tag{4.16}$$

Since $\text{Var}(\hat{G}_0(T)) \geq 0$, this implies $F_Q^{\text{KC}} \geq F_Q^{\text{sc}}$, thereby permitting sensitivities better than Eq. (4.2).

As we saw earlier the already known term $k_0^2 T_\pi^4$ comes from the phase shift between the two arms of the interferometer, while the new term $4\text{Var}(\hat{G}_0(T)) = \frac{T^4}{\hbar^2}\text{Var}(\hat{p}_z) + \frac{4m^2 T^2}{\hbar^2}\text{Var}(\hat{z}) + \frac{4m T^3}{\hbar^2}\text{Cov}(\hat{p}_z, \hat{z})$ is stemming from the propagation of the atom in the gravitational field. For long interferometer times we notice that the old term, $k_0^2 T_\pi^4$, as well as $\frac{T^4}{\hbar^2}\text{Var}(\hat{p}_z)$ from the new term dominate. Hence, this result indicates that we can boost the metrological potential of the interferometer, by engineering appropriate initial atomic states with large momentum variance. In addition, for short interrogation times we notice that $\frac{4m^2 T^2}{\hbar^2}\text{Var}(\hat{z})$ from the new term dominates. This means that the classical noise sources associated with the phase difference term $(k_0^2 T_\pi^4)$, such as the Coriolis effect and the Raman laser misalignment, would have a mitigated effect on the performance of the device. Hence, engineering initial atomic states with large position variance would improve the sensitivity and robustness of high bandwidth sensors for inertial navigation.

To summarize, Eq. (4.16) essentially shows that there are additional sources of information available, which are related to momentum and position variances of the initial atomic state and they are not taken into account by current methods. Thus, we can increase the metrological potential of our device, by appropriately selecting the motional state of the atoms entering the interferometer.

4.4 Classical Fisher Information

Although the QFI gives the best possible sensitivity, it is silent on how to *achieve* this sensitivity. The attainable sensitivity for a particular measurement choice is given by the CFI, which quantifies the information contained in the probability distribution constructed from measurements of a particular observable, and necessarily depends upon this choice of observable. We calculate the CFI via

$$F_C(\hat{\Lambda}) = \int d\lambda \frac{[\partial_g P(\lambda)]^2}{P(\lambda)}, \tag{4.17}$$

where $P(\lambda)$ is the probability of obtaining result λ, when the observable $\hat{\Lambda}$ is measured [86, 132]. As analysed in more detail in Chapter 3, the CFI is bounded by the QCRB $F_C \leq F_Q$, so a measurement that saturates this bound is the optimal measurement.

4.4.1 CFI for Population Difference Measurement

For the standard population difference measurement at the KC interferometer output, $\hat{\Lambda} = \hat{J}_z$ and $F_C(\hat{J}_z) = \sum_{s=a,b}(\partial_g P_s)^2/P_s$, where $P_s = \int dz |\langle s|\langle z|\Psi(T)\rangle|^2$. As detailed in Appendix [A.3], an analytic solution exists in this case. Specifically,

$$P_a = \tfrac{1}{2}(1 + |\mathcal{C}|\sin\alpha), \tag{4.18a}$$

$$P_b = \tfrac{1}{2}\left(1 - |\mathcal{C}|\sin\alpha\right), \tag{4.18b}$$

yielding

$$F_C(\hat{J}_z) = \frac{|\mathcal{C}|^2\cos^2\alpha}{1 - |\mathcal{C}|^2\sin^2\alpha}k_0^2\left(\frac{T^2}{2} - T_1^2\right)^2, \tag{4.19}$$

where

$$\mathcal{C} = \langle\psi_0|e^{i\frac{k_0}{m}(T_2-T_1)\hat{p}_z}|\psi_0\rangle \equiv |C|e^{i\vartheta}, \tag{4.20a}$$

$$\alpha = \phi_f - \phi_g + \vartheta, \tag{4.20b}$$

with $\phi_f = \frac{\hbar k_0^2}{2m}(T_2 - T_1)$ and $\phi_g = k_0 g(\frac{T^2}{2} - T_1^2)$. Throughout the calculation in Appendix [A.3] we encountered all different components of the total phase shift between the two arms of a KC interferometer, which we had introduced in Chapter 2. Here, ϕ_f has exactly the same interpretation as $\Delta\phi_{\text{separation}}$, which was denoted as the phase shift arising when the two wave-packets do not intersect at the final beam-splitter. Also, ϕ_g is the phase shift due to the gravitational field, where for the symmetrical case $T_1 = T_2$ we obtain $\phi_g = k_0 g T_\pi^2$, as first mentioned in Chapter 2. In the intermediate steps of the calculation in Appendix [A.3] we also encountered the phase difference due to the laser pulses $\Delta\phi_{\text{laser}} = \phi_1 - 2\phi_2 + \phi_3$. That is to say that following our analysis we were able to derive all phase shifts coming from the semi-classical approach, but our formalism also takes into account the effect of the gravitational field in the motional state of the particle.

The contrast $|\mathcal{C}|$ is determined by the spatial overlap of the two output wavepackets, since $\frac{\hbar k_0}{m}(T_2 - T_1)$ is the spatial separation. This depends strongly on the time difference $T_2 - T_1$. We can calculate the contrast by using

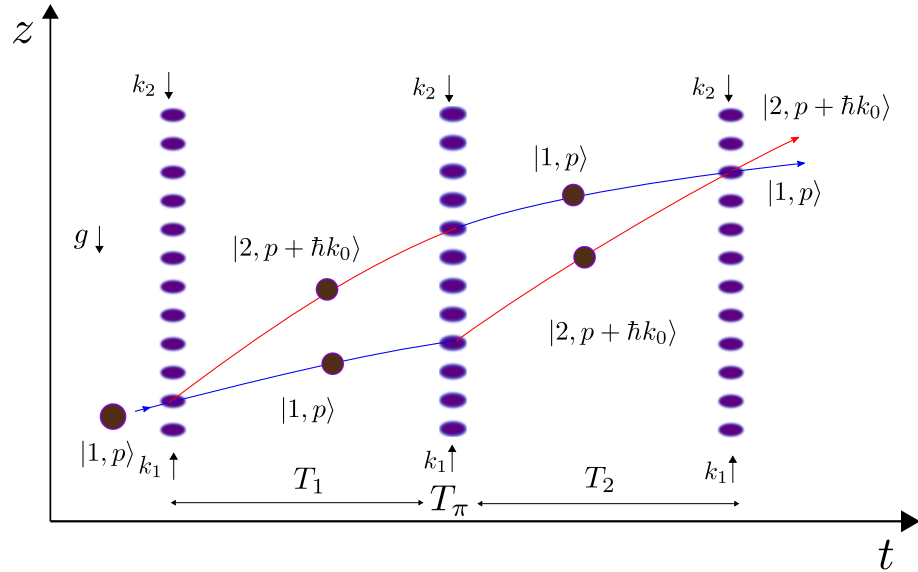$$\mathcal{C} = \int_\infty^\infty P_0(k)e^{i\frac{k_0}{m}\hbar(T_2-T_1)k}dk, \tag{4.21}$$

Figure 4.2: This figure illustrates the conventional structure of a symmetric KC interferometer. In our analysis, we consider a more flexible scheme, where the time of measurement, i.e. the application time of the second beam splitter, is not fixed, but rather we consider that the measurement could happen at each time point. We do that by fixing T_π so the mirror pulse always occurs at $t = T_\pi$ and if $t \leq T_\pi$, then $T_1 = t$, $T_2 = 0$, and the mirror pulse has no meaningful effect; if $t > T_\pi$ then $T_1 = T_\pi$ and $T_2 = t - T_\pi$. This strategy helps to find the resulting Fisher information at all time points, Fig. [4.3] and [4.4], highlighting potential non-conventional structures that could enable us to extract more information.

where in Eq. (4.20a) we have expanded the exponential and we have used the momentum space wave-function, in order to calculate the expectation value. For an initial Gaussian state $\langle z | \psi_0 \rangle = \exp(-z^2/2\sigma^2)/(\pi\sigma^2)^{1/4}$, we find

$$\mathcal{C} = e^{-\frac{\hbar^2 k_0^2}{4m^2\sigma^2}(T_2 - T_1)^2},\tag{4.22}$$

where we also notice that $\theta = 0$.

In the following sections, we are going to calculate the CFI for the population difference as well as the momentum and position distribution measurements using the time evolved atomic state, by numerically solving the Schrödinger equation. We are interested on finding how much information we can extract at each time point of the evolution, considering a more flexible structure than the standard KC interferometer, where the conventional scheme requires the use of the mirror pulse and it always assumes the symmetric case $T_1 = T_2$, Fig. [4.2]. For this reason we apply the following strategy. We fix T_π, so the mirror pulse always occurs at $t = T_\pi$ and we assume that we make a measurement instantaneously

after the second beam splitter. We do not consider a fixed time of measurement, neither that the measurement necessarily happens after $t = T_\pi$. Namely we assume a variable time of measurement that could happen at any time point along the t-axis, Fig. [4.2]. So for example, if we consider a time of measurement such that $t \leq T_\pi$, then $T_1 = t$, $T_2 = 0$, and the mirror pulse has no meaningful effect. Instead, if we consider that the measurement happens for times $t > T_\pi$, then $T_1 = T_\pi$ and $T_2 = t - T_\pi$. Following the logic described above, we created Fig. [4.3], which shows the values of F_Q, $F_C(\hat{J}_z)$, $F_C(\hat{J}_z, \hat{p}_z)$ and $F_C(\hat{J}_z, \hat{z})$ at each time point, considering that each time point under consideration is the time of measurement. When T_1 and T_2 are significantly different, the spatial overlap of the two modes at the interferometer output is poor, so both the contrast and CFI of the population difference are close to zero, Eq. [4.22] and [4.19] respectively. However, $|C| = 1$ when $T_1 = T_2$ and $F_C(\hat{J}_z) = F_Q^{\text{sc}} = k_0^2 T_\pi^4$, giving the same sensitivity as Eq. (4.2). This is still less than F_Q^{KC}, indicating that a different measurement could yield improved sensitivities.

4.4.2 CFI for Momentum Distribution Measurement

Now, consider a measurement that distinguishes internal states *and* fully resolves the z-component of the final momentum distribution, such as reported in Ref. [133]. This measurement yields the CFI

$$F_C(\hat{J}_z, \hat{p}_z) = \sum_{s=a,b} \int dp_z \frac{[\partial_g P_s(p_z)]^2}{P_s(p_z)}, \tag{4.23}$$

where $P_s(p_z) = |\langle s|\langle p_z|\Psi(T)\rangle|^2$. Although no analytic formula exists for $F_C(\hat{J}_z, \hat{p}_z)$, the probabilities can be determined by numerically solving the Schrödinger equation, and the CFI computed from finite differences of these probabilities [134]. This requires an explicit choice of g; although we consider the sensitivity near $g = 0$ for all numerical calculations, a large offset in g is easily accounted for by adjusting the beam splitter phases, as in typical atom gravimeters [38].

Fig. [4.3(a)] shows that $F_C(\hat{J}_z, \hat{p}_z)$ is significantly larger than $F_C(\hat{J}_z)$ and very close to F_Q^{KC}. Additionally, $F_C(\hat{J}_z, \hat{p}_z) \approx F_Q^{\text{KC}}$ even when T_1 and T_2 are vastly different. This is because $P_s(p_z)$ displays interference fringes that are not present in $P_s = \int dp_z P_s(p_z)$, when spatial overlap is poor.

The origin of the increased information in $F_C(\hat{J}_z, \hat{p}_z)$ compared with $F_C(\hat{J}_z)$ is easily understood. Additional to the CFI associated with population exchange (generated by $\hat{G}_e$), there is information due to a shift in the momentum distribution. Concretely, consider

initial momentum distribution $P_0(p_z)$. Under gravity, $\hat{p}_z(t) = \hat{p}_z(0) + mgt$, so $P(p_z, t) = P_0(p_z - mgt)$, giving

$$
\begin{aligned}
F_C(\hat{p}_z) &= \int dp_z \frac{[\partial_g P(p_z, t)]^2}{P(p_z, t)} \\
&= [\partial_g p_z(t)]^2 \int dp_z \frac{[\partial_{p_z} P_0(p_z)]^2}{P_0(p_z)} \\
&\equiv (mt)^2 F_C^{p_z},
\end{aligned}
\tag{4.24}
$$

where $F_C^{p_z}$ is the CFI associated with resolvable small shifts in the momentum distribution. Now, we consider a CFI associated with shifts in a general q-parameter space, defined as

$$
F_C^q \equiv \int_{-\infty}^{\infty} dq \frac{[\partial_q P(q)]^2}{P(q)},
\tag{4.25}
$$

where we consider a Gaussian probability distribution $P(q) = \frac{1}{\sigma\sqrt{\pi}} e^{-\frac{(q-q_0)^2}{\sigma^2}}$, with standard deviation $\Delta q = \sigma/\sqrt{2}$, which also satisfies $\int_{-\infty}^{\infty} P(q) dq = 1$. We calculate $[\partial_q P(q)]^2 = 4(q - q_0)^2 P(q)^2/\sigma^4$ and we obtain

$$
F_C^q = \frac{4}{\sigma^5 \sqrt{\pi}} \int_{\infty}^{\infty} (q - q_0)^2 e^{-\frac{(q-q_0)^2}{\sigma^2}} dq = \frac{2}{\sigma^2}.
\tag{4.26}
$$

Hence, for a Gaussian probability distribution, the CFI associated with shifts in that parameter space is given by the inverse of the probability distribution's variance, i.e.

$$
F_C^q = \frac{1}{\text{Var}(q)}.
\tag{4.27}
$$

Thus, for the Gaussian state we consider here $\text{Var}(\hat{p}_z(t)) = \text{Var}(\hat{p}_z(0)) = \hbar^2/(2\sigma^2)$, and for the CFI associated with shifts in momentum distribution we have $F_C^{p_z} = 1/\text{Var}(\hat{p}_z)$, thus $F_C(p_z)|_{2T_\pi} = 8(mT_\pi\sigma/\hbar)^2$. Adding this additional CFI to $F_C(\hat{J}_z)$ gives $F_C(\hat{J}_z, \hat{p}_z)|_{2T_\pi} = F_Q^{\text{sc}} + 8(mT_\pi\sigma/\hbar)^2$, in perfect agreement with our numerics. Note that this additional information is *not* the result of a phase shift so, unlike a standard KC interferometer, it is *not* affected by additional phase noise.

Our simulations also find near-perfect correlations between internal and momentum states, so a measurement that only resolves momentum (and not $\hat{J}_z$) also has CFI approximating $F_C(\hat{J}_z, \hat{p}_z)|_{2T_\pi}$, since an atom's internal state is inferred from its final momentum. Our analysis therefore holds for interferometers that do not change internal states, such as Bragg-scattering-based interferometers, provided $\hbar k_0 \gg \delta p$, where δp is the wavepacket's initial momentum width [22, 106]. In our simulations $\hbar k_0 \approx 14\delta p$.
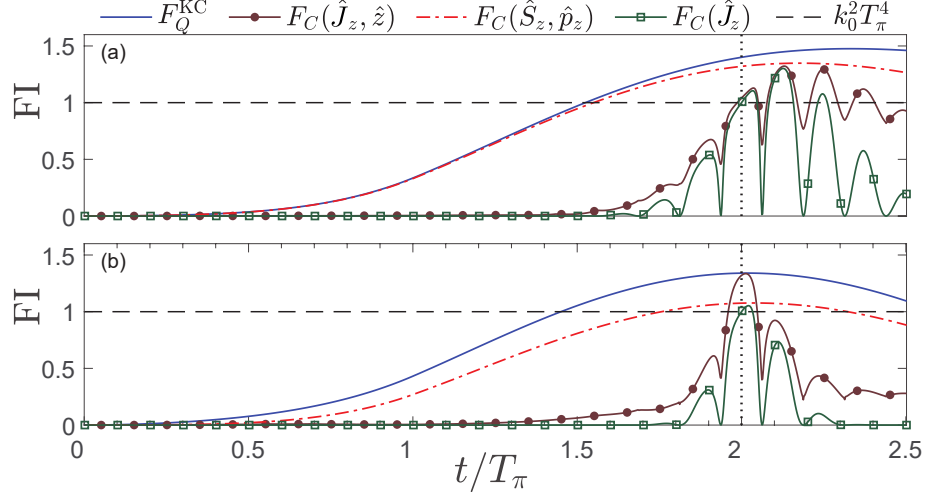
Figure 4.3: Fisher information (FI) for the state $|\Psi(t)\rangle = \hat{U}_{\mathrm{KC}}(t)|\Psi_0\rangle$, where $T_1 = t$ and $T_2 = 0$ for $t \leq T_\pi$, otherwise $T_1 = T_\pi$ and $T_2 = t - T_\pi$, with initial Gaussian motional state (a) $\langle z|\psi_0\rangle = \exp\left(-z^2/2\sigma^2\right)/(\pi\sigma^2)^{1/4}$ and (b) $\langle z|\psi_0\rangle = e^{-(\frac{1}{4}+i)z^2/2\sigma^2}/[\pi(2\sigma)^2]^{1/4}$. FI has units $k_0^2 T_\pi^4$, so when FI > 1 a given measurement scheme achieves a sensitivity better than that predicted by the semiclassical limit Eq. (4.2). The QFI F_Q^{KC} gives the maximum possible FI. Here $\sigma = 10L$ and $T_\pi = 100t_0$, whilst the length $(L = k_0^{-1})$ and time $(t_0 = m/\hbar k_0^2)$ units depend on k_0.

4.4.3 CFI for Position Distribution Measurement

Although the momentum distribution cannot always be resolved, a measurement of the *position* distribution might be possible. Here, the CFI is

$$F_C(\hat{J}_z, \hat{z}) = \sum_{s=a,b} \int dz \frac{[\partial_g P_s(z)]^2}{P_s(z)}, \tag{4.28}$$

where $P_s(z) = |\langle s|\langle z|\Psi(t)\rangle|^2$. Fig. [4.3(a)] shows this is slightly better than the population-difference measurement, although significantly worse than the momentum measurement. Arguing as before, since the position distribution shifts due to $\hat{z}(t) = \hat{z}(0) + \hat{p}_z(0)t/m + \frac{1}{2}gt^2$, the additional CFI is $(t^2/2)^2 F_C^z$, where $F_C^z = \int dz [\partial_z P(z)]^2/P(z)$ is the CFI associated with resolvable shifts in the position distribution. Since

$$\mathrm{Var}(\hat{z}(t)) = \mathrm{Var}(\hat{z}(0)) + \frac{t^2}{m^2}\mathrm{Var}(\hat{p}_z(0))$$
$$+ \frac{t}{2m}\mathrm{Cov}(\hat{p}_z(0), \hat{z}(0)), \tag{4.29}$$

and $F_C^z = 1/\mathrm{Var}(\hat{z})$ for Gaussian states as we showed earlier, and using $\mathrm{Var}(\hat{z}(0)) = \sigma^2/2$, $\mathrm{Var}(\hat{p}_z(0)) = \hbar^2/(2\sigma^2)$, $\mathrm{Cov}(\hat{p}_z(0), \hat{z}(0)) = 0$ we obtain $F_C(\hat{J}_z, \hat{z})|_{2T_\pi} = F_Q^{\mathrm{sc}} +$

$8(\sigma m T_\pi^2)^2/[(\sigma^2 m)^2 + (2\hbar T_\pi)^2]$ for the initial Gaussian state considered in Fig. [4.3(a)], in agreement with numerics.

We can increase $F_C(\hat{J}_z, \hat{z})$ with an initial state that decreases $\mathrm{Var}(\hat{z}(2T_\pi))$ at the interferometer output. This is not achieved by reducing $\mathrm{Var}(\hat{z}(0))$, but rather via an initial state with nontrivial correlations between position and momentum such that $\mathrm{Cov}(\hat{p}_z, \hat{z})$ counteracts the wavepacket's ballistic expansion. Fig. [4.3(b)] shows the QFI and CFI for initial state $\langle z|\psi_0\rangle = e^{-(\frac{1}{4}+i)z^2/2\sigma^2}/[\pi(2\sigma)^2]^{1/4}$. The imaginary term provides the position-momentum correlations and doubling the spatial width increases the ability of the wavepacket to be *focused*. This initial state could be engineered by applying a harmonic potential for a short duration (compared to motional dynamics), creating phase gradient $\psi(z) \to \psi(z)e^{-iz^2/\sigma_t^2}$, for constant σ_t which depends on trap frequency and duration [135]. Then $F_C(\hat{J}_z, \hat{z})$ saturates the QCRB at $T_1 = T_2$, at the cost of reduced $F_C(\hat{J}_z, \hat{p}_z)$.

4.5 Optimum Measurements

Since measurements in different bases yield different sensitivities, is there an accessible measurement basis that saturates the QCRB? Our above analysis suggests yes and, depending on the initial state, this optimum basis lies somewhere *between* position and momentum. We confirm this intuition by revisiting a particle in a gravitational field. We rewrite

$$|\psi(t)\rangle = \hat{U}_g|\psi_0\rangle = \exp\Big(-ig\hat{G}_0'(t)\Big)|\psi_0(t)\rangle, \tag{4.30}$$

where

$$\hat{G}_0'(t) = \hat{U}_p\hat{G}_0(t)\hat{U}_p^\dagger = \frac{t}{\hbar}(m\hat{z} - \tfrac{1}{2}\hat{p}_z t), \tag{4.31}$$

$\hat{U}_p = \exp\big[-it\mathbf{p}^2/(2m\hbar)\big]$, and $|\psi_0(t)\rangle = \hat{U}_p|\psi_0\rangle$ describes free-particle evolution. We can interpret $\hat{G}_0'(t)$ as the generator of displacements in $\hat{Q} = c_1\hat{z} + c_2\hat{p}_z$, where the coefficients c_i are real and satisfy $\frac{1}{2}c_1 + tmc_2 = 1$, since $[\hat{G}_0'(t), \hat{Q}] = i$. Hence, the probability distribution $|\langle q|\psi(t)\rangle|^2 = |\langle q - g|\psi_0(t)\rangle|^2$, where $\hat{Q}|q\rangle = q|q\rangle$. If $|\langle q|\psi_0(t)\rangle|^2$ is Gaussian, then measurements of $\hat{Q}$ saturate the QCRB, since

$$F_C(\hat{Q}) = \frac{1}{\mathrm{Var}(\hat{Q})} = 4\mathrm{Var}(\hat{G}_0'(t)) = F_Q. \tag{4.32}$$

The first equality holds due to Eq. (4.27), while the last one is true due to Eq. (3.133). The second equality is justified as follows, for any two observables satisfying $[\hat{G}_0'(t), \hat{Q}] = i$, the uncertainty relation holds $\mathrm{Var}(\hat{Q})\mathrm{Var}(\hat{G}_0'(t)) \geq 1/4$. However, the equality is being
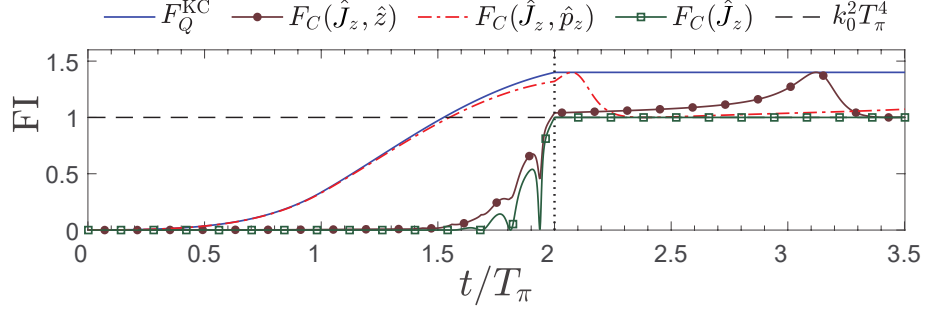
Figure 4.4: Fisher information (FI) for the state $|\Psi(t)\rangle = \hat{U}_{\mathrm{KC}}(t)|\Psi_0\rangle$, where $T_1 = t$ and $T_2 = 0$ for $t \leq T_\pi$, otherwise $T_1 = T_\pi$ and $T_2 = t - T_\pi$, with a harmonic potential applied at $t = 2T_\pi$ and initial Gaussian motional state $\langle z|\psi_0\rangle = \exp(-z^2/2\sigma^2)/(\pi\sigma^2)^{1/4}$. We artificially turned off gravity at $t = 2T_\pi$ (which holds F_Q^{KC} constant) to clearly show the effect of harmonic trapping. Specifically, the application of this harmonic potential can be used to saturate the QCRB with either a position distribution or momentum distribution measurement. Here $\sigma = 10L$, $T_\pi = 100t_0$, and $\omega = 3\pi/(2T_\pi)$. FI has units $k_0^2 T_\pi^4$, and length $(L = k_0^{-1})$ and time $(t_0 = m/\hbar k_0^2)$ units depend on k_0.

satisfied here, because he have considered a Gaussian state. To measure $\hat{Q}$, we mix $\hat{z}$ and $\hat{p}_z$ by applying the potential $V(z) = \frac{1}{2}m\omega^2 z^2$, since $\hat{z}(t) = \hat{z}(0)\cos\omega t + [\hat{p}(0)/m\omega]\sin\omega t$. Subsequently measuring position yields a combination of position and momentum information. This scheme could be implemented using the following procedure:

1. At $t = 2T_\pi$, apply the unitary $\hat{U}_s = |a\rangle\langle a| + |b\rangle\langle b|e^{-ik_0\hat{z}}$, which removes any momentum mismatch between the two modes. A state-selective Bragg transition achieves this.

2. Then apply the potential $V(z) = \frac{1}{2}m\omega^2(z - z_0)^2$, where $z_0 = \hbar k_0 T_\pi/m$ is the matterwave's centre-of-mass displacement at the interferometer output.

3. Finally, at some later time, we apply a beam splitter $\hat{U}_{\mathrm{BS}} = \frac{1}{\sqrt{2}}[\hat{1} + (|a\rangle\langle b| - \mathrm{h.c.})]$ immediately before measurement.

Fig. [4.4] shows $F_C(\hat{J}_z, \hat{z})$ and $F_C(\hat{J}_z, \hat{p}_z)$ for this scheme. Both CFIs oscillate between F_Q^{sc} and the QFI, so a measurement in either the position or momentum basis saturates the QCRB if made at the appropriate time. This improved sensitivity *does* increase the interferometer time. However, the period of CFI oscillations is negligible compared to T_π for sufficiently large ω.

4.6   Improved Interferometry

In KC interferometry, the π pulse ensures that the wavepackets spatially overlap at $t = 2T_\pi$. However, Fig. [4.3] and Fig. [4.4] reveal that spatial overlap is *not* required for a momentum measurement, making the mirror pulse unnecessary. More interestingly, removing the π pulse significantly increases the spatial separation, and therefore the QFI, for the same interrogation time. More precisely, setting $T_1 = 2T_\pi$ and $T_2 = 0$ in Eq. (4.15) gives $F_Q(T) = 4\text{Var}(\hat{G}_0(T)) + 4k_0^2 T_\pi^4$, an increase of $3F_Q^{\text{sc}}$ over symmetric KC interferometry.

We numerically solved the Schrödinger equation for the mirrorless Mach-Zehnder (i.e. Ramsey) configuration, Fig. [4.1(b)]. Fig. [4.5(a)] shows that a momentum measurement is always nearly optimal, and at $t = 2T_\pi$, $F_C(\hat{J}_z, \hat{p}_z)/F_Q^{\text{sc}} \approx 4.4$. Unfortunately, this improved sensitivity has a price. A lack of spatial overlap means that information is encoded in high-frequency interference fringes in the momentum distribution, requiring high-resolution momentum measurements. Following Refs. [136–140], we model imperfect resolution by convolving the momentum distribution at $t = 2T_\pi$ with a Gaussian of width σ_p before constructing $F_C(\hat{J}_z, \hat{p}_z)$, Fig. [4.5(b)]. This imperfect resolution may be due to limitations on the detection system, or other sources of classical noise. The mirrorless configuration is considerably more sensitive to imperfect momentum resolution than KC interferometry, where $F_C(\hat{J}_z, \hat{p}_z)$ begins to degrade only when σ_p is comparable to the initial wavepacket's momentum width. Furthermore, in the limit of a "bad" momentum measurement ($\sigma_p \to \infty$), the CFI goes to zero, whereas the CFI for KC interferometry approaches F_Q^{sc}. Nevertheless, if high-resolution measurements are available (or actively developed), as reported in Ref. [141] for instance, our result suggests that pursuing a mirrorless configuration could yield substantial sensitivity gains.

4.7   Discussion and Outlook

An important experimental consideration is achieving high-resolution momentum measurements. Time-of-flight imaging is a standard technique, where ballistic expansion converts the momentum distribution into a position distribution [142, 143]. However, the expansion time needed for sufficient momentum resolution might be significantly longer than the interrogation time, in which case longer interrogation times are a better route to improved sensitivities. Bragg spectroscopy is perhaps a more promising approach [144, 145].

Reference [35] reports state-of-the-art gravimetry with a Bose-Einstein condensate
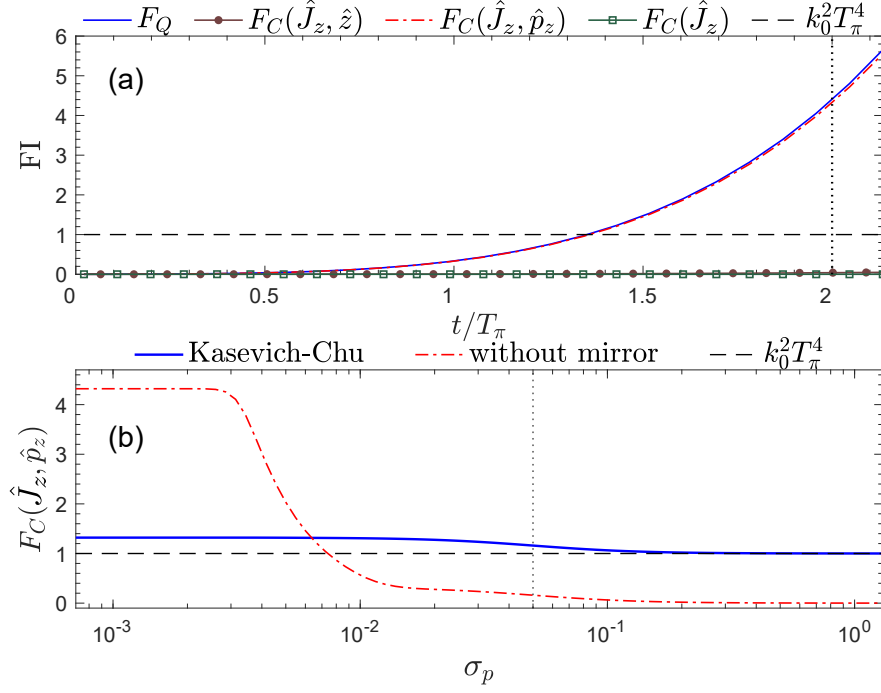
Figure 4.5: (a) FI of the mirrorless configuration for the same initial state and parameters as in Fig. [4.3(a)]. We normalize time by $T_\pi = 100t_0$ only for comparison with Fig. [4.3]. Note that $F_C(\hat{J}_z)$ and $F_C(\hat{J}_z, \hat{z})$ are almost zero throughout the entire evolution, since there is no spatial overlap of the wavepackets and consequently no interference in P_s or the position distribution. (b) $F_C(\hat{J}_z, \hat{p}_z)$ constructed from convolving probability distributions with a Gaussian of width σ_p (units $\hbar k_0$). The vertical line marks the initial state's momentum width: $\delta p_z = \hbar/\sqrt{2}\sigma \approx 0.07\hbar k_0$. The momentum resolution required to extract all the information is $\Delta p = \hbar/(2\Delta x)$, where $\Delta x = \hbar k_0 T/m$ is the spatial separation between the two atomic wave-packets. For our parameter values $\Delta p \approx 3 \times 10^{-3}\hbar k_0$, which perfectly agrees with the numerical results. FI units: $k_0^2 T_\pi^4$.

(BEC), well-described by a pure motional state, and parameters: $\sigma = 40\mu$m, $T_\pi = 130$ms, $k_0 = 1.6 \times 10^7$ m^{-1}, $\delta p_z = 0.18\hbar k_0$. We estimate that $4\text{Var}(\hat{G}_0(T))$ is $\sim 7\%$ of F_Q^{sc}, so there is little gain in making optimal measurements, Eq. [(4.16)]. However, $4\text{Var}(\hat{G}_0(T)) \sim F_Q^{\text{sc}}$ if σ or δp_z were increased by an order of magnitude. This suggests that creating initial (pure) states with large spatial extent, such as quasi-continuous atom lasers [116, 146], could yield substantial sensitivity gains. Additionally, compact and/or high-bandwidth devices could benefit from optimal measurements, since shorter interrogation times increase $\text{Var}(\hat{G}_0(T))$ relative to F_Q^{sc}.

For KC interferometers with thermal (mixed) states, Eq. (4.16) is only an upper bound for the QFI [86]. A calculation of F_Q and F_C for thermal sources gives values substantially

greater than F_Q^{sc} [147], in qualitative agreement with our above analysis, showing that current thermal-atom gravimetry is suboptimal. However, the QFI and CFI are also smaller than Eq. (4.16) for thermal sources, suggesting that BECs possess metrological potential beyond what is possible with thermal sources.

Our approach to evaluating matterwave interferometry could significantly influence the design of future state-of-the-art gravimeters. Typical interferometer design assumes a particular form for the measurement signal (e.g. the population difference at the output varies sinusoidally with g) and looks no further if there is agreement with simple 'best case' formulae such as Eq. (4.2). In contrast, a Fisher analysis gives the full metrological potential of *any* given dynamical scheme without enforcing such *a priori* assumptions by simply considering the available data. Our matterwave gravimetry analysis opens up new routes to improved sensitivity – beyond those few implied by Eq. (4.2). This includes engineering states with high QFI, i.e. large $\text{Var}(\hat{G}_0(T))$, and improving information extraction at the interferometer output. Our mirrorless scheme gives a substantial sensitivity boost if high-resolution momentum measurements are available. In the experimental setup of [35], they considered a BEC of ^{87}Rb atoms, with Bragg laser pulses of $\lambda = 780\,\text{nm}$ realizing the MZ interferometer, and total interrogation time $t = 130\,\text{ms}$. For these parameter values, our mirrorless scheme would result in a $\Delta x \approx 0.8\,\text{mm}$ spatial separation of the two atomic wave-packets at the end of the interferometer. From this, we can identify the momentum resolution, $\Delta p = \hbar/(2\Delta x) \approx 0.8 \times 10^{-4}\hbar k_0$, required to distinguish the fringes in momentum space and obtain all the available information, as shown by the CFI in Fig. [4.5(b)]. This performance is achievable by further developing the $2 \times 10^{-4}\hbar k_0$ resolution measurement of [141]. A Fisher analysis could prove beneficial for evaluating other atom-interferometer-based sensors which produce a complicated output signal, such as schemes utilizing Kapitza-Dirac scattering [148–153], or propagation in crossed wave-guides [154]. In the next two chapters we are going to consider entanglement-enhanced schemes, in order to enhance the sensitivity of quantum sensors based on atom interferometers, which are limited by the atom shot-noise.

Chapter 5

Quantum Non Demolition Measurements of a BEC

In this chapter, we theoretically investigate the use of a quantum non-demolition (QND) measurement scheme, to enhance the sensitivity of atom interferometry with Bose-condensed atoms. In particular, we are concerned with enhancing existing high-precision atom interferometry apparatuses, so we restrict ourselves to dilute atomic samples, and the use of free-propagating light, or optical cavities in the weak-coupling regime. We find the optimum parameter regime that balances between spin squeezing and atomic loss, and find that significant improvements in sensitivity are possible. Finally, we consider the use of squeezed light, and show that this can provide further boosts to the sensitivity.

5.1   Introduction

Atom interferometers are powerful tools for making precision measurements of inertial quantities. A lot of interest has therefore developed in finding ways of improving their performance to gain advantage in different applications. In Chapter 4, we analysed possible routes of improving the performance of these devices. It has been shown that Bose-condensed atomic sources can outperform thermal sources due to their narrow momentum linewidth, despite their reduced atomic flux [34,109,115,146,155]. The use of non-classical atomic states such as spin-squeezed states can offset this reduction in flux even further, by allowing for sensitivities beyond the shot-noise limit (SNL) [39, 48, 49, 156]. In this chapter, we investigate the use of quantum non-demolition measurements in collections of Bose-condensed atoms, to generate quantum states that could be used to enhance their precision, in a range of metrology schemes. So far, the use of light to perform

QND measurements of the collective atomic spin has shown significant spin-squeezing [58,60–62,64,157–160], but these experimental demonstrations have been restricted to cold thermal atoms. In this chapter, we focus on Bose-condensed sources, with the motivation of implementing this quantum enhancement technique on existing high-precision, large space-time area atomic gravimetry set-ups, such as [22]. In particular, the requirement that the Bose-Einstein condensate (BEC) is expanded before the atomic beam-splitting process dictates a minimum spatial size of the source, and prevents excessively elongated samples such as in [159]. Furthermore, we focus on using freely propagating light, and find the optimum parameter regime which balances the spin-squeezing and atomic loss caused by spontaneous emission. We also investigate the effect of BEC interactions in the final sensitivity and we show that we can appropriately adjust the parameter regime, in such a way that we can get the same amount of spin squeezing and avoid their deleterious effect in the sensitivity. Additionally, we consider the use of squeezed light to further enhance the sensitivity. Finally, we examine the use of optical cavities, but restrict ourselves to cavities that are assembled outside the vacuum chamber, so are inherently low-finesse with weak atom-light coupling due to the large cavity volume.

This chapter is structured as follows. In section 5.2, we quantify how spin-squeezing via QND measurements improves the sensitivity. In section 5.3, we introduce a simple model of QND squeezing, which allows us to make some simple analytic scaling predictions. In section 5.4, we present our full model including a freely-propagating multimode optical field and decoherence due to spontaneous emission. In section 5.5, we derive approximate analytic solutions to this model, and in section 5.6 we analyse the system numerically. In section 5.7, we examine how the BEC interactions affect the dynamics, while in 5.8 we investigate how the use of squeezed light enhances the sensitivity. In section 5.9 we investigate the use of an optical cavity.

5.2 Using QND Measurements to Enhance the Sensitivity of a Mach-Zehnder Interferometer.

We have already seen that atom interferometers with the Mach-Zehnder (MZ) configuration are commonly used for inertial sensing and more particularly for measuring the gravitational acceleration. In Chapter 3, we presented an elegant way, in order to describe the operations of such an interferometer, as rotations of the pseudo-spin operators, $\hat{J}_x$, $\hat{J}_y$, $\hat{J}_z$, around the Bloch sphere. Here, we will use the second quantization formalism,

in order to move from the single spin operator to the many particle case, Eq. (2.46), and describe the collective angular momentum operator

$$\hat{J}_j = \frac{1}{2} \int \hat{\boldsymbol{\psi}}^\dagger(z) \sigma_j \hat{\boldsymbol{\psi}}(z) \, dz, \tag{5.1}$$

where σ_j is the jth Pauli matrix, and

$$\hat{\boldsymbol{\psi}}(z) = \begin{bmatrix} \hat{\psi}_1(z) \\ \hat{\psi}_2(z) \end{bmatrix}, \tag{5.2}$$

where $\hat{\psi}_n(z)$ with $n = 1, 2$ are the bosonic field operators that annihilate a particle at point z from internal state $|1\rangle$ and $|2\rangle$ respectively. We have only considered the dynamics in the z direction, as this captures the important physics due to the propagation of the optical field, similarly with what we did in Chapter 2, Sec. [2.6.3]. The field operators satisfy the usual commutation relations as presented in Chapter 2, Eq. (2.50), which we present here for convenience

$$\left[\hat{\psi}_i(z), \hat{\psi}_j^\dagger(z') \right] = \delta_{i,j} \delta(z - z') \tag{5.3a}$$

$$\left[\hat{\psi}_i(z), \hat{\psi}_j(z') \right] = \left[\hat{\psi}_i^\dagger(z), \hat{\psi}_j^\dagger(z') \right] = 0. \tag{5.3b}$$

In Chapter 3, we showed that we can estimate the phase shift between the two arms of a MZ interferometer with sensitivity

$$\Delta\phi = \frac{\xi}{\sqrt{N}}, \tag{5.4}$$

where we had introduced the spin squeezing parameter, which we also present here

$$\xi = \sqrt{N} \frac{\sqrt{\mathrm{Var}(\hat{S}(\phi))}}{|\partial_\phi \langle \hat{S}(\phi) \rangle|}. \tag{5.5}$$

The spin squeezing parameter would help us to identify the cases, where we have spin-squeezing and consequently we can surpass the shot-noise limit (SNL). This is the limit that we obtain, when we use $N = N_a$ uncorrelated atoms, e.g. a coherent spin state (CSS), and we make the common measurement of a population difference at the output of the interferometer, i.e. $\hat{S}_1 = \hat{J}_z$ for $\hat{S}$. Namely, for this case we obtain $\Delta\phi = \frac{1}{\sqrt{N_a}}$, where we also considered small phase shifts $\phi \approx 0$.

The use of input states with quantum correlations such that $\xi = \xi_s < 1$ gives sensitivities better than the SNL. We should point out here that we consider a scheme, where the preparation of the entanglement-enhanced state and the interferometer sequence are two completely separate stages of the whole procedure. Essentially, we initially prepare a

spin-squeezed state, which would be used as the input state of the interferometer. This is the reason why, we will explicitly denote in the following that $\phi = 0$ in the atomic variables, which would anyway be the point of interest, since we expect that the interferometer would create a very small phase shift between the two arms.

We can create appropriate correlations by generating atom-atom entanglement, but this can also be done by creating entanglement between the atoms and some auxiliary field, such as an optical beam. By measuring both fields together, it is possible to create a signal with reduced fluctuations and therefore increased sensitivity. Specifically, by measuring the combined signal

$$\hat{S}_2 = \hat{J}_z(0) - \hat{J}_z^{\text{inf}}, \tag{5.6}$$

where $\hat{J}_z^{\text{inf}} = G\hat{S}_b$ represents an inference of the population difference, based on measurements of some optical observable $\hat{S}_b$. The constant G is a proportionality factor, which is found by minimizing the variance of the total signal $\text{Var}(\hat{S}_2)$ with respect to G

$$G = \frac{\text{Cov}\left(\hat{J}_z(0), \hat{S}_b\right)}{\text{Var}(\hat{S}_b)}, \tag{5.7}$$

which gives

$$\text{Var}(\hat{S}_2) = \text{Var}(\hat{J}_z(0)) - \frac{\text{Cov}^2(\hat{J}_z(0), \hat{S}_b)}{\text{Var}(\hat{S}_b)}. \tag{5.8}$$

Hence, creating atom-light entanglement and measuring the appropriate light observable in such a way that $\frac{\text{Cov}^2(\hat{J}_z(0), \hat{S}_b)}{\text{Var}(\hat{S}_b)} > 0$, yields a reduced signal variance $\text{Var}(\hat{S}_2) < \text{Var}(\hat{J}_z(0)) = \text{Var}(\hat{S}_1)$, increasing the sensitivity over purely measuring the population difference between the two interferometer modes. As aforementioned, we consider the case where we examine the spin squeezing parameter of the atomic ensemble, before entering the interferometer, namely Eq. (5.5) for $\phi = 0$ would give

$$\xi_{s_2} = \frac{\sqrt{N_a}\sqrt{\text{Var}(\hat{S}_2(0))}}{|\langle \hat{J}_x \rangle|}, \tag{5.9}$$

Hence, if we use an atomic state with $\xi_{s_2} < 1$, as the input state of the interferometer that would result in a performance surpassing the SNL ($\Delta\phi < 1/\sqrt{N}$). If the Hamiltonian responsible for the atom-light entanglement commutes with $\hat{J}_z(0)$, then this is an example of a QND measurement, as there is no measurement back-action on the observable being measured. In the next section, we model the atom-light interaction and quantify how the appropriate choice of $\hat{S}_b$ improves the sensitivity.

5.3 Simple Model: Single Mode Light Fields

In order to demonstrate how QND measurement squeezing affects the sensitivity, we begin with a simplified model, where we make the single mode approximation for both the atomic and optical fields. We assume an ensemble of atoms with two ground states, each interacting with a different light field, far-detuned from their corresponding excited states, as described in Fig. [5.1]. The simplified Hamiltonian for the system is
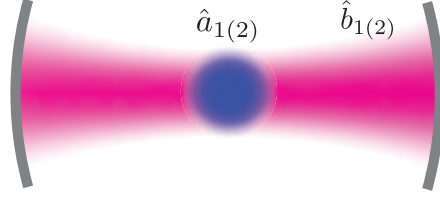

Figure 5.1: Simplified scheme showing QND entanglement via atom-light interaction. An optical mode represented by annihilation operator $\hat{b}_{1(2)}$ interacts with an ensemble of Bose-condensed atoms (annihilation operator $\hat{a}_{1(2)}$).

$$\hat{H}_{\text{int}} = -\hbar\chi_{\text{sm}}(\hat{a}_1^\dagger\hat{a}_1\hat{b}_1^\dagger\hat{b}_1 + \hat{a}_2^\dagger\hat{a}_2\hat{b}_2^\dagger\hat{b}_2), \tag{5.10}$$

where χ_{sm} indicates the interaction strength between the atoms and the light, in our simple model. Also, $\hat{a}_j = \int u_{0j}^*(z)\hat{\psi}_j(z)dz$ annihilates an atom from the ground motional state of the BEC (spatial wavefunction $u_{0j}(z)$), and $\hat{b}_j$ annihilates a photon from the optical mode interacting with atomic state $|j\rangle$, with $j = 1, 2$. The atomic and light operators satisfy $[\hat{a}_i, \hat{a}_j^\dagger] = \delta_{ij}$ and $[\hat{b}_i, \hat{b}_j^\dagger] = \delta_{ij}$ respectively. As both $\hat{a}_j^\dagger\hat{a}_j$ and $\hat{b}_j^\dagger\hat{b}_j$ commute with the Hamiltonian, the solutions to the Heisenberg equations of motion for the system are

$$\hat{a}_j(t) = \hat{a}_j(0)e^{i\chi_{\text{sm}}\hat{b}_j^\dagger(0)\hat{b}_j(0)t} \tag{5.11a}$$

$$\hat{b}_j(t) = \hat{b}_j(0)e^{i\chi_{\text{sm}}\hat{a}_j^\dagger(0)\hat{a}_j(0)t}. \tag{5.11b}$$

Examining the form of Eq. (5.11b), we see that the phase of the optical mode is correlated with the population of the corresponding atomic mode. This motivates us to examine $\hat{Y}_{b_j}$, where $\hat{Y}_{b_j} = i\left(\hat{b}_j - \hat{b}_j^\dagger\right)$ is the phase quadrature of the light field. After making the small angle approximation $\chi_{\text{sm}}t\hat{a}_j^\dagger\hat{a}_j << 1$ we find

$$\hat{Y}_j(t) \approx \hat{Y}_{j0} - \chi_{\text{sm}}\hat{a}_j^\dagger\hat{a}_j t\hat{X}_{j0}, \tag{5.12}$$

where $\hat{Y}_{j0} = i(\hat{b}_j(0)-\hat{b}_j^\dagger(0))$ and $\hat{X}_{j0} = \hat{b}_j(0)+\hat{b}_j^\dagger(0)$, and notice that $\hat{Y}_j(t) \propto \hat{N}_{a_j}$. Hence, we can make an inference about the atomic population difference, by measuring the difference

of the two phase quadratures. In order to calculate the strength of these correlations, we choose Glauber coherent states $|\alpha_j\rangle$ and $|\beta_j\rangle$, with $\text{Im}(\alpha_j) = \text{Im}(\beta_j) = 0$ as the initial state for the atomic and optical modes respectively. This corresponds to an atomic state with the expectation value of the spin aligned to the x-axis, but with a fluctuating total number. The choice of a Glauber coherent state rather than a coherent spin state was for computational convenience. It has previously been shown that for large atom number, this state provides almost identical spin-squeezing predictions [161]. As there is no physical process that couples parts of the Hilbert space corresponding to different values of the *total* atom number, whether this state is a true number superposition, or an incoherent mixture of total atom number has no observable consequence [162]. This state can be obtained by beginning with all the atoms in one state, and applying a rotation around the y-axis (i.e. and atomic beam-splitter). Setting $\hat{S}_b = \hat{Y}_2 - \hat{Y}_1$ we find

$$\text{Var}(\hat{S}_b(t)) \approx 2 + 4\chi_{\text{sm}}^2 N_{\text{ph}} N_a t^2, \tag{5.13}$$

and

$$\text{Var}(\hat{S}_2(t)) = \frac{N_a}{4}\left(1 - \frac{\chi_{\text{sm}}^2 N_a N_{\text{ph}} t^2}{\chi_{\text{sm}}^2 N_a N_{\text{ph}} t^2 + 1/2}\right), \tag{5.14}$$

where $N_{\text{ph}} = |\beta_1|^2 = |\beta_2|^2 = |\beta_0|^2$ is the expectation value of the number of photons. Using this in Eq. (5.9) we find

$$\xi_{s_2} = e^{\chi_{\text{sm}}^2 N_{\text{ph}} t^2}\left(1 - \frac{\chi_{\text{sm}}^2 N_a N_{\text{ph}} t^2}{\chi_{\text{sm}}^2 N_a N_{\text{ph}} t^2 + 1/2}\right)^{1/2}, \tag{5.15}$$

where we have used that $\langle \hat{J}_x(t)\rangle \approx \frac{N_a}{2}e^{-\chi_{\text{sm}}^2 N_{\text{ph}} t^2}$, assuming small exponents $\chi_{\text{sm}}^2 N_{\text{ph}} t^2 \ll 1$. We notice in Fig. [5.2] that we obtain better sensitivities for our signal compared to the SNL, indicating that we have created a spin squeezed state. We find the optimum value for the number of photons $N_{\text{ph}}^{\text{opt}} = \frac{1}{2\chi_{\text{sm}}^2 t^2}$, which gives the minimum value $\left(\xi_{s_2}^{\text{sm}}\right)_{\text{min}} = \sqrt{\frac{e}{N_a}}$.

This section demonstrates that this kind of atom-light interaction creates an atomic spin squeezed state and consequently boosts the interferometer's performance. In the following section, we model the system more rigorously, using the freely propagating light field and including the effects of atomic spontaneous emission.

5.4 Detailed Model Describing Atom-Light Interaction

We now consider a more detailed model that more accurately captures the relevant physics. In particular, in order to model propagating laser beams, we require a multi-mode model for the optical fields (see Fig. [5.3]). We also include spontaneous emission from
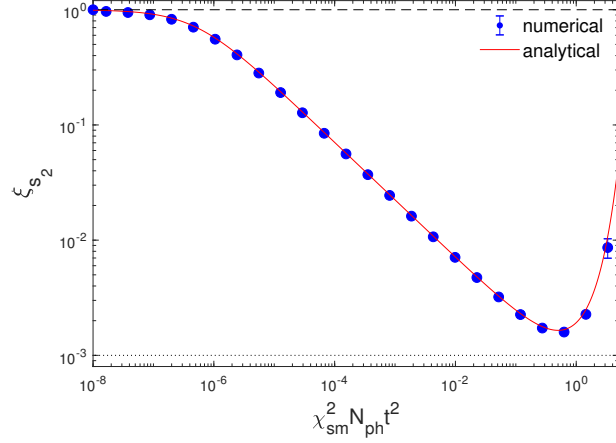
Figure 5.2: Simple model: Analytical (red line) and numerical calculation (blue dots) of ξ_{s_2}, with respect to the collective parameter $\chi^2_{\mathrm{sm}} N_{\mathrm{ph}} t^2$. The numerical calculation was implemented by using the truncated Wigner method, which we analyse in more detail in the following sections. The black dashed line and black dotted line represent the SNL and the Heisenberg limit respectively. The error bars were calculated by taking the standard deviation over many different iterations of the system dynamics.

the excited atomic states, which will limit the amount of QND measurement squeezing in practice.

5.4.1 Equations of Motion Describing Atom-Light Interaction

We assume an ensemble of Bose-condensed atoms with two electronic states $|1\rangle$ and $|2\rangle$, coupled to excited states $|3\rangle$ and $|4\rangle$ respectively, Fig. [5.4]. The coupling is achieved by far-detuned lasers, which are described by annihilation operators $\hat{b}_1(z,t)$ and $\hat{b}_2(z,t)$, satisfying the commutation relations $[\hat{b}_i(z,t), \hat{b}_j^\dagger(z',t)] = \delta_{ij}\delta(z-z')$ for $i,j = 1, 2$. We assume both optical fields have narrow linewidths compared to the natural linewidths of the atomic transitions, with central frequencies given by $\omega_{L_1} = \omega_{13} - \Delta_1$ and $\omega_{L_2} = \omega_{24} - \Delta_2$, where Δ_1 and Δ_2 are the detunings from the $|1\rangle \to |3\rangle$ and $|2\rangle \to |4\rangle$ transitions, respectively. We have examined this case of atom-light interaction in Chapter 2, Sec. [2.6.3], where we had derived the corresponding interaction Hamiltonian, Eq. (2.82). Here, we add the free
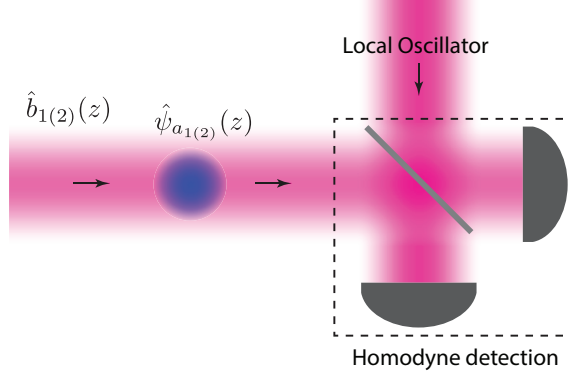
Figure 5.3: Schematic of the free-space QND measurement scheme. After interacting with the atomic ensemble, the freely propagating optical field is measured via homodyne detection. As mentioned in the text, we consider the preparation of the spin-squeezed state and the interferometric sequence as two completely separate stages. This figure depicts only the preparation stage.

atom and light Hamiltonians, as well as we adjust the notation of Eq. (2.82) appropriately

$$
\begin{aligned}
\hat{H}_{\text{tot}} = {} & \hbar \int_{-\infty}^{\infty} dz \left(\omega_{13} \hat{\psi}_3^\dagger(z,t) \hat{\psi}_3(z,t) + \omega_{24} \hat{\psi}_4^\dagger(z,t) \hat{\psi}_4(z,t) \right) \\
& - i\hbar c \int_{-\infty}^{\infty} \hat{b}_1^\dagger(z,t) \partial_z \hat{b}_1(z,t) dz - i\hbar c \int_{-\infty}^{\infty} \hat{b}_2^\dagger(z,t) \partial_z \hat{b}_2(z,t) dz \\
& + \hbar g_{13} \int_{-\infty}^{\infty} \left(\hat{\psi}_1^\dagger(z,t) \hat{\psi}_3(z,t) \hat{b}_1^\dagger(z,t) + \text{h.c} \right) dz \\
& + \hbar g_{24} \int_{-\infty}^{\infty} \left(\hat{\psi}_2^\dagger(z,t) \hat{\psi}_4(z,t) \hat{b}_2^\dagger(z,t) + \text{h.c} \right) dz \,,
\end{aligned}
\tag{5.16}
$$

where $\hat{\psi}_i(z,t)$ is the field operator, which annihilates an atom from atomic state $|i\rangle$ at position z, and $g_{13} = \frac{d_{13}}{\hbar} \left(\frac{\hbar \omega_{L_1}}{2\epsilon_0 A} \right)^{1/2}$ and $g_{24} = \frac{d_{24}}{\hbar} \left(\frac{\hbar \omega_{L_2}}{2\epsilon_0 A} \right)^{1/2}$ are the atom-light coupling constants, where $d_{13} = -e\langle 3|\hat{\mathbf{r}}|1\rangle$ and $d_{24} = -e\langle 4|\hat{\mathbf{r}}|2\rangle$ are the dipole moment matrix elements for the atomic transitions $|1\rangle \to |3\rangle$ and $|2\rangle \to |4\rangle$ respectively. A is the transverse quantization area of the light beam and c is the speed of light. For simplicity, in the following we will present the Heisenberg equations of motion just for one two-level system $\{|1\rangle \to |3\rangle,\ \hat{b}_1(z,t)\}$, since the two systems are de-coupled in the sense that the Heisenberg equations of motion for $|1\rangle \to |3\rangle$ and $|2\rangle \to |4\rangle$ are independent. The corresponding equations hold for the second two-level system $\{|2\rangle \to |4\rangle,\ \hat{b}_2(z,t)\}$ as well.

We incorporate spontaneous emission as a Langevin term in the Heisenberg equation of motion, as we analysed in Chapter 2, Sec. [2.8]. Namely we couple the atoms being in their excited state to a reservoir of vacuum electromagnetic modes, which is then traced over, described by the Hamiltonian $\hat{H}_{\text{bath}} = \hbar \int_{-\infty}^{\infty} dz \int_{-\infty}^{\infty} d\omega\, \omega\, \hat{d}^\dagger(\omega,z) \hat{d}(\omega,z)$, where $\hat{d}(\omega,z)$
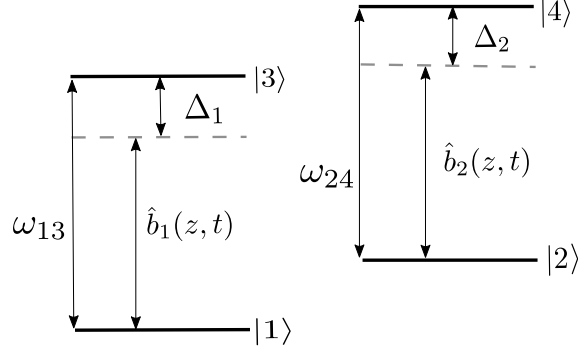
Figure 5.4: Atomic energy diagram of the two 2-level systems. Each atom is placed in a superposition of electronic states $|1\rangle$ and $|2\rangle$, with excited states $|3\rangle$ and $|4\rangle$. Two independent lasers (annihilation operator $\hat{b}_1$ and $\hat{b}_2$) are detuned from the $|1\rangle \rightarrow |3\rangle$ and $|2\rangle \rightarrow |4\rangle$ transitions by detuning Δ_1 and Δ_2, respectively.

is the continuous in space and frequency annihilation operator of the bath satisfying $[\hat{d}(\omega, z), \hat{d}^\dagger(\omega', z')] = \delta(\omega - \omega')\delta(z - z')$. Hence, using Eq. (2.103) after appropriately adjusting the notation, we obtain the equation of motion for $\hat{\psi}_3(z, t)$ in the presence of this Langevin term

$$\partial_t \hat{\psi}_3(z, t) = -\frac{i}{\hbar}\left[\hat{\psi}_3(z, t), \hat{H}_{\text{tot}}\right] - \left(\frac{\gamma_3}{2}\hat{\psi}_3(z, t) + \sqrt{\gamma_3}\hat{d}_{1_{\text{in}}}(z, t)\right) \tag{5.17}$$

$$\hat{d}_{1_{\text{in}}}(z, t) = \frac{1}{\sqrt{2\pi}}\int_{-\infty}^{\infty} d\omega e^{-i\omega(t - t_0)}\hat{d}_0(\omega, z), \tag{5.18}$$

where γ_3 is the spontaneous emission rate from the excited state and $\hat{d}_{1_{\text{in}}}(z, t)$ is the standard Langevin noise term depending on the value of the bath operator at the initial time point t_0, $\hat{d}(\omega, z, t = t_0) = \hat{d}_0(\omega, z)$. After moving to a rotating reference frame, with respect to the central frequency of the light field, ω_{L_1}, we adiabatically eliminate the excited state field operator $\hat{\psi}_3$, [163]. Thus, the Heisenberg equations of motion for $\hat{\psi}_1(z, t)$ and $\hat{b}_1(z, t)$ are

$$\partial_t \hat{\psi}_1(z, t) = ig_{13}^2 \frac{\Delta_1 + i\frac{\gamma_3}{2}}{\Delta_1^2 + \frac{\gamma_3^2}{4}}\hat{b}_1^\dagger(z, t)\hat{b}_1(z, t)\hat{\psi}_1(z, t) + g_{13}\frac{\sqrt{\gamma_3}}{\Delta_1 - i\frac{\gamma_3}{2}}\hat{b}_1^\dagger(z, t)\hat{d}_{1_{\text{in}}}(z, t) \tag{5.19a}$$

$$\left(\frac{1}{c}\partial_t + \partial_z\right)\hat{b}_1(z, t) = i\frac{g_{13}^2}{c}\frac{\Delta_1 + i\frac{\gamma_3}{2}}{\Delta_1^2 + \frac{\gamma_3^2}{4}}\hat{\psi}_1^\dagger(z, t)\hat{\psi}_1(z, t)\hat{b}_1(z, t) + \frac{g_{13}}{c}\frac{\sqrt{\gamma_3}}{\Delta_1 - i\frac{\gamma_3}{2}}\hat{\psi}_1^\dagger(z, t)\hat{d}_{1_{\text{in}}}(z, t). \tag{5.19b}$$

We solve the equation for the light field by making the substitution $z \rightarrow z + ct$. As the timescale for the atomic dynamics is much slower than the timescale for the light to cross the atomic sample, we make the approximation that the light moves between two

arbitrary points z_B to z_C instantaneously, i.e $\hat{b}^\dagger(z_B, t)\hat{b}(z_B, t) = \hat{b}^\dagger(z_C, t)\hat{b}(z_C, t)$, as long as there is no atom-light interaction in $[z_B, z_C]$. In addition, as our system is a Bose-Einstein condensate, we assume that all the atoms are in the ground motional state of the trap, which allows us to make the single mode approximation $\hat{\psi}_1(z, t) = u_{01}(z)\hat{a}_1(t)$. Assuming $\int_{z_L}^{z_R} |u_{01}(z)|^2 dz \approx 1$ for points z_L and z_R sufficiently far to the left and right of the atomic sample respectively, we can write

$$\hat{b}_1(z_R, t) = \hat{b}_{01}(t)e^{i\frac{g_{13}^2}{c}(\Omega + i\Gamma)\hat{a}_1^\dagger(t)\hat{a}_1(t)} + \frac{g_{13}}{c}\frac{\sqrt{\gamma_3}}{\Delta_1 - i\gamma_3/2}\hat{a}_1^\dagger(t)\hat{q}_{1\text{in}}(t), \qquad (5.20)$$

where we have considered the same motional function for the Langevin noise $\hat{d}_{1\text{in}}(z, t) = u_{01}(z)\hat{q}_{1\text{in}}(t)$. We have also defined $\hat{b}_{01}(t) = \hat{b}_1(z_L, t)$, and $\Omega \equiv \frac{\Delta_1}{\Delta_1^2 + \gamma_3^2/4}$, $\Gamma_3 \equiv \frac{\gamma_3/2}{\Delta_1^2 + \gamma_3^2/4}$ for notation simplicity. In order to find a simpler form for the atomic equation, Eq. (5.19a), we make the approximation that $\hat{b}_1^\dagger(z, t)\hat{b}_1(z, t) \approx \hat{b}_1^\dagger(z_L, t)\hat{b}_1(z_L, t)$, i.e. to a good approximation the number of photons in the mode does not change. Hence, after making the single mode approximation again we obtain

$$\partial_t \hat{a}_1(t) = ig_{13}^2 (\Omega + i\Gamma) \hat{b}_{01}^\dagger(t)\hat{b}_{01}(t)\hat{a}_1(t) + g_{13}\frac{\sqrt{\gamma_3}}{\Delta_1 - i\frac{\gamma_3}{2}}\hat{b}_{01}^\dagger(t)\hat{q}_{1\text{in}}(t). \qquad (5.21)$$

5.4.2 Measurement of the Optical Observables

As in Sec. [5.3], we notice that Eq. (5.20) indicates correlations between the atomic number and the phase of the light. We can define the phase quadrature for our multi-mode light field by selecting one specific mode. Specifically, we define $\hat{Y}_{\mathfrak{b}_1} = i\left(\hat{\mathfrak{b}}_1 - \hat{\mathfrak{b}}_1^\dagger\right)$ where

$$\hat{\mathfrak{b}}_1 = \int_0^\tau u_{\text{LO}}^*(t)\hat{b}_1(z_D, t)dt \qquad (5.22)$$

where z_D is the position of the photo-detector. Also, $u_{\text{LO}}(t)$ corresponds to the temporal mode shape of the local oscillator used in the homodyne detection [164], satisfying

$$\int_0^\tau |u_{\text{LO}}(t)|^2 dt = c \qquad (5.23)$$

which ensures $[\hat{\mathfrak{b}}_1, \hat{\mathfrak{b}}_1^\dagger] = 1$ and consequently $[\hat{X}_{\mathfrak{b}_1}, \hat{Y}_{\mathfrak{b}_1}] = -2i$, where $\hat{X}_{\mathfrak{b}_1} = \hat{\mathfrak{b}}_1 + \hat{\mathfrak{b}}_1^\dagger$ is the corresponding amplitude quadrature of $\hat{\mathfrak{b}}_1$. The most appropriate choice of local oscillator for this scheme is one with constant intensity with the frequency matched to the carrier frequency of our optical field, i.e.

$$u_{\text{LO}}(t) = \sqrt{\frac{c}{\tau}}, \qquad (5.24)$$

where we have transformed to the same rotating frame as Eq. (5.19b).

5.5 Approximate Analytic Solutions

We can obtain an analytical estimate of the squeezing parameter, ξ_{s_2}, after making some approximations. Here, we briefly present the basic intermediate steps we made in order to find out ξ_{s_2}, with and without spontaneous emission. A much more detailed presentation of these calculations can be found in the Appendices[B.1 - B.3.4]. For simplicity, we assume that the atom-light interaction strengths as well as the detunings are the same for the two atomic transitions, i.e $g_{13} = g_{24} = g$ and $\Delta_1 = \Delta_2 = \Delta$ respectively. We also consider that initially the atoms and the light fields are in coherent states with the same amplitudes for the two atomic levels $\hat{a}_{1(2)}(0)|\alpha_{1(2)}\rangle = \sqrt{\frac{N_a}{2}}|\alpha_{1(2)}\rangle$ and for the light fields $\hat{b}_{01}(t)|\beta_1\rangle = \beta_0|\beta_1\rangle$, $\hat{b}_{02}(t)|\beta_2\rangle = \beta_0|\beta_2\rangle$, where we also assume that $\beta_0 = \beta_0^*$.

5.5.1 No Spontaneous Emission

Ignoring the effect of spontaneous emission (i.e. $\gamma_3 = 0$), vastly simplifies the problem and allows easy comparison with the simple single-mode model of Sec. [5.3]. In this case, the calculation of the atomic expectation values we are interested in is quite straightforward

$$\langle \hat{N}_{a_1}(t)\rangle = \frac{N_a}{2}, \qquad \langle \hat{N}_{a_1}^2(t)\rangle = \frac{N_a}{2}\left(1 + \frac{N_a}{2}\right). \tag{5.25}$$

We can also find the phase quadrature operator by making the small angle approximation $\frac{g^2}{c\Delta}\hat{a}_1^\dagger(t)\hat{a}_1(t) << 1$

$$\hat{Y}_1(\tau) \approx \hat{Y}_{1_{\text{in}}}(\tau) - \frac{g^2}{\sqrt{c\tau}\Delta}\hat{a}_1^\dagger(\tau)\hat{a}_1(\tau)\int_0^\tau \left(\hat{b}_{01}(t) + \hat{b}_{01}^\dagger(t)\right)dt, \tag{5.26}$$

where $\hat{Y}_{1_{\text{in}}}(\tau) = i\frac{\sqrt{c}}{\sqrt{\tau}}\int_0^\tau \left(\hat{b}_{01}(t) - \hat{b}_{01}^\dagger(t)\right)dt$. Here, we clearly notice that $\hat{Y}_1 \propto \hat{N}_{a_1}$. That supports our choice for the light signal to be $\hat{J}_z^{\text{inf}} \propto \hat{S}_b = \hat{Y}_2 - \hat{Y}_1$. Now, using Eq. (5.25) and (5.26) we can calculate

$$\text{Var}(\hat{S}_b) \approx 2\text{Var}(\hat{Y}_1(\tau)) \approx 2 + 4\chi_{\text{ns}}^2 N_a N_{\text{ph}} \tag{5.27}$$

$$\text{Cov}(\hat{J}_z(\tau), \hat{S}_b(\tau)) = \text{Cov}(\hat{S}_b(\tau), \hat{J}_z(\tau)) \approx \chi_{\text{ns}} N_a \sqrt{N_{\text{ph}}} \tag{5.28}$$

$$\text{Var}(\hat{S}_2(\tau)) \approx \frac{N_a}{4}\left(1 - \frac{\chi_{\text{ns}}^2 N_{\text{ph}} N_a}{\chi_{\text{ns}}^2 N_{\text{ph}} N_a + 1/2}\right), \tag{5.29}$$

where here $N_{\text{ph}} = \beta_0^2\tau$. Also, we have defined $\chi_{\text{ns}} \equiv \frac{g^2}{c\Delta}$, where the subscript denotes no spontaneous emission. We finally find the quantum enhancement parameter

$$\xi_{s_2}^{\text{ns}}(\tau) \approx e^{\chi_{\text{ns}}^2 N_{\text{ph}}}\left(1 - \frac{\chi_{\text{ns}}^2 N_{\text{ph}} N_a}{\chi_{\text{ns}}^2 N_{\text{ph}} N_a + 1/2}\right)^{1/2}, \tag{5.30}$$

where we used that $\langle \hat{J}_x(t) \rangle \approx \frac{N_a}{2} e^{-\chi_{\rm ns}^2 N_{\rm ph}}$ for $\chi_{\rm ns}^2 N_{\rm ph} << 1$. By inspection of Eq. (5.30), we see that the parameters that affect the sensitivity of our signal are the total number of photons $N_{\rm ph}$, the quantization area of the light field A (through g), the detuning Δ, and the total number of atoms N_a. We also notice that we can always increase the sensitivity of our signal by just increasing $\chi_{\rm ns} N_{\rm ph} N_a$ up to a point that the increase of $e^{\chi_{\rm ns}^2 N_{\rm ph}}$ becomes dominant. This is essentially the point that $\langle \hat{J}_x \rangle$ (denominator of Eq. (5.9)) has decreased so much that the sensitivity starts decaying. Following that strategy, we can always achieve better sensitivity than the SNL, as seen in Fig.[5.5]. Here, we find the minimum of $\xi_{s_2}^{\rm ns}$ by taking the derivative with respect to the collective parameter $\nu = \chi_{\rm ns}^2 N_{\rm ph}$:

$$(\xi_{s_2}^{\rm ns})_{\rm min} = \sqrt{\frac{e}{N_a}} \,. \tag{5.31}$$

We see that the minimum depends on the inverse of the number of atoms, while the optimum number of photons for which we take that minimum is

$$N_{\rm ph}^{\rm opt} = \frac{1}{2\chi_{\rm ns}^2} \,. \tag{5.32}$$

5.5.2 Spontaneous Emission

With the inclusion of spontaneous emission ($\gamma_3 > 0$), the calculation of the atomic expectation values is much more complicated. We begin by ignoring the effect that quantum fluctuation in the optical field has on the spontaneous emission. That is

$$e^{-g^2 \Gamma \int_0^t \hat{b}^\dagger(z,t') \hat{b}(z,t') dt'} \approx e^{-g^2 \Gamma \beta_0^2 t} \tag{5.33}$$

such that

$$\langle \hat{N}_{a_1}(t) \rangle \approx \frac{N_a}{2} \epsilon(t), \tag{5.34}$$

where $\epsilon(t) \equiv e^{-2g^2 \Gamma \beta_0^2 t}$ indicates how fast we lose atoms from our system. Following the same strategy as before, we find

$$\mathrm{Var}(\hat{S}_b(\tau)) \approx 2 + 4\chi_1^2 N_{\rm ph} N_a \overline{\epsilon(\tau)} \tag{5.35}$$

$$\mathrm{Cov}(\hat{J}_z(\tau), \hat{S}_b(\tau)) = \mathrm{Cov}(\hat{S}_b(\tau), \hat{J}_z(\tau)) \approx \chi_1 \sqrt{N_{\rm ph}} N_a \epsilon(\tau) \tag{5.36}$$

$$\mathrm{Var}(\hat{S}_2(\tau)) \approx \frac{N_a}{4} \epsilon(\tau) \left(1 - \frac{\chi_1^2 N_{\rm ph} N_a \epsilon(\tau)}{\chi_1^2 N_{\rm ph} N_a \overline{\epsilon(\tau)} + 1/2} \right), \tag{5.37}$$

where we have defined $\chi_1 \equiv \frac{g^2 \Omega}{c}$ and $\overline{\epsilon(\tau)} = \frac{1}{\tau} \int_0^\tau \epsilon(t) dt$, which is the time average of the decay. Note that $\chi_1 = \chi_{\rm ns}$ in the no spontaneous emission case ($\gamma_3 = 0$). By comparing
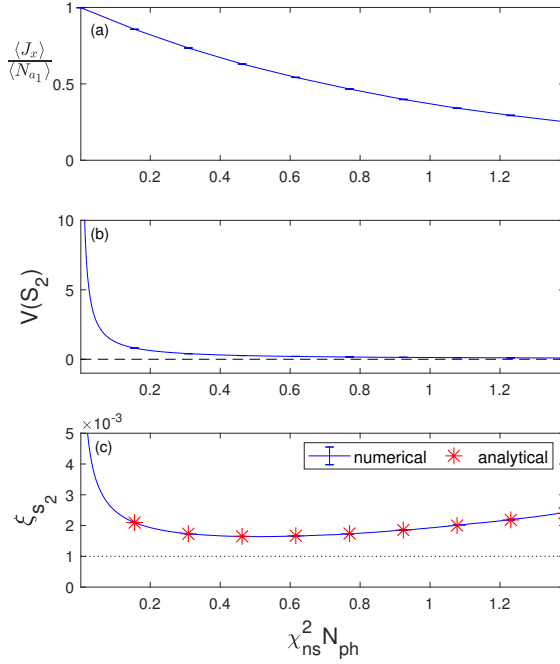
Figure 5.5: (a) $\langle \hat{J}_x \rangle / \langle \hat{N}_{a_1} \rangle$ (b) $\text{Var}(\hat{S}_2)$ and (c) ξ_{s_2} with respect to the collective parameter $\nu = \chi_{ns}^2 N_{ph}$. (a): The decay is due to over-squeezing the state, since we do not consider spontaneous emission here. This causes the squeezing parameter to reach a minimum value (c). The black dashed line in (b), points to zero, just to reassure the $\text{Var}(S_2)$ is always positive. In (c) the black dotted line represents the Heisenberg limit. The parameter values are $A = 10^{-10}\,\text{m}^2$, $\Delta = 10^2\,\text{GHz}$, $N_a = 10^6$. The error bars are barely distinguishable for all lines.

Eq. (5.29) with (5.37) we realise that, except than the apparent effect of particle loss that the atomic spontaneous emission has on the dynamics of the system, there is an additional effect on the variance of the signal, caused by the emergence of the time averaged decay rate in the denominator of Eq. (5.37), which cannot be reproduced from Eq. (5.29), by simply making the substitution $N_a \to N_a \epsilon(t)$. Using that $\langle \hat{J}_x(t) \rangle \approx \frac{N_a}{2} e^{-(\chi_1^2 + 2\chi_2) N_{ph}}$ for $(\chi_1^2 + 2\chi_2) N_{ph} << 1$, the spin-squeezing parameter is

$$\xi_{s_2} \approx e^{(\chi_1^2 + \chi_2) N_{ph}} \left(1 - \frac{\chi_1^2 N_{ph} N_a \epsilon(\tau)}{\chi_1^2 N_{ph} N_a \overline{\epsilon(\tau)} + 1/2} \right)^{1/2}, \qquad (5.38)$$

where we have defined $\chi_2 \equiv \frac{g^2 \Gamma}{c}$ and now the decay factor can be expressed as $\epsilon(\tau) = e^{-2\chi_2 N_{ph}}$. We can also find for the time average of the decay factor that $\overline{\epsilon(\tau)} = \frac{1 - \epsilon(\tau)}{2\chi_2 N_{ph}}$.

By inspecting Eq. (5.38) it is clear that the case with spontaneous emission is more complicated. We notice again that we can increase the sensitivity by increasing the term

$\chi_1^2 N_{ph} N_a \propto \frac{N_{ph} N_a}{A^2 \Delta^2}$ (for $\Delta >> \gamma_3$), but now we are restricted by the atomic loss rate $\epsilon = \exp\{(-2\chi_2 N_{ph})\} \propto \exp\left\{\left(\frac{N_{ph}}{A\Delta^2}\right)\right\}$ (for $\Delta >> \gamma_3$). Hence, we have to find the appropriate parameter regime that balances between spin squeezing and atomic loss.
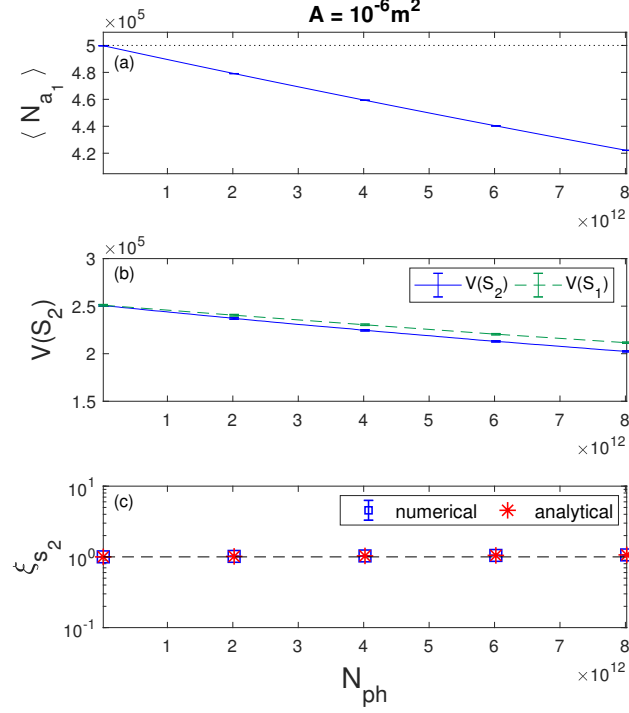

Figure 5.6: (a) $\langle N_{a_1} \rangle$, (b) $\mathrm{Var}(S_1)$ (green dashed line) and $\mathrm{Var}(S_2)$ (blue solid line) (c) ξ_{s_2} numerical (blue squares) and analytical (red asterisks) with respect to number of photons. In (a) the black dotted line shows the initial atomic population, while the black dashed line in (c) represents the SNL. The parameter values are $A = 10^{-6}\,\mathrm{m}^2$, $\Delta = 10^2\,\mathrm{GHz}$, $N_a = 10^6$.

We present simulations of our analytical results for ξ_{s_2}, Fig. [5.6(c)]-[5.8(c)], for three different quantization area values, $A = \left(10^{-3}\,\mathrm{m}\right)^2$, $A = \left(10^{-4}\,\mathrm{m}\right)^2$ and $A = \left(10^{-5}\,\mathrm{m}\right)^2$. For each different area value, we essentially change the number of photons and detuning appropriately in order to obtain best sensitivities . For $A = \left(10^{-3}\,\mathrm{m}\right)^2$ we notice that we never obtain enhanced sensitivity (compared to SNL), since the loss of atoms exceeds the resulting squeezing, Fig.[5.6(c)]. As we decrease A, the atom-light interaction strengthens, increasing the sensitivity of our signal Fig.[5.7, 5.8].

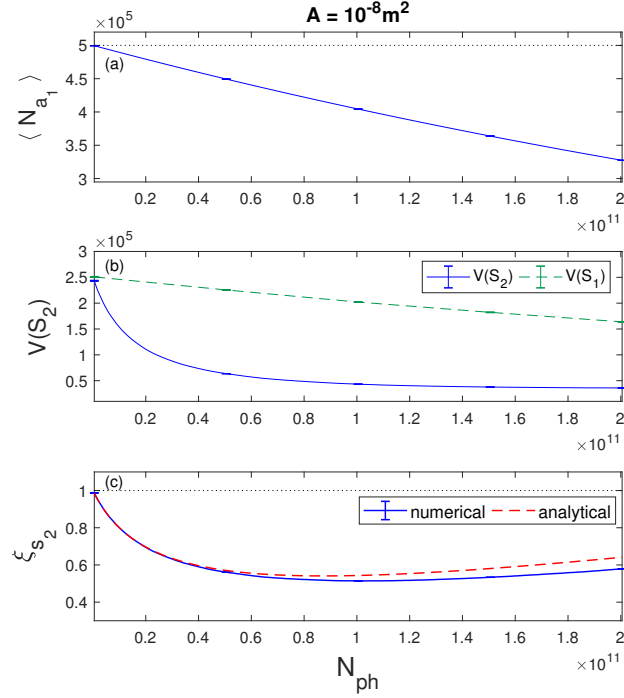In order to find the minimum of ξ_{s_2}, we express Eq. (5.38) in terms of the dimensionless

Figure 5.7: (a) $\langle N_{a_1} \rangle$, (b) $\text{Var}(S_1)$ (green dashed line) and $\text{Var}(S_2)$ (blue solid line) (c) ξ_{s_2} numerical (blue solid line) and analytical (red dashed line) with respect to number of photons. In (a) the black dotted line shows the initial atomic population, while the black dashed line in (c) represents the SNL. The parameter values are $A = 10^{-8}\,\text{m}^2$, $\Delta = 10^2\text{GHz}$, $N_a = 10^6$.

parameters $\mu \equiv \frac{\chi_1^2}{\chi_2} = \frac{g^2 \Omega^2}{c\Gamma}$, $\lambda \equiv \chi_2 N_{\text{ph}}$ and $\zeta \equiv N_a \mu$. Hence, we can now write ξ_{s_2} as

$$\xi_{s_2} = e^{\lambda(1+\mu)} \left(1 - \frac{\zeta \epsilon(\tau)}{\zeta - \zeta \epsilon(\tau) + 1} \right)^{1/2}, \tag{5.39}$$

where the decay can now be expressed as $\epsilon(\tau) = e^{-2\lambda}$. We work in a parameter regime where $\mu << 1$, such that

$$\xi_{s_2} \approx e^{\lambda} \left(1 - \frac{2\zeta \lambda e^{-2\lambda}}{1 + \zeta - \zeta e^{-2\lambda}} \right)^{1/2}. \tag{5.40}$$

In order to simplify things further, we consider the case where $\Delta >> \gamma_e$. In that case $\Omega \to \frac{1}{\Delta}$ and $\Gamma \to \frac{\gamma_3}{2\Delta^2}$, thus $\mu \to \frac{2g^2}{c\gamma_3}$. That means that μ only depends on the atomic properties and the quantization area of the light A (through g) and consequently $\zeta \to \frac{2g^2}{c\gamma_3} N_a$. On the other hand $\lambda \to \frac{g^2 \gamma_3}{2c} \frac{N_{\text{ph}}}{\Delta^2}$ for $\Delta >> \gamma_3$. Hence, if we fix the value of ζ, by choosing a specific value for the number of atoms N_a and the area A, we only need to optimize ξ_{s_2} with respect to λ which is proportional to N_{ph}/Δ^2 in the regime $\Delta >> \gamma_3$. In Fig. [5.9], we followed that procedure for several different values of ζ
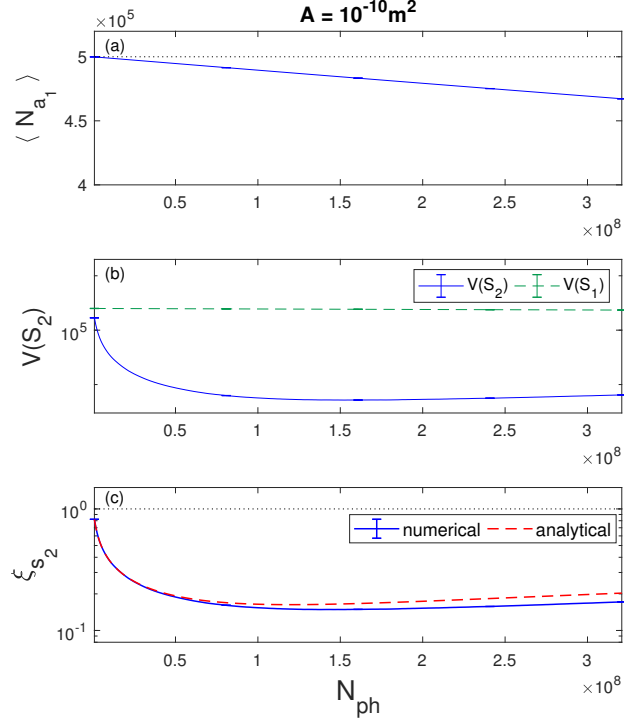
Figure 5.8: (a) $\langle N_{a_1} \rangle$, (b) $\text{Var}(S_1)$ (green dashed line) and $\text{Var}(S_2)$ (blue solid line) (c) ξ_{s_2} numerical (blue solid line) and analytical (red dashed line) with respect to number of photons. In (a) the black dotted line shows the initial atomic population, while the black dashed line in (c) represents the SNL. The parameter values are $A = 10^{-10}\,\text{m}^2$, $\Delta = 10^2\,\text{GHz}$, $N_a = 10^6$.

and found the minimum of ξ_{s_2} with respect to λ using Eq. (5.40). We notice that the sensitivity increases as we increase ζ, which means either increasing N_a or decreasing the area. Just to clarify here that by decreasing the area we also increase the atomic loss rate, which leads to loss of sensitivity. In that case we should also change the other parameters (N_{ph}/Δ^2) appropriately, in order to counteract that effect, resulting at the end in better sensitivities. On the other hand, the increase of N_a does not affect the loss rate of atoms and it solely improves the sensitivity. We should mention here that there are similar analytical calculations available in the literature [165, 166], but they are limited in the small atomic loss and Gaussian state regime, while our calculations go beyond these assumptions. In the following, we are going to present analytical and numerical results in the case of a phase squeezed light field, as well as numerical calculations including interactions amongst the atoms and the introduction of a cavity, which to our knowledge have not been examined before.
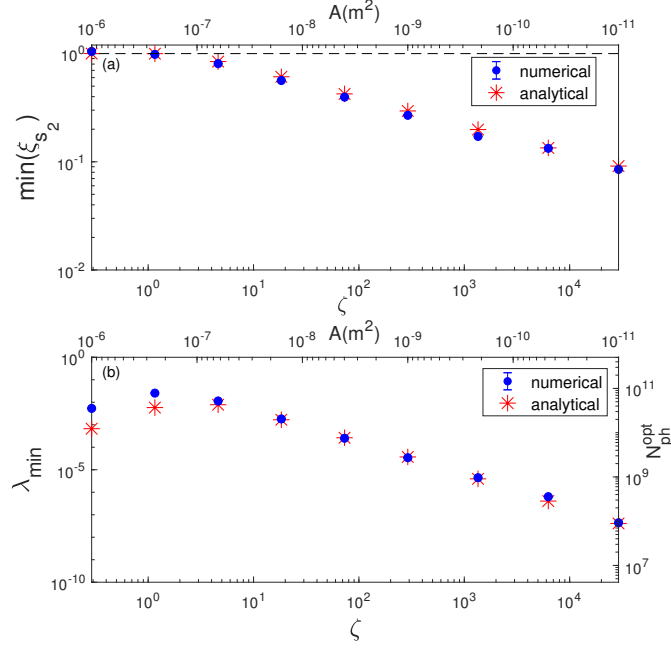
Figure 5.9: (a) Minimum value of ξ_{s_2} with respect to ζ (bottom x-axis) and A (top horizontal-axis), (b) optimum λ (left vertical-axis) and optimum number of photons $N_{\mathrm{ph}}^{\mathrm{opt}}$ (right y-axis) with respect to ζ. In (a) the black dashed line represents the SNL.

5.6 Numerical Solutions

We can solve for the dynamics of the system numerically by using the truncated Wigner (TW) method [75]. The reader can find a detailed discussion about TW method in Appendix [C]. From the Heisenberg equations of motion we can move to Fokker-Plank equations (FPEs), by using correspondences between quantum operators and Wigner variables. After truncating third and higher order terms we can map the FPEs into stochastic differential equations (SDE), which can be solved numerically with respect to the Wigner variables. We make the following correspondences $\hat{a}_1(t) \to \alpha_1(t)$, $\hat{b}_1(z,t) \to \beta_1(z,t)$ and $\hat{q}_{1_{in}}(t) \to \mathfrak{q}_{in}(t)$. We also consider the initial conditions $\alpha_1(0) = \alpha_{10} + \eta_1$, $\beta_{01}(t) = \beta_0 + w_{b_1}(t)$ and $\mathfrak{q}_{in}(t) = w_{q_1}(t)$. η_1 is complex Gaussian noise satisfying $\overline{\eta_1} = 0$ and $\overline{\eta_1^* \eta_1} = \frac{1}{2}$, $w_x(t)$ is a complex Wiener noise satisfying $\overline{w_x(t)} = 0$ where $x = b_1, q_1$. Also, $\overline{w_{b_1}(t)w_{b_1}(t')} = \frac{1}{2c}\delta(t-t')$ and $\overline{w_{q_1}(t)w_{q_1}(t')} = \frac{1}{2}\delta(t-t')$, where the bar represents averaging with respect to a large number of stochastic trajectories.

We consider the D2 transition line of ^{87}Rb $(5^2S_{1/2} \to 5^2P_{3/2})$ for both atomic transitions, where the transition frequency is $\omega_{13} = \omega_{24} = \omega_a = 2\pi c/\lambda$ and $\lambda = 780\,\mathrm{nm}$. The spontaneous emission rate of the excited state is $\gamma_3 = \gamma_4 = 38.11\,\mathrm{MHz}$ [167].

More particularly, we numerically examine the SDEs coming from Eq. (5.20) and (5.21) for the light and the atoms respectively. For the atomic ensemble of each two level system we consider a single mode field, while for the two light fields we make multi-mode simulations. Our numerical calculations give us the ability to examine the true dynamics of the system, namely we consider the atomic spontaneous emission taking place during the unitary dynamics, which generates the spin squeezing. Most importantly, our numerical method enable us to introduce new features in our system, considering the particle interactions of the two BECs Sec. [5.7], as well as examine the cavity case Sec. [5.9] and explore how they affect the final sensitivity, by numerically examining the new more complicated dynamics. In Fig. [5.6]-[5.9], we present the numerical simulations corresponding to the analytical results analysed in the previous section. We notice that our analytical and numerical results have almost perfect agreement, indicating that the approximations we made through the derivations do not have any significant effect in the final results.

5.7 BEC Interactions

So far the formalism we have developed could be applied equivalently to both BECs and cold thermal atoms homogeneously coupled to the light field, since essentially the only assumption we have made is that we work under the simple mode approximation for the atomic ensembles of the two 2-level systems. In this section, we examine how interactions amongst the particles of two BECs could affect the dynamics of the QND measurement scheme and how that could change the results we have already presented. We consider that these interactions are described by a Hamiltonian of the same form with the second term of the BEC Hamiltonian we presented in Chapter 2, Eq. (2.56). However, here we have two different BECs, described by $\hat{\psi}_1(\boldsymbol{r})$ and $\hat{\psi}_2(\boldsymbol{r})$ corresponding to the ground states of each two level system, i.e.

$$\hat{H}_{\mathrm{bec}}^{\mathrm{int}} = \sum_{i,j=1,2} \frac{U_{ij}}{2} \int_{-\infty}^{\infty} \hat{\psi}_i^\dagger(\boldsymbol{r}) \hat{\psi}_j^\dagger(\boldsymbol{r}) \hat{\psi}_i(\boldsymbol{r}) \hat{\psi}_j(\boldsymbol{r}) \, dz, \tag{5.41}$$

where $U_{ij} = \frac{4\pi\hbar^2}{m} a_{ij}$ is the non-linear interaction potential and a_{ij} is the s-wave scattering length between $|i\rangle$ and $|j\rangle$, with $i, j = 1, 2$. In the previous sections we worked under the assumption that the light field propagates only along the z-axis and hence we could analyse the dynamics of the atom-light interactions in the 1-D case. However, here that we focus on the interactions amongst the atoms of the two BECs, we develop a 3-D analysis, since we consider that each atomic ensemble forms a sphere of radius r_{BEC}. We make the

single mode approximation for both BECs, as we did previously

$$\hat{\psi}_1(z,t) = u_{01}(\boldsymbol{r})\hat{a}_1(t), \qquad \hat{\psi}_2(z,t) = u_{02}(\boldsymbol{r})\hat{a}_2(t). \tag{5.42}$$

Substituting that back in Eq. (5.41) we obtain

$$\hat{H}_{\text{bec}}^{\text{int}} = \hbar\chi_{11}\hat{a}_1^\dagger(t)\hat{a}_1^\dagger(t)\hat{a}_1(t)\hat{a}_1(t) + \hbar\chi_{22}\hat{a}_2^\dagger(t)\hat{a}_2^\dagger(t)\hat{a}_2(t)\hat{a}_2(t) + 2\hbar\chi_{12}\hat{a}_1^\dagger(t)\hat{a}_1(t)\hat{a}_2^\dagger(t)\hat{a}_2(t), \tag{5.43}$$

where we defined

$$\chi_{ij} = \frac{U_{ij}}{2\hbar}\int_{-\infty}^{\infty}|u_{0i}(\boldsymbol{r})|^2|u_{0j}(\boldsymbol{r})|^2\,d^3\boldsymbol{r}. \tag{5.44}$$

Alternatively we can use the number density of atoms in order to write

$$\int_{-\infty}^{\infty}|u_{0i}(\boldsymbol{r})|^2|u_{0j}(\boldsymbol{r})|^2\,d^3\boldsymbol{r} = \frac{1}{N_iN_j}\int_{-\infty}^{\infty}n_i(\boldsymbol{r})n_j(\boldsymbol{r})\,d^3\boldsymbol{r}. \tag{5.45}$$

Assuming constant number density we finally find

$$\chi_{11} = \frac{2\pi\hbar}{mV}a_{11} \qquad \chi_{22} = \frac{2\pi\hbar}{mV}a_{22}, \tag{5.46}$$

which represents the strength of the intra-particle interactions in each BEC. If we consider that there are no inter-particle interactions, namely the two BECs are separate, then $\chi_{12} = 0$, while if we assume that they are perfectly overlapping then $\chi_{12} = \frac{2\pi\hbar}{mV}a_{12}$. The Hamiltonian in Eq. (5.43) would add the following terms in the atomic equations of motion for the two 2-level systems

$$\partial_t\hat{a}_1(t) = -2i\left(\chi_{11}\hat{a}_1^\dagger(t)\hat{a}_1(t) + \chi_{12}\hat{a}_2^\dagger(t)\hat{a}_2(t)\right)\hat{a}_1(t) \tag{5.47}$$

$$\partial_t\hat{a}_2(t) = -2i\left(\chi_{22}\hat{a}_2^\dagger(t)\hat{a}_2(t) + \chi_{12}\hat{a}_1^\dagger(t)\hat{a}_1(t)\right)\hat{a}_2(t). \tag{5.48}$$

Hence, now we can numerically examine the full dynamics of the system, with the BEC interactions incorporated, using again the TW method. We can essentially do that by transforming the above operator equations of motion into a FPE and map the result to a SDE, as we did earlier. We add the resulting terms in the SDEs of the previous sections, in order to examine the full dynamics. In our simulations we considered the same scattering lengths as in [120, 168], namely $a_{11} = 100.4\,a_0$, $a_{22} = 95.00\,a_0$ and $a_{12} = 97.66\,a_0$, where a_0 is the Bohr radius. We also assumed that the area of the atomic ensemble should be smaller or equal than the transverse area of the light field. In our numerical calculations we used $A_{\text{BEC}} = 10^{-11}\text{m}^2$, corresponding to a radius $r_{\text{BEC}} = 2\mu\text{m}$ for the BEC.

In the previous sections, where we had not yet added the BEC interactions, we noticed that for fixed values of the area (A), the detuning (Δ) and the number of atoms (N_a), we

can find the minimum of the squeezing parameter, by adjusting the number of photons. That means that the change of the total time of interaction was equivalent with the change of the light intensity. However, now that we consider interactions amongst the atoms, the time would play a more crucial role in the dynamics, since after some time the atom interactions would become significant resulting in decrease of the final sensitivity. This is shown in Fig. [5.10(a)], where we notice that considering intra-particle interactions in two separate BECs degrades the sensitivity, while the case of two overlapping BECs perfectly coincides with the no interaction case, since the total interaction strength amongst the atoms is smaller compared to the two separate BECs case. As aforementioned, the number of photons interacting with the atomic ensemble, is what really matters, since it determines the level of squeezing we obtain in the QND measurement scheme. Hence, we can easily find an appropriate regime, in order to avoid the deleterious effects of atom interactions to the final sensitivity, by increasing the light intensity and appropriately decreasing the total interaction time. In that way, we consider the same number of photons, offering the same level of spin squeezing, while everything happens faster, which means that there is not enough time for the atom interactions to damage the final sensitivity, as shown in Fig. [5.10(b)].

5.8 Squeezed Light

Up to this point we have only considered classical light sources. That is, we have assumed that the incoming light is in a Glauber coherent state, with $\text{Var}(\hat{Y}_{1_{\text{in}}}) = 1$. It is possible to increase the sensitivity of our final signal, by considering a squeezed incoming light, where $\text{Var}(\hat{Y}_{1_{\text{in}}})_{\text{sq}} = e^{-2r}$ and r is the squeeze factor [164]. In that case our analytical calculation for the spontaneous emission case results in

$$\text{Var}(\hat{S}_b)_{\text{sq}} \approx 2\text{Var}(\hat{Y}_1(\tau))_{\text{sq}} \approx 2e^{-2r} + 4\chi_{\text{ns}}^2 N_a N_{\text{ph}}, \tag{5.49}$$

while the covariances remain the same. Hence, the squeezing parameter becomes

$$\xi_{s_2} \approx e^{(\chi_1^2 + \chi_2)N_{\text{ph}}} \left(1 - \frac{\chi_1^2 N_{\text{ph}} N_a \epsilon(\tau)}{\chi_1^2 N_{\text{ph}} N_a \overline{\epsilon(\tau)} + e^{-2r}/2} \right)^{1/2}. \tag{5.50}$$

In Fig. [5.11] we notice that we obtain better sensitivity for all three area values compared to the coherent incident light (Fig. [5.6(c)]-5.8(c)]). In Fig. [5.12] we show the numerical and analytical $\min(\xi_{s_2})$ for the three different area values, with respect to the
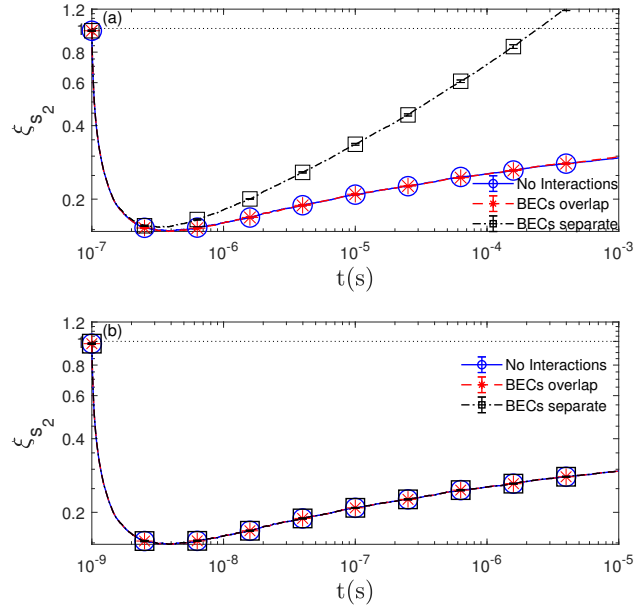
Figure 5.10: ξ_{s_2} with respect to time considering three different cases, (i) no atom interactions (blue solid line with open circles), (ii) atom interactions where the two BECs perfectly overlap (red dashed line with asterisks) and (iii) atom interactions, where the two BECs are separate (black dash-dotted line with squares). In (a) we consider smaller light intensity and larger total interaction time compared to (b), i.e. in (a) we have $\beta_0^2 = 10^{12}$ photons/s and $\tau = 1$ms, while in (b) $\beta_0^2 = 10^{14}$ photons/s and $\tau = 0.01$ms. The other parameter values are: $N_a = 10^6$, $\Delta = 10^{11}$, $A = 10^{-10}$m^2, $A_{\mathrm{BEC}} = 10^{-11}$m^2. The black dotted lines denote the SNL.

degree of optical squeezing in the incoming light, $\mathcal{S}$, defined by

$$\mathcal{S} = 10\log\left(\frac{\sqrt{\mathrm{Var}(\tilde{Y}_{b_1})}}{\sqrt{\mathrm{Var}(Y_{b_1})}}\right)\ \mathrm{dB}\,, \tag{5.51}$$

where $\mathrm{Var}(Y_{b_1}) = 1$ is the variance for a coherent state and $\mathrm{Var}(\tilde{Y}_{b_1}) = e^{-2r}$. Using squeezed incoming light gives an exponential rate of decrease for ξ_s for all cases (for $A = 10^{-6}$ that holds for $\gtrsim 5$dB). In addition, for a light field with improvement $\gtrsim 5$dB we see that we can surpass the SNL even for the $A = 10^{-6}$m^2 case, while that was impossible when we used a coherent initial state for the light field, Fig. [5.6](c). Finally, we notice in Fig [5.12] that our analytical approximative model (red stars) given by Eq. (5.50) agrees well with our numerical results (blue circles).
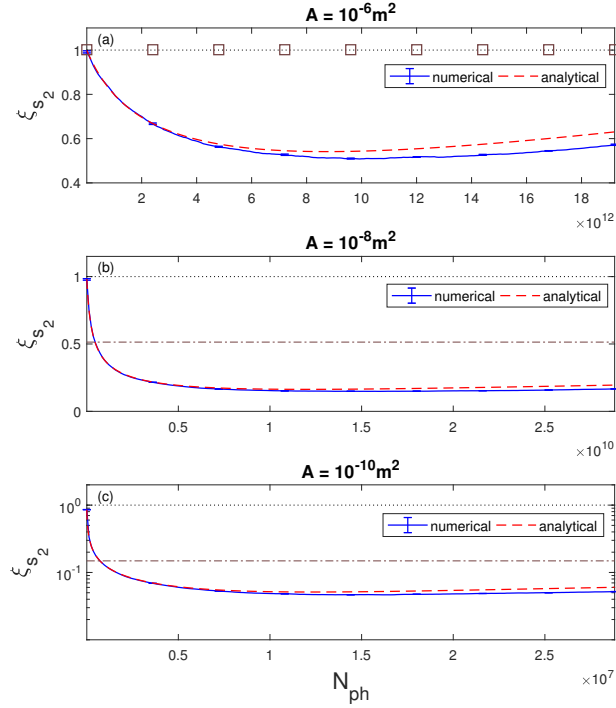
Figure 5.11: We consider squeezed incoming light and we examine the numerical (blue solid line) and analytical (red dashed line) evolution of ξ_{s_2} with respect to the number of photons for all three area values. The brown squares in (a) and brown dash-dotted lines in (b) and (c) show the $\min(\xi_{s_2})$ of the corresponding cases in Fig. [5.6] - [5.8]. The black dotted lines denote the SNL. The other parameter values are $r = \ln 10$, $\Delta = 10^2$ GHz, $N_a = 10^6$.

5.9   Cavity Dynamics

We can further boost the sensitivity of our signal with the addition of an optical cavity, as it essentially increases the atom-light coupling, Fig. [5.13]. We consider a dual-frequency cavity with resonant frequencies ω_{c_1} and ω_{c_2} detuned from the two atomic transitions $|1\rangle \to |3\rangle$ and $|2\rangle \to |4\rangle$ by detunings Δ_1 and Δ_2 respectively. In the Hamiltonian of our system, Eq. (5.16) we interchange the continuous light field annihilation operators $\hat{b}_1(z, t)$
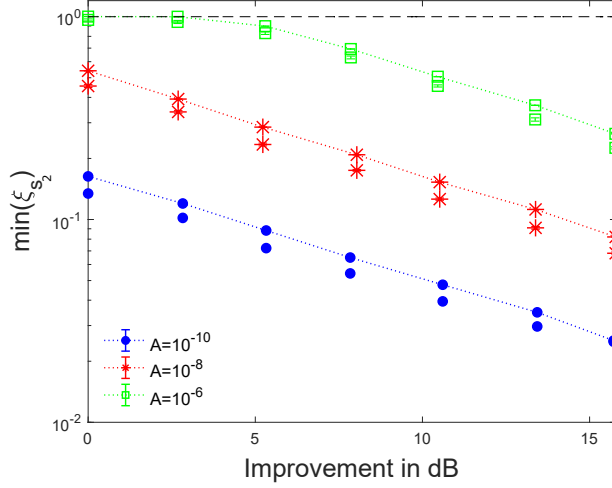
Figure 5.12: Analytical (dotted lines with markers) and numerical (markers) calculation of the minimum value of ξ_{s_2} with respect to the improvement in dB of the incoming light field, for the three different area values. The dashed line represents the SNL. The other parameter values are $\Delta = 10^2$ GHz, $N_a = 10^6$.

and $\hat{b}_2(z,t)$ with the cavity mode annihilation operators $\hat{c}_1$ and $\hat{c}_2$, giving

$$
\begin{aligned}
\hat{H}^c_{\text{tot}} = & \hbar\omega_{c_1}\hat{c}_1^\dagger\hat{c}_1 + \hbar\omega_{c_2}\hat{c}_2^\dagger\hat{c}_2 \\
& + \hbar \int_{-\infty}^{\infty} dz \left(\omega_{13}\hat{\psi}_3^\dagger(z,t)\hat{\psi}_3(z,t) + \omega_{24}\hat{\psi}_4^\dagger(z,t)\hat{\psi}_4(z,t) \right) \\
& + \hbar g_{c_1} \int_{-\infty}^{\infty} dz \left(\hat{\psi}_1^\dagger(z,t)\hat{\psi}_3(z,t)\hat{c}_1^\dagger(t) + \text{h.c} \right) + \hbar g_{c_2} \int_{-\infty}^{\infty} dz \left(\hat{\psi}_2^\dagger(z,t)\hat{\psi}_4(z,t)\hat{c}_2^\dagger(t) + \text{h.c} \right)
\end{aligned}
$$

(5.52)

The coupling strength constants are defined as $g_{c_1} = \frac{d_{13}}{\hbar}\left(\frac{\hbar\omega_{c_1}}{2\epsilon_0 V}\right)^{1/2}$ and $g_{c_2} = \frac{d_{24}}{\hbar}\left(\frac{\hbar\omega_{c_2}}{2\epsilon_0 V}\right)^{1/2}$ where $V = AL$ is the volume of the cavity, A is the light quantization transverse area and L is the cavity length. Using the standard input output formalism, which we analysed in Chapter 2, Sec. [2.9], we obtain the equation of motion for $\hat{c}_1$

$$
\partial_t\hat{c}_1 = -\frac{i}{\hbar}\left[\hat{c}_1, \hat{H}^c_{\text{tot}}\right] - \frac{\kappa}{2}\hat{c}_1 + \sqrt{\kappa}\hat{b}_{1_{\text{in}}}(t),
$$

(5.53)

where κ is the cavity photon decay rate, and $\hat{b}_{1_{\text{in}}}(t) = \sqrt{c}\hat{b}_1(z_L, t)$ where c is the speed of light and $\hat{b}_1(z_L, t)$ is the continuous in space annihilation operator of the incoming light field used in the previous sections. $\hat{b}_{1_{\text{in}}}(t)$ also satisfies the commutation relation $[\hat{b}_{1_{\text{in}}}(t), \hat{b}_{1_{\text{in}}}(t')] = \delta(t - t')$. Another important quantity is the light field leaking out of the cavity

$$
\hat{b}_{1_{\text{out}}}(t) = \sqrt{\kappa}\hat{c}_1(t) - \hat{b}_{1_{\text{in}}}(t).
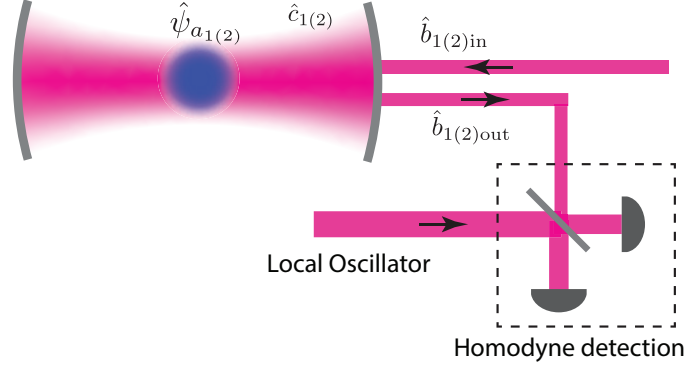$$

(5.54)

Figure 5.13: QND measurement interaction boosted by an optical cavity. After interacting with the atomic ensemble, the light exiting the cavity $\hat{b}_{1(2)\text{out}}$ is measured via homodyne detection.

In this case, $\hat{b}_{1_{\text{in}}}(t)$ is an input light field that coherently drives the dynamics of the cavity, but now the mode of the cavity, $\hat{c}_1$, is the one that interacts with the atomic ensemble and is entangled with the atomic ground-state number operator. Again, we incorporate spontaneous emission following the same method as in Sec. [5.4], i.e. we use Eq. (5.17) in order to eliminate $\hat{\psi}_3(z,t)$ from the equations of motion for $\hat{\psi}_1(z,t)$ and $\hat{c}_1$. After making the single mode approximation for $\hat{\psi}_1(z,t)$ and $\hat{d}_{1_{\text{in}}}(z,t)$, using again the same mode functions for both of them, and moving to a rotating frame with respect to the cavity resonance frequency we obtain

$$\partial_t \hat{a}_1(t) = ig_{c_1}^2 (\Omega + i\Gamma)\tilde{c}_1^\dagger(t)\tilde{c}_1(t)\hat{a}_1(t) + g_{c_1}\frac{\sqrt{\gamma_3}}{\Delta_1 - i\gamma_3/2}\tilde{c}_1^\dagger(t)\tilde{q}_{1_{\text{in}}}(t) \tag{5.55a}$$

$$\partial_t \tilde{c}_1(t) = \left[ig_{c_1}^2(\Omega + i\Gamma)\hat{a}_1^\dagger \hat{a}_1 - \frac{\kappa}{2} \right]\tilde{c}_1(t) + g_{c_1}\frac{\sqrt{\gamma_3}}{\Delta_1 - i\gamma_3/2}\hat{a}_1^\dagger(t)\tilde{q}_{1_{\text{in}}}(t) + \sqrt{\kappa}\,\tilde{b}_{1_{\text{in}}}(t), \tag{5.55b}$$

where $\tilde{c}_1(t) = \hat{c}(t)e^{i\omega_{c_1}t}$, $\tilde{b}_{1_{\text{in}}}(t) = \hat{b}_{1_{\text{in}}}(t)e^{i\omega_{c_1}t}$, $\tilde{q}_{1_{\text{in}}}(t) = \hat{q}_{1_{\text{in}}}(t)e^{i\omega_{c_1}t}$.

To investigate the dynamics, we use the TW method again, making the appropriate correspondences, in order to numerically examine the dynamics of our system. In Fig. [5.14] we plot the time evolution of the number of atoms and the number of cavity photons, as well as the intensity of the input and output fields. We see that the cavity comes into its steady state after time $t \gg 1/\kappa$. As such, the rate of incoming photons should be larger than the rate of loss, i.e. $\langle \hat{b}_{1_{\text{in}}}^\dagger \hat{b}_{1_{\text{in}}} \rangle \gg \kappa$, to ensure $\langle \hat{N}_{c_1} \rangle = \langle \hat{c}_1^\dagger \hat{c}_1 \rangle \gg 1$. In our numerical simulations, we have fixed the total interaction time $\tau = 10^{-4} >> 1/\kappa = 10^{-6}$ and we change the number of cavity photons, which is the parameter affecting the dynamics of our system, by just changing the intensity of the incoming light field $\langle \hat{b}_{1_{\text{in}}}^\dagger \hat{b}_{1_{\text{in}}} \rangle$.

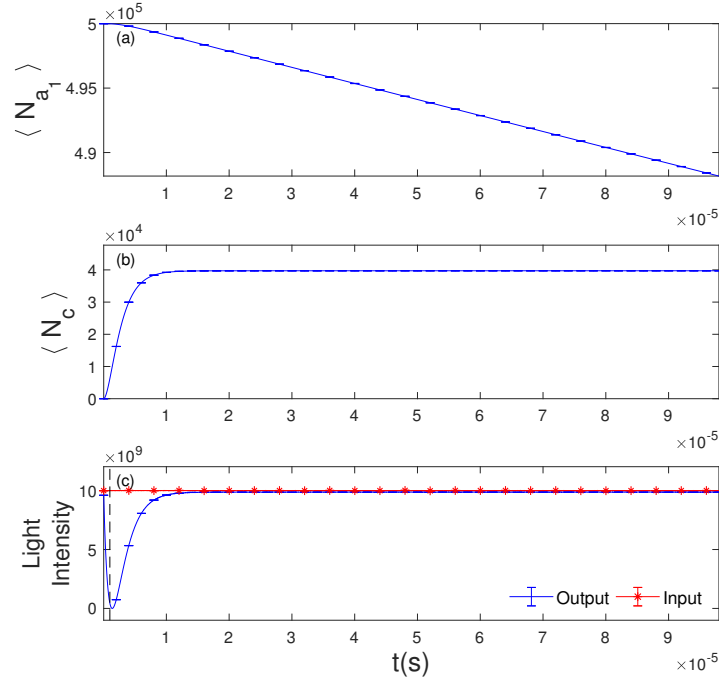We measure a combined signal of the same form as in the free space case, but now we

Figure 5.14: Cavity dynamics: time evolution of (a) mean number of atoms in state $|1\rangle$, $\langle N_{a_1} \rangle$, (b) mean number of cavity photons $\langle N_{c_1} \rangle$, (c) Intensity of input light (red solid line with asterisks) and intensity of the leaking output light field from the cavity (blue solid line). The vertical black dashed line is drawn at the time point $1/\kappa$. We notice that we need $\tau \gg 1/\kappa$, in order to reach the cavity steady state. Other parameter values: $A = 10^{-8} \mathrm{m}^2$, $\Delta = 10^2 \, \mathrm{GHz}$, $N_a = 10^6$ and $\kappa = 1 \, \mathrm{MHz}$.

measure an observable of the output field, $\hat{b}_{1_{\mathrm{out}}}(t)$, since we do not have any direct access to the cavity mode. The output field contains information about atomic observables through Eq. (5.54). Similarly with Sec. [5.4.2] we use as our light observable the difference of the phase quadratures of a specific mode of the output fields.

We plot ξ_{s_2} for the same area values as for Fig. [5.6-5.8] with $\kappa = 1\mathrm{MHz}$. Here, we noticed that for $\Delta = 10^2 \mathrm{GHz}$ and area values smaller than $A = 10^{-8}\mathrm{m}^2$ we have to decrease the incoming light intensity at a level that we tend to a regime where $\langle \hat{N}_{c_1} \rangle \to 1$. We can avoid that by just increasing appropriately the detuning $\Delta = 10^4 \mathrm{GHz}$, in order to obtain the same interaction strength. Assuming a cavity of length $L = 10$ cm, this corresponds to a finesse of $\sim 10^4$. Our choice of cavity parameters is motivated by a cavity that could be added to an existing atom interferometry set-up, and can be installed outside the vacuum system. We use a range of different intensities for the incoming light field to determine the best sensitivity. Comparing Fig. [5.6(c)-5.8(c)] with Fig. [5.15] it is

apparent that we achieve better sensitivities by adding a cavity, than just using free space light fields. Although we don't have any analytical results for the case of the cavity, due to the complexity of that model, we examined numerically if the dynamics of the system has the same behaviour as in the free space case. We concluded that we can find the optimum of the sensitivity using the same procedure as in Sec. [5.6]. Namely for a particular value of A (or equivalently $V = AL$) and N_a we can find the minimum of ξ_{s_2} with respect to the remaining parameters N_{c_1}/Δ_1^2. Here we have one parameter more, the photon decay rate from the cavity, κ. We notice that we have better sensitivities for smaller values of κ, thus for larger cavity quality factors (see Fig. [5.16]). However, in the cavity case we are more constrained on the parameter values we could use, as they should satisfy $\langle \hat{b}_{1_{\mathrm{in}}}^\dagger \hat{b}_{1_{\mathrm{in}}} \rangle > \kappa$ and $\tau > 1/\kappa$ as we discussed earlier.
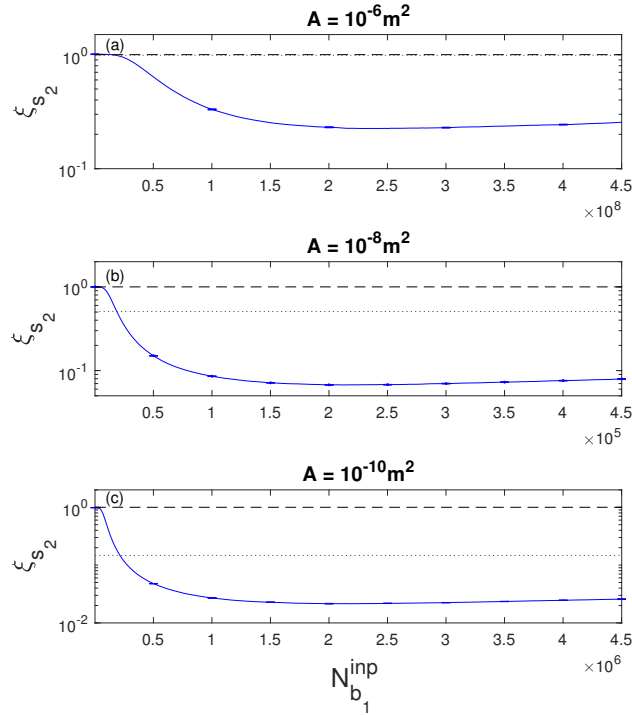

Figure 5.15: Cavity: ξ_{s_2} with respect to $N_{b_1}^{\mathrm{inp}}$ for different values of A. The brown dotted lines show the $\min(\xi_{s_2})$ of the corresponding cases in Fig. [5.6(c)]-[5.8(c)]. The parameter values are $N_a = 10^6$, $k = 1\,\mathrm{MHz}$ and $\Delta = 10^2\,\mathrm{GHz}$, except (c) where we used $\Delta = 10^4\,\mathrm{GHz}$, for the reasons discussed in the main text.
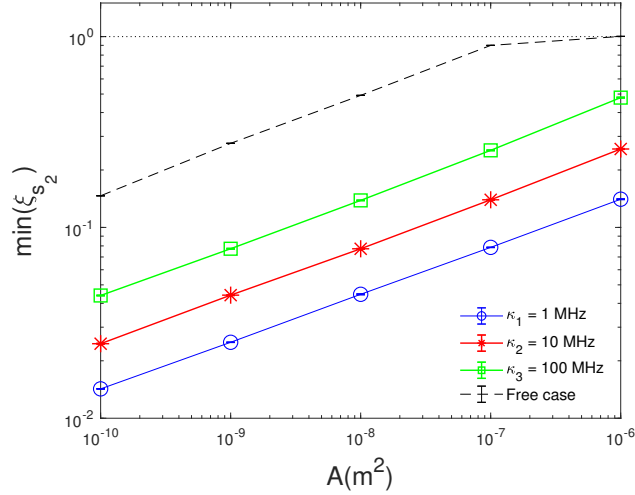
Figure 5.16: Minimum value of ξ_{s_2} with respect to the area, for three different values of κ for the cavity case. We also plot the free space case (black dashed line). The black dotted line represents the SNL. The other parameter values are $N_a = 10^6$ and $\Delta = 10^2\,\mathrm{GHz}$, except for the area values $A = 10^{-9}\mathrm{m}^2$ and $A = 10^{-10}\mathrm{m}^2$ in all cavity lines where we used $\Delta = 10^4\mathrm{GHz}$, for the reasons we mentioned in the main text.

5.10   Conclusions

We have analysed the creation of spin-squeezing in an ensemble of Bose-condensed atoms via a quantum non-demolition measurement scheme, considering both freely propagating light, and optical cavities. We found that the determining factor in the quality of spin-squeezing produced was the cross-sectional area of the optical beam used to probe the spin of the atomic system, with small areas leading to higher atom-light coupling, and a larger phase shift on the light for a given level of spontaneous emission. Of course, varying the intensity, detuning, or duration of the incoming light also affects the level of spin squeezing. However, for a given area, fixing two of these parameters, while adjusting the remaining one would always lead to the same optimum. For the D2 transition in ^{87}Rb atoms, we found that for the case of freely propagating light, no squeezing was possible when the cross-sectional area of the atom-light interaction was larger than $\sim 10^{-6}$ m^2 due to loss of atoms caused by spontaneous emission, regardless of the intensity or detuning of the incoming light. For a potential experimental setup, where we consider the D2 transition in 10^6 ^{87}Rb atoms and we can achieve a quantization area of the laser beam $\sim 3 \times 10^{-11}$ m^2, with laser power $0.25\,\mathrm{mW}$, atomic resonance detuning $100\,\mathrm{GHz}$ and total interaction time $\tau = 100\,\mathrm{ns}$, we conclude to a squeezing value of ~ 0.1, which corresponds

to a potential improvement of atom interferometric sensitivity of ~ 10. This is equivalent to increasing the number of atoms by a factor of 100. The use of optical squeezing improved the level of quantum enhancement further, and relaxed the restrictions on the area of the light. Finally, we considered the use of an optical cavity. For reasonably achievable cavity parameters, we found approximately an order of magnitude increase over what was achievable in the free space case.

Chapter 6

Improving One-Axis Twisting Using Cavity Feedback

6.1 Introduction

In this chapter we examine the creation of spin-squeezed states using the non-linear one-axis-twisting (OAT) Hamiltonian. Spin squeezed states created via the OAT dynamics, were first introduced by [49] and originally realised by atom-atom interactions. In [61, 62] they created spin squeezed states, using effective OAT dynamics, realised by the interaction of an atomic ensemble with a far detuned light field mode of a cavity. Here, we show how we can transform from the QND measurement scheme with the cavity, we examined in the previous chapter, to such a system that effectively reproduces OAT dynamics. Hence, we employ the same techniques as in Chapter 5, in order to examine numerically the dependence of the spin squeezing parameter and consequently the final sensitivity, to the other parameters of the system. We also compare the effective OAT dynamics that is being reproduced by the cavity scheme, with a simple model that produces the original OAT dynamics. Through our analysis we clarify the differences between those two models and we identify the sources of noise that limit the performance of the cavity model. Our analysis incorporates atomic spontaneous emission, as well as other decoherence mechanisms, such as photon shot noise, which is an inherent feature of the cavity OAT scheme. Hence, we aim to find the optimum parameter regime that balances out the level of spin-squeezing and all the other decoherence processes, and finally provides us with the best available sensitivity of that scheme. Our numerical analysis gives us the ability to compare the performance of the effective OAT scheme with the cavity QND measurement model, as both systems depend on the same parameters. This comparison

shows that the QND measurement scheme gives better results compared to the cavity OAT dynamics working in the same parameter regimes. In addition, we try more complicated schemes, in order to find any additional improvements. Firstly, in the cavity OAT scheme we measure the light leaking out of the cavity, and we use that signal in order to extract some information about the atomic ensemble, similarly with the process we followed in the QND measurement scheme. This is a hybrid scheme, which takes elements from both cavity OAT and QND measurement dynamics. This complicated scheme provides us with results surpassing the sensitivity obtained from the QND measurement and the cavity OAT scheme separately. We also present further improvements by using squeezed incoming light for all schemes under consideration (cavity QND measurement, cavity OAT, combined), where we optimized over the light squeeze factor and angle, in order to find optimal results.
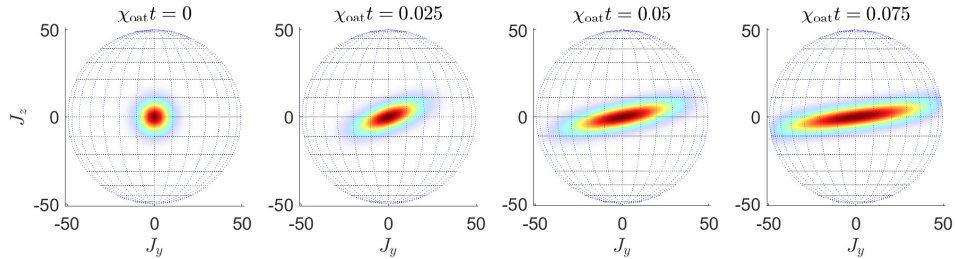
6.2   Simple One-Axis Twisting Scheme

Figure 6.1: Husimi Q representation of a state produced by applying the OAT Hamiltonian, Eq. (6.1), on a maximal $\hat{J}_x$ eigenstate, for four different values of the squeezing strength $\chi_{\mathrm{oat}}t$.

For a coherent spin state (CSS) aligned in the x-axis, as the initial state of the atomic ensemble, the well-known OAT Hamiltonian is given by

$$\hat{H}_{\mathrm{oat}} = \hbar\chi_{\mathrm{oat}}\hat{J}_z^2. \tag{6.1}$$

As shown in Fig. [6.1], this Hamiltonian generates a rotation of each spin around the z-axis with rate proportional to $\hat{J}_z$ creating a shearing of the initial CSS. The noise is not suppressed along the z-direction, but instead we have to make a rotation of $\hat{J}_z$ around the

x-axis by an angle α, in order to find the optimally squeezed direction

$$\hat{J}_\alpha = e^{-i\hat{J}_x\alpha}\hat{J}_z e^{i\hat{J}_x\alpha} = \hat{J}_z\cos\alpha + \hat{J}_y\sin\alpha. \tag{6.2}$$

There are available analytical results giving the angle α with respect to the number of atoms N and the squeezing strength $\chi_{\text{oat}}t$ [49]

$$\alpha(N,\chi_{\text{oat}}t) = -\frac{1}{2}\arctan\left[\frac{4\sin(\chi_{\text{oat}}t)\cos(\chi_{\text{oat}}t)^{N-2}}{1-\cos(2\chi_{\text{oat}}t)^{N-2}}\right], \tag{6.3}$$

where for $N \gg 1$ it reduces to [169]

$$\alpha(N,\chi_{\text{oat}}t) \approx -\frac{1}{2}\arctan\left(N^{-1/3}\right). \tag{6.4}$$

We can realise the OAT dynamics given by Eq. (6.1), by considering a simple model of two 2-level systems. We are motivated to consider the two 2-level system configuration instead of just using Eq. (6.1), in order to have a direct connection between the system considered here and the QND measurement scheme examined in Chapter 5, Fig. [5.4]. In the following, we will show that these two descriptions are equivalent. We know that the z component of the angular momentum operator, as well as the total number of atoms are given by

$$\hat{J}_z = \frac{1}{2}\left(\hat{N}_{a_1} - \hat{N}_{a_2}\right) \tag{6.5}$$

$$\hat{N} = \hat{N}_{a_1} + \hat{N}_{a_2}. \tag{6.6}$$

Using these two equations in Eq. (6.1) we obtain

$$\hat{H}_{\text{oat}} = \frac{1}{2}\hbar\chi_{\text{oat}}\left(\hat{N}_{a_1}^2 + \hat{N}_{a_2}^2 - \frac{1}{2}\hat{N}^2\right). \tag{6.7}$$

Also by considering a constant total number of particles, we can eliminate the last term of the above Hamiltonian, by just making an appropriate rotation

$$\hat{H}_{\text{oat}} = \hat{H}_1 + \hat{H}_2 = \frac{1}{2}\hbar\chi_{\text{oat}}\left(\hat{N}_{a_1}^2 + \hat{N}_{a_2}^2\right), \tag{6.8}$$

where

$$\hat{H}_i = \frac{1}{2}\hbar\chi_{\text{oat}}\hat{N}_{a_i}^2, \tag{6.9}$$

with $i = 1, 2$. Hence, this Hamiltonian, Eq. (6.8), which is realised by a two 2-level system is equivalent with Eq. (6.1). Similarly with Chapter 5, we can see that the Hamiltonians of the two 2-level systems are de-coupled, so we can examine the dynamics of only the one

system and the corresponding results would hold for the second as well. Hence, we find the equation of motion for the atomic operator of the first 2-level system

$$\partial_t \hat{a}_1 = -i\chi_{\text{oat}} \left(\hat{N}_{a_1} + \frac{1}{2} \right) \hat{a}_1. \tag{6.10}$$

From the above result, we can deduce that the original OAT dynamics is based on the dependence of the energy shift of the atomic ground state on the actual number of atoms being in the ground state. This is how the atom-atom interactions create an entangled state. As we are going to see in the following section, in the effective OAT scheme this kind of interaction and entanglement generation is produced with the help of a cavity mode and an incoming coherent light field, which is frequency detuned from the cavity resonance. This detuning means that the number of photons entering the cavity depends on the number of atoms being in the ground state. Also, the atom-light interaction produces an energy shift of the atomic ground state that is proportional to the number of photons in the cavity, which as mentioned above also depends on the number of atoms. This is how the interaction between light and atoms effectively reproduces the OAT dynamics and creates an entangled state.

6.3 One-Axis Twisting via Cavity Feedback

We can create OAT dynamics effectively by considering atom-light interactions using a cavity mode. We actually consider the exact same system as in Sec. [5.9], but instead of moving to a rotating frame in order to cancel the cavity resonance frequency, we rotate our system in order to create detuning between the cavity and the incoming light field frequencies. Hence, we do that by simply transforming Eq. (5.55b) into a rotating frame with frequency $\Delta_{c_1} = \omega_{L_1} - \omega_{c_1}$

$$\partial_t \tilde{c}'_1(t) = i \left[\Delta_{c_1} + g_{c_1}^2 (\Omega + i\Gamma)\hat{a}_1^\dagger \hat{a}_1 + i\frac{\kappa}{2} \right] \tilde{c}'_1(t) +$$
$$+ g_{c_1} \frac{\sqrt{\gamma_3}}{\Delta_1 - i\gamma_3/2} \hat{a}_1^\dagger(t)\tilde{q}'_{1_{\text{in}}}(t) + \sqrt{\kappa}\, \tilde{b}'_{1_{\text{in}}}(t), \tag{6.11}$$

where $\tilde{c}'_1(t) = \hat{c}(t)e^{i\omega_{L_1}t}$, $\tilde{b}_{1_{\text{in}}}(t) = \hat{b}_{1_{\text{in}}}(t)e^{i\omega_{L_1}t}$, $\tilde{q}_{1_{\text{in}}}(t) = \hat{q}_{1_{\text{in}}}(t)e^{i\omega_{L_1}t}$ and ω_{L_1} is the central frequency of the incoming light. The atomic equation, Eq. (5.55a), remains the same, which we present here for convenience

$$\partial_t \hat{a}_1(t) = ig_{c_1}^2 (\Omega + i\Gamma)\tilde{c}'^\dagger_1(t)\tilde{c}'_1(t)\hat{a}_1(t) + g_{c_1} \frac{\sqrt{\gamma_3}}{\Delta_1 - i\gamma_3/2} \tilde{c}'^\dagger_1(t)\tilde{q}'_{1_{\text{in}}}(t). \tag{6.12}$$

The first term in Eq. (6.12) represents the differential energy shift of the atomic ground state $|1\rangle$, due to the interaction with the cavity mode. In addition, in Eq. (6.11), where we

now have a cavity detuning, the second term in the right hand side indicates a frequency shift of the cavity resonance, depending on the atom population in state $|1\rangle$. In that way, the number of photons transmitted into the cavity depends on $\hat{N}_{a_1}$. The spin correlations amongst atoms are generated from the fact that the atomic energy shift of each atom depends, as aforementioned on the number of photons and consequently on the total number of atoms in the ground state. Putting it differently, Eq. (6.11) indicates that the number of intra-cavity photons has a linear dependence on the number of atoms, i.e. $\hat{N}_{c_1} \propto \hat{N}_{a_1}$. Substituting that into Eq. (6.12) provides unitary dynamics similar with Eq. (6.10), which is produced by a Hamiltonian of the form $\hat{H} \propto \hat{N}_{a_1}^2$, indicating effective OAT dynamics. This is how the spin-spin effective interaction is realised, via atom-light interactions using a cavity mode. In the following, we are going to examine in more detail how the equations of motion relates $\hat{N}_{c_1}$ with $\hat{N}_{a_1}$ linearly.

In order to do so, we consider the simple case of no spontaneous emission ($\gamma_3 = 0$, $\Omega = \frac{1}{\Delta}$ and $\Gamma = 0$). Also, we are actually interested on how the quantum fluctuations in the number of atoms and photons affect the unitary dynamics of the system. This is the reason why we consider, that both number operators can be decomposed in a large constant expectation value and small quantum fluctuations, i.e. $\hat{N}_{a_1} = \langle \hat{N}_{a_1} \rangle + \delta\hat{N}_{a_1}$ and $\hat{N}_{c_1} = \langle \hat{N}_{c_1} \rangle + \delta\hat{N}_{c_1}$. Finally, after making those substitutions, in Eq. (6.11) and (6.12), and transforming to an appropriate rotating frame, in order to eliminate the constant expectation values, $\langle \hat{N}_{a_1} \rangle$ and $\langle \hat{N}_{c_1} \rangle$, we obtain

$$\partial_t \tilde{c}_1'(t) = i \left[\Delta_{c_1} + \frac{g_{c_1}^2}{\Delta} \delta\hat{N}_{a_1} + i\frac{\kappa}{2} \right] \tilde{c}_1'(t) + \sqrt{\kappa}\, \tilde{b}_{1_{\text{in}}}'(t) \tag{6.13a}$$

$$\partial_t \hat{a}_1(t) = i\frac{g_{c_1}^2}{\Delta} \delta\hat{N}_{c_1} \hat{a}_1(t). \tag{6.13b}$$

As we pointed out in Chapter 5, the number of photons inside the cavity is determined by balancing between the intensity of the incoming laser beam ($\hat{b}_{1_{\text{in}}}^\dagger \hat{b}_{1_{\text{in}}}$) and the rate of photons leaking out of the cavity (κ). The cavity reaches its steady state after time $\tau \gg 1/\kappa$. We can find the cavity operator at its steady state

$$\tilde{c}_1' = \frac{\sqrt{\kappa}\hat{b}_{1_{\text{in}}}}{\frac{\kappa}{2} + i(\Delta_{c_1} + \frac{g_{c_1}^2}{\Delta}\delta\hat{N}_{a_1})}, \tag{6.14}$$

which gives the steady state photon number operator

$$\hat{N}_{c_1} = \frac{\kappa \hat{b}_{1_{\text{in}}}^\dagger \hat{b}_{1_{\text{in}}}}{\frac{\kappa^2}{4} + (\Delta_{c_1} + \delta\hat{x})^2}, \tag{6.15}$$

where for simplicity we defined $\delta\hat{x} = \frac{g_{c_1}^2}{\Delta}\delta\hat{N}_{a_1}$. In the even simpler case where we do not have any atoms, the relationship between the number of intra-cavity photons and

the cavity detuning would be given by the Lorentzian $\hat{N}_{c_1} = \frac{\sqrt{\kappa}\hat{b}_{1_{\text{in}}}^{\dagger}\hat{b}_{1_{\text{in}}}}{\frac{\kappa^2}{4}+\Delta_{c_1}^2}$. For $\Delta_{c_1} = \kappa/2$ we obtain the steepest slope between $\hat{N}_{c_1}$ and Δ_{c_1}, meaning that around $\Delta_{c_1} = \kappa/2$ we obtain the strongest linear dependence between them. We are interested on that point, because if we incorporate again the atoms we want to focus on the regime where $\hat{N}_{c_1} \propto \Delta_{c_1} - \delta\hat{x} \propto \Delta_{c_1} - \delta\hat{N}_{a_1}$, since that would reproduce the OAT dynamics. For the parameter values we examine here $\delta\hat{x} << 1$, so we can expand $\hat{N}_{c_1}$ with respect to $\delta\hat{x}$ around zero, and we keep terms up to first order in $\delta\hat{x}$

$$\hat{N}_{c_1} = \hat{N}_{c_1}(0) + \left.\frac{\partial\hat{N}_{c_1}}{\partial\delta\hat{x}}\right|_0 \delta\hat{x}. \tag{6.16}$$

After calculating the derivative and using $\Delta_{c_1} = \kappa/2$ as explained earlier, we find

$$\hat{N}_{c_1} = \frac{2\hat{b}_{1_{\text{in}}}^{\dagger}\hat{b}_{1_{\text{in}}}}{\kappa} - \frac{4\hat{b}_{1_{\text{in}}}^{\dagger}\hat{b}_{1_{\text{in}}}}{\kappa^2}\delta\hat{x}. \tag{6.17}$$

From here we can calculate the photon number expectation value

$$\langle\hat{N}_{c_1}\rangle = 2\frac{\beta_0^2}{\kappa}, \tag{6.18}$$

since $\langle\delta\hat{x}\rangle = 0$. We now decompose the incoming intensity light operator $\hat{b}_{1_{\text{in}}}^{\dagger}\hat{b}_{1_{\text{in}}} = \beta_0^2 + \delta\left(\hat{b}_{1_{\text{in}}}^{\dagger}\hat{b}_{1_{\text{in}}}\right)$, in order to obtain

$$\delta\hat{N}_{c_1} = \frac{2}{\kappa}\delta\left(\hat{b}_{1_{\text{in}}}^{\dagger}\hat{b}_{1_{\text{in}}}\right) - \frac{4g_{c_1}^2}{\kappa^2\Delta}\left[\beta_0^2 + \delta\left(\hat{b}_{1_{\text{in}}}^{\dagger}\hat{b}_{1_{\text{in}}}\right)\right]\delta\hat{N}_{a_1}. \tag{6.19}$$

Hence, now we notice the aforementioned linear dependence between the quantum fluctuations of the number of cavity photons and atoms, which effectively realises the OAT dynamics. We also see that the quantum fluctuations of the incoming light disrupt the linear relationship between those two, and that would have deleterious effects in the final spin-squeezing, as we are going to analyse later. We can compare the effective OAT dynamics produced by the cavity feedback scheme, with the original OAT dynamics, by comparing the corresponding atomic equations of motion. In order to do so, we substitute Eq. (6.19) into (6.13b), and we find the atomic equation of motion for the cavity case

$$\partial_t\hat{a}_1(t) = i\left[\frac{2g_{c_1}^2}{\kappa\Delta}\delta\left(\hat{b}_{1_{\text{in}}}^{\dagger}\hat{b}_{1_{\text{in}}}\right) - \frac{4g_{c_1}^4}{\kappa^2\Delta^2}\left[\beta_0^2 + \delta\left(\hat{b}_{1_{\text{in}}}^{\dagger}\hat{b}_{1_{\text{in}}}\right)\right]\delta\hat{N}_{a_1}\right]\hat{a}_1. \tag{6.20}$$

We also go back to the atomic equation of motion for the simple model, Eq. (6.10), and we decompose $\hat{N}_{a_1} = \langle\hat{N}_{a_1}\rangle + \delta N_{a_1}$ as we are interested on the quantum fluctuations of the field, and move to an appropriate rotating frame, in order to eliminate the large mean value ($\langle\hat{N}_{a_1}\rangle$), as we did earlier. Hence, for the simple model we obtain

$$\partial_t\hat{a} = -i\chi_{\text{oat}}\delta\hat{N}_{a_1}\hat{a}_1. \tag{6.21}$$

Comparing Eq. (6.20) with (6.21) we notice that the corresponding χ_{oat} term in the cavity case would be an operator depending on the noise of the incoming light field

$$\hat{\chi}_{\mathrm{oat}}^c = \frac{4g_{c_1}^4}{\kappa^2\Delta^2}\left[\beta_0^2 + \delta\left(\hat{b}_{1_{\mathrm{in}}}^\dagger\hat{b}_{1_{\mathrm{in}}}\right)\right] \tag{6.22}$$

with expectation value given by

$$\langle\hat{\chi}_{\mathrm{oat}}^c\rangle = \frac{4g_{c_1}^4\beta_0^2}{\kappa^2\Delta^2}, \tag{6.23}$$

where we used that $\left\langle\delta\left(\hat{b}_{1_{\mathrm{in}}}^\dagger\hat{b}_{1_{\mathrm{in}}}\right)\right\rangle = 0$ and the superscript c denotes explicitly that we refer to the cavity case. We can separately define the noisy part as

$$\delta\hat{\chi}_{\mathrm{oat}}^c = \frac{4g_{c_1}^4}{\kappa^2\Delta^2}\delta\left(\hat{b}_{1_{\mathrm{in}}}^\dagger\hat{b}_{1_{\mathrm{in}}}\right), \tag{6.24}$$

in order to be able to write $\hat{\chi}_{\mathrm{oat}}^c$ in a more elegant form

$$\hat{\chi}_{\mathrm{oat}}^c = \langle\hat{\chi}_{\mathrm{oat}}^c\rangle + \delta\hat{\chi}_{\mathrm{oat}}^c. \tag{6.25}$$

Importantly, we also notice that there is an additional term in the atomic equation of motion of the cavity scheme, which we denote as

$$\delta\hat{\omega} = \frac{2g_{c_1}^2}{\kappa\Delta}\delta\left(\hat{b}_{1_{\mathrm{in}}}^\dagger\hat{b}_{1_{\mathrm{in}}}\right), \tag{6.26}$$

which is being generated by the quantum fluctuations of the incoming light as well. Hence, we can now write Eq. (6.20) in a more convenient form

$$\partial_t\hat{a}_1(t) = -i\langle\hat{\chi}_{\mathrm{oat}}^c\rangle\delta\hat{N}_{a_1}\hat{a}_1 + -i\delta\hat{\chi}_{\mathrm{oat}}^c\delta\hat{N}_{a_1}\hat{a}_1 + i\delta\hat{\omega}\hat{a}_1 \tag{6.27}$$

We can easily notice now that the second and third terms in Eq. (6.27) differentiate the cavity scheme from the simple OAT dynamics, Eq. (6.21), and they are both stemming from the quantum fluctuations of the incoming light field. In the next section, where we will examine the dynamics of our system numerically using the TW method, we will show how these two terms affect the sensitivity of the cavity model compared to the simple scheme. We will show that, by comparing both models through simulating the simple OAT scheme with a noisy χ_{oat} term as in Eq. (6.22), and by adding an additional noise source in the corresponding equation of motion, as Eq. (6.27) indicates.

6.4 Numerical Solutions

We numerically examine the dynamics of our system using again the TW method. We follow the same strategy with Chapter 5, Sec. [5.6], in order to determine correspondences

between quantum operators and Wigner variables as well as their initial conditions, as explained in Appendix [C]. Here we calculate the squeezing parameter

$$\xi_s = \sqrt{N} \frac{\sqrt{\text{Var}(\hat{S}(0))}}{|\langle \hat{J}_x \rangle|}, \qquad (6.28)$$

using as our signal $\hat{S} = \hat{J}_\alpha$, which is the rotated $\hat{J}_z$ angular momentum component, with respect to angle α, over the x-axis, as explained in Sec. [6.2]. Here, we essentially consider that we prepare a spin squeezed state using the cavity OAT scheme, before the atomic ensemble enters an atom interferometer. This is the reason why, we again considered that $\phi = 0$, as we did in Chapter 5. We determine the angle α, by numerically minimizing $\text{Var}(\hat{J}_\alpha)$ over α, using a gradient descent algorithm. We firstly examine the simple case with no spontaneous emission, namely we use the SDEs coming from Eq. (6.13a) and (6.13b) for the cavity case and Eq. (6.21) for the simple model. In both schemes we use parameter values, in order to reach the minimum value of ξ_s, due to over-squeezing the state. In Fig. [6.2], we notice that the cavity scheme qualitatively reproduces the OAT
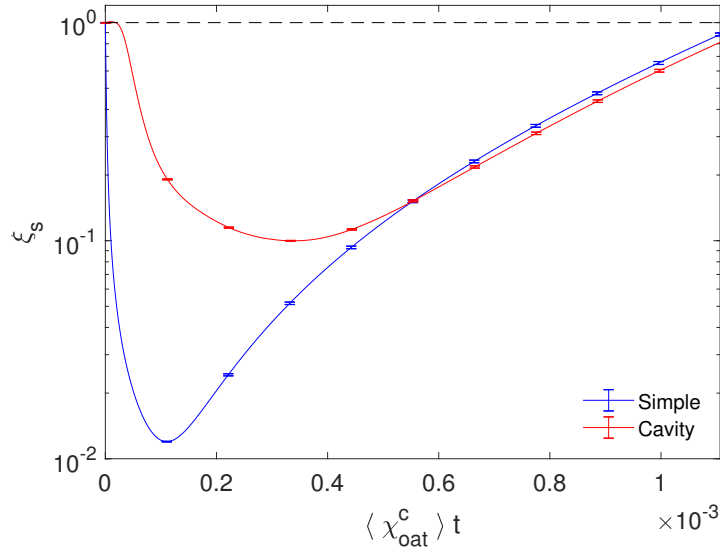

Figure 6.2: ξ_s with respect to $\langle \hat{\chi}^c_{\text{oat}} \rangle t$ for the original OAT dynamics (blue line) and for the cavity scheme (red line). The black dashed line denotes the SNL.

dynamics, as expected. However, the level of squeezing that produces is almost an order of magnitude less than the one generated by the simple model, as well as the optimum value occurs a bit slower, i.e. for a larger value of $\langle \hat{\chi}^c_{\text{oat}} \rangle t$.

Aiming to find the reason of the decreased performance in the cavity case, we also present the relationship between the Wigner variables corresponding to $\delta \hat{N}_{c_1}$ and $\delta \hat{N}_{a_1}$

Fig. [6.3(a)]. Each blue dot corresponds to a different trajectory of the Wigner variables, while the red line depicts a linear fit amongst them. It is clear that the blue dots indicate a linear dependence between the fluctuations of the number of cavity photons and atoms, which is the source of the effective OAT dynamics. However, this linearity is not perfect, due to the aforementioned two new contributions in the dynamics, caused by the noise of the incoming light field, as indicated by Eq. (6.19). We can numerically calculate the Wigner variable corresponding to $\hat{\chi}_{\text{oat}}^c$, by evaluating the slope of the linear fit between the Wigner variables δN_{c_1} and δN_{a_1} at each time point. We notice that this calculation results in a noisy behaviour of $\hat{\chi}_{\text{oat}}^c$, which lies around its expectation value given by Eq (6.23), as depicted in Fig. [6.3(b)].
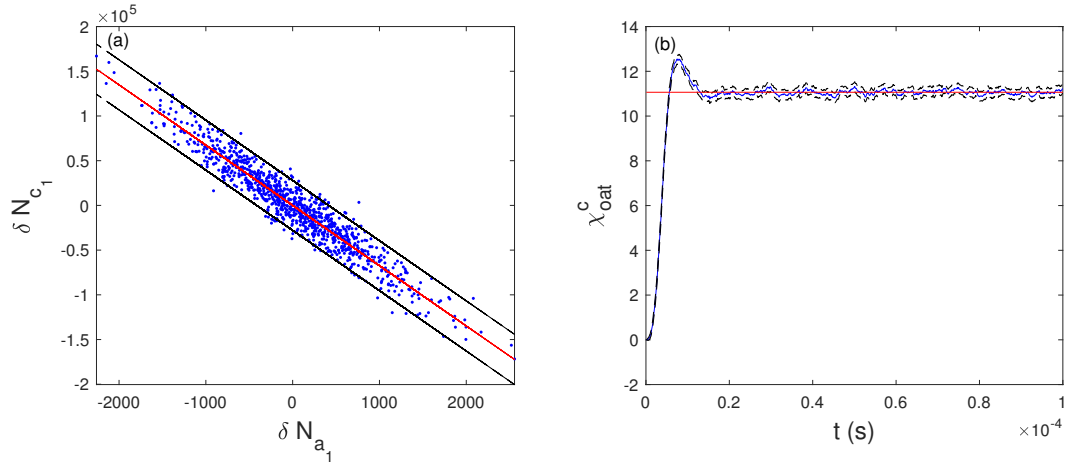

Figure 6.3: (a) Scatter plot of the Wigner variables δN_{c_1} and δN_{a_1} at a specific time point. The red line is a linear fit corresponding to the blue dots, while the black lines were found by applying $\pm 2\sigma_{\text{fit}}$ to the linear fit, where σ_{fit} is the standard deviation of the distribution of the blue dots. (b) χ_{oat}^c as a Wigner variable with respect to time. It is calculated by taking the slope of the linear fit of the blue dots in (a) at each time point. The red line denotes its expectation value calculated by Eq. (6.23), while the black lines were found by applying $\pm 2\frac{g_{c_1}^2}{\Delta}\sigma_{\text{slope}}$ to the mean value, where σ_{slope} is the error of the slope of the linear fit at each time point, which was calculated numerically.

The disagreement between the two models, shown in Fig. [6.2], should be coming from the differences between their atomic equations of motion. As we identified in the previous section, in the cavity model we have two additional terms, compared to the simple model. Firstly, χ_{oat} is no more just a constant number, but instead it has a noisy part depending on the noise of the incoming light field. We also have the presence of an entirely new term

in the dynamics, $\delta\hat{\omega}$, again depending on the noise of the incoming light.

We can compare those two contributions by taking the ratios of Eq. (6.26) and (6.24), where $\frac{\delta\hat{\omega}}{\delta\hat{\chi}_{\text{oat}}^c} = \frac{\kappa\Delta}{2g_{c_1}^2} >> 1$ for all parameter regimes we examined. Hence, we expect that $\delta\hat{\omega}$ will dominate and that this is the noise term, which mainly damages the linear relationship between $\delta\hat{N}_{c_1}$ and $\delta\hat{N}_{a_1}$ and consequently decreases the final sensitivity of the cavity model. We can also show that, by numerically examining the simple OAT scheme incorporating those new terms in the corresponding equation of motion, and explore how they affect the dynamics of the system. We essentially examine the evolution of the SDE coming from Eq. (6.27). In Fig. [6.4], we explore all different combinations of adding those noise contributions in the simple OAT model, namely we examine the case where we only add the $\delta\hat{\chi}_{\text{oat}}^c$ noise (blue stars), or only the $\delta\hat{\omega}$ term (red stars), as well as the case where we incorporate both noise terms (green line) and we compare them with the lines shown in Fig. [6.2]. We notice that the $\delta\hat{\chi}_{\text{oat}}^c$ term does not have a visible effect in the sensitivity, while all the damage comes from $\delta\hat{\omega}$, as expected. We can also see that the line produced from the original OAT dynamics with the $\delta\hat{\omega}$ noise incorporated produce almost identical results with the cavity case, with the only difference being that the cavity line is slightly shifted in the horizontal axis, due to the time needed to reach its steady state. Hence, this analysis indicates that the cavity model indeed produces effective OAT dynamics, but noise coming from the incoming light field acts as mechanism of decoherence, which limits the final sensitivity that could be achieved by this scheme, compared with the original OAT dynamics.

Now we move to the more complicated case, where we incorporate atomic spontaneous emission, by examining the numerical evolution of the SDEs coming from Eq. (6.11) and (6.12). In Fig. [6.5], we simulate the dynamics of the cavity. We notice a similar picture with the QND case, namely atomic loss is present, as well the cavity reaches its steady state after some time $\tau >> 1/\kappa$.

After incorporating the effect of spontaneous emission, we can find parameter regimes, which provide us with better sensitivity, balancing between the squeezing strength $\hat{\chi}_{\text{oat}}t$ and the atomic loss rate. We numerically examine the squeezing parameter for different interaction area values, as we did in the QND case. In Fig. [6.6], we present the evolution of ξ_s with respect to the squeezing strength $\langle\hat{\chi}_{\text{oat}}^c\rangle t$. We also find the value of angle α, which denotes the optimum direction of angular momentum operators with less noise, at each time point, by minimizing $\text{Var}(\hat{J}_\alpha)$, as explained earlier, and we compare that with the analytical result found by Eq. (6.3). We do that for three different area values
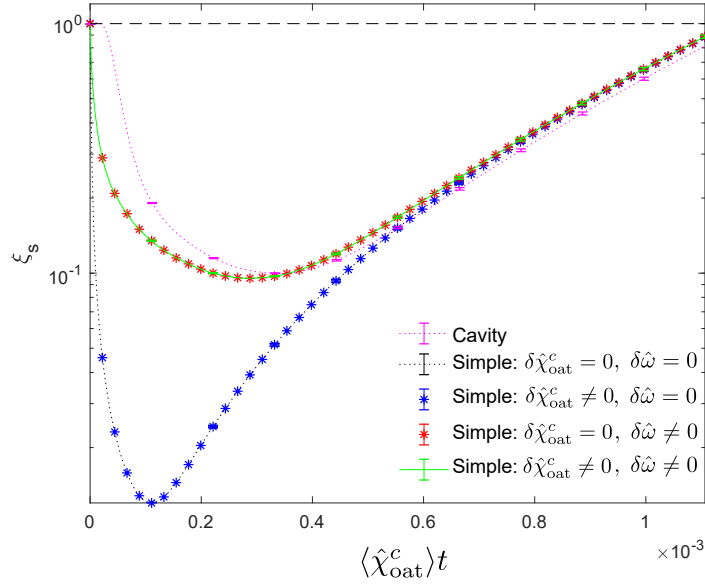
Figure 6.4: ξ_s with respect to $\langle \hat{\chi}^c_{\text{oat}} \rangle t$ for the cavity (magenta dotted line) and the simple model. Here, we examine several different cases for the simple model, namely simple model without any noise (black dotted line), simple model with only $\delta \hat{\chi}_{\text{oat}^c}$ incorporated (blue stars), simple model with only $\delta \omega$ incorporated (red stars), and simple model with both noises incorporated (green line). The black dashed line denotes the SNL.

$A = 10^{-8} \text{m}^2$, $A = 10^{-6} \text{m}^2$, $A = 10^{-4} \text{m}^2$. We notice that for $A = 10^{-8} \text{m}^2$ we almost get the minimum of ξ_s due to over-squeezing the state ($\approx 10^{-1}$), as shown in Fig. [6.2]. However, for the other two area values we get worse performance, due to the deleterious effects of spontaneous emission. We also notice that in all three cases, the optimum angle takes small values, indicating that the optimum measurement is close to the z-direction, which is the conventional measurement for an atom interferometer.

From investigating the equations of motion, as well as numerically examining the dynamics of the system we found that the atomic loss rate is proportional to $\frac{\beta_0^2}{V \kappa \Delta^2}$. We notice that the squeezing strength and the atomic loss rate follow the same relationship patterns as in the QND case, Sec. [5.6, 5.9]. Hence, we are going to employ the same method in order to find the optimum parameter regime, namely for a fixed number of atoms, volume and lifetime of the cavity, N_a, V, κ respectively, we find the optimum squeezing with respect to $N_{\text{ph}}^{\text{inp}}/\Delta^2$, where $N_{\text{ph}}^{\text{inp}} = \beta_0^2 t$.

In Fig. [6.7 (a)], we notice that for the same parameter values of N_a, V and κ, the QND scheme produces significantly improved level of squeezing, compared to the cavity OAT dynamics. In addition, we see that the OAT line cannot surpass the minimum we found
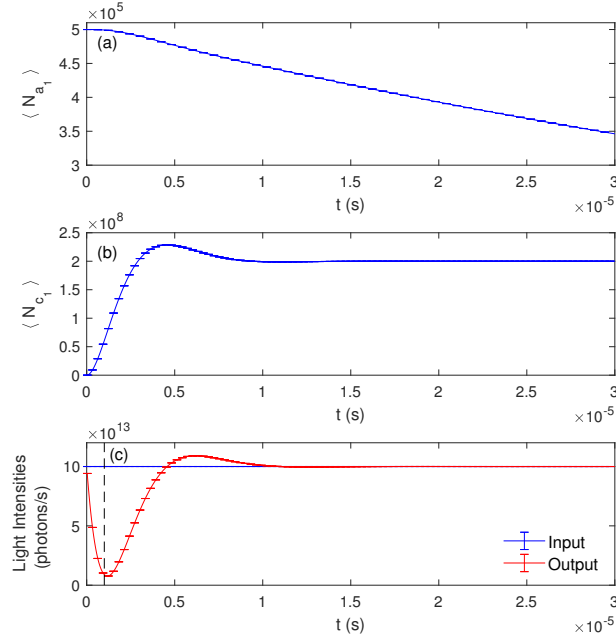
Figure 6.5: Dynamics for the cavity one-axis twisting scheme with atomic spontaneous emission incorporated. (a) Atom number expectation value with respect to time. (b) Mean cavity photon number with respect to time. (c) Input and output light intensities with respect to time. The black dashed vertical line denotes the time $1/\kappa$. Parameter values: $N_a = 10^6$, $\Delta = 10^2 \mathrm{MHz}$, $\kappa = 1\,\mathrm{MHz}$, $A = 10^{-6}\mathrm{m}^2$.

for the no spontaneous emission case ($\approx 10^{-1}$) in Fig. [6.2], in contrast to the QND case, where its minimum due to over-squeezing is close to the Heisenberg limit ($\approx 2 \times 10^{-3}$) Fig. [5.2].

6.5 Combined Scheme

One additional mechanism of decoherence, existing in the cavity OAT scheme, is the photons leaking out of the cavity. This is true since they contain information about the atomic ensemble, due to the atom-light interaction. We can extract this extra information by measuring a light observable following a similar strategy with Chapter 5. Hence, we measure the combined signal

$$\hat{S}_3 = \hat{J}_\alpha(0) - \hat{J}_\alpha^{\mathrm{inf}}, \tag{6.29}$$

where $\hat{J}_\alpha$ is calculated via Eq. (6.2) and $\hat{J}_\alpha^{\mathrm{inf}} = G_\alpha \hat{S}_b^\alpha$ is an inference we can make by measuring an appropriate light observable. As in the previous chapter, we consider that
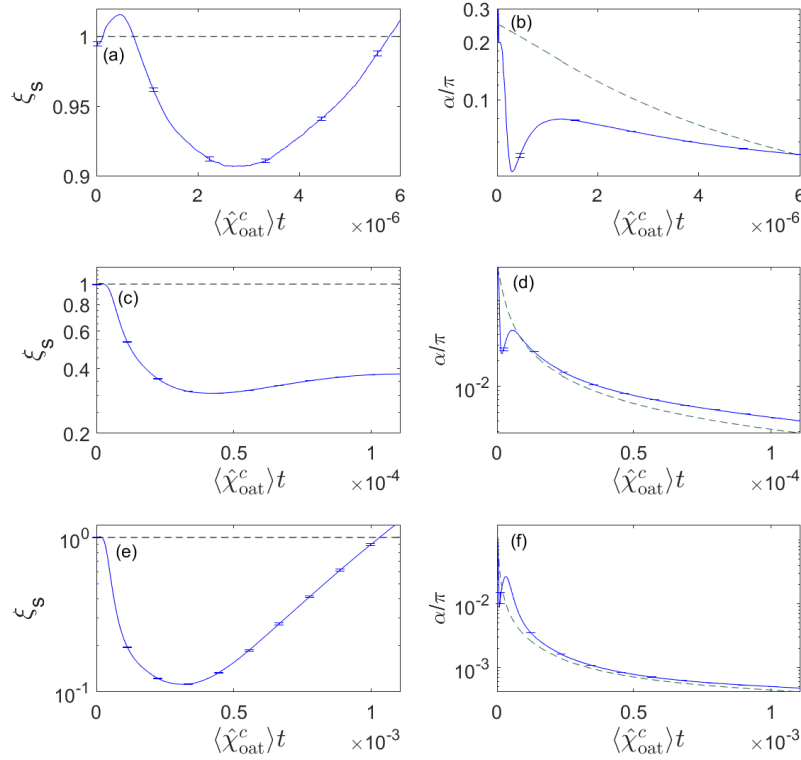
Figure 6.6: Left column: ξ_s with respect to $\langle\hat{\chi}^c_{\text{oat}}\rangle t$. Right Column: α with respect to $\langle\hat{\chi}^c_{\text{oat}}\rangle t$. (a), (b) $A = 10^{-4}\text{m}^2$, (c), (d) $A = 10^{-6}\text{m}^2$, (e), (f) $A = 10^{-8}\text{m}^2$. The black dashed line denotes the SNL. The other parameter values are: $L = 10\text{cm}$, $\Delta = 10^2\text{MHz}$, $N_a = 10^6$ and $\kappa = 1\,\text{MHz}$.

the preparation stage of the entanglement-enhanced state is completely separate from the interferometer stage. Hence, we choose G_α in such a way, in order to minimize the variance of the combined signal $\text{Var}(\hat{S}_3)$, thus $G_\alpha = \frac{\text{Cov}(\hat{J}_\alpha(0),\hat{S}^\alpha_b)}{\text{Var}(\hat{S}^\alpha_b)}$. However, here we can not extract this extra information by simply measuring the difference of the phase quadrature of the two light fields, because the dynamics is much more complicated compared to the scheme in Chapter 5. This is the reason why we use $\hat{S}^\alpha_b = \hat{X}^{(2)}_\theta - \hat{X}^{(1)}_\theta$ where $\hat{X}^{(i)}_\theta$ with $i = 1, 2$ is the generalised quadrature

$$\hat{X}^{(i)}_\theta = e^{i\theta}\hat{b}_{i_{\text{out}}} + e^{-i\theta}\hat{b}^\dagger_{i_{\text{out}}}. \tag{6.30}$$

We remind the reader here that we have already introduced the generalised quadrature in Chapter 3, Sec. [3.2.2], but in that case we used the index ϕ_{sq} rather than θ, because we were examining the concept of quadrature squeezing in different phase-space reference frames. So, here θ determines a new reference frame, rotated with respect to the original
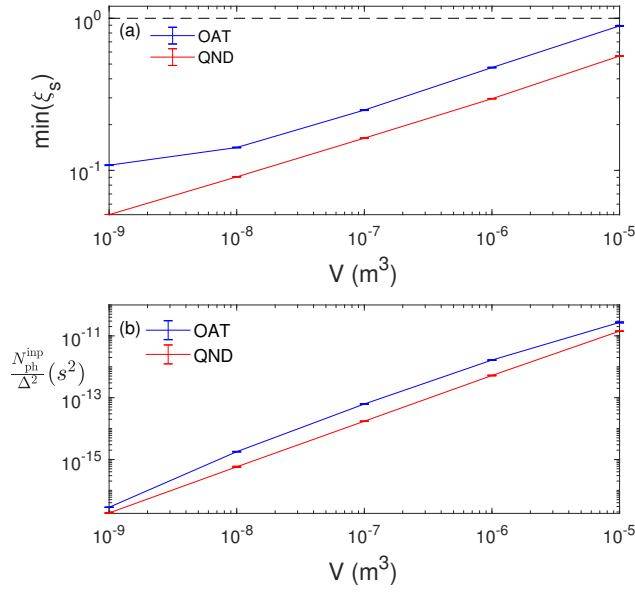
Figure 6.7: (a) $\min(\xi_s)$ with respect to the cavity volume V. For a specific value of V, $N_a = 10^6$ and $\kappa = 1\,\mathrm{MHz}$, we find the minimum of ξ_s with respect to $N_{\mathrm{ph}}^{\mathrm{inp}}/\Delta^2$. (b) We present the optimum values of $N_{\mathrm{ph}}^{\mathrm{inp}}/\Delta^2$ at which the minimum of ξ_s occurs. The black dashed line denotes the SNL.

one, as was depicted in Fig.[3.7]. For example, for $\theta = 0$ and $\theta = \pi/2$ we obtain the amplitude and phase quadratures respectively. In the next section, where we will examine the case of using squeezed incoming light we will use ϕ_{sq} again, in order to specifically denote the angle over which we squeeze the quadrature. We calculate $\hat{X}_{\theta_i}$ using a specific mode of the outgoing light field

$$\hat{b}_i = \int_0^\tau u_{\mathrm{LO}}^*(t)\hat{b}_{i_{\mathrm{out}}}dt, \tag{6.31}$$

where $u_{\mathrm{LO}}(t) = \sqrt{\frac{1}{\tau}}$, since here we do not consider a spatial dependence for the light field, and consequently $\hat{b}_{i_{\mathrm{out}}}^\dagger \hat{b}_{i_{\mathrm{out}}}$ represents the number of photons per time.

We numerically examine the time evolution of our system again using the SDEs created from Eq. (6.11) and (6.12), but now our final signal would be $\hat{S}_3(\alpha, \theta)$, which depends on the two angles α and θ. We determine those angles by numerically minimizing $\mathrm{Var}(\hat{S}_3)$ over both α and θ, by using a two parameter gradient descent algorithm. In Fig.[6.8], we show the time evolution of ξ_s, α and θ for the three different area values we examined previously as well, $A = 10^{-8}\mathrm{m}^2$, $A = 10^{-6}\mathrm{m}^2$, $A = 10^{-4}\mathrm{m}^2$. We additionally present the corresponding lines for the cavity QND measurement and cavity OAT schemes. We notice that the combined model offers significant improvements over the cavity OAT scheme for

all area values, as well as it shows smaller improvements even compared to the cavity QND measurement case. We also can see a similar behaviour of α for the combined and the OAT cavity scheme.
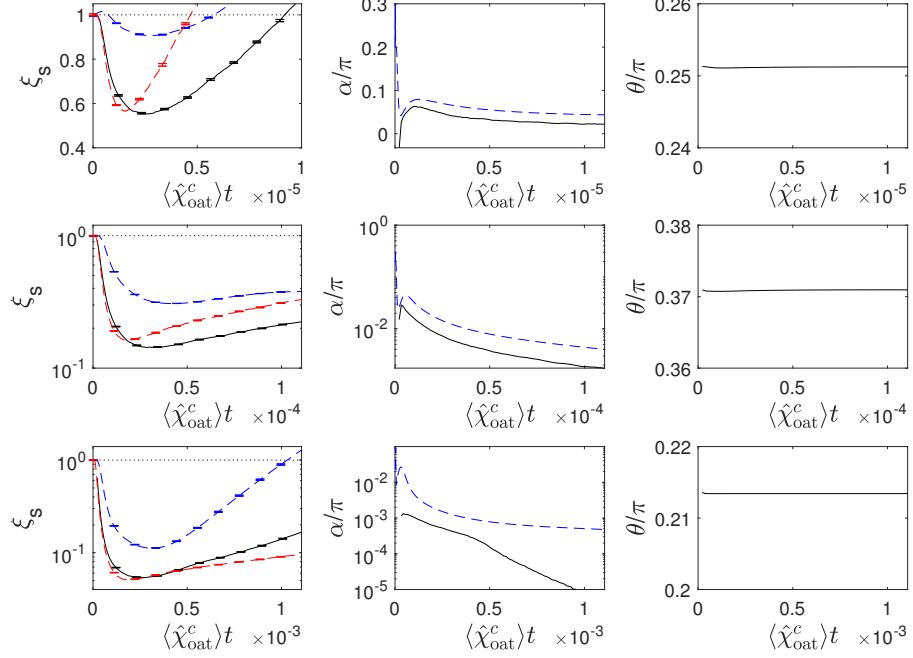

Figure 6.8: First column: ξ_s with respect to $\langle\hat{\chi}^c_{\mathrm{oat}}\rangle t$ for the combined scheme (black line), the cavity QND measurement scheme (red dashed line) and the cavity OAT scheme (blue dashed line). Second column: α/π with respect to $\langle\hat{\chi}^c_{\mathrm{oat}}\rangle t$, for the combined scheme (black line) and for the cavity OAT scheme (blue dashed line). Third column θ/π with respect to $\langle\hat{\chi}^c_{\mathrm{oat}}\rangle t$. In the first row we used $A = 10^{-4}\mathrm{m}^2$, in the second row $A = 10^{-6}\mathrm{m}^2$, and finally in the third row $A = 10^{-8}\mathrm{m}^2$. The black dotted line denotes the SNL. The other parameter values are: $L = 10\mathrm{cm}$, $\Delta = 10^2\mathrm{MHz}$, $N_a = 10^6$ and $\kappa = 1\,\mathrm{MHz}$.

We aim to compare the combined scheme with both cavity OAT and QND schemes, in a more clear way, by finding the corresponding optimum parameter regimes, following the same procedure as previously. Namely, we consider a fixed value for N_a, V and κ and we optimize ξ_s over $\frac{N_{\mathrm{ph}}^{\mathrm{inp}}}{\Delta^2}$. We use the same parameter values as in Fig. [6.7 (a)] and we compare the QND and cavity OAT schemes with the combined one, Fig. [6.9]. We find that the complicated scheme surpasses the level of squeezing provided by solely the OAT and QND schemes for all cavity volume values and for the range $10^{-9}\mathrm{m}^3 < V < 10^{-5}\mathrm{m}^3$ respectively. For smaller values of the cavity volume the OAT dynamics reaches its minimum due to over-squeezing (as we noticed in Fig. (6.2)), which also seems to damage the sensitivity of
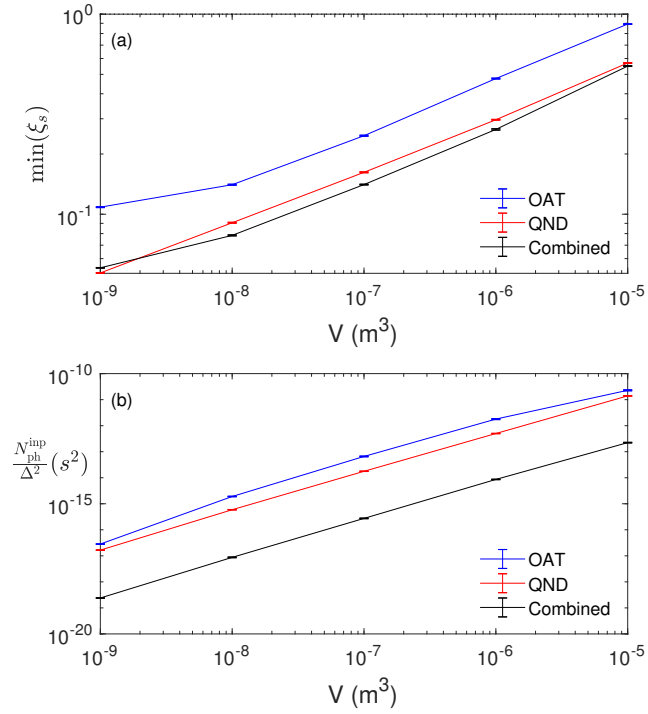
Figure 6.9: (a) $\min(\xi_s)$ with respect to the cavity volume V. For a specific value of V, $N_a = 10^6$ and $\kappa = 1\,\mathrm{MHz}$, we find the minimum of ξ_s with respect to $N_{\mathrm{ph}}^{\mathrm{inp}}/\Delta^2$. (b) We present the optimum values of $N_{\mathrm{ph}}^{\mathrm{inp}}/\Delta^2$ at which the minimum of ξ_s occurs.

the combined scheme, giving slightly worse results than the QND dynamics.

6.6 Squeezed Light

In our analysis we have been considering classical incoming light up to this point, which means that $\mathrm{Var}(\hat{X}_{\phi_{\mathrm{sq}}}^{(i)}) = \mathrm{Var}(\hat{Y}_{\phi_{\mathrm{sq}}}^{(i)}) = 1$ for all values of ϕ_{sq} and for both light fields $i = 1,\ 2$. Now, we try squeezed incoming light with reduced noise in one direction, $\mathrm{Var}(\hat{X}_{\phi_{\mathrm{sq}}}^{(i)}) = e^{-2r}$, at the expense of corresponding increase in the perpendicular direction $\mathrm{Var}(\hat{Y}_{\phi_{\mathrm{sq}}}^{(i)}) = e^{2r}$, where r and ϕ_{sq} are the squeeze factor and angle respectively, as analysed in Chapter 3, Sec. [3.2.2].

In the free space light field case in Chapter 5, we found that the final sensitivity increases exponentially with the squeeze factor r, Fig. [5.12]. However, we do not have the same situation here, namely the sensitivity increases with respect to r up to an optimum value. We find that value by minimizing ξ_s over r in both QND and OAT schemes, using a gradient descent algorithm. Due to the different source of squeezing of the QND and OAT dynamics, we should squeeze different quadratures of the incoming light in each

scheme, in order to enhance more the final sensitivity of the atomic state. In the QND dynamics, information about the atomic state population is encoded in the phase of the light field, while in the OAT dynamics the squeezing comes from correlations between the number of intra-cavity photons with the number of atoms in the ground state. Hence, we can further boost the final sensitivity, if we use incoming light with squeezed phase quadrature $\phi_{sq} = \pi/2$ in the former, and squeezed amplitude quadrature $\phi_{sq} = 0$ in the latter. The dynamics of the combined scheme, is much more complicated hindering us from developing a similar logic about the value of ϕ_{sq} we should use there. Ideally, we should optimize over all four related parameters, r, ϕ_{sq}, α and θ, in order to find the optimum case for the combined scheme using squeezed light. However, the fact that two of those parameters, r and ϕ_{sq}, determine the dynamical evolution of the system, while the other two α and θ, determine the final signal we measure, which has to be optimized at each time point, makes the optimization over all four parameters an impenetrable task. This is the reason why, we tried to make a simplification by using a constant value for the squeeze factor in the combined scheme, $r = 1$, since we noticed that most of the optimal squeeze factor values in the QND and OAT schemes are close to one. Also, we used the best result we obtained from using a grid of ten different values for ϕ_{sq}, while we appropriately optimized over α and θ using a two parameter gradient descent algorithm at each time point. For $V = (10^{-9},\ 10^{-8},\ 10^{-5})\,\mathrm{m}^3$ the optimum squeeze angle was $\phi_{sq}/\pi = 0.33$, while for $V = (10^{-7},\ 10^{-6})\,\mathrm{m}^3$ we found $\phi_{sq}/\pi = 0.44$.

In Fig. [6.10] we notice that the use of squeezed light provides us with further improvements in all quantum enhanced schemes under consideration. Although, we used a simplified procedure in order to find the optimum case for the combined scheme with squeezed light, it still provides us with the better performance, even if it almost coincides with the corresponding QND measurement scheme.

6.7 Conclusions

In this chapter, we examined the effective OAT dynamics produced via a cavity feedback scheme, as well as we explored new more complicated schemes that could offer increased sensitivity. We firstly compared this cavity model with the original OAT dynamics. Using the TW method, in order to numerically examine both schemes, we concluded that noise contributions in the cavity scheme, coming from the photon noise of the incoming field, limit the level of squeezing we can achieve compared with the original OAT model. This analysis nicely agrees with similar work already existing in the literature, but our
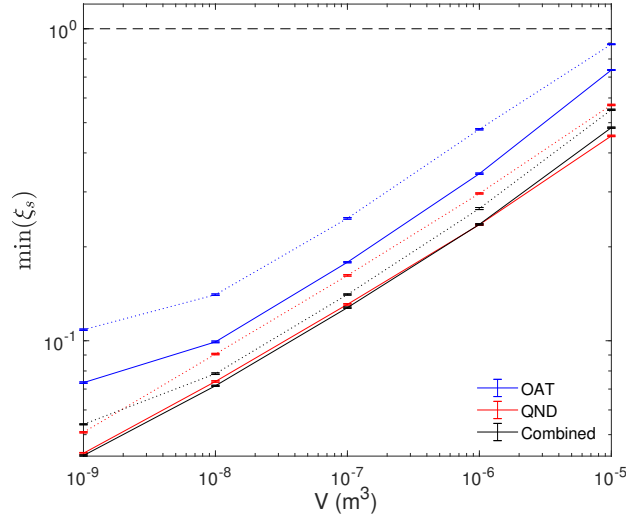
Figure 6.10: $\min(\xi_s)$ with respect to V, where we optimized over N_{ph}/Δ^2, using squeezed light (solid lines). We compare them with the corresponding cases of no squeezed light (dotted lines). The black dashed line denotes the SNL. We used the following parameter values: $N_a = 10^6$, $\kappa = 1\,\mathrm{MHz}$.

numerical method helps to acquire a deeper insight of how OAT dynamics is being reproduced in the cavity case, as well as how the aforementioned noise contributions damage the final sensitivity. In addition, our analysis enabled us to make a direct comparison of the cavity OAT scheme with the QND measurement model using a cavity, presented in the previous chapter. Again, we found for the cavity OAT scheme the same relationship patterns amongst parameters of the system that we have found for the QND case. Our results show that the QND measurement scheme achieves better performance for the same parameter values. We also considered a hybrid scheme that combines characteristics from both OAT and QND models, which outperforms both of them, giving slightly better results compared to the QND measurement model.

For a potential experimental setup we consider the D2 transition of an ensemble of 10^6 ^{87}Rb atoms inside a cavity with volume $V = 10^{-8}\mathrm{m}^3$. We also consider the following experimental values: detuning from the atomic resonance $\Delta = 100\,\mathrm{GHz}$, power of the incoming laser beam $25\,\mathrm{nW}$, cavity lifetime $\kappa = 1\,\mathrm{MHz}$ and total interaction time $\tau = 0.1\,\mathrm{ms}$. The effective OAT scheme gives a squeezing factor of ~ 0.14, leading to potential sensitivity improvement of ~ 7, which is equivalent with increasing the number of atoms by a factor of ~ 50. For the same experimental values the combined scheme provides us with a squeezing factor ~ 0.078, which results in a sensitivity improvement of a factor of

~ 13, which corresponds to an increased number of atoms by a factor of ~ 150, which is a slightly better result compared to the one offered by the QND measurement scheme. We improved the performance of all three schemes further, by using squeezed incoming light with optimized squeezing factor and angle values.

Chapter 7

Conclusions and Outlook

In this thesis we have examined different ways of enhancing the sensitivity of atom interferometers with a focus on atom gravimeters. These devices provide us with a promising alternative to current classical gravimeters, since they are not susceptible to long term drifts, as their function does not depend on any mechanical object. Although, they have shown comparable or even better performance than spring and falling corner cube gravimeters respectively, they have not been able to surpass the precision offered by superconducting gravimeters. This, as well as the demand for increased precision by several geophysical applications have been the main reasons for exploring methods to increase the sensitivity of atom gravimeters. Considerable efforts have been made in that direction focused on finding methods of increasing the phase shift at the output of the interferometer, by increasing the total interferometer time or the space-time area.

The performance of current atom gravimeters is limited by experimental imperfections, such as noise in the laser pulses realising the optical elements of the interferometer and vibrations. However, after surpassing those noise limits we reach the fundamental shot-noise limit (SNL), which constraints all atom interferometers that use uncorrelated states. Many entanglement schemes have been realised experimentally and have shown tremendous sensitivity improvements over the SNL. However, many of these schemes are incompatible with the classical routes of improvement of atom interferometers, namely large atom flux, long interrogation times and large space-time areas. This results in devices that can surpass the shot-noise limit, but for less quantum resources and consequently they cannot offer better sensitivities than current state of the art gravimeters.

The two main purposes of this thesis are to enhance the performance of atom gravimeters by 1) developing a theoretical model that describes the dynamics of an atomic ensemble propagating into the gravitational field, and using metrics from estimation the-

ory, in order to rigorously quantify the performance of these devices and by 2) exploring entanglement-enhanced schemes that are compatible with current state of the art atom gravimeters.

7.1   Sensitivity of Current Atom Gravimeters

In Chapter 4, we examined the quantum mechanical evolution of a particle passing through a Kasevich-Chu (KC) interferometer. Additionally, we used the quantum Fisher information (QFI) as our metric, in order to quantify the metrological potential of this device. Our analysis showed that the semi-classical approaches that estimate the gravitational acceleration, by taking into account only the resulted phase difference between the two arms of the interferometer are unable to capture the full dynamics of the system. Through our model we were able to reproduce all phase differences coming from those approaches, but we also found an additional source of metrological information, due to the effect of the gravitational field on the atomic wave-function itself. That means that there is more metrological potential than what is currently considered. This additional source of information is related to variations of the position and momentum atomic distribution, due to the motion of the particle in the gravitational field. After looking over all the available information that the configuration of a KC interferometer contains, we wanted to quantify how much of this information we can attain by making a particular measurement. For this reason, we used the classical Fisher information (CFI) as our metric. We showed that the common population difference measurement optimally extracts the information related to the phase difference between the two arms of the interferometer. Hence, now that we had proved that there is additional metrological information, this measurement is not any longer optimal. For this reason, we tried different innovative measurements, such as the position and momentum distributions of the atom that could retrieve the information coming from the effect of the gravitational field on the atomic wave-function. We showed that such a measurement could be optimal depending on the initial motional state of the atom. Hence, our analysis extends the possible routes of sensitivity improvement of atom gravimeters, by adding considerations related to the variance of the momentum and position distributions of the initial motional state. Our work also provides us with a rigorous way to quantify the performance of atom gravimeters that could inspire and affect the design of future devices, as we will analyse in the following, Sec. [7.3].

7.2 Quantum Enhanced Atom Interferometers

In Chapters 5 and 6, we explored quantum entanglement schemes that could enhance the sensitivity of atom interferometers limited by the SNL. We focused on schemes that are compatible with current state of the art devices and hence they could be easily employed in them. This is the reason why, we considered atom-light interaction schemes, in order to create entanglement and spin-squeezed states. Essentially, the main idea is to devote some time in order to prepare the spin-squeezed states and then use these states as the input of the interferometer, in order to increase the final sensitivity.

More particularly, in Chapter 5 we examined a quantum non-demolition (QND) measurement scheme by considering the interaction of a BEC with a free propagating light field. Using free light field instead of a cavity mode would be easier to implement in a current working gravimeter, but for completeness we also examined the case of a weak interacting cavity that could be attached to the current construction of such a device. We also took into account the atomic spontaneous emission, which has deleterious effects in the final sensitivity. We analysed the final sensitivity with respect to all the parameters of the system and we found which of them play a significant role in the dynamics, by balancing between the level of spin-squeezing and atomic loss. We also found that the use of a light field with squeezed phase quadrature, rather than a coherent state laser beam could further boost the final atomic sensitivity. Finally, we showed that the use of a low finesse cavity enhances the atom-light interaction and provides us we better spin-squeezing compared with the free light case. Our analysis provides us with a numerical and an approximative analytical model that describes the dynamics of a QND measurement scheme. This model helps us to determine the final sensitivity as a function of the parameters of the system and in such a way we can find the optimal parameter regime with respect to the level of spin-squeezing, under which we should work given the available quantum resources and decoherence processes.

In Chapter 6, we examined the second method of creating spin-squeezed states through atom-light interactions, namely we realised effective one-axis-twisting (OAT) dynamics by using a cavity feedback. Firstly, we compared the cavity OAT scheme, with the conventional OAT dynamics, namely we simply used the OAT Hamiltonian ($\propto \hat{J}_z^2$). We noticed that the cavity OAT scheme indeed offers similar behaviour with the simple OAT model, but its sensitivity is degraded by almost one order of magnitude due to the photon-shot noise of the incoming light field, which drives the dynamics of the system. Here, we also

showed that we can easily convert the dynamics of our system, from a cavity QND measurement scheme to a cavity feedback OAT dynamics scheme, by simply adding a detuning between the frequencies of the incoming light field and the cavity mode. In such a way, we showed that it was possible to create correlations amongst the atoms and consequently produce a spin squeezed state. Again, we considered the effect of atomic spontaneous emission in the total dynamics of the system and we applied the same method as Chapter 5, in order to find relationship patterns amongst all system parameters and balance between spin-squeezing and atomic loss. Interestingly, we found that the same relationship patterns with the QND case hold. Hence, using our numerical models it was easy to compare the two different schemes, working in the same parameter regime. It is clear that for the same area, atom number and cavity lifetime values and by optimizing over the remaining parameters with respect to the final level of squeezing, the QND scheme provides us with much better sensitivities compared to the cavity OAT case. Finally, we considered a scheme that combined both dynamics, namely in the cavity OAT scheme we measured the photons leaking out of the cavity and in such a way we gained more information about the atomic state, increasing the final sensitivity. Because of the increased complexity of the dynamics we did not just measure the phase quadrature of the outgoing light field as we did in Chapter 5, but instead we optimized with respect to the final level of squeezing over the angles that determine the measured light field quadrature and the optimal direction of spin-squeezing. The results were impressive finding better performances for all parameter values compared to solely considering cavity OAT dynamics, but more importantly we found a parameter regime, where this combined scheme offered better sensitivities even compared to the QND case. Finally, we investigated the use of squeezed light in all entanglement-enhanced schemes and we found additional further improvements.

7.3   Future Work

We believe that the work presented in this thesis would have contributions in boosting the performance of future atom gravimeters. Our results presented in Chapter 4 could offer short and long term improvements to the performance of these devices. Firstly, we can have quick-wins in the precision of current atom gravimeters by engineering appropriate atomic motional states and making innovative measurements, in order to extract all the available information, being offered by the configuration of a KC interferometer. In addition, in Chapter 4 we showed that a modified scheme from the conventional KC design, could offer improved metrological information, which as we showed can be optimally extracted

by measuring the final momentum distribution of the atoms. Hence, this evidence suggests that we need to completely rethink how sensors are designed. Most quantum sensors are based on a conventional two mode operation, where we have a phase shift between the two arms of an atom interferometer, which we measure by observing the quantum interference of matter-waves. Although, this design is quite helpful for our human intuition, in order to understand the dynamics of the system, this conventional scheme does not necessarily provide us with the optimal metrological potential given the available quantum resources and experimental constraints under consideration. That means that the construction of a sensor should be designed by trying to answer the following question: "How could we use the available set of tools, in order to build a sensor that has optimal metrological potential, i.e. the largest possible value for the quantum Fisher information, given relevant experimental constraints?". For example, in the case of the KC interferometer we have three laser pulses with equal timings amongst each other, we could however apply many laser pulses, with their parameters determined by optimizing the sensitivity. The only constraints would be for the total interferometer time and the specification of the lasers to meet realistic experimental values. The resulted scheme would probably be extremely complicated and unintuitive to our understanding. However, we could use the classical Fisher information as our metric, in order to find measurements that optimally extracts all the available information. Although the work presented in Chapter 4 focuses on the performance of atom gravimeters, similar formalisms can be developed in order to quantify and optimize the performance of different quantum sensors, where their function is based on atom interferometers.

Given that we are at the situation, where the performance of an atom interferometer is limited by the SNL, the work presented in Chapters 5 and 6 would offer crucial contributions, in order to find improved entanglement-enhanced schemes. Our analysis of the QND measurement and the effective OAT schemes sheds light on what is the optimal regime we could work in both schemes, balancing between squeezing strength and decoherence processes. We tried to find the optimum parameter regimes in both schemes that give the best squeezing, by finding relationship patterns amongst the parameters of the system, as well as suggesting several modifications that could enhance the level of spin-squeezing in both models, such as using squeezed incoming light or combining the OAT and QND schemes. Although, we managed to find parameter regimes and alternative schemes in order to present improvements compared to current cavity OAT and QND measurement schemes, the dynamics of these systems are extremely complicated and re-

quire a more systematic analysis. Hence, these human intuitive strategies we employed cannot find the absolute optimum spin-squeezing we could achieve, given the available quantum resources and decoherence processes. For example, in the entanglement schemes we considered in this thesis, we have assumed from the very beginning that we split the total time into preparation time, where we create the spin-squeezed state, and interrogation time where the atoms pass through the interferometer. However, this method is not the optimal one, since there is common criticism that the time taken to prepare the quantum entanglement could often be better spent by simply increasing the interrogation time of the interferometer, thus increasing the precision through conventional methods. In that sense, using the spin-squeezing parameter, or again the QFI as our metrics, we could find the optimal entanglement-enhanced scheme, by optimizing over all parameters of the system, with respect to these metrics. The complexity of these schemes requires the use of more advanced multi-parameter optimization algorithms, which would find the optimal entanglement-enhanced design given the specific system under consideration (available quantum resources and experimental limitations).

Bibliography

[1] C. Davisson and L. H. Germer, "Diffraction of electrons by a crystal of nickel," *Phys. Rev.*, vol. 30, pp. 705–740, Dec 1927. 1

[2] G. P. Thomson, "Experiments on the diffraction of cathode rays.—ii," *Proceedings of the Royal Society of London. Series A, Containing Papers of a Mathematical and Physical Character*, vol. 119, no. 783, pp. 651–663, 1928. 1

[3] P. Meystre, *Atom optics*, vol. 33. Springer Science & Business Media, 2001. 1

[4] H. Metcalf and P. Van der Straten, "Laser cooling and trapping of atoms," 1999. 1

[5] S. Chu, L. Hollberg, J. E. Bjorkholm, A. Cable, and A. Ashkin, "Three-dimensional viscous confinement and cooling of atoms by resonance radiation pressure," *Phys. Rev. Lett.*, vol. 55, pp. 48–51, Jul 1985. 1

[6] P. D. Lett, R. N. Watts, C. I. Westbrook, W. D. Phillips, P. L. Gould, and H. J. Metcalf, "Observation of atoms laser cooled below the Doppler limit," *Phys. Rev. Lett.*, vol. 61, pp. 169–172, Jul 1988. 1

[7] J. Dalibard and C. Cohen-Tannoudji, "Laser cooling below the Doppler limit by polarization gradients: simple theoretical models," *JOSA B*, vol. 6, no. 11, pp. 2023–2045, 1989. 1

[8] M. Kasevich and S. Chu, "Laser cooling below a photon recoil with three-level atoms," *Phys. Rev. Lett.*, vol. 69, pp. 1741–1744, Sep 1992. 1

[9] J. E. Bjorkholm, R. R. Freeman, A. Ashkin, and D. B. Pearson, "Observation of focusing of neutral atoms by the dipole forces of resonance-radiation pressure," *Phys. Rev. Lett.*, vol. 41, pp. 1361–1364, Nov 1978. 1

[10] V. Balykin, V. Letokhov, and A. Sidorov, "Focusing atomic beams by the dissipative radiation," *JETP Lett*, vol. 43, no. 0, pp. 4–25, 1986. 1

[11] V. Balykin, V. Letokhov, Y. B. Ovchinnikov, and A. Sidorov, "Reflection of an atomic beam from a gradient of an optical field," *JETP Lett*, vol. 45, no. 6, pp. 353–356, 1987. 1

[12] M. A. Kasevich, D. S. Weiss, and S. Chu, "Normal-incidence reflection of slow atoms from an optical evanescent wave," *Optics letters*, vol. 15, no. 11, pp. 607–609, 1990. 1

[13] P. E. Moskowitz, P. L. Gould, S. R. Atlas, and D. E. Pritchard, "Diffraction of an atomic beam by standing-wave radiation," *Physical Review Letters*, vol. 51, no. 5, p. 370, 1983. 1

[14] O. Carnal and J. Mlynek, "Young's double-slit experiment with atoms: A simple atom interferometer," *Physical Review Letters*, vol. 66, no. 21, p. 2689, 1991. 2, 30, 31

[15] D. W. Keith, C. R. Ekstrom, Q. A. Turchette, and D. E. Pritchard, "An interferometer for atoms," *Physical Review Letters*, vol. 66, no. 21, p. 2693, 1991. 2, 30, 31

[16] F. Riehle, T. Kisters, A. Witte, J. Helmcke, and C. J. Bordé, "Optical Ramsey spectroscopy in a rotating frame: Sagnac effect in a matter-wave interferometer," *Phys. Rev. Lett.*, vol. 67, pp. 177–180, Jul 1991. 2, 30, 31

[17] M. Kasevich and S. Chu, "Atomic interferometry using stimulated Raman transitions," *Phys. Rev. Lett.*, vol. 67, pp. 181–184, Jul 1991. 2, 30, 31, 66

[18] M. Kasevich and S. Chu, "Measurement of the gravitational acceleration of an atom with a light-pulse atom interferometer," *Applied Physics B: Lasers and Optics*, vol. 54, pp. 321–332, 1992. 10.1007/BF00325375. 2, 31

[19] A. Peters, K. Y. Chung, and S. Chu, "Measurement of gravitational acceleration by dropping atoms," *Nature*, vol. 400, pp. 849–852, 08 1999. 2, 66

[20] A. Peters, K. Y. Chung, and S. Chu, "High-precision gravity measurements using atom interferometry," *Metrologia*, vol. 38, no. 1, p. 25, 2001. 2, 66

[21] H. Müller, S.-w. Chiow, S. Herrmann, S. Chu, and K.-Y. Chung, "Atom-interferometry tests of the isotropy of post-Newtonian gravity," *Phys. Rev. Lett.*, vol. 100, p. 031101, Jan 2008. 2

[22] P. A. Altin, M. T. Johnsson, V. Negnevitsky, G. R. Dennis, R. P. Anderson, J. E. Debs, S. S. Szigeti, K. S. Hardman, S. Bennetts, G. D. McDonald, L. D. Turner, J. D. Close, and N. P. Robins, "Precision atomic gravimeter based on Bragg diffraction," *New Journal of Physics*, vol. 15, no. 2, p. 023009, 2013. 2, 66, 67, 74, 82

[23] S. M. Dickerson, J. M. Hogan, A. Sugarbaker, D. M. S. Johnson, and M. A. Kasevich, "Multiaxis inertial sensing with long-time point source atom interferometry," *Phys. Rev. Lett.*, vol. 111, p. 083001, Aug 2013. 2

[24] B. Barrett, L. Antoni-Micollier, L. Chichet, B. Battelier, T. Lévèque, A. Landragin, and P. Bouyer, "Dual matter-wave inertial sensors in weightlessness," *Nature Communications*, vol. 7, no. 1, pp. 1–9, 2016. 2

[25] B. Canuel, F. Leduc, D. Holleville, A. Gauguet, J. Fils, A. Virdis, A. Clairon, N. Dimarcq, C. J. Bordé, A. Landragin, and P. Bouyer, "Six-axis inertial sensor using cold-atom interferometry," *Phys. Rev. Lett.*, vol. 97, p. 010402, Jul 2006. 2

[26] T. Müller, M. Gilowski, M. Zaiser, P. Berg, C. Schubert, T. Wendrich, W. Ertmer, and E. Rasel, "A compact dual atom interferometer gyroscope based on laser-cooled rubidium," *The European Physical Journal D*, vol. 53, no. 3, pp. 273–281, 2009. 2

[27] A. V. Rakholia, H. J. McGuinness, and G. W. Biedermann, "Dual-axis high-data-rate atom interferometer via cold ensemble exchange," *Phys. Rev. Applied*, vol. 2, p. 054012, Nov 2014. 2

[28] S. Riedl, G. Hoth, B. Pelle, J. Kitching, and E. Donley, "Compact atom-interferometer gyroscope based on an expanding ball of atoms," in *Journal of Physics: Conference Series*, vol. 723, p. 012058, IOP Publishing, 2016. 2

[29] M. J. Snadden, J. M. McGuirk, P. Bouyer, K. G. Haritos, and M. A. Kasevich, "Measurement of the earth's gravity gradient with an atom interferometer-based gravity gradiometer," *Phys. Rev. Lett.*, vol. 81, pp. 971–974, Aug 1998. 2, 66

[30] J. M. McGuirk, G. T. Foster, J. B. Fixler, M. J. Snadden, and M. A. Kasevich, "Sensitive absolute-gravity gradiometry using atom interferometry," *Phys. Rev. A*, vol. 65, p. 033608, Feb 2002. 2

[31] G. Tackmann, P. Berg, S. Abend, C. Schubert, W. Ertmer, and E. M. Rasel, "Large-area Sagnac atom interferometer with robust phase read out," *Comptes Rendus Physique*, vol. 15, no. 10, pp. 884–897, 2014. 2

[32] I. Dutta, D. Savoie, B. Fang, B. Venon, C. L. Garrido Alzar, R. Geiger, and A. Landragin, "Continuous cold-atom inertial sensor with 1 nrad/sec rotation stability," *Phys. Rev. Lett.*, vol. 116, p. 183003, May 2016. 2

[33] T. H. Kim, S. H. Yim, K. M. Shim, and S. Lee, "Spatial-contrast analysis in a cold-atom Sagnac interferometer with a single large Raman beam," *Phys. Rev. A*, vol. 95, p. 033632, Mar 2017. 2

[34] J. E. Debs, P. A. Altin, T. H. Barter, D. Döring, G. R. Dennis, G. McDonald, R. P. Anderson, J. D. Close, and N. P. Robins, "Cold-atom gravimetry with a Bose-Einstein condensate," *Phys. Rev. A*, vol. 84, p. 033610, Sep 2011. 2, 67, 81

[35] K. S. Hardman, P. J. Everitt, G. D. McDonald, P. Manju, P. B. Wigley, M. A. Sooriyabandara, C. C. N. Kuhn, J. E. Debs, J. D. Close, and N. P. Robins, "Simultaneous precision gravimetry and magnetic gradiometry with a Bose-Einstein condensate: A high precision, quantum sensor," *Phys. Rev. Lett.*, vol. 117, p. 138501, Sep 2016. 2, 66, 78, 80, 158

[36] M. H. Anderson, J. R. Ensher, M. R. Matthews, C. E. Wieman, and E. A. Cornell, "Observation of Bose-Einstein condensation in a dilute atomic vapor," *Science*, vol. 269, no. 5221, pp. 198–201, 1995. 2

[37] K. B. Davis, M.-O. Mewes, M. R. Andrews, N. J. van Druten, D. S. Durfee, D. Kurn, and W. Ketterle, "Bose-Einstein condensation in a gas of sodium atoms," *Physical Review Letters*, vol. 75, no. 22, p. 3969, 1995. 2

[38] K. S. Hardman, C. C. N. Kuhn, G. D. McDonald, J. E. Debs, S. Bennetts, J. D. Close, and N. P. Robins, "Role of source coherence in atom interferometery," *Phys. Rev. A*, vol. 89, p. 023626, Feb 2014. 2, 67, 73

[39] L. Pezzè, A. Smerzi, M. K. Oberthaler, R. Schmied, and P. Treutlein, "Quantum metrology with nonclassical states of atomic ensembles," *Rev. Mod. Phys.*, vol. 90, p. 035005, Sep 2018. 2, 37, 38, 40, 81

[40] J. B. Fixler, G. Foster, J. McGuirk, and M. Kasevich, "Atom interferometer measurement of the Newtonian constant of gravity," *Science*, vol. 315, no. 5808, pp. 74–77, 2007. 2

[41] R. Bouchendira, P. Cladé, S. Guellati-Khélifa, F. Nez, and F. Biraben, "New determination of the fine structure constant and test of the quantum electrodynamics," *Physical Review Letters*, vol. 106, no. 8, p. 080801, 2011. 2

[42] S. Dimopoulos, P. W. Graham, J. M. Hogan, and M. A. Kasevich, "Testing general relativity with atom interferometry," *Phys. Rev. Lett.*, vol. 98, p. 111102, Mar 2007. 2, 66

[43] D. Crossley, J. Hinderer, and U. Riccardi, "The measurement of surface gravity," *Reports on Progress in physics*, vol. 76, no. 4, p. 046101, 2013. 3, 4

[44] M. Hauth, C. Freier, V. Schkolnik, A. Peters, H. Wziontek, and M. Schilling, "Atom interferometry for absolute measurements of local gravity," in *Proceedings of the International School of Physics" Enrico Fermi*, vol. 188, pp. 557–586, 2014. 3, 4

[45] C. Freier, M. Hauth, V. Schkolnik, B. Leykauf, M. Schilling, H. Wziontek, H.-G. Scherneck, J. Müller, and A. Peters, "Mobile quantum gravity sensor with unprecedented stability," *Journal of Physics: Conference Series*, vol. 723, no. 1, p. 012050, 2016. 3, 4, 66

[46] H. Strobel, W. Muessel, D. Linnemann, T. Zibold, D. B. Hume, L. Pezzè, A. Smerzi, and M. K. Oberthaler, "Fisher information and entanglement of non-Gaussian spin states," *Science*, vol. 345, no. 6195, pp. 424–427, 2014. 5, 45

[47] R. McConnell, H. Zhang, J. Hu, S. Cuk, and V. Vuletic, "Entanglement with negative Wigner function of almost 3,000 atoms heralded by one photon," *Nature*, vol. 519, pp. 439–442, 03 2015. 5

[48] D. J. Wineland, J. J. Bollinger, W. M. Itano, F. L. Moore, and D. J. Heinzen, "Spin squeezing and reduced quantum noise in spectroscopy," *Phys. Rev. A*, vol. 46, pp. R6797–R6800, Dec 1992. 5, 40, 81

[49] M. Kitagawa and M. Ueda, "Squeezed spin states," *Phys. Rev. A*, vol. 47, pp. 5138–5143, Jun 1993. 5, 81, 109, 111

[50] C. A. Sackett, D. Kielpinski, B. E. King, C. Langer, V. Meyer, C. J. Myatt, M. Rowe, Q. Turchette, W. M. Itano, D. J. Wineland, *et al.*, "Experimental entanglement of four particles," *Nature*, vol. 404, no. 6775, pp. 256–259, 2000. 5

[51] V. Meyer, M. Rowe, D. Kielpinski, C. Sackett, W. M. Itano, C. Monroe, and D. J. Wineland, "Experimental demonstration of entanglement-enhanced rotation angle

estimation using trapped ions," *Physical Review Letters*, vol. 86, no. 26, p. 5870, 2001. 5

[52] J. G. Bohnet, B. C. Sawyer, J. W. Britton, M. L. Wall, A. M. Rey, M. Foss-Feig, and J. J. Bollinger, "Quantum spin dynamics and entanglement generation with hundreds of trapped ions," *Science*, vol. 352, no. 6291, pp. 1297–1301, 2016. 5

[53] A. Sørensen, L.-M. Duan, J. I. Cirac, and P. Zoller, "Many-particle entanglement with Bose-Einstein condensates," *Nature*, vol. 409, no. 6816, pp. 63–66, 2001. 5, 45

[54] C. Orzel, A. Tuchman, M. Fenselau, M. Yasuda, and M. Kasevich, "Squeezed states in a Bose-Einstein condensate," *Science*, vol. 291, no. 5512, pp. 2386–2389, 2001. 5

[55] C. Gross, T. Zibold, E. Nicklas, J. Esteve, and M. K. Oberthaler, "Nonlinear atom interferometer surpasses classical precision limit," *Nature*, vol. 464, pp. 1165–1169, 04 2010. 5, 67

[56] J. Esteve, C. Gross, A. Weller, S. Giovanazzi, and M. K. Oberthaler, "Squeezing and entanglement in a Bose-Einstein condensate," *Nature*, vol. 455, no. 7217, p. 1216, 2008. 5

[57] A. Kuzmich, L. Mandel, and N. P. Bigelow, "Generation of spin squeezing via continuous quantum nondemolition measurement," *Phys. Rev. Lett.*, vol. 85, pp. 1594–1597, Aug 2000. 5

[58] J. Appel, P. J. Windpassinger, D. Oblak, U. B. Hoff, N. Kjaergaard, and E. S. Polzik, "Mesoscopic atomic entanglement for precision measurements beyond the standard quantum limit," *Proceedings of the National Academy of Sciences*, vol. 106, no. 27, pp. 10960–10965, 2009. 5, 82

[59] K. C. Cox, G. P. Greve, J. M. Weiner, and J. K. Thompson, "Deterministic squeezed states with collective measurements and feedback," *Physical Review Letters*, vol. 116, no. 9, p. 093602, 2016. 5

[60] M. H. Schleier-Smith, I. D. Leroux, and V. Vuletić, "States of an ensemble of two-level atoms with reduced quantum uncertainty," *Phys. Rev. Lett.*, vol. 104, p. 073604, Feb 2010. 5, 82

[61] M. H. Schleier-Smith, I. D. Leroux, and V. Vuletić, "Squeezing the collective spin of a dilute atomic ensemble by cavity feedback," *Phys. Rev. A*, vol. 81, p. 021804, Feb 2010. 6, 82, 109

[62] I. D. Leroux, M. H. Schleier-Smith, and V. Vuletić, "Implementation of cavity squeezing of a collective atomic spin," *Phys. Rev. Lett.*, vol. 104, p. 073602, Feb 2010. 6, 82, 109

[63] I. D. Leroux, M. H. Schleier-Smith, H. Zhang, and V. Vuletić, "Unitary cavity spin squeezing by quantum erasure," *Physical Review A*, vol. 85, no. 1, p. 013803, 2012. 6

[64] O. Hosten, N. J. Engelsen, R. Krishnakumar, and M. A. Kasevich, "Measurement noise 100 times lower than the quantum-projection limit using entangled atoms," *Nature*, vol. 529, pp. 505 EP –, 01 2016. 6, 67, 82

[65] O. Hosten, R. Krishnakumar, N. J. Engelsen, and M. A. Kasevich, "Quantum phase magnification," *Science*, vol. 352, no. 6293, pp. 1552–1555, 2016. 6

[66] J. J. Sakurai, J. Napolitano, *et al.*, *Modern quantum mechanics*, vol. 185. Pearson Harlow, 2014. 10, 11

[67] D. F. Walls and G. J. Milburn, *Quantum Optics.* Berlin and Heidelberg: Springer-Verlag, 2 ed., 2008. 12, 21, 47, 50, 170

[68] M. O. Scully and M. S. Zubairy, *Quantum Optics.* Cambridge University Press, 1 ed., 1997. 12, 22, 24, 47, 50

[69] M. Orszag, *Quantum optics: including noise reduction, trapped ions, quantum trajectories, and decoherence.* Springer, 2016. 12, 21, 23, 47, 51, 170

[70] R. Loudon, *The quantum theory of light.* OUP Oxford, 2000. 12, 15, 21

[71] A. J. Leggett, "Bose-Einstein condensation in the alkali gases: Some fundamental concepts," *Rev. Mod. Phys.*, vol. 73, pp. 307–356, Apr 2001. 18

[72] C. J. Pethick and H. Smith, *Bose-Einstein condensation in dilute gases.* Cambridge university press, 2008. 18

[73] S. A. Haine, *An Atom Laser for Quantum-Atom Optics.* PhD thesis, Australian National University, 2007. 20

[74] S. S. Szigeti *et al.*, *Controlled Bose-Condensed Sources for Atom Interferometry.* PhD thesis, Australian National University, 2013. 20, 171, 172

[75] C. W. Gardiner and P. Zoller, *Quantum Noise: A Handbook of Markovian and Non-Markovian Quantum Stochastic Methods with Applications to Quantum Optics*. Berlin and Heidelberg: Springer, 3rd ed., 2004. 28, 29, 97, 169, 171, 172, 173

[76] C. Gardiner and M. Collett, "Input and output in damped quantum systems: Quantum stochastic differential equations and the master equation," *Physical Review A*, vol. 31, no. 6, p. 3761, 1985. 30

[77] L.-V. de Broglie, *On the theory of quanta*. PhD thesis, University of Paris, 1924. 30

[78] P. Storey and C. Cohen-Tannoudji, "The Feynman path integral approach to atomic interferometry. a tutorial," *Journal de Physique II*, vol. 4, no. 11, pp. 1999–2027, 1994. 33

[79] H. Jason, *Towards Precision Tests of General Relativity using atom interferometer*. PhD thesis, Stanford University, 2010. 33

[80] W. P. Schleich, D. M. Greenberger, and E. M. Rasel, "A representation-free description of the Kasevich–Chu interferometer: a resolution of the redshift controversy," *New Journal of Physics*, vol. 15, no. 1, p. 013007, 2013. 33, 34, 35

[81] P. Wolf, L. Blanchet, C. J. Bordé, S. Reynaud, C. Salomon, and C. Cohen-Tannoudji, "Atom gravimeters and gravitational redshift," *Nature*, vol. 467, no. 7311, pp. E1–E1, 2010. 33

[82] B. Yurke, S. L. McCall, and J. R. Klauder, "SU(2) and SU(1,1) interferometers," *Phys. Rev. A*, vol. 33, pp. 4033–4054, Jun 1986. 40, 42

[83] N. Samuel, *Non-classical states in ultra-cold atoms for robust, high precision metrology*. PhD thesis, University of Queensland, 2018. 40, 171, 174, 178, 179, 183, 186

[84] L. Pezzé and A. Smerzi, "Entanglement, nonlinear dynamics, and the Heisenberg limit," *Phys. Rev. Lett.*, vol. 102, p. 100401, Mar 2009. 45

[85] M. Fox, *Quantum optics: an introduction*, vol. 15. OUP Oxford, 2006. 50

[86] R. Demkowicz-Dobrzanski, M. Jarzyna, and J. Kolodynski, "Quantum limits in optical interferometry," *Progress in Optics*, vol. 60, p. 345, 2015. 52, 71, 79

[87] C. M. Caves, "Quantum-mechanical noise in an interferometer," *Phys. Rev. D*, vol. 23, pp. 1693–1708, Apr 1981. 52

[88] B. P. Abbott, R. Abbott, T. Abbott, M. Abernathy, F. Acernese, K. Ackley, C. Adams, T. Adams, P. Addesso, R. Adhikari, *et al.*, "Observation of gravitational waves from a binary black hole merger," *Physical Review Letters*, vol. 116, no. 6, p. 061102, 2016. 53

[89] M. Tse, H. Yu, N. Kijbunchoo, A. Fernandez-Galiana, P. Dupej, L. Barsotti, C. Blair, D. Brown, S. Dwyer, A. Effler, *et al.*, "Quantum-enhanced advanced LIGO detectors in the era of gravitational-wave astronomy," *Physical Review Letters*, vol. 123, no. 23, p. 231107, 2019. 53

[90] L. Pezze and A. Smerzi, "Quantum theory of phase estimation," *arXiv preprint arXiv:1411.5164*, 2014. 53

[91] Z.-K. Hu, B.-L. Sun, X.-C. Duan, M.-K. Zhou, L.-L. Chen, S. Zhan, Q.-Z. Zhang, and J. Luo, "Demonstration of an ultrahigh-sensitivity atom-interferometry absolute gravimeter," *Phys. Rev. A*, vol. 88, p. 043610, Oct 2013. 66

[92] M. Hauth, C. Freier, V. Schkolnik, A. Senger, M. Schmidt, and A. Peters, "First gravity measurements using the mobile atom interferometer gain," *Applied Physics B*, vol. 113, pp. 49–55, Oct 2013. 66

[93] G. Stern, B. Battelier, R. Geiger, G. Varoquaux, A. Villing, F. Moron, O. Carraz, N. Zahzam, Y. Bidel, W. Chaibi, F. Pereira Dos Santos, A. Bresson, A. Landragin, and P. Bouyer, "Light-pulse atom interferometry in microgravity," *The European Physical Journal D*, vol. 53, pp. 353–357, 2009. 66

[94] F. Sorrentino, Q. Bodart, L. Cacciapuoti, Y.-H. Lien, M. Prevedelli, G. Rosi, L. Salvi, and G. M. Tino, "Sensitivity limits of a Raman atom interferometer as a gravity gradiometer," *Phys. Rev. A*, vol. 89, p. 023607, Feb 2014. 66

[95] G. W. Biedermann, X. Wu, L. Deslauriers, S. Roy, C. Mahadeswaraswamy, and M. A. Kasevich, "Testing gravity with cold-atom interferometers," *Phys. Rev. A*, vol. 91, p. 033629, Mar 2015. 66

[96] G. D'Amico, F. Borselli, L. Cacciapuoti, M. Prevedelli, G. Rosi, F. Sorrentino, and G. M. Tino, "Bragg interferometer for gravity gradient measurements," *Phys. Rev. A*, vol. 93, p. 063628, Jun 2016. 66

[97] P. Asenbaum, C. Overstreet, T. Kovachy, D. D. Brown, J. M. Hogan, and M. A. Kasevich, "Phase shift in an atom interferometer due to spacetime curvature across its wave function," *Phys. Rev. Lett.*, vol. 118, p. 183602, May 2017. 66

[98] Y. Bidel, N. Zahzam, C. Blanchard, A. Bonnin, M. Cadoret, A. Bresson, D. Rouxel, and M. Lequentrec-Lalancette, "Absolute marine gravimetry with matter-wave interferometry," *Nature Communications*, vol. 9, no. 1, pp. 1–9, 2018. 66

[99] J. A. Richeson, *Gravity Gradiometer Aided Inertial Navigation Within Non-GNSS Environments.* PhD thesis, University of Maryland, January 2008. 66

[100] M. I. Evstifeev, "The state of the art in the development of onboard gravity gradiometers," *Gyroscopy and Navigation*, vol. 8, pp. 68–79, Jan 2017. 66

[101] S. Fray, C. A. Diez, T. W. Hänsch, and M. Weitz, "Atomic interferometer with amplitude gratings of light and its applications to atom based tests of the equivalence principle," *Phys. Rev. Lett.*, vol. 93, p. 240404, Dec 2004. 66

[102] D. Schlippert, J. Hartwig, H. Albers, L. L. Richardson, C. Schubert, A. Roura, W. P. Schleich, W. Ertmer, and E. M. Rasel, "Quantum test of the universality of free fall," *Phys. Rev. Lett.*, vol. 112, p. 203002, May 2014. 66

[103] G. Amelino-Camelia, C. Lämmerzahl, F. Mercati, and G. M. Tino, "Constraining the energy-momentum dispersion relation with Planck-scale sensitivity using cold atoms," *Phys. Rev. Lett.*, vol. 103, p. 171302, Oct 2009. 66

[104] D. Gao and M. Zhan, "Constraining the generalized uncertainty principle with cold atoms," *Phys. Rev. A*, vol. 94, p. 013607, Jul 2016. 66

[105] C. Borde, "Atomic interferometry with internal state labelling," *Physics Letters A*, vol. 140, no. 1, pp. 10 – 12, 1989. 66

[106] H. Müller, S.-w. Chiow, Q. Long, S. Herrmann, and S. Chu, "Atom interferometry with up to 24-photon-momentum-transfer beam splitters," *Phys. Rev. Lett.*, vol. 100, p. 180405, May 2008. 67, 74

[107] P. Cladé, S. Guellati-Khélifa, F. Nez, and F. Biraben, "Large momentum beam splitter using Bloch oscillations," *Phys. Rev. Lett.*, vol. 102, no. 24, p. 240402, 2009. 67

[108] S.-w. Chiow, T. Kovachy, H.-C. Chien, and M. A. Kasevich, "$102\hbar k$ large area atom interferometers," *Phys. Rev. Lett.*, vol. 107, p. 130403, Sep 2011. 67

[109] G. D. McDonald, C. C. N. Kuhn, S. Bennetts, J. E. Debs, K. S. Hardman, M. Johnsson, J. D. Close, and N. P. Robins, "$80\hbar k$ momentum separation with Bloch oscillations in an optically guided atom interferometer," *Phys. Rev. A*, vol. 88, p. 053620, Nov 2013. 67, 81

[110] T. Mazzoni, X. Zhang, R. Del Aguila, L. Salvi, N. Poli, and G. M. Tino, "Large-momentum-transfer Bragg interferometer with strontium atoms," *Phys. Rev. A*, vol. 92, p. 053619, Nov 2015. 67

[111] B. Lücke, M. Scherer, J. Kruse, L. Pezze, F. Deuretzbacher, P. Hyllus, O. Topic, J. Peise, W. Ertmer, J. Arlt, L. Santos, A. Smerzi, and C. Klempt, "Twin matter waves for interferometry beyond the classical limit," *Science*, vol. 334, pp. 773–776, 11 2011. 67

[112] D. Linnemann, H. Strobel, W. Muessel, J. Schulz, R. J. Lewis-Swan, K. V. Kheruntsyan, and M. K. Oberthaler, "Quantum-enhanced sensing based on time reversal of nonlinear dynamics," *Phys. Rev. Lett.*, vol. 117, p. 013001, Jun 2016. 67

[113] G. Colangelo, F. Martin Ciurana, G. Puentes, M. W. Mitchell, and R. J. Sewell, "Entanglement-enhanced phase estimation without prior phase information," *Phys. Rev. Lett.*, vol. 118, p. 233603, Jun 2017. 67

[114] A. Louchet-Chauvet, T. Farah, Q. Bodart, A. Clairon, A. Landragin, S. Merlet, and F. Pereira Dos Santos, "The influence of transverse motion within an atomic gravimeter," *New Journal of Physics*, vol. 13, no. 6, p. 065025, 2011. 67

[115] S. S. Szigeti, J. E. Debs, J. J. Hope, N. P. Robins, and J. D. Close, "Why momentum width matters for atom interferometry with Bragg pulses," *New Journal of Physics*, vol. 14, no. 2, p. 023009, 2012. 67, 81

[116] N. P. Robins, P. A. Altin, J. E. Debs, and J. D. Close, "Atom lasers: Production, properties and prospects for precision inertial measurement," *Physics Reports*, vol. 529, pp. 265–296, 8 2013. 67, 79

[117] P. A. Altin, G. McDonald, D. Döring, J. E. Debs, T. H. Barter, J. D. Close, N. P. Robins, S. A. Haine, T. M. Hanna, and R. P. Anderson, "Optically trapped atom

interferometry using the clock transition of large ^{87}Rb Bose-Einstein condensates," *New Journal of Physics*, vol. 13, no. 6, p. 065020, 2011. 67

[118] S. A. Haine and A. J. Ferris, "Surpassing the standard quantum limit in an atom interferometer with four-mode entanglement produced from four-wave mixing," *Phys. Rev. A*, vol. 84, p. 043624, Oct 2011. 67

[119] S. A. Haine, "Information-recycling beam splitters for quantum enhanced atom interferometry," *Phys. Rev. Lett.*, vol. 110, p. 053002, Jan 2013. 67

[120] S. A. Haine, J. Lau, R. P. Anderson, and M. T. Johnsson, "Self-induced spatial dynamics to enhance spin squeezing via one-axis twisting in a two-component Bose-Einstein condensate," *Phys. Rev. A*, vol. 90, p. 023613, Aug 2014. 67, 99

[121] S. S. Szigeti, B. Tonekaboni, W. Y. S. Lau, S. N. Hood, and S. A. Haine, "Squeezed-light-enhanced atom interferometry below the standard quantum limit," *Phys. Rev. A*, vol. 90, p. 063630, Dec 2014. 67

[122] B. Tonekaboni, S. A. Haine, and S. S. Szigeti, "Heisenberg-limited metrology with a squeezed vacuum state, three-mode mixing, and information recycling," *Phys. Rev. A*, vol. 91, p. 033616, Mar 2015. 67

[123] S. A. Haine, S. S. Szigeti, M. D. Lang, and C. M. Caves, "Heisenberg-limited metrology with information recycling," *Phys. Rev. A*, vol. 91, p. 041802, Apr 2015. 67

[124] S. A. Haine and S. S. Szigeti, "Quantum metrology with mixed states: When recovering lost information is better than never losing it," *Phys. Rev. A*, vol. 92, p. 032317, Sep 2015. 67

[125] S. P. Nolan, J. Sabbatini, M. W. J. Bromley, M. J. Davis, and S. A. Haine, "Quantum enhanced measurement of rotations with a spin-1 Bose-Einstein condensate in a ring trap," *Phys. Rev. A*, vol. 93, p. 023616, Feb 2016. 67

[126] S. A. Haine and W. Y. S. Lau, "Generation of atom-light entanglement in an optical cavity for quantum enhanced atom interferometry," *Phys. Rev. A*, vol. 93, p. 023607, Feb 2016. 67

[127] S. S. Szigeti, R. J. Lewis-Swan, and S. A. Haine, "Pumped-up SU(1,1) interferometry," *Phys. Rev. Lett.*, vol. 118, p. 150401, Apr 2017. 67

[128] S. A. Haine, "Quantum noise in bright soliton matterwave interferometry," *New Journal of Physics*, vol. 20, no. 3, p. 033009, 2018. 67

[129] S.-Y. Lan, P.-C. Kuan, B. Estey, P. Haslinger, and H. Müller, "Influence of the coriolis force in atom interferometry," *Phys. Rev. Lett.*, vol. 108, p. 090402, Feb 2012. 67

[130] V. Schkolnik, B. Leykauf, M. Hauth, C. Freier, and A. Peters, "The effect of wavefront aberrations in atom interferometry," *Applied Physics B*, vol. 120, pp. 311–316, Aug 2015. 67

[131] S. Qvarfort, A. Serafini, P. Barker, and S. Bose, "Gravimetry through non-linear optomechanics," *arXiv:1706.09131*, (2017). 67

[132] G. Tóth and I. Apellaniz, "Quantum metrology from a quantum information science perspective," *Journal of Physics A: Mathematical and Theoretical*, vol. 47, no. 42, p. 424006, 2014. 71

[133] M. R. Matthews, B. P. Anderson, P. C. Haljan, D. S. Hall, M. J. Holland, J. E. Williams, C. E. Wieman, and E. A. Cornell, "Watching a superfluid untwist itself: Recurrence of Rabi oscillations in a Bose-Einstein condensate," *Phys. Rev. Lett.*, vol. 83, pp. 3358–3361, Oct 1999. 73

[134] S. A. Haine, "Mean-field dynamics and Fisher information in matter wave interferometry," *Phys. Rev. Lett.*, vol. 116, p. 230404, Jun 2016. 73

[135] H. Ammann and N. Christensen, "Delta kick cooling: A new method for cooling atoms," *Phys. Rev. Lett.*, vol. 78, pp. 2088–2091, Mar 1997. 76

[136] L. Pezzé and A. Smerzi, "Ultra sensitive two-mode interferometry with single-mode number squeezing," *Phys. Rev. Lett.*, vol. 110, p. 163604, Apr 2013. 78

[137] M. Gabbrielli, L. Pezzè, and A. Smerzi, "Spin-mixing interferometry with Bose-Einstein condensates," *Phys. Rev. Lett.*, vol. 115, p. 163002, Oct 2015. 78

[138] S. P. Nolan, S. S. Szigeti, and S. A. Haine, "Optimal and robust quantum metrology using interaction-based readouts," *Phys. Rev. Lett.*, vol. 119, p. 193601, Nov 2017. 78

[139] S. S. Mirkhalaf, S. P. Nolan, and S. A. Haine, "Robustifying twist-and-turn entanglement with interaction-based readout," *Phys. Rev. A*, vol. 97, p. 053618, May 2018. 78

[140] S. A. Haine, "Using interaction-based readouts to approach the ultimate limit of detection-noise robustness for quantum-enhanced metrology in collective spin systems," *Phys. Rev. A*, vol. 98, p. 030303(R), Sep 2018. 78

[141] I. Gotlibovych, T. F. Schmidutz, A. L. Gaunt, N. Navon, R. P. Smith, and Z. Hadzibabic, "Observing properties of an interacting homogeneous Bose-Einstein condensate: Heisenberg-limited momentum spread, interaction energy, and free-expansion dynamics," *Phys. Rev. A*, vol. 89, p. 061604, Jun 2014. 78, 80

[142] W. Ketterle, D. S. Durfee, and D. M. Stamper-Kurn, "Making, probing and understanding Bose-Einstein condensates," in *Proceedings of the International School of Physics "Enrico Fermi"* (M. Ingusci, S. Stringari, and C. Wieman, eds.), vol. 140, p. 67, 1999. 78

[143] K. S. Hardman, P. B. Wigley, P. J. Everitt, P. Manju, C. C. N. Kuhn, and N. P. Robins, "Time-of-flight detection of ultra-cold atoms using resonant frequency modulation imaging," *Opt. Lett.*, vol. 41, pp. 2505–2508, Jun 2016. 78

[144] J. Stenger, S. Inouye, A. P. Chikkatur, D. M. Stamper-Kurn, D. E. Pritchard, and W. Ketterle, "Bragg spectroscopy of a Bose-Einstein condensate," *Phys. Rev. Lett.*, vol. 82, pp. 4569–4573, Jun 1999. 78

[145] S. Richard, F. Gerbier, J. H. Thywissen, M. Hugbart, P. Bouyer, and A. Aspect, "Momentum spectroscopy of 1D phase fluctuations in Bose-Einstein condensates," *Phys. Rev. Lett.*, vol. 91, p. 010405, Jul 2003. 78

[146] M. Johnsson, S. Haine, J. Hope, N. Robins, C. Figl, M. Jeppesen, J. Dugué, and J. Close, "Semiclassical limits to the linewidth of an atom laser," *Phys. Rev. A*, vol. 75, p. 043618, Apr 2007. 79, 81

[147] S. S. Szigeti and S. A. Haine. in preparation. 80

[148] S. Gerlich, L. Hackermüller, K. Hornberger, A. Stibor, H. Ulbricht, M. Gring, F. Goldfarb, T. Savas, M. Müri, M. Mayor, *et al.*, "A Kapitza–Dirac–Talbot–Lau interferometer for highly polarizable molecules," *Nature Physics*, vol. 3, no. 10, pp. 711–715, 2007. 80

[149] R. E. Sapiro, R. Zhang, and G. Raithel, "Atom interferometry using Kapitza-Dirac scattering in a magnetic trap," *Phys. Rev. A*, vol. 79, p. 043630, Apr 2009. 80

[150] B. Gadway, D. Pertot, R. Reimann, M. G. Cohen, and D. Schneble, "Analysis of Kapitza-Dirac diffraction patterns beyond the Raman-Nath regime," *Opt. Express*, vol. 17, pp. 19173–19180, Oct 2009. 80

[151] W. Li, T. He, and A. Smerzi, "Multimode Kapitza-Dirac interferometry with trapped cold atoms," *Phys. Rev. Lett.*, vol. 113, p. 023003, Jul 2014. 80

[152] T. He and P. Niu, "Multimode Kapitza–Dirac interferometer on Bose-Einstein condensates with atomic interactions," *Physics Letters A*, vol. 381, no. 12, pp. 1087 – 1091, 2017. 80

[153] J. Fekete, S. Chai, S. A. Gardiner, and M. F. Andersen, "Resonant transfer of large momenta from finite-duration pulse sequences," *Phys. Rev. A*, vol. 95, p. 033601, Mar 2017. 80

[154] V. Guarrera, R. Moore, A. Bunting, T. Vanderbruggen, and Y. B. Ovchinnikov, "Distributed quasi-Bragg beam splitter in crossed atomic waveguides," *Scientific Reports*, vol. 7, no. 1, p. 4749, 2017. 80

[155] M. Kritsotakis, S. S. Szigeti, J. A. Dunningham, and S. A. Haine, "Optimal matter-wave gravimetry," *Phys. Rev. A*, vol. 98, p. 023629, Aug 2018. 81

[156] A. S. Sørensen and K. Mølmer, "Entanglement and extreme spin squeezing," *Phys. Rev. Lett.*, vol. 86, pp. 4431–4434, May 2001. 81

[157] A. Louchet-Chauvet, J. Appel, J. J. Renema, D. Oblak, N. Kjaergaard, and E. S. Polzik, "Entanglement-assisted atomic clock beyond the projection noise limit," *New Journal of Physics*, vol. 12, no. 6, p. 065032, 2010. 82

[158] M. Koschorreck, M. Napolitano, B. Dubost, and M. W. Mitchell, "Quantum non-demolition measurement of large-spin ensembles by dynamical decoupling," *Phys. Rev. Lett.*, vol. 105, p. 093602, Aug 2010. 82

[159] R. J. Sewell, M. Koschorreck, M. Napolitano, B. Dubost, N. Behbood, and M. W. Mitchell, "Magnetic sensitivity beyond the projection noise limit by spin squeezing," *Phys. Rev. Lett.*, vol. 109, p. 253605, Dec 2012. 82

[160] R. J. Sewell, M. Napolitano, N. Behbood, G. Colangelo, F. Martin Ciurana, and M. W. Mitchell, "Ultrasensitive atomic spin measurements with a nonlinear interferometer," *Phys. Rev. X*, vol. 4, p. 021045, Jun 2014. 82

[161] S. S. Szigeti, S. P. Nolan, J. D. Close, and S. A. Haine, "High-precision quantum-enhanced gravimetry with a bose-einstein condensate," *Phys. Rev. Lett.*, vol. 125, p. 100402, Sep 2020. 86

[162] S. A. Haine and M. T. Johnsson, "Dynamic scheme for generating number squeezing in Bose-Einstein condensates through nonlinear interactions," *Phys. Rev. A*, vol. 80, p. 023611, Aug 2009. 86

[163] E. Brion, L. H. Pedersen, and K. Mølmer, "Adiabatic elimination in a lambda system," *Journal of Physics A: Mathematical and Theoretical*, vol. 40, no. 5, p. 1033, 2007. 89

[164] H. A. Bachor and T. C. Ralph, *A Guide to Experiments in Quantum Optics*. Wiley, 2nd ed., 2004. 90, 100

[165] L.-M. Duan, J. I. Cirac, P. Zoller, and E. S. Polzik, "Quantum communication between atomic ensembles using coherent light," *Phys. Rev. Lett.*, vol. 85, pp. 5643–5646, Dec 2000. 96

[166] L. B. Madsen and K. Mølmer, "Spin squeezing and precision probing with light and samples of atoms in the Gaussian description," *Physical Review A*, vol. 70, no. 5, p. 052324, 2004. 96

[167] D. A. Steck, "Rubidium 87 D line data," *revision 2.1.5, 13 January*, 2015. 97

[168] K. Mertes, J. Merrill, R. Carretero-González, D. Frantzeskakis, P. Kevrekidis, and D. Hall, "Nonequilibrium dynamics and superfluid ring excitations in binary Bose-Einstein condensates," *Physical Review Letters*, vol. 99, no. 19, p. 190402, 2007. 99

[169] J. Ma, X. Wang, C.-P. Sun, and F. Nori, "Quantum spin squeezing," *Physics Reports*, vol. 509, no. 2-3, pp. 89–165, 2011. 111

[170] N. P. Robins, C. Figl, S. A. Haine, A. K. Morrison, M. Jeppesen, J. J. Hope, and J. D. Close, "Achieving peak brightness in an atom laser," *Phys. Rev. Lett.*, vol. 96, p. 140403, Apr 2006. 158

[171] M. T. Johnsson and S. A. Haine, "Generating quadrature squeezing in an atom laser through self-interaction," *Phys. Rev. Lett.*, vol. 99, p. 010401, Jul 2007. 158

[172] K. Jacobs, *Stochastic processes for physicists: Understanding noisy systems*. Cambridge University Press, 2010. 171

[173] P. B. Blakie, A. S. Bradley, M. J. Davis, R. J. Ballagh, and C. W. Gardiner, "Dynamics and statistical mechanics of ultra-cold Bose gases using c-field techniques," *Advances in Physics*, vol. 57, pp. 363–455, 2012/02/04 2008. 174, 178, 179

Appendix A

Optimal Matterwave Gravimetry

A.1 QFI of a Particle in a Gravitational Field

Here, we give a more detailed derivation of Eq. (4.10a). Approximating the gravitational field as a linear potential $mg\hat{z}$, the state of the particle after time T is $|\Psi(T)\rangle = \hat{U}_g(T)|\Psi_0\rangle$, where

$$\hat{U}_g(T) = \exp\left[-\frac{iT}{\hbar}\left(\frac{\hat{\mathbf{p}}^2}{2m} + mg\hat{z}\right)\right].\tag{A.1}$$

In order to isolate the contribution due to the gravitational field g, we make use of the Baker-Campbell-Hausdorff (BCH) formula:

$$e^{\hat{X}+\hat{Y}} = e^{\hat{X}}e^{\hat{Y}}e^{-\frac{1}{2}[\hat{X},\hat{Y}]}e^{\frac{1}{6}\left(2[\hat{Y},[\hat{X},\hat{Y}]]+[\hat{X},[\hat{X},\hat{Y}]]\right)},\tag{A.2}$$

where $\hat{X}$ and $\hat{Y}$ are operators satisfying the commutation relations

$$[[[\hat{X},\hat{Y}],\hat{X}],\hat{X}] = [[[\hat{X},\hat{Y}],\hat{X}],\hat{Y}] = [[[\hat{X},\hat{Y}],\hat{Y}],\hat{Y}] = 0.\tag{A.3}$$

This is true for $\hat{X} = -\frac{iT}{\hbar}\frac{\hat{\mathbf{p}}^2}{2m}$ and $\hat{Y} = -\frac{iT}{\hbar}mg\hat{z}$, where

$$\left[\hat{X},\hat{Y}\right] = \frac{igT^2}{\hbar}\hat{p}_z,\tag{A.4a}$$

$$\left[\hat{Y},\left[\hat{X},\hat{Y}\right]\right] = \frac{img^2T^3}{\hbar},\tag{A.4b}$$

$$\left[\hat{X},\left[\hat{X},\hat{Y}\right]\right] = 0.\tag{A.4c}$$

Thus, Eq. (A.2) gives:

$$e^{-\frac{iT}{\hbar}(\frac{\hat{\mathbf{p}}^2}{2m}+mg\hat{z})} = e^{-\frac{iT}{\hbar}\frac{\hat{\mathbf{p}}^2}{2m}}e^{-\frac{iT}{\hbar}mg\hat{z}}e^{-\frac{igT^2}{2\hbar}\hat{p}_z}e^{\frac{img^2T^3}{3\hbar}}.\tag{A.5}$$

We use Eq. (A.2) again with the choice $\hat{X} = \frac{-iT}{\hbar}mg\hat{z}$ and $\hat{Y} = -\frac{igT^2}{2\hbar}\hat{p}_z$, where $\left[\hat{X},\hat{Y}\right] = -\frac{img^2T^3}{2\hbar}$, which allows us to combine $\exp[-i(T/\hbar)mg\hat{z}]$ and $\exp\left[-igT^2\hat{p}_z/(2\hbar)\right]$ into a single exponential:

$$e^{-\frac{iT}{\hbar}mg\hat{z}}e^{-\frac{igT^2}{2\hbar}\hat{p}_z} = e^{-ig\hat{G}_0(T)}e^{-\frac{img^2T^3}{4\hbar}},\tag{A.6}$$

where $\hat{G}_0(T) = \frac{T}{\hbar}\left(\frac{T}{2}\hat{p}_z + m\hat{z}\right)$. Thus, the evolution operator $\hat{U}_g(T)$ can be written as:

$$\hat{U}_g(T) = e^{-\frac{iT}{\hbar}\left(\frac{\hat{\mathbf{P}}^2}{2m} + mg\hat{z}\right)}$$
$$= e^{-i\frac{T}{\hbar}\frac{\hat{\mathbf{P}}^2}{2m}} e^{-ig\hat{G}_0(T)} e^{i\frac{mg^2T^3}{12\hbar}}. \tag{A.7}$$

We can ignore $\exp\left[img^2T^3/(12\hbar)\right]$, since this is just a global phase factor, and so the state of the particle after time T is

$$|\Psi(T)\rangle = e^{-\frac{iT}{\hbar}\frac{\hat{\mathbf{P}}^2}{2m}} e^{-ig\hat{G}_0(T)}|\Psi_0\rangle. \tag{A.8}$$

It is now simple to compute the derivative of $|\Psi(T)\rangle$ with respect to g:

$$|\partial_g\Psi(T)\rangle = -ie^{-\frac{iT}{\hbar}\frac{\hat{\mathbf{P}}^2}{2m}}\hat{G}_0(T)e^{-ig\hat{G}_0(T)}|\Psi_0\rangle. \tag{A.9}$$

Consequently,

$$\langle\partial_g\Psi(T)|\partial_g\Psi(T)\rangle = \langle\Psi_0|\hat{G}_0(T)^2|\Psi_0\rangle, \tag{A.10a}$$

$$\langle\Psi(T)|\partial_g\Psi(T)\rangle = -i\langle\Psi_0|\hat{G}_0(T)|\Psi_0\rangle. \tag{A.10b}$$

Substituting these into Eq. (3.116) gives our final expression for the QFI, Eq. (4.10a).

A.2 QFI of a Particle After KC Interferometry

Here we provide a derivation of Eq. (4.15). The total evolution of a particle due to KC interferometry is given by the unitary operator

$$\hat{U}_{\text{KC}} = \hat{U}_{\frac{\pi}{2}}^{\phi_3}\hat{U}_g(T_2)\hat{U}_\pi^{\phi_2}\hat{U}_g(T_1)\hat{U}_{\frac{\pi}{2}}^{\phi_1}, \tag{A.11}$$

where $\hat{U}_{\frac{\pi}{2}}^{\phi_{1,3}}$ and $\hat{U}_\pi^{\phi_2}$ denote $\pi/2$ (50/50 beam splitting) and π (mirror) pulses, respectively, and the evolution due to the gravitational field, $\hat{U}_g(T)$, was derived above [see Eq. (A.7)]. This assumes that the $\pi/2$ and π pulses are instantaneous (strictly, occur on times much shorter than the interrogation times T_1 and T_2).

To begin, the final $\pi/2$ pulse does not change the QFI, whilst the first $\pi/2$ pulse simply gives a new initial state for the particle [see Eq. (4.12)]:

$$|\Psi_0'\rangle = \hat{U}_{\frac{\pi}{2}}^{\phi_1}|\Psi_0\rangle$$
$$= \frac{1}{\sqrt{2}}\left(|\psi_0\rangle|a\rangle - ie^{i(k_0\hat{z}-\phi_1)}|\psi_0\rangle|b\rangle\right), \tag{A.12}$$

where $|\Psi_0\rangle = |a\rangle|\psi_0\rangle$ and ϕ_1 is the phase of this first laser pulse. Consequently, the QFI can be computed from the product of operators $\hat{U}_g(T_2)\hat{U}_\pi^{\phi_2}\hat{U}_g(T_1)$, provided expectations are taken with respect to the state $|\Psi_0'\rangle$.

As in Appendix [A.1], our goal is to isolate the g-dependence of the evolution. We first consider the product $\hat{U}_g(T_2)\hat{U}_\pi^{\phi_2}$, where [see Eq. (4.12)]

$$\hat{U}_\pi^{\phi_2} = -i\left(e^{-i(k_0\hat{z}-\phi_2)}|a\rangle\langle b| + e^{i(k_0\hat{z}-\phi_2)}|b\rangle\langle a|\right), \tag{A.13}$$

and ϕ_2 is the phase of this mirror pulse. The BCH formula Eq. (A.2) implies that

$$e^{\hat{X}}e^{\hat{Y}}e^{-\frac{1}{2}[\hat{X},\hat{Y}]}e^{\frac{1}{6}\left(2[\hat{Y},[\hat{X},\hat{Y}]]+[\hat{X},[\hat{X},\hat{Y}]]\right)} = e^{\hat{Y}}e^{\hat{X}}e^{\frac{1}{2}[\hat{X},\hat{Y}]}e^{-\frac{1}{6}\left(2[\hat{X},[\hat{X},\hat{Y}]]+[\hat{Y},[\hat{X},\hat{Y}]]\right)}. \tag{A.14}$$

The application of Eq. (A.14) with $\hat{X} = -ig\hat{G}_0(T_2)$ and $\hat{Y}_\pm = \pm ik_0\hat{z}$ gives

$$e^{-ig\hat{G}_0(T_2)}e^{\pm ik_0\hat{z}} = e^{\pm ik_0\hat{z}}e^{-ig\hat{G}_0(T_2)}e^{\mp i\frac{1}{2}gk_0T_2^2}, \tag{A.15}$$

where we have used $\left[\hat{X},\hat{Y}_\pm\right] = \mp igk_0T_2^2/2$. Therefore, after neglecting the global phase factor $\exp\left[img^2T_2^3/(12\hbar)\right]$ in $\hat{U}_g(T)$

$$\begin{aligned}\hat{U}_g(T_2)\hat{U}_\pi^{\phi_2} = -ie^{-\frac{iT_2}{\hbar}\frac{\hat{\mathbf{p}}^2}{2m}}&\left(e^{-i(k_0\hat{z}-\phi_2)}e^{-ig\hat{G}_0(T_2)}e^{i\frac{1}{2}gk_0T_2^2}|a\rangle\langle b|\right.\\&\left.+ e^{i(k_0\hat{z}+\phi_2)}e^{-ig\hat{G}_0(T_2)}e^{-i\frac{1}{2}gk_0T_2^2}|b\rangle\langle a|\right)\\= -ie^{-\frac{iT_2}{\hbar}\frac{\hat{\mathbf{p}}^2}{2m}}&\left(e^{-i(k_0\hat{z}-\phi_2)}e^{i\frac{1}{2}gk_0T_2^2}|a\rangle\langle b| + e^{i(k_0\hat{z}+\phi_2)}e^{-i\frac{1}{2}gk_0T_2^2}|b\rangle\langle a|\right)e^{-ig\hat{G}_0(T_2)}.\end{aligned}$$

Note that $\hat{G}_0(T_2)$ acts only on the motional state of the particle and therefore commutes with any operators that act on the internal states $|a\rangle$ and $|b\rangle$.

Now, the internal states $|a\rangle$ and $|b\rangle$ are the eigenvectors of $\hat{J}_z = \frac{1}{2}\left(|a\rangle\langle a| - |b\rangle\langle b|\right)$ satisfying $\hat{J}_z|a\rangle = \frac{1}{2}|a\rangle$ and $\hat{J}_z|b\rangle = -\frac{1}{2}|b\rangle$. Therefore, for an arbitrary operator $\hat{O}$ which solely acts on the motional state of the particle:

$$e^{\hat{O}\hat{J}_z}|a\rangle = e^{\frac{1}{2}\hat{O}}|a\rangle, \qquad e^{\hat{O}\hat{J}_z}|b\rangle = e^{-\frac{1}{2}\hat{O}}|b\rangle. \tag{A.16}$$

This allows us to write

$$\langle a|e^{-i\frac{1}{2}gk_0T_2^2} = \langle a|e^{-igk_0T_2^2\hat{J}_z} = \langle a|e^{-ig\hat{G}_e}, \tag{A.17a}$$

$$\langle b|e^{i\frac{1}{2}gk_0T_2^2} = \langle b|e^{-igk_0T_2^2\hat{J}_z} = \langle b|e^{-ig\hat{G}_e}, \tag{A.17b}$$

where $\hat{G}_e = k_0T_2^2\hat{J}_z$. Therefore,

$$\hat{U}_g(T_2)\hat{U}_\pi^{\phi_2} = e^{-\frac{iT_2}{\hbar}\frac{\hat{\mathbf{p}}^2}{2m}}\hat{U}_\pi^{\phi_2}e^{-ig\hat{G}_e}e^{-ig\hat{G}_0(T_2)}. \tag{A.18}$$

Next, we again use Eq. (A.14) with $\hat{X} = -ig\hat{G}_0(T_2)$ and $\hat{Y} = -\frac{iT_1}{\hbar}\frac{\hat{\mathbf{p}}^2}{2m}$, where

$$\left[\hat{X},\hat{Y}\right] = -\frac{igT_1T_2}{\hbar}\hat{p}_z, \tag{A.19a}$$

$$\left[\hat{X},\left[\hat{X},\hat{Y}\right]\right] = -\frac{img^2T_1T_2^2}{\hbar}, \tag{A.19b}$$

to obtain

$$e^{-ig\hat{G}_0(T_2)}e^{-i\frac{T_1}{\hbar}\frac{\hat{\mathbf{p}}^2}{2m}} = e^{-i\frac{T_1}{\hbar}\frac{\hat{\mathbf{p}}^2}{2m}}e^{-ig\hat{G}_0(T_2)}e^{-ig\frac{T_1 T_2}{\hbar}\hat{p}_z}e^{i\frac{m}{2\hbar}g^2 T_1 T_2^2}, \tag{A.20}$$

and therefore (ignoring the global phase factor $\exp\left[img^2 T_1 T_2^2/(2\hbar)\right]$)

$$\hat{U}_g(T_2)\hat{U}_\pi^{\phi_2}\hat{U}_g(T_1) = e^{-i\frac{T_2}{\hbar}\frac{\hat{\mathbf{p}}^2}{2m}}\hat{U}_\pi^{\phi_2}e^{-ig\hat{G}_e}e^{-i\frac{T_1}{\hbar}\frac{\hat{\mathbf{p}}^2}{2m}}e^{-ig\hat{G}_0(T_2)}$$
$$\times\, e^{-ig\frac{T_1 T_2}{\hbar}\hat{p}_z}e^{-ig\hat{G}_0(T_1)}. \tag{A.21}$$

We combine the final three exponentials into one, using Eq. (A.2)

$$\hat{U}_g(T_2)\hat{U}_\pi^{\phi_2}\hat{U}_g(T_1) = e^{-i\frac{T_2}{\hbar}\frac{\hat{\mathbf{p}}^2}{2m}}\hat{U}_\pi^{\phi_2}e^{-i\frac{T_1}{\hbar}\frac{\hat{\mathbf{p}}^2}{2m}}e^{-ig\left(\hat{G}_0(T)+\hat{G}_e\right)}, \tag{A.22}$$

where $T = T_1 + T_2$ and we have neglected all the global phases produced during the calculation.

Including the first and second $\pi/2$ pulses (although the second pulse is *not* needed for calculating the QFI), we arrive at the following simplified expression for the full KC interferometer evolution

$$\hat{U}_{\text{KC}} = \hat{U}_0 e^{-ig\left(\hat{G}_0(T)+\hat{G}_e\right)}\hat{U}_{\frac{\pi}{2}}^{\phi_1}, \tag{A.23}$$

where $\hat{U}_0 = \hat{U}_{\frac{\pi}{2}}^{\phi_3}e^{-i\frac{T_2}{\hbar}\frac{\hat{\mathbf{p}}^2}{2m}}\hat{U}_\pi^{\phi_2}e^{-i\frac{T_1}{\hbar}\frac{\hat{\mathbf{p}}^2}{2m}}$ is independent of g. The state of the particle after interrogation time T is therefore

$$|\Psi(T)\rangle = \hat{U}_{\text{KC}}|\Psi_0\rangle = \hat{U}_0 e^{-ig\left(\hat{G}_0(T)+\hat{G}_e\right)}|\Psi_0'\rangle, \tag{A.24}$$

which is Eq. (4.13). Taking the derivative with respect to g gives

$$\langle\partial_g\Psi(T)|\partial_g\Psi(T)\rangle = \langle\Psi_0'|(\hat{G}_0(T)+\hat{G}_e)^2|\Psi_0'\rangle, \tag{A.25a}$$

$$\langle\Psi(T)|\partial_g\Psi(T)\rangle = -i\langle\Psi_0'|(\hat{G}_0(T)+\hat{G}_e)|\Psi_0'\rangle. \tag{A.25b}$$

The QFI is therefore

$$F_Q^{\text{KC}} = 4\text{Var}\left(\hat{G}_0(T)+\hat{G}_e\right), \tag{A.26}$$

where the variance is taken with respect to $|\Psi_0'\rangle$. We use Eq. (A.12) to relate this to expectations taken with respect to the initial state $|\Psi_0\rangle$

$$F_Q^{\text{KC}} = 4\text{Var}(\hat{G}_0(T)) + \frac{1}{4}k_0^2\left(T^2 - 2T_2^2\right)^2, \tag{A.27}$$

which is Eq. (4.15).

A.3 $F_C(\hat{J}_z)$ of KC Interferometer

To calculate the CFI $F_C(\hat{J}_z)$, Eq. (4.19), we need to determine expressions for the probabilities $P_a(T)$ and $P_b(T)$ that the particle is detected in state $|a\rangle$ and $|b\rangle$, respectively, at the interferometer output. This first requires expressing $\hat{U}_{\mathrm{KC}}$ in a more convenient form. To begin, we use Eq. (A.14) with $\hat{X} = -i\frac{T_2}{\hbar}\frac{\hat{\mathbf{p}}^2}{2m}$ and $\hat{Y}_\pm = \pm ik_0\hat{z}$ to obtain

$$e^{-i\frac{T_2}{\hbar}\frac{\hat{\mathbf{p}}^2}{2m}}e^{\pm ik_0\hat{z}} = e^{\pm ik_0\hat{z}}e^{-i\frac{T_2}{\hbar}\frac{\hat{\mathbf{p}}^2}{2m}}e^{\mp i\frac{k_0 T_2}{m}\hat{p}_z}e^{-i\frac{\hbar k_0^2 T_2}{2m}}, \tag{A.28}$$

where we used $[\hat{X}, \hat{Y}_\pm] = \mp\frac{ik_0 T_2}{m}\hat{p}_z$ and $[\hat{Y}_\pm, [\hat{X}, \hat{Y}_\pm]] = \frac{i\hbar k_0^2 T_2}{m}$. This allows us to commute $e^{-i\frac{T_2}{\hbar}\frac{\hat{\mathbf{p}}^2}{2m}}$ and $\hat{U}_\pi^{\phi_2}$:

$$e^{-i\frac{T_2}{\hbar}\frac{\hat{\mathbf{p}}^2}{2m}}\hat{U}_\pi^{\phi_2} = \hat{U}_\pi^{\phi_2}e^{-i\frac{T_2}{\hbar}\frac{\hat{\mathbf{p}}^2}{2m}}e^{-2i\frac{k_0 T_2}{m}\hat{p}_z\hat{J}_z}e^{-i\frac{\hbar k_0^2 T_2}{2m}}, \tag{A.29}$$

where we have again used Eq. (A.16). Neglecting the global phase factor $\exp\left[-i\hbar k_0^2 T_2/(2m)\right]$, we can therefore write Eq. (A.23) in the convenient form

$$\hat{U}_{\mathrm{KC}} = \hat{U}_{\mathrm{int}}\hat{U}_{\mathrm{ext}}\hat{U}_{\frac{\pi}{2}}^{\phi_1}, \tag{A.30}$$

where

$$\hat{U}_{\mathrm{int}} \equiv \hat{U}_{\frac{\pi}{2}}^{\phi_3}\hat{U}_\pi^{\phi_2}e^{-2i\frac{k_0 T_2}{m}\hat{p}_z\hat{J}_z}e^{-ig\hat{G}_e}, \tag{A.31}$$

$$\hat{U}_{\mathrm{ext}} \equiv e^{-i\frac{T}{\hbar}\frac{\hat{\mathbf{p}}^2}{2m}}e^{-ig\hat{G}_0(T)}. \tag{A.32}$$

$\hat{U}_{\mathrm{ext}}$ only acts on the external (i.e. motional) degrees of freedom, whereas $\hat{U}_{\mathrm{int}}$ acts on *both* the internal and motional degrees of freedom. Note that $\hat{U}_{\mathrm{int}}$ and $\hat{U}_{\mathrm{ext}}$ do not commute.

The state of the particle at the output of the interferometer after interrogation time T is therefore

$$\begin{aligned}|\Psi(T)\rangle &= \hat{U}_{\mathrm{int}}\hat{U}_{\mathrm{ext}}\hat{U}_{\frac{\pi}{2}}^{\phi_1}|\Psi_0\rangle \\ &= \frac{1}{\sqrt{2}}\left(\hat{U}_{\mathrm{int}}|a\rangle\hat{U}_{\mathrm{ext}}|\psi_0\rangle - i\hat{U}_{\mathrm{int}}|b\rangle\hat{U}_{\mathrm{ext}}e^{i(k_0\hat{z}-\phi_1)}|\psi_0\rangle\right).\end{aligned} \tag{A.33}$$

From Eq. (4.12) we get

$$\hat{U}_{\frac{\pi}{2}}^{\phi_3}\hat{U}_\pi^{\phi_2} = -\frac{1}{\sqrt{2}}\left(e^{-i(\phi_2-\phi_3)}|a\rangle\langle a| + e^{i(\phi_2-\phi_3)}|b\rangle\langle b|\right) \tag{A.34}$$

$$-\frac{i}{\sqrt{2}}\left(e^{-i(k_0\hat{z}-\phi_2)}|a\rangle\langle b| + e^{i(k_0\hat{z}-\phi_2)}|b\rangle\langle a|\right), \tag{A.35}$$

where ϕ_2 and ϕ_3 are the phases of the second and the third laser pulses, respectively.

Using this and Eq. (A.16), we obtain

$$\hat{U}_{\text{int}}|a\rangle = -\frac{1}{\sqrt{2}}\left[e^{-i(\phi_2-\phi_3)}|a\rangle + ie^{i(k_0\hat{z}-\phi_2)}|b\rangle\right]$$

$$\times e^{-i\frac{k_0T_2}{m}\hat{p}_z}e^{-ig\frac{k_0T_2^2}{2}}, \tag{A.36a}$$

$$\hat{U}_{\text{int}}|b\rangle = -\frac{1}{\sqrt{2}}\left[e^{i(\phi_2-\phi_3)}|b\rangle + ie^{-i(k_0\hat{z}-\phi_2)}|a\rangle\right]$$

$$\times e^{i\frac{k_0T_2}{m}\hat{p}_z}e^{ig\frac{k_0T_2^2}{2}}. \tag{A.36b}$$

Substituting Eqs. (A.36) into Eq. (A.33) gives

$$|\Psi(T)\rangle = -\frac{1}{2}\left[\left(e^{-i(\phi_2-\phi_3)}e^{-i\frac{k_0T_2}{m}\hat{p}_z}e^{-ig\frac{k_0T_2^2}{2}}\hat{U}_{\text{ext}}|\psi_0\rangle\right.\right.$$

$$\left.+ e^{-i(k_0\hat{z}-\phi_2)}e^{i\frac{k_0T_2}{m}\hat{p}_z}e^{\frac{i}{2}gk_0T_2^2}\hat{U}_{\text{ext}}e^{i(k_0\hat{z}-\phi_1)}|\psi_0\rangle\right)|a\rangle$$

$$+ i\left(e^{i(k_0\hat{z}-\phi_2)}e^{-i\frac{k_0T_2}{m}\hat{p}_z}e^{-ig\frac{k_0T_2^2}{2}}\hat{U}_{\text{ext}}|\psi_0\rangle\right.$$

$$\left.\left.- e^{i(\phi_2-\phi_3)}e^{i\frac{k_0T_2}{m}\hat{p}_z}e^{\frac{i}{2}gk_0T_2^2}\hat{U}_{\text{ext}}e^{i(k_0\hat{z}-\phi_1)}|\psi_0\rangle\right)|b\rangle\right]$$

Defining $|\Psi_a(T)\rangle \equiv \langle a|\Psi(T)\rangle$, the probability of finding the particle in the internal state $|a\rangle$ at the output port of the interferometer is

$$P_a(T) = \langle\Psi_a(T)|\Psi_a(T)\rangle$$

$$= \tfrac{1}{2}[1 + \tfrac{1}{2}(e^{i(gk_0T_2^2-\Delta\Phi_{\text{laser}})}\langle\psi_0|\hat{Q}|\psi_0\rangle + \text{h.c}], \tag{A.37}$$

where $\Delta\Phi_{\text{laser}} = \phi_1 - 2\phi_2 + \phi_3$, as we have already defined in Chapter 2 and

$$\hat{Q} \equiv e^{ig\hat{G}_0(T)}e^{i\frac{T}{\hbar}\frac{\hat{P}^2}{2m}}e^{i\frac{k_0T_2}{m}\hat{p}_z}e^{-ik_0\hat{z}}$$

$$\times e^{i\frac{k_0T_2}{m}\hat{p}_z}e^{-i\frac{T}{\hbar}\frac{\hat{P}^2}{2m}}e^{-ig\hat{G}_0(T)}e^{ik_0\hat{z}},$$

$$= e^{i\frac{\hbar k_0^2}{2m}(T_2-T_1)}e^{-igk_0T(T_2-T_1)}e^{-ig\frac{k_0T^2}{2}}e^{i\frac{k_0}{m}(T_2-T_1)\hat{p}_z}. \tag{A.38}$$

This final simplification follows from repeated application of Eq. (A.14), and allows us to express the probability as

$$P_a(T) = \tfrac{1}{2}\left[1 + \tfrac{1}{2}\left(e^{-i\Delta\Phi_{\text{laser}}}e^{i\frac{\hbar k_0^2}{2m}(T_2-T_1)}e^{-igk_0(\frac{T^2}{2}-T_1^2)}\right.\right.$$

$$\left.\left.\times \langle\psi_0|e^{i\frac{k_0}{m}(T_2-T_1)\hat{p}_z}|\psi_0\rangle + \text{h.c}\right)\right]. \tag{A.39}$$

If we choose the phases of our laser pulses such that $\phi_1 = \phi_2 = 0$, $\phi_3 = \pi/2$, thereby operating at the point of maximum sensitivity, we can express the probabilities in the

following way:

$$P_a(T) = \frac{1}{2} \left[1 - \frac{i}{2} \left(\mathcal{C} e^{i(\phi_f - \phi_g)} - \mathcal{C}^* e^{-i(\phi_f - \phi_g)} \right) \right], \tag{A.40a}$$

$$P_b(T) = \frac{1}{2} \left[1 + \frac{i}{2} \left(\mathcal{C} e^{i(\phi_f - \phi_g)} - \mathcal{C}^* e^{-i(\phi_f - \phi_g)} \right) \right], \tag{A.40b}$$

where

$$\phi_f \equiv \frac{\hbar k_0^2}{2m} (T_2 - T_1), \tag{A.41a}$$

$$\phi_g \equiv k_0 g \left(\frac{T^2}{2} - T_1^2 \right), \tag{A.41b}$$

$$\mathcal{C} \equiv \langle \psi_0 | e^{i \frac{k_0}{m} (T_2 - T_1) \hat{p}_z} | \psi_0 \rangle. \tag{A.41c}$$

ϕ_f represents the phase difference due to the non-symmetrical free evolution of the wave-packets in the two arms of the interferometer, while ϕ_g is the phase difference due to gravity. Expressing $\mathcal{C} = |\mathcal{C}| e^{i\vartheta}$ allows us to write Eq. (A.40) in the simplified form of Eqs. (4.18). Here $|\mathcal{C}|$ is interpreted as the *fringe contrast* and $\alpha = \phi_f - \phi_g + \vartheta$ denotes the total phase shift.

If we measure the population difference of the two internal states, $\hat{J}_z$, at the output of the interferometer, the CFI is given by

$$F_C(\hat{J}_z) = \sum_{j=a,b} \frac{(\partial_g P_j)^2}{P_j} = \frac{(\partial_g P_a)^2}{P_a P_b}, \tag{A.42}$$

where the last equality follows from the relation $P_a + P_b = 1 \Rightarrow \partial_g P_a = -\partial_g P_b$. Noting that

$$P_a(T) P_b(T) = \frac{1}{4} \left(1 - |\mathcal{C}|^2 \sin^2 \alpha \right), \tag{A.43a}$$

$$\partial_g P_a(T) = -\frac{1}{2} |\mathcal{C}| k_0 \left(\frac{T^2}{2} - T_1^2 \right) \cos \alpha, \tag{A.43b}$$

we arrive at Eq. (4.19).

A.4 Beam Splitter Transformation: Derivation of Eq. (4.12)

A Raman beam splitter is typically modelled by the Hamiltonian

$$\hat{H}_{\mathrm{BS}} = \frac{\hat{\mathbf{p}}^2}{2m} - \hbar \delta |b\rangle \langle b| + \frac{\hbar \Omega}{2} (|b\rangle \langle a| e^{i(k_0 \hat{z} - \phi)} + \mathrm{h.c.}), \tag{A.44}$$

where δ is the two-photon detuning and $\Omega = \Omega_1 \Omega_2 / \Delta$ is the effective two-photon Rabi frequency, which depends on the single-photon Rabi frequencies $\Omega_{1,2}$ and the single-photon

detuning Δ [170, 171]. The two-photon detuning is typically set to the two-photon resonance condition $\delta = \hbar k_0^2/(2m)$. Evolution under this Hamiltonian for a duration Δt is given by the unitary time-evolution operator

$$
\begin{aligned}
U_\theta^\phi &= \exp\left[\frac{-i\Delta t}{\hbar}\hat{H}_{BS}\right] \\
&= e^{-i\left(\frac{\hat{\mathbf{p}}^2}{2m\hbar} - \frac{\hbar k_0^2}{2m}|b\rangle\langle b|\right)\frac{\theta}{\Omega} - i\frac{\theta}{2}\left(|b\rangle\langle a|e^{i(k_0\hat{z}-\phi)}+\text{h.c.}\right)},
\end{aligned}
\tag{A.45}
$$

where we have defined $\theta = \Omega\Delta t$. If $\hbar\Omega$ is significantly greater than the spread in kinetic energy of the initial state, we can ignore the first term and obtain

$$
\begin{aligned}
U_\theta^\phi &= \exp\left[-i\frac{\theta}{2}\left(|b\rangle\langle a|e^{i(k_0\hat{z}-\phi)} + \text{h.c.}\right)\right] \\
&= \hat{1}\cos\left(\tfrac{\theta}{2}\right) - i(|b\rangle\langle a|e^{i(k_0\hat{z}-\phi)} + \text{h.c.})\sin\left(\tfrac{\theta}{2}\right),
\end{aligned}
\tag{A.46}
$$

which is Eq. (4.12).

Fig. [A.1] shows the QFI and CFI, when the evolution due to the beam splitter and mirror pulses is treated as Schrödinger evolution under Hamiltonian Eq. (A.44). This evolution was solved numerically for different values of Δt. We used the same initial state as Fig. [2(a)]. We set Ω such that $\Omega\Delta t = \pi/2$ for the two beam splitter pulses, and the duration of the interaction was doubled for the mirror pulse, resulting in $\Omega(2\Delta t) = \pi$. We find excellent agreement with the ideal beam splitter case as long as $\Delta t \ll T_\pi$. In the regime $\Delta t \sim T_\pi$, there is significant motional dynamics during the beam splitter period, and our approximation is no longer valid. For example, for the maximum value of Δt simulated ($\Delta t = 0.4T_\pi$), the total interferometer sequence time, which is the time from the commencement of the first beam splitter to the conclusion of the second beam splitter, is $3.6T_\pi$ (compared to $2T_\pi$ for instantaneous beam splitters). For typical experiments, such as Ref. [35], $\Delta t/T_\pi \sim 10^{-4}$.
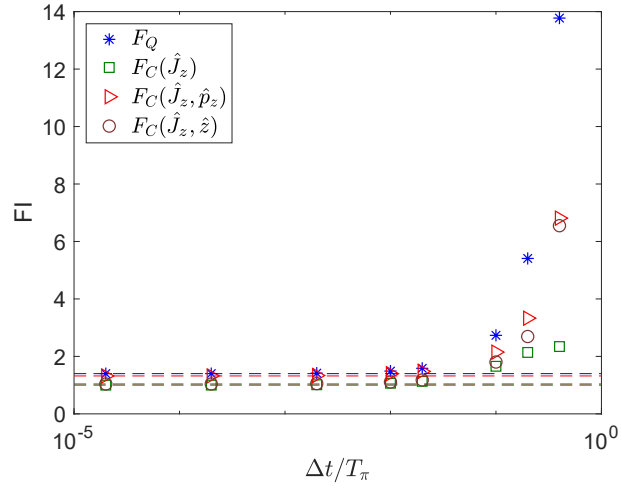
Figure A.1: (a) QFI and CFI computed using Eq. (A.44) rather than Eq. (A.46) as a function of Δt. Provided $\Delta t/T_\pi \ll 1$, Eq. (A.46) (shown by dashed lines of the appropriate colour) is an excellent approximation to the true dynamics. Fisher information is presented in units of $k_0^2 T_\pi^4$.

Appendix B

Quantum Non Demolition Measurements of a BEC

B.1 Introduction

We consider the combined signal

$$\hat{S}_2(\tau) = \hat{J}_z(\tau) - \hat{J}_z^{\text{inf}}(\tau), \tag{B.1}$$

where

$$\hat{J}_z^{\text{inf}}(\tau) = G\hat{S}_b(\tau) \qquad \hat{S}_b(\tau) = \hat{Y}_2(\tau) - \hat{Y}_1(\tau). \tag{B.2}$$

For simplicity in the following we will present the time dependence explicitly only in our final results or when it is considered necessary. The variance of $\hat{S}_2$ would be given by

$$\text{Var}(\hat{S}_2) = \text{Var}(\hat{J}_z) + G^2\text{Var}(\hat{S}_b) - 2G\text{Cov}(\hat{J}_z, \hat{S}_b), \tag{B.3}$$

since $\text{Cov}(\hat{J}_z, \hat{S}_b) = \text{Cov}(\hat{S}_b, \hat{J}_z)$. We minimise $\text{Var}(\hat{S}_2)$ with respect to G

$$G = \frac{\text{Cov}(\hat{J}_z, \hat{S}_b)}{\text{Var}(\hat{S}_b)}. \tag{B.4}$$

Inserting that back in Eq. (B.3) we get

$$\text{Var}(\hat{S}_2) = \text{Var}(\hat{J}_z) - \frac{\text{Cov}^2(\hat{J}_z, \hat{S}_b)}{\text{Var}(\hat{S}_b)}. \tag{B.5}$$

So, in order to calculate $\text{Var}(\hat{S}_2)$ we need the covariance between $\hat{J}_z$ and $\hat{S}_b$, $\text{Cov}(\hat{J}_z, \hat{S}_b)$, and the variance of the phase quadrature of the light field $\text{Var}(\hat{Y}_1)$, since $\text{Var}(\hat{Y}_1) = \text{Var}(\hat{Y}_2)$ and $\text{Cov}(\hat{Y}_2, \hat{Y}_1) = 0$, thus $\text{Var}(\hat{S}_b) = 2\text{Var}(\hat{Y}_1)$. At the end we calculate the squeezing parameter, which in our case $(\theta = 0)$ is given by

$$\xi_{s_2} = \sqrt{N_a}\frac{\sqrt{\text{Var}(\hat{S}_2)}}{\langle \hat{J}_x \rangle}. \tag{B.6}$$

B.2 No Spontaneous Emission

B.2.1 Atomic Expectation Values

The atomic equations with no spontaneous emission are given by

$$\hat{a}_1(t) = \hat{a}_1(0)e^{i\frac{g^2}{\Delta}\int_0^t \hat{b}_{01}^\dagger(t')\hat{b}_{01}(t')dt'} \tag{B.7}$$

$$\hat{a}_1^\dagger(t) = \hat{a}_1^\dagger(0)e^{-i\frac{g^2}{\Delta}\int_0^t \hat{b}_{01}^\dagger(t')\hat{b}_{01}(t')dt'}. \tag{B.8}$$

Hence, the atomic population operator is independent of time

$$\hat{N}_{a_1}(t) = \hat{a}_1^\dagger(t)\hat{a}_1(t) = \hat{a}_1^\dagger(0)\hat{a}_1(0). \tag{B.9}$$

We consider that our total state initially is given by the product

$$|\Psi\rangle = |\alpha_1\rangle \otimes |\alpha_2\rangle \otimes |\beta_1\rangle \otimes |\beta_2\rangle \otimes |0\rangle, \tag{B.10}$$

meaning that the atomic ensemble, as well as the two light fields are in coherent states while the bath is described by the vacuum state, giving the following expectation values

$$\hat{a}_1(0)|\alpha_1\rangle = \sqrt{\frac{N_a}{2}}|\alpha_1\rangle, \qquad \hat{b}_{01}(t)|\beta_1\rangle = \beta_0|\beta_1\rangle, \qquad \hat{q}_{1_{\text{in}}}(t)|0\rangle = 0|0\rangle$$

$$\hat{a}_2(0)|\alpha_2\rangle = \sqrt{\frac{N_a}{2}}|\alpha_2\rangle \qquad \hat{b}_{02}(t)|\beta_2\rangle = \beta_0|\beta_2\rangle \qquad \hat{q}_{2_{in}}(t)|0\rangle = 0|0\rangle, \tag{B.11}$$

where we have used again $\hat{b}_{0j}(t) = \hat{b}_j(z_L, t)$ with $j = 1, 2$ for simplicity, and we have considered that $\alpha_1(0) = \alpha_2(0) = \sqrt{N_a/2}$ and $\hat{b}_{01}(t) = \hat{b}_{02}(t) = \beta_0$. Now it is really simple to calculate the atomic expectation values in that case

$$\langle\hat{N}_{a_1}(t)\rangle = \frac{N_a}{2}, \qquad \langle\hat{N}_{a_1}^2(t)\rangle = \langle\hat{N}_{a_1}^2(t')\rangle = \langle\hat{N}_{a_1}^2(0)\rangle = \frac{N_a}{2} + \frac{N_a^2}{4}. \tag{B.12}$$

B.2.2 Phase Quadrature

The light equation in the case of no spontaneous emission is

$$\hat{b}_1(z_R, t) = \hat{b}_{01}(t)e^{i\frac{g^2}{c\Delta}\hat{a}_1^\dagger(t)\hat{a}_1(t)}, \tag{B.13}$$

We select a specific mode of the light field

$$\hat{b}_1(\tau) = \frac{\sqrt{c}}{\sqrt{\tau}}\int_0^\tau \hat{b}_1(z_R, t)dt. \tag{B.14}$$

Here the atomic population is constant, thus

$$\hat{b}_1(\tau) = \frac{\sqrt{c}}{\sqrt{\tau}}e^{i\frac{g^2}{c\Delta}\hat{a}_1^\dagger(t)\hat{a}_1(t)}\int_0^\tau \hat{b}_{01}(t)dt. \tag{B.15}$$

We know that the incident light field obeys the following commutation relation $[\hat{b}_{01}(t), \hat{b}_{01}^\dagger(t')] = \frac{1}{c}\delta(t - t')$. We find the phase quadrature of the specific mode

$$\hat{Y}_1(\tau) \equiv i(\hat{b}_1(\tau) - \hat{b}_1^\dagger(\tau)) = i\frac{\sqrt{c}}{\sqrt{\tau}}\left(e^{i\frac{g^2}{c\Delta}\hat{a}_1^\dagger(t)\hat{a}_1(t)}\int_0^\tau \hat{b}_{01}(t)dt - e^{-i\frac{g^2}{c\Delta}\hat{a}_1^\dagger(t)\hat{a}_1(t)}\int_0^\tau \hat{b}_{01}^\dagger(t)dt\right). \tag{B.16}$$

We make the small angle approximation

$$\frac{g^2}{c\Delta}\hat{a}_1^\dagger(t)\hat{a}_1(t) << 1, \tag{B.17}$$

and we get

$$\hat{Y}_1(\tau) \approx \hat{Y}_{1_{\text{in}}}(\tau) - \frac{g^2}{\sqrt{c\tau}\Delta}\hat{a}_1^\dagger(\tau)\hat{a}_1(\tau)\int_0^\tau \left(\hat{b}_{01}(t) + \hat{b}_{01}^\dagger(t)\right)dt, \tag{B.18}$$

where

$$\hat{Y}_{1_{\text{in}}}(\tau) = i\frac{\sqrt{c}}{\sqrt{\tau}}\int_0^\tau \left(\hat{b}_{01}(t) - \hat{b}_{01}^\dagger(t)\right)dt. \tag{B.19}$$

We calculate the expectation value of the phase quadrature

$$\langle\hat{Y}_1(\tau)\rangle \approx -\frac{g^2 N_a \beta_0 \tau}{\Delta\sqrt{c\tau}}, \tag{B.20}$$

where we have used that $\langle\hat{Y}_{1_{\text{in}}}(\tau)\rangle = 0$ and assumed that $\beta_0 = \beta_0^*$. We calculate the square of the phase quadrature

$$\hat{Y}_1^{\,2}(\tau) \approx \hat{Y}_{1_{\text{in}}}^2(\tau) + \frac{g^4}{c\tau\Delta^2}\hat{a}_1^\dagger(\tau)\hat{a}_1(\tau)\hat{a}_1^\dagger(\tau)\hat{a}_1(\tau)\int_0^\tau\int_0^\tau dtdt'\,\left(\hat{b}_{01}(t) + \hat{b}_{01}^\dagger(t)\right)\left(\hat{b}_{01}(t') + \hat{b}_{01}^\dagger(t')\right). \tag{B.21}$$

For simplicity we calculate separately

$$Q_1 = \int_0^\tau\int_0^\tau dtdt'\,\left(\hat{b}_{01}(t)\hat{b}_{01}(t') + \hat{b}_{01}(t)\hat{b}_{01}^\dagger(t') + \hat{b}_{01}^\dagger(t)\hat{b}_{01}(t') + \hat{b}_{01}^\dagger(t)\hat{b}_{01}^\dagger(t')\right). \tag{B.22}$$

After using the commutation relation $\left[\hat{b}_{01}(t), \hat{b}_{01}^\dagger(t')\right] = \frac{1}{c}\delta(t - t')$ and the delta function property $\int_0^\tau \delta(t - t')dt' = 1$ we obtain

$$\langle Q_1\rangle = 4\beta_0^2\tau^2 + \frac{\tau}{c}. \tag{B.23}$$

Making use of the same commutation relation and the same property of the delta function we find that $\langle\hat{Y}_{1_{\text{in}}}^2(\tau)\rangle = 1$. Thus,

$$\langle\hat{Y}_1^2(\tau)\rangle \approx 1 + \frac{g^4}{c\tau\Delta^2}\left(\frac{N_a}{2} + \frac{N_a^2}{4}\right)\left(4\beta_0^2\tau^2 + \frac{\tau}{2c}\right), \tag{B.24}$$

where we have used Eq. (B.12). For simplicity, we can ignore the last term of Eq. (B.24) since $4\beta_0^2\tau^2 >> \tau/2c$

$$\langle \hat{Y}_1^2(\tau) \rangle \approx 1 + \frac{4g^4\beta_0^2\tau^2}{c\tau\Delta^2}\left(\frac{N_a}{2} + \frac{N_a^2}{4}\right). \tag{B.25}$$

From Eq. (B.20) we have

$$\langle \hat{Y}_1(\tau) \rangle^2 \approx \frac{g^4\beta_0^2 N_a^2 \tau^2}{c\tau\Delta^2}. \tag{B.26}$$

Hence, we finally have

$$\mathrm{Var}(\hat{Y}_1(\tau)) \approx 1 + 2\chi_{\mathrm{ns}}^2 N_a N_{\mathrm{ph}}, \tag{B.27}$$

and

$$\mathrm{Var}(\hat{S}_b) = 2\mathrm{Var}(\hat{Y}_1(\tau)) \approx 2 + 4\chi_{\mathrm{ns}}^2 N_a N_{\mathrm{ph}}, \tag{B.28}$$

where we have defined

$$\chi_{\mathrm{ns}} \equiv \frac{g^2}{c\Delta} \qquad N_{\mathrm{ph}} \equiv \beta_0^2\tau. \tag{B.29}$$

B.2.3 Covariances

The covariance of $\hat{J}_z(\tau)$ and $\hat{S}_b(\tau)$ is defined as

$$\mathrm{Cov}(\hat{J}_z(\tau), \hat{S}_b(\tau)) = \langle \hat{J}_z(\tau)\hat{S}_b(\tau) \rangle - \langle \hat{J}_z(\tau) \rangle \langle \hat{S}_b(\tau) \rangle. \tag{B.30}$$

We know that $\langle \hat{S}_b(\tau) \rangle = 0$, since $\hat{S}_b = \hat{Y}_2 - \hat{Y}_1$. Hence,

$$\mathrm{Cov}(\hat{J}_z(\tau), \hat{S}_b(\tau)) = \langle \hat{J}_z(\tau)\hat{Y}_2(\tau) \rangle - \langle \hat{J}_z(\tau)\hat{Y}_1(\tau) \rangle. \tag{B.31}$$

Using $\hat{J}_z(\tau) = (\hat{N}_{a_1}(\tau) - \hat{N}_{a_2}(\tau))/2$, Eq. (B.18) and the atomic expectation values from Sec. (B.2.1) we obtain

$$\mathrm{Cov}(\hat{J}_z(\tau), \hat{S}_b(\tau)) \approx \chi_{\mathrm{ns}} N_a \sqrt{N_{\mathrm{ph}}}. \tag{B.32}$$

B.2.4 Quantum Enhancement Parameter ξ_s

Inserting Eq. (B.32) and (B.28) in (B.5) we obtain

$$\mathrm{Var}(\hat{S}_2(\tau)) \approx \frac{N_a}{4}\left(1 - \frac{\chi_{\mathrm{ns}}^2 N_{\mathrm{ph}} N_a}{\chi_{\mathrm{ns}}^2 N_{\mathrm{ph}} N_a + 1/2}\right). \tag{B.33}$$

Using the atomic equations of motion we find for small exponents $\chi_{\mathrm{ns}}^2 N_{\mathrm{ph}} << 1$

$$\langle \hat{J}_x(\tau) \rangle \approx \frac{N_a}{2}e^{-\chi_{\mathrm{ns}}^2 N_{\mathrm{ph}}}. \tag{B.34}$$

Finally, from Eq. (B.6) we obtain

$$\xi_{s_2}^{ns}(\tau) \approx e^{\chi_{\mathrm{ns}}^2 N_{\mathrm{ph}}}\left(1 - \frac{\chi_{\mathrm{ns}}^2 N_{\mathrm{ph}} N_a}{\chi_{\mathrm{ns}}^2 N_{\mathrm{ph}} N_a + 1/2}\right)^{1/2}. \tag{B.35}$$

B.3   Spontaneous Emission

B.3.1   Atomic Expectation Values

In the case where we have incorporated spontaneous emission the calculation of the atomic expectation values is more complicated, since we use the following atomic equations

$$\hat{a}_1(t) = \hat{a}_1(0)e^{ig^2(\Omega+i\Gamma)\int_0^t \hat{b}_{01}^\dagger(t')\hat{b}_{01}(t')dt'} +$$

$$+ \frac{g\sqrt{\gamma_3}}{\Delta - i\gamma_3/2}e^{ig^2(\Omega+i\Gamma)\int_0^t \hat{b}_{01}^\dagger(t')\hat{b}_{01}(t')dt'} \int_0^t dt'\hat{b}_{01}^\dagger(t')\hat{q}_{1_{\text{in}}}(t')e^{-ig^2(\Omega+i\Gamma)\int_0^{t'} \hat{b}_{01}^\dagger(t'')\hat{b}_{01}(t'')dt''}$$

$$\text{(B.36a)}$$

$$\hat{a}_1^\dagger(t) = \hat{a}_1^\dagger(0)e^{-ig^2(\Omega-i\Gamma)\int_0^t \hat{b}_{01}^\dagger(t')\hat{b}_{01}(t')dt'} +$$

$$+ \frac{g\sqrt{\gamma_3}}{\Delta + i\gamma_3/2}e^{-ig^2(\Omega-i\Gamma)\int_0^t \hat{b}_{01}^\dagger(t')\hat{b}_{01}(t')dt'} \int_0^t dt'\hat{b}_{01}(t')\hat{q}_{1_{\text{in}}}^\dagger(t')e^{ig^2(\Omega-i\Gamma)\int_0^{t'} \hat{b}_{01}^\dagger(t'')\hat{b}_{01}(t'')dt''}.$$

$$\text{(B.36b)}$$

For simplicity we assume that the intensity operator in the exponentials does not depend on time, namely is a constant number $\hat{b}_{01}^\dagger(t)\hat{b}_{01}(t) \approx \beta_0^2$. We essentially assume here that the atomic loss is due to the average field intensity. We also ignore the unitary part of the exponentials, since they would cancel out during the calculation of the atomic expectation values. So, we finally have

$$\hat{a}_1(t) = \underbrace{\sqrt{\epsilon(t)}\hat{a}_1(0)}_{\hat{A}_1(t)} + \underbrace{\frac{g\sqrt{\gamma_3}}{\Delta - i\gamma_3/2}\sqrt{\epsilon(t)}\int_0^t \sqrt{\epsilon^{-1}(t')}\hat{b}_{01}^\dagger(t')\hat{q}_{1_{\text{in}}}(t')dt'}_{\hat{A}_2(t)} \qquad \text{(B.37)}$$

$$\hat{a}_1^\dagger(t) = \underbrace{\sqrt{\epsilon(t)}\hat{a}_1^\dagger(0)}_{\hat{A}_1^\dagger(t)} + \underbrace{\frac{g\sqrt{\gamma_3}}{\Delta + i\gamma_3/2}\sqrt{\epsilon(t)}\int_0^t \sqrt{\epsilon^{-1}(t')}\hat{b}_{01}(t')\hat{q}_{1_{\text{in}}}^\dagger(t')dt'}_{\hat{A}_2^\dagger(t)}, \qquad \text{(B.38)}$$

where we have defined

$$\epsilon(t) \equiv e^{-2g^2\Gamma\beta_0^2 t}. \qquad \text{(B.39)}$$

We calculate the expectation value of atoms in state $|1\rangle$

$$\langle \hat{N}_{a_1}(t)\rangle = \langle \hat{a}_1^\dagger(t)\hat{a}_1(t)\rangle = \frac{N_a}{2}\epsilon(t), \qquad \text{(B.40)}$$

where $\epsilon(t)$ indicates the atomic rate of loss in our system at time t. Now we are going to calculate the more complicated expectation value $\langle \hat{N}_{a_1}(t)\hat{N}_{a_1}(t')\rangle$. We have named each

term of Eq. (B.37) and (B.38) for simplicity, in order to clearly show which terms finally survive

$$\langle \hat{N}_{a_1}(t)\hat{N}_{a_1}(t')\rangle = \langle \hat{A}_1^\dagger(t)\hat{A}_1(t)\hat{A}_1^\dagger(t')\hat{A}_1(t')\rangle + \langle \hat{A}_1^\dagger(t)\hat{A}_2(t)\hat{A}_2^\dagger(t')\hat{A}_1(t')\rangle, \tag{B.41}$$

where all the other terms in this product are zero since $\langle \hat{q}_{1_{\text{in}}}\rangle = \langle \hat{q}_{1_{\text{in}}}^\dagger\rangle = \langle \hat{q}_{1_{\text{in}}}^\dagger \hat{q}_{1_{\text{in}}}\rangle = 0$. The first term of the above equation is easily calculated

$$\langle \hat{A}_1^\dagger(t)\hat{A}_1(t)\hat{A}_1^\dagger(t')\hat{A}_1(t')\rangle = \left(\frac{N_a}{2} + \frac{N_a^2}{4}\right)\epsilon(t)\epsilon(t'). \tag{B.42}$$

However the second term is more complicated

$$\langle \hat{A}_1^\dagger(t)\hat{A}_2(t)\hat{A}_2^\dagger(t')\hat{A}_1(t')\rangle = 2g^2\Gamma\epsilon(t)\epsilon(t')\langle \hat{a}_1^\dagger(0)\hat{a}_1(0)\rangle\times$$
$$\times \int_0^t\int_0^{t'}d\xi ds \sqrt{\epsilon^{-1}(s)}\sqrt{\epsilon^{-1}(\xi)}\langle \hat{b}_{01}^\dagger(s)\hat{b}_{01}(\xi)\rangle\langle \hat{q}_{1_{\text{in}}}(s)\hat{q}_{1_{\text{in}}}^\dagger(\xi)\rangle. \tag{B.43}$$

We use the commutation relation for the temporal part of the Langevin noise

$$\left[\hat{q}_{1_{\text{in}}}(s), \hat{q}_{1_{\text{in}}}^\dagger(\xi)\right] = \delta(\xi - s). \tag{B.44}$$

We also make use of the following property of the delta function

$$\int_0^{t'}d\xi f(\xi)\delta(\xi - s) = f(s)\Theta(t' - s), \tag{B.45}$$

where $\Theta(t' - s)$ is the Heaviside step function and using $\langle \hat{b}_{01}^\dagger(s)\hat{b}_{01}(s)\rangle = \beta_0^2$ we obtain

$$\langle \hat{A}_1^\dagger(t)\hat{A}_2(t)\hat{A}_2^\dagger(t')\hat{A}_1(t')\rangle = g^2\Gamma N_a\beta_0^2\epsilon(t)\epsilon(t')\int_0^t ds\, \epsilon^{-1}(s)\Theta(t' - s). \tag{B.46}$$

For $t \geq t'$ we have

$$\langle \hat{A}_1^\dagger(t)\hat{A}_2(t)\hat{A}_2^\dagger(t')\hat{A}_1(t')\rangle = \frac{N_a}{2}\epsilon(t)\left(1 - \epsilon(t')\right), \tag{B.47}$$

and using Eq. (B.41), (B.42) and (B.47) we get

$$\langle \hat{N}_{a_1}(t)\hat{N}_{a_1}(t')\rangle = \frac{N_a^2}{4}\epsilon(t)\epsilon(t') + \frac{N_a}{2}\epsilon(t), \tag{B.48}$$

while for $t < t'$ we have

$$\langle \hat{A}_1^\dagger(t)\hat{A}_2(t)\hat{A}_2^\dagger(t')\hat{A}_1(t')\rangle = \frac{N_a}{2}\epsilon(t')\left(1 - \epsilon(t)\right), \tag{B.49}$$

and

$$\langle \hat{N}_{a_1}(t)\hat{N}_{a_1}(t')\rangle = \frac{N_a^2}{4}\epsilon(t)\epsilon(t') + \frac{N_a}{2}\epsilon(t'). \tag{B.50}$$

We notice that we obtain the same result for the double integral with respect to t and t' for both cases, $t \geq t'$ and for $t < t'$

$$\int_0^\tau \int_0^\tau dt\, dt' \, \langle \hat{N}_{a_1}(t)\hat{N}_{a_1}(t') \rangle = \frac{N_a^2}{4}I_1^2 + \frac{N_a}{2}I_1\tau, \tag{B.51}$$

but distinguishing between the two cases would be important when we calculate the covariance of $\hat{J}_z(\tau)$ and $\hat{S}_b(\tau)$. For simplicity, we have also defined

$$I_1(\tau) \equiv \int_0^\tau dt\, \epsilon(t) = \frac{1 - \epsilon(\tau)}{2g^2\Gamma\beta_0^2}. \tag{B.52}$$

We can now calculate

$$\int_0^\tau dt \langle \hat{N}_{a_1}(t) \rangle = \frac{N_a}{2}I_1. \tag{B.53}$$

B.3.2 Phase Quadrature

In the case of spontaneous emission the photon operator is given by the following equation

$$\hat{b}_1(z_R, t) = \hat{b}_{01}(t)e^{i\frac{g^2}{c}(\Omega + i\Gamma)\hat{a}_1^\dagger(t)\hat{a}_1(t)} + \frac{g}{c}\frac{\sqrt{\gamma_3}}{\Delta - i\gamma_3/2}\hat{a}_1^\dagger(t)\hat{q}_{1\text{in}}(t). \tag{B.54}$$

Again, we define the phase quadrature operator of a specific mode of the light field

$$\hat{Y}_1(\tau) = i(\hat{b}_1(\tau) - \hat{b}_1^\dagger(\tau)), \tag{B.55}$$

where

$$\hat{b}_1(t) = \frac{\sqrt{c}}{\sqrt{\tau}}\int_0^\tau \hat{b}_{01}(t)dt. \tag{B.56}$$

Making the small angle approximation $g^2(\Omega + i\Gamma)\hat{a}_1^\dagger\hat{a}_1/c << 1$ we obtain

$$\hat{Y}_1 \approx \hat{Y}_{1\text{in}} - \frac{g^2\Omega}{\sqrt{c\tau}}\int_0^\tau \left(\hat{b}_{01}(t) + \hat{b}_{01}^\dagger(t)\right)\hat{a}_1^\dagger(t)\hat{a}_1(t)dt - \frac{g^2\Gamma}{\sqrt{c\tau}}\int_0^\tau \left(\hat{b}_{01}(t) - \hat{b}_{01}^\dagger(t)\right)\hat{a}_1^\dagger(t)\hat{a}_1(t)dt +$$

$$+ i\frac{g\Omega\sqrt{\gamma_3}}{\sqrt{c\tau}}\int_0^\tau dt \left(\hat{q}_{1\text{in}}(t)\hat{a}_1^\dagger(t) - \hat{q}_{1\text{in}}^\dagger(t)\hat{a}_1(t)\right) - i\frac{g\Gamma\sqrt{\gamma_3}}{\sqrt{c\tau}}\int_0^\tau dt \left(\hat{q}_{1\text{in}}(t)\hat{a}_1^\dagger(t) + \hat{q}_{1\text{in}}^\dagger(t)\hat{a}_1(t)\right), \tag{B.57}$$

where

$$\hat{Y}_{1\text{in}}(\tau) \equiv i\frac{\sqrt{c}}{\sqrt{\tau}}\int_0^\tau dt \left(\hat{b}_{01}(t) - \hat{b}_{01}^\dagger(t)\right). \tag{B.58}$$

We calculate the expectation value of $\hat{Y}_1(\tau)$

$$\langle \hat{Y}_1(\tau) \rangle \approx -\frac{2\beta_0\Omega g^2}{\sqrt{c\tau}}\int_0^\tau dt \langle \hat{N}_{a_1}(t) \rangle. \tag{B.59}$$

From Eq. (B.53) we get

$$\langle \hat{Y}_1 \rangle^2 \approx \frac{g^4 \Omega^2 \beta_0^2 N_a^2 I_1^2}{c\tau}. \tag{B.60}$$

Now we are going to calculate $\langle \hat{Y}_1^2 \rangle$, where for simplicity we keep only the terms coming from the the first two terms of Eq. (B.57), since they are the dominant terms

$$\langle \hat{Y}_1^2 \rangle \approx 1 + \frac{4g^4 \Omega^2}{c\tau} \beta_0^2 \int_0^\tau \int_0^\tau dt dt' \langle \hat{N}_{a_1}(t') \hat{N}_{a_1}(t) \rangle. \tag{B.61}$$

Substituting Eq. (B.51) in (B.61) and using (B.60) we obtain

$$\mathrm{Var}(\hat{Y}_1(\tau)) \approx 1 + 2\chi_1^2 N_{\mathrm{ph}} N_a \overline{\epsilon(\tau)}, \tag{B.62}$$

where we have defined $\chi_1 \equiv \frac{g^2 \Omega}{c}$ and $\overline{\epsilon(\tau)} = \frac{1}{\tau} \int_0^\tau \epsilon(t) dt$ which is the time average of the decay. We notice that $\chi_1 = \chi_{\mathrm{ns}}$ in the no spontaneous emission case ($\gamma_3 = 0$). As we mentioned before $\mathrm{Var}(\hat{S}_b) = 2\mathrm{Var}(\hat{Y}_1)$, thus

$$\mathrm{Var}(\hat{S}_b(\tau)) \approx 2 + 4\chi_1^2 N_{\mathrm{ph}} N_a \overline{\epsilon(\tau)}. \tag{B.63}$$

B.3.3   Covariances

Again, the covariance of $\hat{J}_z$ and $\hat{S}_b$ is given by $\mathrm{Cov}(\hat{J}_z(\tau), \hat{S}_b(\tau)) = \langle \hat{J}_z(\tau)\hat{Y}_2(\tau) \rangle - \langle \hat{J}_z(\tau)\hat{Y}_1(\tau) \rangle$, which gives

$$\mathrm{Cov}(\hat{J}_z(\tau), \hat{S}_b(\tau)) = \frac{2g^2 \Omega \beta_0}{\sqrt{c\tau}} \int_0^\tau dt \left(\langle \hat{N}_{a_1}(\tau)\hat{N}_{a_1}(t) \rangle - \langle \hat{N}_{a_1}(\tau)\hat{N}_{a_2}(t) \rangle \right), \tag{B.64}$$

since

$$\langle \hat{N}_{a_1}(\tau)\hat{N}_{a_1}(t) \rangle = \langle \hat{N}_{a_2}(\tau)\hat{N}_{a_2}(t) \rangle \qquad \langle \hat{N}_{a_1}(\tau)\hat{N}_{a_2}(t) \rangle = \langle \hat{N}_{a_2}(\tau)\hat{N}_{a_1}(t) \rangle. \tag{B.65}$$

Now we have to be a bit more careful, compared to the no spontaneous emission case, because we have two different expressions for $\langle \hat{N}_{a_1}(t)\hat{N}_{a_1}(t') \rangle$ depending on whether $t \geq t'$ or $t < t'$. That's why we are going to calculate $\mathrm{Cov}(\hat{S}_b(\tau), \hat{J}_z(\tau))$ as well

$$\mathrm{Cov}(\hat{S}_b(\tau), \hat{J}_z(\tau)) = \frac{2g^2 \Omega \beta_0}{\sqrt{c\tau}} \int_0^\tau dt \left(\langle \hat{N}_{a_1}(t)\hat{N}_{a_1}(\tau) \rangle - \langle \hat{N}_{a_1}(t)\hat{N}_{a_2}(\tau) \rangle \right). \tag{B.66}$$

For the first covariance, where $\tau \geq t$ we use Eq. (B.48), hence

$$\int_0^\tau dt \langle \hat{N}_{a_1}(\tau)\hat{N}_{a_1}(t) \rangle = \frac{N_a^2}{4} \epsilon(\tau) I_1 + \frac{N_a}{2} \epsilon(\tau) \tau. \tag{B.67}$$

We calculate the simpler term

$$\langle \hat{N}_{a_1}(\tau)\hat{N}_{a_2}(t) \rangle = \frac{N_a^2}{4} \epsilon(\tau)\epsilon(t), \tag{B.68}$$

since $\hat{a}_1(t)$ commutes with $\hat{a}_2(t')$ for all t and t'. Thus,

$$\int_0^\tau dt \, \langle \hat{N}_{a_1}(\tau)\hat{N}_{a_2}(t)\rangle = \frac{N_a^2}{4}\epsilon(\tau)I_1. \tag{B.69}$$

We finally have

$$\text{Cov}(\hat{J}_z(\tau), \hat{S}_b(\tau)) = \chi_1\sqrt{N_{\text{ph}}}N_a\epsilon(\tau), \tag{B.70}$$

where we used again $\chi = \frac{g^2\Omega}{c}$. For the second covariance we use Eq. (B.50) for $t < t'$ and we obtain

$$\int_0^\tau dt \, \langle \hat{N}_{a_1}(t)\hat{N}_{a_1}(\tau)\rangle = \frac{N_a^2}{4}\epsilon(\tau)I_1 + \frac{N_a}{2}\epsilon(\tau)\tau \tag{B.71}$$

$$\int_0^\tau dt \, \langle \hat{N}_{a_1}(t)\hat{N}_{a_2}(\tau)\rangle = \frac{N_a^2}{4}\epsilon(\tau)I_1. \tag{B.72}$$

Hence, we finally get the same result for both covariances as we expected

$$\text{Cov}(\hat{J}_z(\tau), \hat{S}_b(\tau)) = \text{Cov}(\hat{S}_b(\tau), \hat{J}_z(\tau) = \chi_1\sqrt{N_{\text{ph}}}N_a\epsilon(\tau). \tag{B.73}$$

B.3.4   Quantum Enhancement Parameter ξ_s

Substituting Eq. (B.63) and (B.73) into Eq. (B.5) we get

$$\text{Var}(\hat{S}_2(\tau)) \approx \frac{N_a}{4}\epsilon(\tau)\left(1 - \frac{\chi_1^2 N_{\text{ph}}N_a\epsilon(\tau)}{\chi_1^2 N_{\text{ph}}N_a\overline{\epsilon(\tau)} + 1/2}\right). \tag{B.74}$$

Using the atomic equations we find the expectation value of $\hat{J}_x$ for $(\chi_1^2 + 2\chi_2)N_{\text{ph}} << 1$

$$\langle \hat{J}_x(t)\rangle \approx \frac{N_a}{2}e^{-(\chi_1^2+2\chi_2)N_{\text{ph}}}, \tag{B.75}$$

where we have defined $\chi_2 \equiv g^2\Gamma/c$. Now we can express $\epsilon(\tau)$ in a more convenient way $\epsilon(\tau) = e^{-2\chi_2 N_{\text{ph}}}$. Finally, the squeezing parameter is given by

$$\xi_{s_2} \approx e^{(\chi_1^2+\chi_2)N_{\text{ph}}}\left(1 - \frac{\chi_1^2 N_{\text{ph}}N_a\epsilon(\tau)}{\chi_1^2 N_{\text{ph}}N_a\overline{\epsilon(\tau)} + 1/2}\right)^{1/2}, \tag{B.76}$$

where for convenience we present again all the parameter definitions we made throughout this calculation

$$\chi_1 \equiv \frac{g^2\Omega}{c}, \qquad \chi_2 \equiv \frac{g^2\Gamma}{c}, \qquad \overline{\epsilon(\tau)} \equiv \frac{1}{\tau}\int_0^\tau \epsilon(t)dt, \qquad \epsilon(\tau) = e^{-2\chi_2 N_{\text{ph}}}. \tag{B.77}$$

Appendix C

Truncated Wigner Method

A classical system consisting of N distinguishable particles, in the d-dimensional case, can be simply described by $2Nd$ real numbers. The factor 2 comes from the need to describe both the position and velocity of each particle. Thus, the dimensionality of this system increases linearly with N. However, in the quantum case the situation becomes more complicated. In the case of many indistinguishable particles, considering M available modes, the general state is given by

$$|\Psi\rangle = \sum_{n_1=0}^{N} \sum_{n_2=0}^{N} ... \sum_{n_M=0}^{N} C_{n_1,n_2,...,n_M}(t)|n_1, n_2, ..., n_M\rangle, \tag{C.1}$$

where we have assumed that each mode can be occupied by N particles. We need $\propto N^M$ complex numbers in order to describe that state. Hence, the dimensionality of this system grows tremendously faster with the number of particles, compared to the classical case. Thus, it is apparent that the numerical solution of the dynamics of such a system becomes easily intractable even for modest values of N and M.

Phase-space methods, which allow us to describe the dynamics of the system by examining the time evolution of a quasi-probability distribution, could help us deal with that problem. We find the equation of motion for the corresponding distribution, which is a partial differential equation (PDE), by determining correspondences between operators of the master equation and complex variables of the distribution. Luckily, in some cases the equation of motion for the probability distribution has the form of a Fokker-Plank equation (FPE), which is used to describe the drift and diffusion of classical distributions. All FPEs can be mapped to an ensemble of stochastic differential equations (SDEs) [75]. So, we can describe the dynamics of a system with N indistinguishable particles and M modes using only M different SDEs. Hence, this process leads to the reduction of the dimensionality of the system, as now it scales with the number of the available modes and

not with the size of the Hilbert space. In our case, we are going to focus on a specific phase-space method, the truncated Wigner (TW) approximation.

In this appendix, we start by introducing the Wigner function. We then give a brief presentation of the tools from stochastic calculus, which are necessary in order to be able to describe the whole process of moving from the master equation to a PDE and then to a SDE. We are going to examine the simple example of an anharmonic oscillator, in order to see in practise how the whole process works. Also, we will see how we can calculate symmetrically ordered expectation values and how we are going to implement them numerically. The TW method, and generally phase-space methods, go beyond the mean field theory we examined in Chapter 2, since they include the quantum fluctuations of the field under consideration. This is the reason why, we used the powerful method of the TW approximation in Chapters 5 and 6, where the quantum fluctuations of both the atomic and light fields play a significant role to the whole dynamics of the system.

C.1 Wigner Function

Commonly, the Wigner function is introduced in the literature [67, 69] as the Fourier transformation of the symmetric characteristic function $\chi[\hat{\rho}, \lambda]$,

$$W(\alpha) = \frac{1}{\pi^2} \int d^2\lambda e^{\lambda^* \alpha - \lambda \alpha^*} \chi[\hat{\rho}, \lambda], \tag{C.2}$$

which is defined as the expectation value of the displacement operator

$$\chi[\hat{\rho}, \lambda] = \text{Tr}\left[\hat{D}(\lambda)\hat{\rho}\right] = \text{Tr}\left[\hat{\rho}e^{\lambda \hat{a}^\dagger - \lambda^* \hat{a}}\right]. \tag{C.3}$$

Here, $\hat{\rho}$ is the density matrix of the system under consideration, $\hat{a}$ is the usual annihilation operator of a simple harmonic oscillator and λ is a complex number. The Wigner function can be used in order to calculate symmetrically ordered expectation values [67, 69]

$$\left\langle \left\{ (\hat{a}^\dagger)^n, \hat{a}^m \right\}_{\text{sym}} \right\rangle = \int d^2\alpha W(\alpha)(\alpha^*)^n \alpha^m = \overline{(\alpha^*)^n \alpha^m}, \tag{C.4}$$

where $\{...\}_{sym}$ denotes symmetric ordering, meaning an equally weighted average of every possible permutation of the non-commuting operators. Also, in the second equality we essentially treat the Wigner function as a probability distribution, since we take the average of an arbitrary function $f(\alpha, \alpha^*) = (\alpha^*)^n \alpha^m$, which depends on the phase-space variables, over $W(\alpha)$. More precisely, the Wigner function is referred as quasi-probability distribution, as it is not necessarily positive, but in many cases it is either positive or it is well approximated by a positive function. In these cases we can calculate the expectation value

of any symmetrically ordered operator, by randomly sampling α and α^* from $W(\alpha, \alpha^*)$ and calculating the corresponding average function, $f(\alpha, \alpha^*)$, over many such samples, as Eq.(C.4) indicates. We are going to analyse this procedure in more detail in the following sections.

C.2 Stochastic Calculus

In this section, we give a brief introduction of some concepts of stochastic calculus that we are going to need, in order to describe the mapping from PDEs of probability distributions to SDEs, which we will analyse in the following sections. Excellent descriptions presenting these concepts with clarity and at some points in more detail could be found in the following theses [74, 83]. The interested reader, who wants a more in depth understanding of those concepts is referred to [75, 172].

We begin from the differential equation describing the time evolution of some physical quantity $x(t)$:

$$\frac{dx}{dt} = a(x,t) + b(x,t)\xi(t), \tag{C.5}$$

where $a(x,t)$ and $b(x,t)$ are considered known functions of x and t, while $\xi(t)$ is a rapidly fluctuating random term in time. Consequently $x(t)$, which is the variable of interest would be a random variable. This is the reason why the solution of Eq. (C.5) is called a stochastic process. The random variable $\xi(t)$ is called white noise and it is an idealization of a realistic fluctuating signal, since its correlation function is given by a delta function, $\langle \xi(t)\xi(t') \rangle = \delta(t - t')$. That means that $\xi(t)$ and $\xi(t')$ are statistically independent for $t \neq t'$. Also $\langle \xi(t) \rangle = 0$, as any non-zero mean value could be included in $a(x,t)$ [75]. We expect Eq. (C.5) to be integrable, so we define the integral of white noise as

$$W(t) = \int_0^t dt' \xi(t'). \tag{C.6}$$

$W(t)$ is called a Wiener process and while it is a continuous function it is non-differentiable, which means that Eq.(C.5) is not well defined. However, we can write the corresponding integral equation

$$x(t) - x(0) = \int_0^t a(x(s), s)ds + \int_0^t b(x(s), s)\xi(s)ds, \tag{C.7}$$

which can be now interpreted consistently, but we should define the Ito stochastic integral first, in order the last term to make sense.

C.2.1   Ito Integral

The stochastic integral of an arbitrary function $g(t)$ between t_0 and t is of Rieman-Stieltjes type. That means that we should divide our variable t into n sub-intervals, e.g the ith one is $[t_{i-1}, t_i]$, as we used to do in the traditional Rieman integrals. We also have τ_i, which are intermediate points of each interval, e.g $t_{i-1} \leq \tau_i \leq t_i$. The stochastic integral would be given by the limit of the partial sums of all subintervals

$$\int_0^t g(s)dW(s) = \lim_{n\to\infty} \sum_{i=1}^n g(\tau_i) \left[W(t_i) - W(t_{i-i}) \right]. \tag{C.8}$$

For traditional Rieman integrals the choice of τ_i does not have any effect on the result, but this is not the case for stochastic integrals. We can choose $\tau_i = t_{i-1}$, which gives zero for the ensemble average of the integral [75]

$$\overline{\int_0^t g(s)dW(s)} = 0. \tag{C.9}$$

This choice ($\tau_i = t_{i-1}$) defines the so-called Ito stochastic integral, which is given by

$$\int_0^t g(s)dW(s) = \lim_{n\to\infty} \sum_{i=1}^n g(t_{i-1}) \left[W(t_i) - W(t_{i-i}) \right]. \tag{C.10}$$

C.2.2   Ito's Formula

We can now use the Wiener increment

$$dW(t) = W(t + dt) - W(t) = \xi(t)dt, \tag{C.11}$$

in order to write Eq.(C.5) in a more convenient form

$$dx = a(x,t)dt + b(x,t)dW(t). \tag{C.12}$$

In the following we are going to use the so-called Ito differential rules, which we just present here $dW^2 = dt$, $dtdW = 0$ and dW is of the order $dt^{1/2}$, but the corresponding derivations can be found in [75]. We also consider that all infinitesimals of order greater than dt are zero [74]. For a general function $f[x(t)]$, which depends on the stochastic process $x(t)$, but does not depend explicitly on time t, we find the infinitesimal change by expanding $f[x(t) + dx(t)]$ around $x(t)$

$$df\left[x(t)\right] = f\left[x(t) + dx(t)\right] - f\left[x(t)\right]$$

$$= f[x(t)] + \frac{\partial f}{\partial x}[x(t) + dx(t) - x(t)] + \frac{1}{2}\frac{\partial^2 f}{\partial x^2}[x(t) + dx(t) - x(t)]^2 - f[x(t)]. \tag{C.13}$$

We substitute Eq. (C.12) in the above equation and use the Ito differential rules, in order to get

$$df = \left(a(x,t)\frac{\partial f}{\partial x} + \frac{1}{2}\frac{\partial^2 f}{\partial x^2}b(x,t)^2 \right) dt + b(x,t)\frac{\partial f}{\partial x}dW(t), \tag{C.14}$$

where as aforementioned, we kept only infinitesimals of order up to dt.

C.2.3 Connection Between Fokker-Planck Equation and SDE

Now, we want to find the connection between a FPE and a SDE. We consider that the stochastic process $x(t)$ has a probability density function $P(x,t)$, thus the ensemble average of an arbitrary function of the stochastic process, $f(x)$, would be given by

$$\overline{f(x)} = \int dx f(x) P(x,t). \tag{C.15}$$

We find the time evolution of the ensemble average of $f(x)$ using Ito's formula, Eq. (C.14)

$$\overline{\frac{\partial f}{\partial t}} = \overline{\left(a(x,t)\frac{\partial f}{\partial x} + \frac{1}{2}\frac{\partial^2 f}{\partial x^2}b^2(x,t) \right)}, \tag{C.16}$$

where we used the property of the Wiener process $\overline{dW(t)} = 0$ [75]. Using Eq. (C.15) in both sides of Eq. (C.16) and remembering that f has no explicit time dependence we obtain

$$\int dx f(x)\frac{\partial P}{\partial t} = \int dx P(x,t)a(x,t)\frac{\partial f}{\partial x} + \frac{1}{2}\int dx P(x,t)\frac{\partial^2 f}{\partial x^2}b^2(x,t). \tag{C.17}$$

For the first term in the right hand side we integrate by parts and apply vanishing boundary conditions, namely we obtain

$$\int dx P(x,t)a(x,t)\frac{\partial f}{\partial x} = -\int dx f(x)\frac{\partial}{dx}\left[P(x,t)a(x,t) \right]. \tag{C.18}$$

Similarly for the second integral in the right hand side of Eq. (C.17) we integrate by parts twice and set again vanishing boundary conditions, which gives

$$\int dx P(x,t)\frac{\partial^2 f}{\partial x^2}b^2(x,t) = \int dx \frac{\partial^2 f}{\partial x^2}f(x)b^2(x,t). \tag{C.19}$$

Hence, we finally get

$$\frac{\partial P}{\partial t} = -\frac{\partial}{\partial x}\left[P(x,t)a(x,t) \right] + \frac{1}{2}\frac{\partial^2 P(x,t)}{\partial x^2}b^2(x,t). \tag{C.20}$$

This is the Fokker-Plank equation with $a(x,t)$ and $b^2(x,t)$ being the drift and diffusion coefficients respectively. Eq. (C.12) and Eq. (C.20) realise two equivalent pictures describing a stochastic process $x(t)$, in the sense that both descriptions give the same ensemble averages of physical quantities. Hence, that means that we can map a FPE, Eq. (C.20), to a SDE, Eq. (C.12).

C.3   Operator Correspondences

Here, we aim to show how we can move from the master equation, which shows the time evolution of the density matrix and involves operators, to a PDE, which would give us the time evolution of the Wigner function and involves only complex variables. So, we essentially want to find the appropriate operator correspondences, in order to map the master equation to a PDE. The most clear and understandable way to show this procedure is to examine a specific example. We consider the well known [83, 173] single-mode anharmonic oscillator with Hamiltonian

$$\hat{H} = \hbar\omega\hat{a}^\dagger\hat{a} + \frac{\hbar\Omega}{2}\hat{a}^\dagger\hat{a}^\dagger\hat{a}\hat{a}. \tag{C.21}$$

The master equation is given by

$$\frac{d\hat{\rho}}{dt} = -\frac{i}{\hbar}\left[\hat{H}, \rho\right] = -i\omega(\hat{a}^\dagger\hat{a}\hat{\rho} - \hat{\rho}\hat{a}^\dagger\hat{a}) - i\frac{\chi}{2}(\hat{a}^\dagger\hat{a}^\dagger\hat{a}\hat{a}\hat{\rho} - \hat{\rho}\hat{a}^\dagger\hat{a}^\dagger\hat{a}\hat{a}). \tag{C.22}$$

The Wigner-Weyl representation of an arbitrary operator $\hat{A}(\hat{a}, \hat{a}^\dagger)$ is denoted as $A(\alpha, \alpha^*)$ and is given by the Fourier transformation of the corresponding symmetric characteristic function $\chi_A(\lambda) = \text{Tr}\left[\hat{A}e^{\lambda\hat{a}^\dagger - \lambda^*\hat{a}}\right]$, i.e

$$A(\alpha, \alpha^*) = \frac{1}{\pi^2}\int d^2\lambda\, e^{\lambda^*\alpha - \lambda\alpha^*}\text{Tr}\left[\hat{A}e^{\lambda\hat{a}^\dagger - \lambda^*\hat{a}}\right]. \tag{C.23}$$

Apparently, the Wigner function $W(\alpha)$ is the Wigner-Weyl representation of the density matrix $\hat{\rho}$, and consequently the Wigner-Weyl representation of $d\hat{\rho}/dt$ is simply the time derivative of the Wigner function

$$\frac{\partial W}{\partial t} = \frac{1}{\pi^2}\int \chi\left[\frac{d\hat{\rho}}{dt}, \lambda\right]e^{\lambda^*\alpha - \lambda\alpha^*}d^2\lambda. \tag{C.24}$$

Similarly, we are going to find the Wigner-Weyl representation of all operators being involved in the master equation, Eq. (C.22). Our strategy would be to find a relation between the characteristic function of the operators of interest and $\chi[\hat{\rho}, \lambda]$, and then to find their Wigner-Weyl representation with respect to $W(\alpha)$ (which is the Wigner-Weyl representation for $\chi[\hat{\rho}, \lambda]$), by making the corresponding Fourier transformations. We should also point out here that throughout this process we consider λ and λ^* as two independent parameters, and that we use the Baker-Campbell-Hausdorff formula, in order to write $\hat{D}(\lambda) = e^{\lambda\hat{a}^\dagger - \lambda^*\hat{a}} = e^{\lambda\hat{a}^\dagger}e^{-\lambda^*\hat{a}}e^{-|\lambda|^2/2}$. We firstly calculate the derivative of $\hat{D}(\lambda)$ with respect to λ

$$\frac{\partial\hat{D}(\lambda)}{\partial\lambda} = \hat{a}^\dagger\hat{D}(\lambda) - \frac{\lambda^*}{2}\hat{D}(\lambda) \Rightarrow \tag{C.25}$$

$$\hat{a}^\dagger\hat{D}(\lambda) = \left(\frac{\partial}{\partial\lambda} + \frac{\lambda^*}{2}\right)\hat{D}(\lambda) \tag{C.26}$$

We also take the derivative with respect to λ^*

$$\frac{\partial \hat{D}(\lambda)}{\partial \lambda^*} = \hat{D}(\lambda)\hat{a} - \frac{\lambda}{2}\hat{D}(\lambda) \Rightarrow \tag{C.27}$$

$$\hat{D}(\lambda)\hat{a} = -\left(\frac{\partial}{\partial \lambda^*} + \frac{\lambda}{2}\right)\hat{D}(\lambda) \tag{C.28}$$

Using Eq. (C.26) we can find the characteristic function of $\hat{\rho}\hat{a}^\dagger$ with respect to $\chi\left[\hat{\rho}, \lambda\right]$

$$\chi\left[\hat{\rho}\hat{a}^\dagger, \lambda\right] = \mathrm{Tr}\left[\hat{\rho}\hat{a}^\dagger\hat{D}(\lambda)\right] = \left(\frac{\partial}{\partial \lambda} + \frac{\lambda^*}{2}\right)\chi\left[\hat{\rho}, \lambda\right]. \tag{C.29}$$

Hence, the Wigner-Weyl representation of $\hat{\rho}\hat{a}^\dagger$ would be

$$\frac{1}{\pi^2}\int\int d^2\lambda\, \chi\left[\hat{\rho}\hat{a}^\dagger, \lambda\right] e^{\lambda^*\alpha - \lambda\alpha^*}$$

$$= \frac{1}{\pi^2}\int\int d^2\lambda \left(\frac{\partial}{\partial \lambda}\chi\left[\hat{\rho}, \lambda\right]\right) e^{\lambda^*\alpha - \lambda\alpha^*} + \frac{1}{2\pi^2}\int\int \lambda^*\chi\left[\hat{\rho}, \lambda\right] e^{\lambda^*\alpha - \lambda\alpha^*} d^2\lambda$$

$$= \left(\alpha^* + \frac{1}{2}\frac{\partial}{\partial \alpha}\right)W(\alpha), \tag{C.30}$$

where in the last step we integrated by parts and we discarded the surface terms. Now, we are going to use Eq. (C.28), in order to find the characteristic function for the operator $\hat{a}\hat{\rho}$

$$\chi\left[\hat{a}\hat{\rho}, \lambda\right] = \mathrm{Tr}\left[\hat{\rho}\hat{D}(\lambda)\hat{a}\right] = -\left(\frac{\partial}{\partial \lambda^*} + \frac{\lambda}{2}\right)\chi\left[\hat{\rho}, \lambda\right]. \tag{C.31}$$

Hence, the Wigner-Weyl representation of $\hat{a}\hat{\rho}$ is

$$\frac{1}{\pi^2}\int\int d^2\lambda\chi\left[\hat{a}\hat{\rho}, \lambda\right] e^{\lambda^*\alpha - \lambda\alpha^*}$$

$$= -\frac{1}{\pi^2}\int\int d^2\lambda \left(\frac{\partial}{\partial \lambda^*}\chi\left[\hat{\rho}, \lambda\right]\right) e^{\lambda^*\alpha - \lambda\alpha^*} - \frac{1}{2\pi^2}\int\int \lambda\chi\left[\hat{\rho}, \lambda\right] e^{\lambda^*\alpha - \lambda\alpha^*} d^2\lambda$$

$$= \left(\alpha + \frac{1}{2}\frac{\partial}{\partial \alpha^*}\right)W(\alpha), \tag{C.32}$$

where again in the final step we integrated by parts. Now, in order to do the same for the characteristic function of $\hat{\rho}\hat{a}$, we firstly need to find a way to commute $\hat{a}$ with $\hat{D}(\lambda)$. Thus, by using the relation $\left(\hat{a}^\dagger\right)^n\hat{a} = \hat{a}\left(\hat{a}^\dagger\right)^n - n\left(\hat{a}^\dagger\right)^{n-1}$, which simply comes from the basic commutation relation $[\hat{a}, \hat{a}^\dagger] = 1$, we find

$$\hat{a}\hat{D}(\lambda) = \hat{D}(\lambda)\left(\hat{a} + \lambda\right). \tag{C.33}$$

Following the same procedure, but now for $\hat{D}(\lambda)\hat{a}^\dagger$, we obtain

$$\hat{D}(\lambda)\hat{a}^\dagger = \left(\hat{a}^\dagger - \lambda^*\right)\hat{D}(\lambda) \tag{C.34}$$

Using Eq. (C.33) we find the following relation for the characteristic function of $\hat{\rho}\hat{a}$

$$\chi\left[\hat{\rho}\hat{a},\lambda\right] = \text{Tr}\left[\hat{\rho}\hat{a}\hat{D}(\lambda)\right] = \text{Tr}\left[\hat{\rho}\hat{D}(\lambda)\left(\hat{a}+\lambda\right)\right] = \chi\left[\hat{a}\hat{\rho},\lambda\right] + \lambda\chi\left[\hat{\rho},\lambda\right], \tag{C.35}$$

and we can easily calculate the corresponding Wigner-Weyl representation

$$\frac{1}{\pi^2}\int\int d^2\lambda\chi\left[\hat{\rho}\hat{a},\lambda\right]e^{\lambda^*\alpha-\lambda\alpha^*}$$
$$= \left(\alpha+\frac{1}{2}\frac{\partial}{\partial\alpha^*}\right)W(\alpha) - \frac{1}{\pi^2}\frac{\partial}{\partial\alpha^*}\int\int d^2\lambda\chi\left[\hat{\rho},\lambda\right]e^{\lambda^*\alpha-\lambda\alpha^*}$$
$$= \left(\alpha-\frac{1}{2}\frac{\partial}{\partial\alpha^*}\right)W(\alpha). \tag{C.36}$$

Similarly using Eq. (C.34) for the characteristic function of $\hat{a}^\dagger\hat{\rho}$ we have

$$\chi\left[\hat{a}^\dagger\hat{\rho},\lambda\right] = \text{Tr}\left[\hat{\rho}\left(\hat{a}^\dagger-\lambda^*\right)\hat{D}(\lambda)\right] = \chi\left[\hat{\rho}\hat{a}^\dagger,\lambda\right] - \lambda^*\chi\left[\hat{\rho},\lambda\right] \tag{C.37}$$

and the corresponding Wigner-Weyl representation is

$$\frac{1}{\pi^2}\int\int d^2\lambda\chi\left[\hat{a}^\dagger\hat{\rho},\lambda\right]e^{\lambda^*\alpha-\lambda\alpha^*}$$
$$= \left(\alpha^*+\frac{1}{2}\frac{\partial}{\partial\alpha}\right)W(\alpha) - \frac{1}{\pi^2}\frac{\partial}{\partial\alpha}\int\int d^2\lambda\chi\left[\hat{\rho},\lambda\right]e^{\lambda^*\alpha-\lambda\alpha^*}$$
$$= \left(\alpha^*-\frac{1}{2}\frac{\partial}{\partial\alpha}\right)W(\alpha). \tag{C.38}$$

To summarize we present here all the Wigner-Weyl representations we found

$$\hat{\rho}\hat{a}^\dagger \rightarrow \left(\alpha^*+\frac{1}{2}\frac{\partial}{\partial\alpha}\right)W(\alpha) \tag{C.39}$$

$$\hat{a}\hat{\rho} \rightarrow \left(\alpha+\frac{1}{2}\frac{\partial}{\partial\alpha^*}\right)W(\alpha) \tag{C.40}$$

$$\hat{\rho}\hat{a} \rightarrow \left(\alpha-\frac{1}{2}\frac{\partial}{\partial\alpha^*}\right)W(\alpha) \tag{C.41}$$

$$\hat{a}^\dagger\hat{\rho} \rightarrow \left(\alpha^*-\frac{1}{2}\frac{\partial}{\partial\alpha}\right)W(\alpha). \tag{C.42}$$

Finally, we find the characteristic function of the operator $\hat{a}^\dagger\hat{a}\hat{\rho}$ through $\hat{a}\hat{a}^\dagger\hat{\rho}$, since those two are related via

$$\chi\left[\hat{a}^\dagger\hat{a}\hat{\rho},\lambda\right] = \chi\left[\hat{a}\hat{a}^\dagger\hat{\rho},\lambda\right] - \chi\left[\hat{\rho},\lambda\right]. \tag{C.43}$$

Now, for the characteristic function of $\hat{a}\hat{a}^\dagger\hat{\rho}$ we have

$$\chi\left[\hat{a}\hat{a}^\dagger\hat{\rho},\lambda\right] = \text{Tr}\left[\hat{\rho}\hat{D}(\lambda)\hat{a}\hat{a}^\dagger\right], \tag{C.44}$$

and using Eq. (C.28), (C.34) and (C.26) we obtain

$$\chi\left[\hat{a}\hat{a}^\dagger\hat{\rho}, \lambda\right] = -\left(\frac{\partial}{\partial\lambda^*} + \frac{\lambda}{2}\right)\left[\left(\frac{\partial}{\partial\lambda} + \frac{\lambda^*}{2}\right) - \lambda^*\right]\chi\left[\hat{\rho}, \lambda\right], \tag{C.45}$$

and consequently through Eq. (C.43)

$$\chi\left[\hat{a}^\dagger\hat{a}\hat{\rho}, \lambda\right] = \left[-\left(\frac{\partial}{\partial\lambda^*} + \frac{\lambda}{2}\right)\left(\frac{\partial}{\partial\lambda} + \frac{\lambda^*}{2}\right) + \left(\frac{\partial}{\partial\lambda^*} + \frac{\lambda}{2}\right)\lambda^* - 1\right]\chi\left[\hat{\rho}, \lambda\right] \tag{C.46}$$

Here, we just present the Wigner-Weyl representations of each resulted term from the above equation

$$\frac{1}{\pi^2}\int\int d^2\lambda\,\chi\left[\hat{\rho}, \lambda\right]|\lambda|^2 e^{\lambda^*\alpha - \lambda\alpha^*} = -\frac{\partial}{\partial\alpha}\frac{\partial}{\partial\alpha^*}W(\alpha) \tag{C.47}$$

$$\frac{1}{\pi^2}\int\int d^2\lambda\left(\frac{\partial}{\partial\lambda^*}\frac{\partial}{\partial\lambda}\chi\left[\hat{\rho}, \lambda\right]\right)e^{\lambda^*\alpha - \lambda\alpha^*} = -|\alpha|^2 W(\alpha) \tag{C.48}$$

$$\frac{1}{2\pi^2}\int\int d^2\lambda\left(\frac{\partial}{\partial\lambda^*}\lambda^*\chi\left[\hat{\rho}, \lambda\right]\right)e^{\lambda^*\alpha - \lambda\alpha^*} = -\frac{1}{2}\alpha\frac{\partial}{\partial\alpha}W(\alpha) \tag{C.49}$$

$$\frac{1}{2\pi^2}\int\int d^2\lambda\left(\frac{\partial}{\partial\lambda}\chi\left[\hat{\rho}, \lambda\right]\right)\lambda e^{\lambda^*\alpha - \lambda\alpha^*} = -\frac{1}{2}\left(1 + \alpha^*\frac{\partial}{\partial\alpha^*}\right)W(\alpha), \tag{C.50}$$

where we integrated by parts and discarded all surface terms during all calculations. We finally present the Wigner-Weyl representation of $\hat{a}^\dagger\hat{a}\hat{\rho}$

$$\hat{a}^\dagger\hat{a}\hat{\rho} \to \left(\alpha^* - \frac{1}{2}\frac{\partial}{\partial\alpha}\right)\left(\alpha + \frac{1}{2}\frac{\partial}{\partial\alpha^*}\right)W(\alpha). \tag{C.51}$$

We notice that we could have obtained the same result, by simply combining equations (C.40) and (C.42), in the appropriate order, so as to form $\hat{a}^\dagger\hat{a}\hat{\rho}$.

Using these correspondences we can transform the master equation, Eq.(C.22), into a PDE, which describes the time evolution of the Wigner function and involves only complex variables

$$\frac{\partial W}{\partial t} = i\left[\frac{\partial}{\partial\alpha}\left(\omega\alpha W + \Omega\left(|\alpha|^2 - \frac{1}{2}\right)\alpha W\right) - \frac{\Omega}{4}\frac{\partial^3}{\partial^2\alpha\partial\alpha^*}(\alpha W)\right] + \text{c.c.} \tag{C.52}$$

C.4   Truncated Wigner Approximation

Up to this point we haven't made any approximations yet, and hence Eq. (C.52) perfectly matches with the master equation Eq. (C.22). However, this is still quite hard to solve, due to the final term. Hence, we make the truncated Wigner approximation, by ignoring third order derivatives

$$\frac{\partial W}{\partial t} = i\frac{\partial}{\partial\alpha}\left(\omega\alpha W + \Omega\left(|\alpha|^2 - \frac{1}{2}\right)\alpha W\right) + \text{c.c.} \tag{C.53}$$

We notice that this has the form of a Fokker-Planck equation, Eq. (C.20) with no diffusion term. Hence, this can be mapped to an SDE for the stochastic process of α, as we showed in Sec. (C.2.3)

$$i\frac{d\alpha}{dt} = \omega\alpha + \Omega\left(|\alpha|^2 - \frac{1}{2}\right)\alpha. \tag{C.54}$$

We can find the corresponding SDE for α^*, by taking the conjugate of the above equation. The fact that the FPE, Eq. (C.53), does not have a diffusion term, results in no explicit noise term in the SDE and hence we end up with an ordinary differential equation Eq. (C.54). However, the initial conditions are stochastic and need to be appropriately sampled from the initial Wigner function, as we are going to analyse when we will try to implement numerically the TW method.

C.5   Truncated Wigner for a Multi-Mode Field

In the previous sections we examined the simple case of a single mode field. We can move to a multi-mode field consisting of M modes, by generalizing the formalism we have already structured for the single case. We use the following notation for the M-mode Wigner variable vector $[\alpha_1, \alpha_2..., \alpha_M]^{\mathrm{T}}$, as well as for the complex number λ we have $[\lambda_1, \lambda_2..., \lambda_M]^{\mathrm{T}}$. Thus,

$$\int d^2\boldsymbol{\lambda} = \prod_{j=1}^{M}\int d^2\lambda_j. \tag{C.55}$$

Hence, the M-mode Wigner function would be given by [173]

$$W(\boldsymbol{\alpha}, \boldsymbol{\alpha}^*) = \frac{1}{\pi^{2M}}\int d^2\boldsymbol{\lambda}\, e^{\boldsymbol{\lambda}^\dagger\boldsymbol{\alpha} - \boldsymbol{\alpha}^\dagger\boldsymbol{\lambda}}\chi\left[\hat{\rho}, \boldsymbol{\lambda}\right], \tag{C.56}$$

where $\boldsymbol{\alpha}^\dagger = (\boldsymbol{\alpha}^*)$. This can be written in the more clear form

$$W(\boldsymbol{\alpha}, \boldsymbol{\alpha}^*) = \frac{1}{\pi^{2M}}\int d^2\lambda_1... \int d^2\lambda_M \prod_{j=1}^{M} e^{\lambda_j^*\alpha_j - \lambda_j\alpha_j^*}\chi\left[\hat{\rho}, \boldsymbol{\lambda}\right], \tag{C.57}$$

with the multi-mode characteristic function [83]

$$\chi\left[\hat{\rho}, \boldsymbol{\lambda}\right] = \mathrm{Tr}\left[\hat{\rho}\prod_{n=1}^{M} e^{\lambda_n^*\hat{a}_n - \lambda_n\hat{a}_n^\dagger}\right]. \tag{C.58}$$

We use the field operator $\hat{\psi}(x) = \sum_{n=1}^{M}\phi_n(x)\hat{a}_n$, in order to properly describe a multi-mode field, and we make the obvious generalization to a multi-mode phase space field $\psi(x) = \sum_{n=1}^{M}\phi_n(x)\alpha_n$. Remember that using the Winger function we can calculate symmetrically ordered operator averages, hence we can generalise Eq. (C.4) to

$$\langle\{(\hat{\psi}^\dagger)^n, \hat{\psi}^m\}_{sym}\rangle = \int d^2\boldsymbol{\alpha}(\psi^*)^n\psi^m W(\boldsymbol{\alpha}, \boldsymbol{\alpha}^*) = \overline{(\psi^*)^n\psi^m}. \tag{C.59}$$

For the particular case of $\hat{\psi}^\dagger(x)\hat{\psi}(x)$ we obtain the very interesting result

$$\int d^2\boldsymbol{\alpha}|\psi(x)|^2 W(\boldsymbol{\alpha},\boldsymbol{\alpha}^*) = \left\langle \frac{\hat{\psi}^\dagger(x)\hat{\psi}(x) + \hat{\psi}(x)\hat{\psi}^\dagger(x)}{2} \right\rangle \Rightarrow$$

$$\overline{|\psi(x)|^2} = \left\langle \hat{\psi}^\dagger(x)\hat{\psi}(x) \right\rangle + \frac{\delta(0)}{2}, \tag{C.60}$$

where we used the commutation relation for the field operator $[\hat{\psi}(x),\hat{\psi}(x')] = \delta(x-x')$. This is a very crucial result as it indicates physics beyond the mean field theory. The last term in the above equation realizes quantum fluctuations as it accounts for half a quantum per noise mode, something that it is not incorporated in the mean filed theory [173]. We should mention here that this term $\delta(0)/2$ diverges in case we consider all infinite possible modes of the field, but in our case we consider a finite number of modes and that means that this term would give us a finite contribution to the stochastic average, as we will see in the following sections, where we will discretize our grid. Using the functional derivatives

$$\frac{\delta}{\delta\psi(x)} = \sum_{n=1}^{M} \phi_n^*(x)\frac{\partial}{\partial\alpha_n} \tag{C.61}$$

$$\frac{\delta}{\delta\psi^*(x)} = \sum_{n=1}^{M} \phi_n(x)\frac{\partial}{\partial\alpha_n^*}, \tag{C.62}$$

we can find the correspondences between the density matrix and the Wigner function for the multi-mode case [83, 173]

$$\hat{\rho}\hat{\psi}^\dagger(x) \rightarrow \left(\psi^*(x) + \frac{1}{2}\frac{\delta}{\delta\psi(x)} \right) W \tag{C.63}$$

$$\hat{\psi}^\dagger(x)\hat{\rho} \rightarrow \left(\psi^*(x) - \frac{1}{2}\frac{\delta}{\delta\psi(x)} \right) W \tag{C.64}$$

$$\hat{\rho}\hat{\psi}(x) \rightarrow \left(\psi(x) - \frac{1}{2}\frac{\delta}{\delta\psi^*(x)} \right) W \tag{C.65}$$

$$\hat{\psi}(x)\hat{\rho} \rightarrow \left(\psi(x) + \frac{1}{2}\frac{\delta}{\delta\psi^*(x)} \right) W. \tag{C.66}$$

We consider the multi-mode Hamiltonian

$$\hat{H} = \int dx\hat{\psi}^\dagger(x)\hat{H}_0\hat{\psi}(x) + \frac{U}{2}\int d^3x\hat{\psi}^\dagger(x)\hat{\psi}^\dagger(x)\hat{\psi}(x)\hat{\psi}(x), \tag{C.67}$$

where $\hat{H}_0 = -\frac{\hbar^2}{2m}\nabla^2 + V(x)$ is the single particle Hamiltonian. Using the operator correspondences we found earlier, we can find the time evolution of the Wigner function, corresponding to the master equation $\frac{\partial\hat{\rho}}{\partial t} = -\frac{i}{\hbar}\left[\rho,\hat{H}\right]$

$$i\hbar\frac{\partial W}{\partial t} = -\int d^3x \left\{ \frac{\delta}{\delta\psi}\left[\hat{H}_{sp} + \frac{U}{2}\left(|\psi(x,t)|^2 - \frac{\delta(0)}{2} \right)\psi W \right] \right\}, \tag{C.68}$$

where we have truncated third order derivatives. We can map the resulted Fokker-Planck equation to an SDE as we did in the single mode case

$$i\hbar\frac{\partial}{\partial t}\psi(x,t) = \left[\frac{\hbar^2}{2m}\nabla^2 + V(x) + \frac{U}{2}\left(|\psi(x,t)|^2 - \frac{\delta(0)}{2}\right)\right]\psi(x,t), \qquad \text{(C.69)}$$

where the $\delta(0)$ term has no observable consequence in this case, since it just results in a global phase.

C.6 Numerical Implementation

C.6.1 Single-Mode

In the previous sections we moved from the density matrix description of the system to the Wigner phase-space representation, and in the special case where the time evolution of the Wigner function takes the form of a FPE, we can finally map the dynamics of the system to a SDE. It is conceptually easier to understand the meaning of a SDE, by having in mind that it is something similar to the Heisenberg equation of motion for a system's operator, in the sense that it gives the dynamical evolution of the system, through the Wigner's complex variable. As briefly aforementioned at the end of the previous section, additional noise terms should be included in the initial conditions of the Wigner variables, to model the quantum mechanical fluctuations. This cannot be done exactly, but a good approximation would be to stochastically sample the Wigner distribution of the system's initial state. Here we consider that our initial state is a Glauber coherent state $|\alpha_0\rangle$, since they constitute a good approximation for describing Bose-Einstein condensates, as analysed in Chapter 2, Sec. [2.5.1]. Firstly, we present the well known expectation values of the first and second moments of the amplitude and phase quadratures, defined as $\hat{X} = \hat{a} + \hat{a}^\dagger$ and $\hat{Y} = i(\hat{a} - \hat{a}^\dagger)$, for a coherent state $|\alpha_0\rangle$

$$\langle\hat{X}\rangle = 2\text{Re}(\alpha_0), \qquad\qquad \langle\hat{Y}\rangle = -2\text{Im}(\alpha_0) \qquad \text{(C.70)}$$

$$\langle\hat{X}^2\rangle = 4\text{Re}^2(\alpha_0) + 1, \qquad\qquad \langle\hat{Y}^2\rangle = -4\text{Im}^2(\alpha_0) + 1. \qquad \text{(C.71)}$$

Now, we consider the following initial condition for the Wigner variable

$$\alpha_w(0) = \alpha_0 + \eta, \qquad \text{(C.72)}$$

where η is a complex noise term given by

$$\eta = \frac{1}{2}\left(\xi + i\xi'\right), \qquad \text{(C.73)}$$

where the properties of ξ and ξ' would be determined in such a way, in order Eq.(C.70) and (C.71) to be satisfied. Making use of the Wigner's function property of calculating expectation values of symmetrically ordered operators, we find the corresponding expectation values for the Wigner variables of the amplitude and phase quadratures, $X_w(0) = \alpha_w(0) + \alpha_w^*(0)$ and $Y_w(0) = i(\alpha_w(0) - \alpha_w^*(0))$. Hence, we have

$$\langle X_w(0) \rangle = 2\overline{\text{Re}(\alpha_w(0))}, \qquad\qquad \langle Y_w(0) \rangle = -2\overline{\text{Im}(\alpha_w(0))} \qquad (C.74)$$

$$\langle X_w^2(0) \rangle = 4\overline{\text{Re}^2(\alpha_w(0))}, \qquad\qquad \langle Y_w^2(0) \rangle = -4\overline{\text{Im}^2(\alpha_w(0))}. \qquad (C.75)$$

From the equality of the expectations values $\langle \hat{X} \rangle = \langle X_w(0) \rangle$ and $\langle \hat{Y} \rangle = \langle Y_w(0) \rangle$, we find $\overline{\xi} = 0$ and $\overline{\xi'} = 0$ respectively. Moreover, from the equality of the second moment expectation values $\langle \hat{X}^2 \rangle = \langle X_w^2(0) \rangle$ and $\langle \hat{Y}^2 \rangle = \langle Y_w^2(0) \rangle$ we obtain that $\overline{\xi^2} = 1$ and $\overline{\xi'^2} = 1$ respectively. Hence, ξ and ξ' are noise terms following a Gaussian distribution with mean zero and variance one. Thus, we can now find the consequent relations for η, $\overline{\eta} = 0$ and $\overline{|\eta|^2} = 1/2$. In Fig. [C.1], we depict the Wigner variables of the amplitude and phase quadratures, using $\alpha_w(0)$. We notice that Eq. (C.72) and the corresponding noise relations, reproduces the expected picture for Glauber coherent states, as we had introduced in Chapter 3, Fig. [3.6].
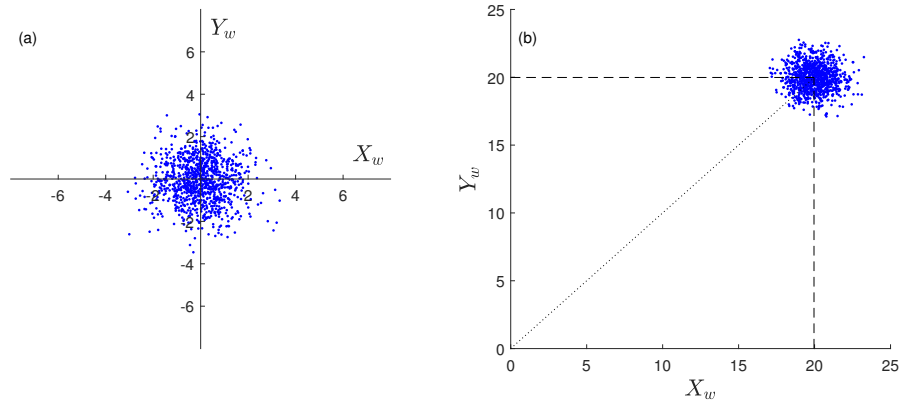

Figure C.1: Scatter plot of the amplitude and phase quadrature using the truncated Wigner method for 10^3 different points, considering (a) a vacuum coherent state, and (b) a coherent state with $N = 100$.

Now that we have managed to find the appropriate initial conditions for the Wigner variables, we can summarize how the whole process works. We begin by sampling random points from the initial state's Wigner function and we find the time evolution of each point using the SDE, Eq. (C.54). So, we obtain many different trajectories, each one

corresponding to the time evolution of each initial random point. Finally, we have to take the average over all these trajectories, in order to calculate any expectation value of symmetrically ordered operators Eq. (C.4).

C.6.2   Multiple Modes

Now, we are moving to the numerical implementation of the M mode field. We have already seen that, if we try to calculate expectation values of symmetrically ordered field operators we encounter the rather awkward situation, where we have a $\delta(0)$ term in our equations, Eq. (C.60). However, as we have already mentioned, that term does not go to infinity, because we do not consider an infinite number of modes. In order to calculate the contribution of that term we should move from the continuous to the discretized case, where we divide our space in M evenly spaced points, since we consider M modes. The step between these points would be given by $\Delta x = x_i - x_{i-1}$, where $[i-1, i]$ is the i-th point. Now all integrals can be converted into sums

$$\int_{-\infty}^{\infty} f(x)dx \rightarrow \sum_{i=1}^{M} f(x_i)\Delta x. \tag{C.76}$$

Also, the Dirac function $\delta(x)$ is converted to the Kronecker delta δ_{ij} via

$$\delta(x_m - x_n) \rightarrow \frac{\delta_{mn}}{\Delta x}. \tag{C.77}$$

So, in our case we can express $\delta(0)$ in the discretized case as

$$\delta(0) \rightarrow \frac{1}{\Delta x}. \tag{C.78}$$

Hence, the number operator $\hat{N} = \int_{-\infty}^{\infty} dx \hat{\psi}^{\dagger}(x)\hat{\psi}(x)$ can now be written as a discrete sum

$$\hat{N} = \sum_{i=1}^{M} \hat{\psi}^{\dagger}(x_i)\hat{\psi}(x_i)\Delta x. \tag{C.79}$$

Let's write now Eq. (C.60) in its descritized form

$$\overline{|\psi(x_i)|^2} = \langle \hat{\psi}^{\dagger}(x_i)\hat{\psi}(x_i) \rangle + \frac{1}{2\Delta x}. \tag{C.80}$$

We take the sum over i and multiply with Δx

$$\sum_{i=1}^{M} \overline{|\psi(x_i)|^2}\Delta x = \left\langle \sum_{i=1}^{M} \hat{\psi}^{\dagger}(x_i)\hat{\psi}(x_i)\Delta x \right\rangle + \sum_{i=1}^{M} \frac{1}{2\Delta x}\Delta x, \tag{C.81}$$

which finally gives the expectation value of the number of particles of the M mode field

$$\sum_{i=1}^{M} \overline{|\psi(x_i)|^2}\Delta x = \langle \hat{N} \rangle + \frac{M}{2}. \tag{C.82}$$

After that result and based on the same strategy we developed in the single mode case, in order to find the initial condition of the Wigner phase space variable we generalize Eq. (C.72) in the following way

$$\psi(x_i, 0) = \sqrt{N}\phi(x_i) + \eta(x_i), \tag{C.83}$$

where now we have the multi-mode noise [83]

$$\eta(x_i) = \frac{1}{2\sqrt{\Delta x}}\left[\xi(x_i) + i\xi'(x_i)\right], \tag{C.84}$$

where as in the single mode case $\xi(x_i)$ and $\xi'(x_i)$ are random numbers, which are statistically independent and both have mean zero, but now this is the case for each point of our grid. Thus, we have [83]

$$\overline{\eta^*(x_n)\eta(x_m)} = \frac{1}{2}\delta(x_n - x_m) = \frac{\delta_{nm}}{2\Delta x}. \tag{C.85}$$

Again, we have chosen the noise properties properly, in order the initial condition Eq. (C.83) to reproduce the right expectation values. For example, this is true for the initial population expectation value, which is given by Eq. (C.82) with $\langle \hat{N} \rangle = N$, since we consider again a coherent initial state, and because the multi-mode noise term satisfies

$$\sum_{i=1}^{M} \overline{|\eta(x_i)|^2} = \frac{M}{2}. \tag{C.86}$$

C.6.3 Single-Mode Expectation Values

In this subsection we present some expectation values calculated using the single mode Wigner function. In general, we calculate the expectation value of only symmetrically ordered operators by using Eq.(C.4). If we are interested on calculating the expectation value of an operator, which is not originally symmetrically ordered, we can simply use Eq.(C.4) for the symmetrical version of the operator and then one of the terms which constitute the symmetrical ordering of the original operator, would be the operator we are interested on.

Firstly, let's consider the simple case of an operator consisting of two operators commuting with each other, for example $\hat{A} = \hat{a}_1\hat{a}_2$, then this straightforwardly gives $\langle \hat{A} \rangle = \langle \hat{a}_1\hat{a}_2 \rangle = \overline{\alpha_1\alpha_2}$, since the symmetric ordering of $\hat{A}$ is equal to itself $\{\hat{a}_1\hat{a}_2\}_{sym} = \hat{a}_1\hat{a}_2$. A nice example that clearly shows that, are the amplitude and phase quadratures of the single mode field, $\hat{X} = \frac{1}{2}(\hat{a} + \hat{a}^\dagger)$ and $\hat{Y} = -\frac{i}{2}(\hat{a} - \hat{a}^\dagger)$, where

$$\langle \hat{X} \rangle = \frac{1}{2}\overline{(\alpha + \alpha^*)} \tag{C.87}$$

$$\langle \hat{Y} \rangle = -\frac{i}{2}\overline{(\alpha - \alpha^*)}. \tag{C.88}$$

On the other hand, when we deal with operators that do not commute with each other, e.g $\hat{A} = \hat{a}^\dagger \hat{a}$, then we are going to get some corrections terms, coming from their non-commutability. The most profound example is the number operator $\hat{N} = \hat{a}^\dagger \hat{a}$, where the expectation value of its symmetric ordering is

$$\left\langle \{\hat{a}^\dagger, \hat{a}\}_{\text{sym}} \right\rangle = \frac{1}{2} \left\langle \left(\hat{a}^\dagger \hat{a} + \hat{a}\hat{a}^\dagger \right) \right\rangle \tag{C.89}$$

$$= \langle \hat{N} \rangle + \frac{1}{2}, \tag{C.90}$$

where in the second equality we used the commutation relation $[\hat{a}, \hat{a}^\dagger] = 1$. From Eq.(C.4) we also know that $\left\langle \{\hat{a}^\dagger, \hat{a}\}_{\text{sym}} \right\rangle = \overline{|\alpha|^2}$, hence the expectation value for the number operator is given by

$$\langle \hat{N} \rangle = \overline{|\alpha|^2} - \frac{1}{2}. \tag{C.91}$$

Following the same procedure we calculate $\langle \hat{N}^2 \rangle$. Here, the corresponding symmetric ordering is more complicated

$$\left\{ (\hat{a}^\dagger)^2, \hat{a}^2 \right\}_{\text{sym}} = \frac{1}{6} \left(\hat{a}^\dagger \hat{a}^\dagger \hat{a}\hat{a} + \hat{a}^\dagger \hat{a}\hat{a}^\dagger \hat{a} + \hat{a}^\dagger \hat{a}\hat{a}\hat{a}^\dagger + \hat{a}\hat{a}^\dagger \hat{a}^\dagger \hat{a} + \hat{a}\hat{a}^\dagger \hat{a}\hat{a}^\dagger + \hat{a}\hat{a}\hat{a}^\dagger \hat{a}^\dagger \right). \tag{C.92}$$

Again, using several times the commutation relation $[\hat{a}, \hat{a}^\dagger] = 1$ and obtaining the expectation values of all terms in the above equation, we have

$$\left\langle \left\{ (\hat{a}^\dagger)^2, \hat{a}^2 \right\}_{\text{sym}} \right\rangle = \langle \hat{a}^\dagger \hat{a}\hat{a}^\dagger \hat{a} \rangle + \langle \hat{a}^\dagger \hat{a} \rangle + \frac{1}{2}. \tag{C.93}$$

After using Eq.(C.4), which gives $\left\langle \left\{ (\hat{a}^\dagger)^2, \hat{a}^2 \right\}_{\text{sym}} \right\rangle = \overline{|\alpha|^4}$, and Eq. (C.91) we finally obtain

$$\langle \hat{N}^2 \rangle = \overline{|\alpha|^4} - \overline{|\alpha|^2}. \tag{C.94}$$

Let's calculate the expectation values of the angular momentum operators of a single mode two component system. For convenience, we write their definitions here

$$\hat{J}_x = \frac{1}{2}(\hat{a}_1^\dagger \hat{a}_2 + \hat{a}_1 \hat{a}_2^\dagger) \tag{C.95}$$

$$\hat{J}_y = -\frac{i}{2}(\hat{a}_1^\dagger \hat{a}_2 - \hat{a}_1 \hat{a}_2^\dagger) \tag{C.96}$$

$$\hat{J}_z = \frac{1}{2}(\hat{a}_1^\dagger \hat{a}_1 - \hat{a}_2^\dagger \hat{a}_2). \tag{C.97}$$

From these we notice that the expectation values of $\hat{J}_x$ and $\hat{J}_y$ are easily calculated, since they constitute by products of commuting operators, while for $\hat{J}_z$ we see that the resulted

correction terms cancel out, hence

$$\langle \hat{J}_x \rangle = \frac{1}{2}\overline{(\alpha_1^* \alpha_2 + \alpha_1 \alpha_2^*)} \tag{C.98}$$

$$\langle \hat{J}_y \rangle = -\frac{i}{2}\overline{(\alpha_1^* \alpha_2 - \alpha_1 \alpha_2^*)} \tag{C.99}$$

$$\langle \hat{J}_z \rangle = \frac{1}{2}\overline{(|\alpha_1|^2 + |\alpha_2|^2)}. \tag{C.100}$$

By calculating the expectation values of the squared angular momentum operators we will get correction terms, since by taking their square we create non-commuting terms

$$\langle \hat{J}_x^2 \rangle = \frac{1}{4}\overline{(\alpha_1^* \alpha_2 + \alpha_1 \alpha_2^*)} - \frac{1}{8} \tag{C.101}$$

$$\langle \hat{J}_y^2 \rangle = -\frac{i}{4}\overline{(\alpha_1^* \alpha_2 - \alpha_1 \alpha_2^*)} - \frac{1}{8} \tag{C.102}$$

$$\langle \hat{J}_z^2 \rangle = \frac{1}{4}\overline{(|\alpha_1|^2 + |\alpha_2|^2)} - \frac{1}{8}. \tag{C.103}$$

In Chapters 5 and 6, we needed to calculate the covariances of angular momentum operators, e.g $\mathrm{Cov}(\hat{J}_x, \hat{J}_z) = \langle \hat{J}_x \hat{J}_z \rangle - \langle \hat{J}_x \rangle \langle \hat{J}_z \rangle$, but in order to do so, we should firstly find the expectation value of their product

$$\langle \hat{J}_z \hat{J}_x \rangle = \frac{1}{4}\overline{(|\alpha_1|^2 - |\alpha_2|^2)(\alpha_1 \alpha_2^* + \alpha_1^* \alpha^2)} - \frac{i}{2}\langle \hat{J}_y \rangle \tag{C.104}$$

$$\langle \hat{J}_z \hat{J}_y \rangle = -\frac{i}{4}\overline{(|\alpha_1|^2 - |\alpha_2|^2)(\alpha_1 \alpha_2^* - \alpha_1^* \alpha^2)} + \frac{i}{2}\langle \hat{J}_x \rangle \tag{C.105}$$

$$\langle \hat{J}_x \hat{J}_y \rangle = -\frac{i}{4}\overline{(\alpha_1 \alpha_2^* + \alpha_1^* \alpha^2)(\alpha_1 \alpha_2^* - \alpha_1^* \alpha^2)} - \frac{i}{2}\langle \hat{J}_z \rangle. \tag{C.106}$$

More precisely, we usually encounter the sum of covariances, of the form $\mathrm{Cov}(\hat{J}_x, \hat{J}_z) + \mathrm{Cov}(\hat{J}_z, \hat{J}_x)$, so we need $\langle \hat{J}_z \hat{J}_x \rangle + \langle \hat{J}_x \hat{J}_z \rangle$ thus the correction terms cancel out.

C.6.4 Multi-Mode Expectation Values

Here, we briefly present some expectation values of symmetrically ordered operators in the M-mode case. We follow the same strategy with the single mode case, but now we have to use the commutation relation $[\hat{\psi}(x_i), \hat{\psi}(x_j)] = \delta(x_i - x_j)$, move to the descritized case $\delta(x_i - x_j) = \delta_{ij}/\Delta x$ and then take the corresponding sums in order to form the expectation values of interest. We have already seen that for the number operator we obtain

$$\langle \hat{N} \rangle = \sum_{i=1}^{M} \overline{|\psi(x_i)|^2} \Delta x - \frac{M}{2}. \tag{C.107}$$

For the number squared we have

$$\langle \hat{N}^2 \rangle = \overline{\left(\sum_{j=1}^{M} |\psi(x_j)|^2 \Delta x \right)^2} - M\langle \hat{N} \rangle - \frac{M^2 + M}{4}. \tag{C.108}$$

In order to examine the expectation values of the angular momentum operators we need two multi-mode fields which satisfy $[\hat{\psi}_a(x_i), \hat{\psi}(x_j)] = \delta_{ab}\delta(x_i - x_j)$. Thus, we can now write

$$\hat{J}_x = \frac{1}{2} \int \left(\hat{\psi}_a^\dagger(x)\hat{\psi}_b(x) + \hat{\psi}_a(x)\hat{\psi}_b^\dagger(x) \right) dx \to \frac{1}{2} \sum_{j=1}^{M} \left(\hat{\psi}_a^\dagger(x_j)\hat{\psi}_b(x_j) + \hat{\psi}_a(x_j)\hat{\psi}_b^\dagger(x_j) \right) \Delta x \tag{C.109}$$

$$\hat{J}_y = -\frac{i}{2} \int \left(\hat{\psi}_a^\dagger(x)\hat{\psi}_b(x) - \hat{\psi}_a(x)\hat{\psi}_b^\dagger(x) \right) dx \to -\frac{i}{2} \sum_{j=1}^{M} \left(\hat{\psi}_a^\dagger(x_j)\hat{\psi}_b(x_j) - \hat{\psi}_a(x_j)\hat{\psi}_b^\dagger(x_j) \right) \Delta x \tag{C.110}$$

$$\hat{J}_z = \frac{1}{2} \int \left(\hat{\psi}_a^\dagger(x)\hat{\psi}_a(x) - \hat{\psi}_b^\dagger(x)\hat{\psi}_b(x) \right) dx \to \frac{1}{2} \sum_{j=1}^{M} \left(\hat{\psi}_a^\dagger(x_j)\hat{\psi}_a(x_j) - \hat{\psi}_b^\dagger(x_j)\hat{\psi}_b(x_j) \right) \Delta x, \tag{C.111}$$

where we have also written their descritized form. Now, we can calculate their expectation values

$$\langle \hat{J}_x \rangle = \frac{1}{2} \overline{\sum_{j=1}^{M} \left(\psi_a^\dagger(x_j)\psi_b(x_j) + \psi_a(x_j)\psi_b^\dagger(x_j) \right) \Delta x} \tag{C.112}$$

$$\langle \hat{J}_y \rangle = -\frac{i}{2} \overline{\sum_{j=1}^{M} \left(\psi_a^\dagger(x_j)\psi_b(x_j) - \psi_a(x_j)\psi_b^\dagger(x_j) \right) \Delta x} \tag{C.113}$$

$$\langle \hat{J}_z \rangle = \frac{1}{2} \overline{\sum_{j=1}^{M} \left(|\psi_a(x_j)|^2 - |\psi_b(x_j)|^2 \right) \Delta x}. \tag{C.114}$$

Finally, for the squared angular momentum operators we get the obvious generalization of the single mode case, but now we are going to have a correction term for each mode of the field [83]

$$\langle \hat{J}_x^2 \rangle = \frac{1}{4} \overline{\sum_{j=1}^{M} \left[\left(\psi_a^\dagger(x_j)\psi_b(x_j) + \psi_a(x_j)\psi_b^\dagger(x_j) \right) \Delta x \right]^2} - \frac{M}{8} \tag{C.115}$$

$$\langle \hat{J}_y^2 \rangle = -\frac{1}{4} \overline{\sum_{j=1}^{M} \left[\left(\psi_a^\dagger(x_j)\psi_b(x_j) - \psi_a(x_j)\psi_b^\dagger(x_j) \right) \Delta x \right]^2} - \frac{M}{8} \tag{C.116}$$

$$\langle \hat{J}_z^2 \rangle = \frac{1}{4} \overline{\sum_{j=1}^{M} \left[\left(|\psi_a(x_j)|^2 - |\psi_b(x_j)|^2 \right) \Delta x \right]^2} - \frac{M}{8}. \tag{C.117}$$